## Title

Optimization, Validation, and Acceleration of Magnetic Resonance Vascular Fingerprinting to Measure Cerebrovascular Function



## Author

Wheeler, Gregory James

## Publication Date

2024

Peer reviewed|Thesis/dissertation

Optimization, Validation, and Acceleration of Magnetic Resonance Vascular Fingerprinting to Measure Cerebrovascular Function

By

GREGORY JAMES WHEELER

DISSERTATION

Submitted in partial satisfaction of the requirements for the degree of

DOCTOR OF PHILOSOPHY

in

BIOMEDICAL ENGINEERING

in the

OFFICE OF GRADUATE STUDIES

of the

UNIVERSITY OF CALIFORNIA

DAVIS

Approved:

Audrey Fan, Chair

David Bissig

Abhijit Chaudhari

Simon Cherry

Committee in Charge

2024

## Abstract

Vascular contributions to cognitive impairment and dementia (VCID) are the second leading cause of dementia and increasing in prevalence as lifespans increase. Clinical MRI traditionally relies on structural abnormalities to identify this vascular dysfunction but lacks microstructure and functional information that could be critical for early identification and assessment of disease. Cerebrovascular dysfunction is one of the only contributors to dementia that can currently be treated, and therefore, earlier identification and subsequent intervention could prevent irreversible structural changes that lead to cognitive decline.

Magnetic resonance fingerprinting (MRF) is a novel approach to MRI acquisition and reconstruction using biophysical modeling in parallel to image acquisition for the simultaneous collection of quantitative, multiparametric brain maps. MRF can be adapted to specifically measure cerebrovascular parameters via MR vascular fingerprinting (MRvF), which produces quantitative cerebral blood volume (CBV), microvascular vessel radius (R), and tissue oxygen saturation maps ($SO_2$) of the whole brain. This dissertation aims to advance MRvF for contrast-free, dynamic mapping of cerebrovascular function.

First, we compare MRvF to another quantitative MRI method, quantitative blood oxygen level dependent (BOLD) imaging, and show consistency between the techniques, reliable oxygen extraction fraction (OEF) measurements, and expected changes in OEF in response to hypoxia and hyperoxia. Next, we describe a new MRvF pattern-matching algorithm developed for improved mapping without contrast agents, investigate the tradeoffs between SNR, sensitivity, and temporal resolution, and optimize an accelerated spin- and gradient-echo (SAGE) sequence for dynamic MRvF. We show adequate SNR with the SAGE sequence from just one repetition for robust whole-brain vascular parameter mapping every 4.5 seconds. Following this, we demonstrate a novel protocol in which this optimized SAGE sequence allows for dynamic and simultaneous acquisition of MRvF and BOLD measures. By combining this with a tailored hypercapnic (5% $CO_2$) breathing paradigm, we show parameter consistency over time and regional changes in BOLD, CBV, R, and $SO_2$ in response to this stimulus, enabling the calculation of cerebrovascular reactivity (CVR). Finally, we use this newly developed imaging paradigm to compare differences in MRvF-derived CVR measurements in healthy young and healthy old adults. We juxtapose these CVR results against more commonly utilized techniques of measuring CVR to compare and validate our MRvF metrics.

Collectively, we demonstrate the development of dynamic MRvF in an ongoing effort toward new quantitative functional imaging biomarkers of cerebrovascular dysfunction with the potential to enable better understanding and earlier diagnoses of diseases like VCID.

## Acknowledgements

This dissertation would not have been possible to complete without the help of many other individuals throughout graduate school. First, I would like to thank my research mentor, Dr. Audrey Fan, who without, I would likely have given up on my goal to pursue a Ph.D. Her support and guidance through the last several years have enabled tremendous technical and personal growth for me as a researcher. She has served as a great role model to look up to both professionally and in how she treats others. I want to thank Dr. David Bissig for providing clinical insight and feedback on this work through his role on my committee. Additionally, allowing me to shadow him in his clinic helped me gain a holistic perspective on this research and left me with impressions from those patients that I will carry with me. Next, I would like to thank Drs. Abhijit Chaudhari and Simon Cherry for serving on my dissertation committee, providing critical technical feedback, and giving me the opportunity to present this research at PEMI meetings over the years.

I want to acknowledge all of those who made these experiments possible. First, a special thanks to the research participants who trusted me enough to volunteer for these studies. Thank you to the Imaging Research Center at UC Davis, especially Jerry Sonico and Dr. Costin Tanase, for teaching me the ins and outs of operating the MRI scanners at Davis. Thanks to Drs. Mary Kate Manhard and Berkin Bilgic for providing and helping us troubleshoot the SAGE sequence critical to many of these studies. Thanks to Dr. Peiying Liu for sending us the breathing apparatus needed for the hypercapnic imaging studies. Lastly, thank you to Drs. Aurélien Delphin and Thomas Christen for providing essential insight into vascular fingerprinting and the biophysical simulations platform.

Next, I want to acknowledge how grateful I am to my lab mates and friends who helped me while conducting this work. Thank you to the IDeA lab for providing significant computational help and, more importantly, for providing me companionship in the office. Thank you to all my lab mates throughout the years: Dakota, Christian, Maisee, Corinne, Linh, Quimby, David, Jessica, Emily, Ice, Anjan, Claire, and everyone else whom I was lucky enough to cross paths with. Your contributions to my growth through your research support and friendship were invaluable. To the additional friends I made at UC Davis, Greg, Bobby, Conary, and Zach, thank you all for making my time in Davis enjoyable and always being there for me.

Finally, I want to express my sincere gratitude to my family. Thank you to Ben, Charley, and Paige for showing me unconditional love and support always. To my parents, thank you for always believing in me, being there for me, and helping me become who I am today. I am incredibly lucky to call you my mom and dad.

# Table of Contents

## List of Figures

## List of Tables

## List of Abbreviations

| | |
|---|---|
| **ACA** | anterior cerebral artery |
| **AD** | Alzheimer's Disease |
| **ADC** | apparent diffusion coefficient |
| **ASL** | arterial spin labeling |
| **BBB** | blood-brain barrier |
| **BOLD** | blood oxygen level dependent |
| **CBF** | cerebral blood flow |
| **CBV** | cerebral blood volume |
| **$CMRO_2$** | cerebral metabolic rate of oxygen consumption |
| **$CO_2$** | carbon dioxide gas |
| **CT** | computed tomography |
| **CVR** | cerebrovascular reactivity |
| **DBV** | deoxygenated blood volume |
| **DCE** | dynamic contrast enhanced |
| **dHb** | deoxygenated hemoglobin |
| **DL** | deep learning |
| **DSC** | dynamic susceptibility contrast |
| **DTI** | diffusion tensor imaging |
| **DWI** | diffusion-weighted imaging |
| **EPI** | echo planar imaging |
| **$EtCO_2$** | end-tidal carbon dioxide |
| **FDG** | [$^{18}$F]-fluorodeoxyglucose |
| **FID** | free-induction decay |
| **FLAIR** | fluid-attenuated inversion recovery |
| **fMRI** | functional magnetic resonance imaging |
| **FOV** | filed-of-view |
| **FT** | Fourier transform |
| **GESFIDE** | gradient echo sampling of the free induction decay and echo |
| **GM** | gray matter |
| **GRE** | gradient echo |
| **Hb** | oxygenated hemoglobin |
| **ICA** | internal carotid artery |
| **ICAD** | intracranial atherosclerotic disease |
| **IP** | inner product |
| **MCA** | middle cerebral artery |
| **MCI** | mild cognitive impairment |
| **ML** | machine learning |
| **MNI** | Montreal Neurological Institute |
| **MR** | magnetic resonance |
| **MRA** | magnetic resonance angiography |
| **MRF** | magnetic resonance fingerprinting |
| **MRI** | magnetic resonance imaging |
| **MRvF** | magnetic resonance vascular fingerprinting |

| | |
|---|---|
| **$N_2$** | nitrogen gas |
| **NMR** | nuclear magnetic resonance |
| **NVU** | neurovascular unit |
| **$O_2$** | oxygen gas |
| **OEF** | oxygen extraction fraction |
| **pASL** | pulsed arterial spin labeling |
| **PC** | phase contrast |
| **PCA** | posterior cerebral artery |
| **$PCO_2$** | partial pressure of carbon dioxide |
| **PD** | proton density |
| **PE** | phase-encoding |
| **PET** | positron emission tomography |
| **$PO_2$** | partial pressure of oxygen |
| **qBOLD** | quantitative blood oxygen level dependent |
| **qMRI** | quantitative magnetic resonance imaging |
| **QSM** | quantitative susceptibility mapping |
| **R** | microvascular vessel radii |
| **$R_2$** | irreversible relaxation rate |
| **$R_2$*** | effective relaxation rate |
| **$R_2$'** | reversible relaxation rate |
| **RF** | radiofrequency |
| **RMSE** | root mean square error |
| **ROI** | region of interest |
| **rSNR** | relative signal-to-noise ratio |
| **SAGE** | spin and gradient echo |
| **$S_aO_2$** | arterial oxygen saturation |
| **SE** | spin echo |
| **SMC** | smooth muscle cell |
| **SMS** | simultaneous multi-slice |
| **SNR** | signal-to-noise ratio |
| **SPECT** | single photon emission computed tomography |
| **$SO_2$** | oxygen saturation |
| **SVD** | small vessel disease |
| **SWI** | susceptibility-weighted imaging |
| **T** | Tesla |
| **TE** | echo time |
| **TOF** | time-of-flight |
| **TR** | repetition time |
| **TSE** | turbo spin echo |
| **VCID** | vascular contributions to cognitive impairment and dementia |
| **VA** | vertebral artery |
| **VASO** | vascular space occupancy |
| **WM** | white matter |
| **WMH** | white matter hyperintensity |

# Chapter 1 – Motivation, Introduction, and Overview

Increasing lifespans and aging populations are leading to an increased prevalence of dementia, with over 50 million people afflicted worldwide and almost 10 million new cases a year.[1] Vascular contributions to cognitive impairment and dementia (VCID) is the second most common cause of dementia, but the heterogeneous mechanisms by which vascular risk factors lead to cognitive decline in VCID are not well understood.[2] Current neuroimaging biomarkers of VCID using magnetic resonance imaging (MRI) rely on structural changes like white matter hyperintensities (WMH).[3,4] There are limitations with this approach to diagnosis and subsequent treatment as physiological changes from vascular disease may precede structural abnormalities, and WMH are non-specific and may reflect many underlying processes. Noninvasive imaging of cerebrovascular function, therefore, may offer an opportunity for earlier detection and intervention.

Current hemodynamic MRI scans are acquired separately and often require contrast agents, leading to a lack of translatable physiological imaging methods to understand and diagnose cerebrovascular diseases. MRI in clinical practice relies almost exclusively on qualitatively weighted images (e.g., $T_1$-weighted, $T_2$-weighted). These images have provided tremendous value since their inception, but their qualitative nature limits their potential. The importance of reproducibility and repeatability are becoming more prevalent as medicine moves further into an era of computational radiology, and qualitative images lack the ability to be precisely compared across time points, scanners, locations, or different subjects.[5–7] Some techniques like quantitative MRI relaxation mapping and arterial spin labeling (ASL) have been developed to produce quantitative data, but these still suffer from other limitations, including low signal-to-noise ratio (SNR) and motion artifacts. Additionally, from a practical standpoint, MRIs are typically long in duration, as each contrast collected requires a separate sequence. This increased scan length is unpleasant or exclusionary for subjects averse to being in tight spaces

for long periods of time, increases the likelihood of subject motion, and increases the cost per patient.

Magnetic resonance fingerprinting (MRF) is a relatively new technique that innovatively leverages MRI acquisition and reconstruction in order to overcome some of these limitations of traditional MRI.[8] MRF utilizes image acquisition in combination with computational magnetic resonance (MR) signal simulations for quantitative multiparametric mapping. The technical benefits of MRF demonstrate a significant advancement, with high translational and clinical potential impact. The ability to generate quantitative maps, as opposed to contrast-weighted images, makes imaging more reproducible and improves the ability for direct intra- and inter-patient comparisons. Reliable quantitative measures will improve patient monitoring over time and provide more useful metrics for comparison while also reducing bias across different sites or scanners in future research. Generating multiparametric maps from a single scan will decrease total scan time, lower costs, and increase ease of access for patients. Faster scans also specifically benefit pediatric, geriatric, cognitively impaired, and other populations who may struggle to lay still in a scanner for upwards of an hour at a time.

MRF was initially implemented to generate quantitative $T_1$ and $T_2$ relaxation maps and other common clinical MR metrics. However, another advantageous aspect of MRF is its flexibility to look at a wide variety of both structural and functional parameters. Essentially, if a parameter that affects MR signal can be described with a biophysical equation for computational modeling, the parameter can be incorporated into the simulations and ultimately extracted from the collected images. MR vascular fingerprinting (MRvF) leveraged this framework to extract cerebrovascular information from MR signals sensitive to oxygenation using the fingerprinting method.[9]

In this dissertation, we describe our contributions to and applications of MRvF and a set of novel techniques and protocols that enable acquisition of multiple quantitative physiological metrics of cerebrovascular function. The long-term goal is to increase the pathophysiological understanding of cerebrovascular diseases and advance the capabilities of the MRvF framework

to be robust for contrast-free and dynamic imaging with the hope of eventually developing MRvF-based imaging biomarkers of cerebrovascular diseases, like VCID.

This dissertation is organized into eight chapters, including this introduction:

**Chapter 2** provides necessary background information on brain anatomy and physiology and how cerebrovascular function changes with age and disease. It also details physiological responses to specific gas stimuli, how those are measured, and how they serve as biomarkers of diseases.

**Chapter 3** broadly reviews different modalities used in brain imaging before discussing specific MRI techniques for imaging cerebrovascular structure and function. It then introduces quantitative MRI techniques and the advantages and principles of magnetic resonance fingerprinting.

**Chapter 4** compares quantitative techniques for measuring brain oxygenation with MRI and performs a retrospective analysis validating those techniques in a study of healthy volunteers experiencing acute hypoxia and hyperoxia.

**Chapter 5** describes the optimization of MRvF acquisition and processing to enable dynamic studies of cerebrovascular function through simulations, retrospective analyses, and prospective analyses that improve accuracy, sensitivity, and temporal resolution.

**Chapter 6** introduces a hypercapnic imaging paradigm that demonstrates the ability of MRvF to measure meaningful changes in cerebrovascular reactivity due to a prescribed hypercapnic stimulus.

**Chapter 7** utilizes the hypercapnic imaging paradigm described in Chapter 6 to investigate how metrics of cerebrovascular reactivity differ between a young cohort and an old cohort of healthy subjects.

**Chapter 8** highlights the key findings and contributions made through this work, gives perspectives on expansions of the work, provides thoughts on future directions of the field, and summarizes the overall significance of the dissertation.

# Chapter 2 – Cerebrovascular Structure and Function

## *2.1 | Cerebrovascular Anatomy and Physiology*

Cerebrovascular anatomy and physiology form the basis for how the brain is nourished, how it responds to various physiological demands, and how pathologies affect its function. This chapter will cover the critical aspects of cerebrovascular structure and function, setting the stage for the value of imaging studies based on cerebrovascular physiology.

The cerebrovascular system encompasses arteries, veins, and capillaries and is pivotal in delivering oxygen-rich blood to the brain and removing carbon dioxide and metabolic waste. This intricate network is sustained by two major pairs of vessels, the internal carotid arteries (ICAs) and the vertebral arteries (VAs). The ICAs branch into the anterior and middle cerebral arteries (ACAs and MCAs), which supply blood to the frontal, parietal, and temporal lobes of the brain. The VAs merge to form the basilar artery, giving rise to the posterior cerebral arteries (PCAs) that provide circulation to the occipital and inferior temporal lobes. A key component of this network is the Circle of Willis, a connected ring at the base of the brain where the ACAs meet with a posterior communicating artery from the PCAs, allowing for collateral circulation in the event of blockage or narrowing in any part of the system. As these arteries disperse throughout the brain, they split and penetrate deeper tissues as smaller vessels called arterioles and eventually capillaries where oxygen is extracted from the blood by the surrounding brain tissues.

The proportion of oxygen that is extracted from the blood as it traverses through the capillaries is known as the oxygen extraction fraction (OEF). The OEF reflects the efficiency of oxygen utilization by brain tissue and is therefore proportional to the cerebral metabolic rate of oxygen consumption ($CMRO_2$) and inversely proportional to the cerebral blood flow (CBF).[10] This oxygen metabolism within the cerebrovascular system involves the intricate process of oxygen being carried by hemoglobin in red blood cells before diffusing across the blood-brain barrier (BBB) and into neurons and glial cells for aerobic metabolism.[11] This diffusion process is driven

by the oxygen concentration gradient between blood and brain tissue and directs the delivery of oxygen to areas of high metabolic demand. Glucose, the brain's primary energy source, follows a similar path but is transported across the BBB via specific glucose transporters, and then utilized in cellular respiration to generate ATP, with oxygen acting as the final electron acceptor in the mitochondrial electron transport chain.[12] After these nutrients are extracted from the blood within the capillaries, the venous system drains the deoxygenated blood back towards the heart. The venous drainage is facilitated from capillaries into venules that converge into the dural venous sinuses, leading to the internal jugular veins and completing the cerebral circulation loop.

A unique aspect of cerebrovascular physiology is the aforementioned BBB, which acts as a selectively permeable divider to protect the brain from pathogens and regulate the exchange of materials between the bloodstream and the brain tissue. It is maintained by endothelial cells, astrocytes, and pericytes. These cells, along with neurons, are components of the neurovascular unit (NVU) that ensure adequate CBF to meet neuronal metabolic demands (**Figure 2.1**). Through neurovascular coupling, the NVU dynamically adjusts vascular tone in response to neuronal activity. The NVU also plays a crucial role in the formation and maintenance of the BBB, which is vital for protecting the brain from systemic influences and maintaining the ionic balance necessary for neuronal activity. The CBF quantifying the blood passing through 100 grams of brain tissue per minute, is finely tuned to about 50 mL/100g/min on average in healthy adults, with higher CBF (~80 mL/100g/min) in gray matter and lower CBF (~20 mL/100g/min) in white matter, demonstrating the brain's regulatory precision.[13,14] This regulation is achieved through cerebral autoregulation, a homeostatic mechanism that allows consistent blood flow despite fluctuations in systemic blood pressure, and is influenced by factors such as carbon dioxide levels, oxygen levels, and the metabolic demands of brain tissue.

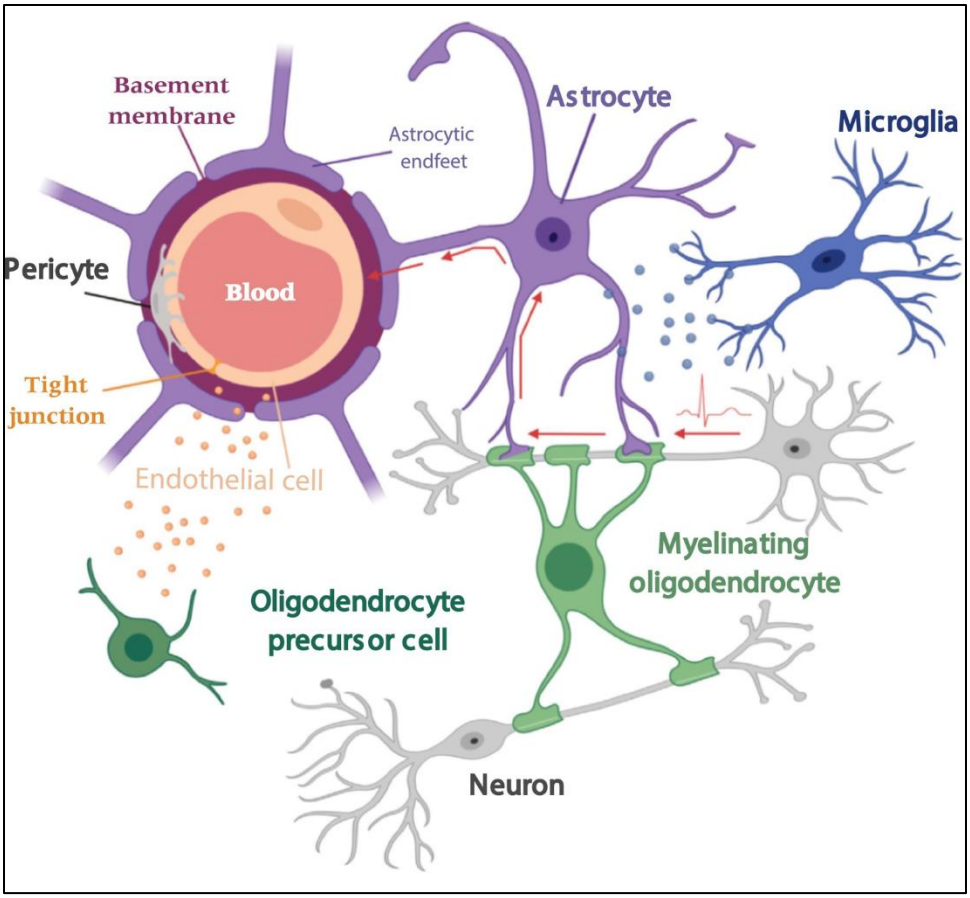


**Figure 2.1. The Neurovascular Unit** (from Quick et al.[15]). The neurovascular unit (NVU) is an intricate cellular assembly essential for maintaining cerebral homeostasis, regulating blood-brain barrier (BBB) permeability, and ensuring proper cerebral blood flow (CBF) in response to neuronal activity. The NVU's components include endothelial cells, astrocytes, pericytes, neurons, and the extracellular matrix, each playing a distinct role in cerebrovascular physiology and pathology. Endothelial cells line the interior surface of blood vessels and are pivotal in forming the BBB. They regulate exchange between the bloodstream and the brain, maintaining a selective barrier that protects neural tissue from toxins and pathogens while allowing essential nutrients to pass. Astrocyte cells extend their end-feet to envelop blood vessels, facilitating communication between neurons and the vascular system. Pericytes are contractile cells located on the capillary walls, closely associated with endothelial cells. Neuron cells are the functional units of the brain, responsible for processing and transmitting information. They communicate with astrocytes and endothelial cells to regulate CBF according to metabolic demands, a process known as neurovascular coupling. While not directly part of the NVU, microglia and oligodendrocytes support, maintain, and protect neurons.

Neurovascular coupling enables the dynamic relationship between neuronal activity and CBF, where increased brain activity prompts enhanced blood flow to specific regions in the brain. Therefore, proper cerebrovascular function is critical to cognitive function, and dysfunction can lead to severe pathologies, including stroke, aneurysms, and, with chronic conditions, to hypertension and diabetes. For instance, stroke can emerge from arterial blockage (ischemic) or vessel rupture (hemorrhagic), leading to significant brain tissue damage and eventual cognitive decline due to inadequate blood supply.

The cerebrovascular system's anatomy and physiology are intricate, with anatomical variety and asymmetry across the population, yet have precise mechanisms to ensure constant supply of nutrients and oxygen. This system's complexity and its role in maintaining cerebral homeostasis underscore the importance of advanced, non-invasive imaging techniques to understand brain vascular function and diagnosing when there is dysfunction. Understanding cerebral hemodynamics, vascular integrity, and metabolic demands is indispensable for developing new methods to diagnose, treat, and prevent cerebrovascular diseases and providing deeper insights into brain function and its response to pathological conditions.

### *2.2 | Cerebrovascular Function with Aging*

The cerebrovascular system undergoes significant changes as part of the normal aging process. These alterations can affect the brain's structure and function, influencing cognitive abilities and the risk of cerebrovascular diseases. Here we will discuss some common cellular, molecular, and tissue-level changes associated with normal aging, how they are observed, and their impact on cerebrovascular anatomy and physiology.

Aging is associated with endothelial dysfunction in cerebral vessels, characterized by reduced endothelium-dependent vasodilation and altered BBB function. This is partly due to decreased production of nitric oxide, an essential vasodilator, and increased oxidative stress, leading to the accumulation of reactive oxygen species. These changes can compromise the BBB integrity, affecting cerebral blood flow regulation and nutrient transport.[16] Aging can also bring about pro-inflammatory responses within the cerebrovascular system. The upregulation of inflammatory markers, like cytokines and adhesion molecules, facilitates the adherence of leukocytes to the endothelium and impairs vascular function.[17] This chronic low-grade inflammation contributes to the progression of atherosclerosis and other vascular pathologies.[18]

One of the most significant tissue-level changes is the increased stiffness of large arteries, due to cellular and molecular alterations.[19] The smooth muscle cells (SMCs) in the vascular wall

experience changes in their contractile and structural proteins, impacting their ability to regulate vessel tone. This can lead to arterial stiffness, reduce the compliance of cerebral vessels, and affect the brain's autoregulatory capacity. Alterations in the extracellular matrix of the vascular wall, including increased collagen deposition and changes in elastin fibers, contribute to arterial stiffness and can alter the microvascular architecture, impacting blood flow distribution within the brain. Arterial stiffness affects pulse wave velocity, leading to poor timing of blood flow to the brain.[19]

Aging is also associated with a reduction in microvascular density, known as microvascular rarefaction. This process reduces the overall surface area available for nutrient and oxygen exchange, which in turn can reduce OEF, and potentially lead to hypoxic conditions within the brain tissue.[18] In some individuals, there is an accumulation of amyloid-beta protein aggregates within the walls of cerebral arteries and arterioles. While more commonly associated with Alzheimer's disease, this can also occur in healthy aging, contributing to vascular dysfunction and increasing the risk of stroke.[20]

Advanced imaging techniques, play a crucial role in observing the cerebrovascular changes associated with aging. Techniques measuring cerebral blood flow and vascular reactivity can assess the impact of these changes on cerebral autoregulation and neurovascular coupling. Some ways in which these are measured include transcranial doppler ultrasound that measures blood flow velocity in the major cerebral arteries, near-infrared spectroscopy that measures changes in oxygenated and deoxygenated hemoglobin concentrations in cortical tissues, positron emission tomography (PET) which can assess cerebral metabolism and blood flow, and MRI which can provide information on the structure and function of the deep brain vasculature.[21] In normal aging, these techniques directly and indirectly detect reduced cerebral blood flow[22], reduced reactivity[23], increased arterial stiffness[24], and reduced cerebral metabolic rates.[25] Combining these diverse techniques can offer a comprehensive picture of how aging affects the

cerebrovascular system, facilitate early detection of dysfunction, and help us better understand the aging process itself.

Overall, the cumulative effect of these aging-related changes is a gradual reduction in the cerebrovascular system's resilience and adaptability. The diminished capacity for vasodilation, along with arterial stiffness and microvascular changes, challenges the ability to maintain stable blood flow under varying metabolic demands. This can lead to increased risk of ischemia and potentially contribute to cognitive decline with aging. Understanding these vascular changes is essential for interpreting data from advanced neuroimaging techniques and for developing improved diagnostic methods to allow for earlier detection of cerebrovascular dysfunction and maintaining good cerebrovascular health into old age.

### *2.3 | Cerebrovascular Pathophysiology in Disease*

Cerebrovascular dysfunction plays a pivotal role in the pathophysiology of many diseases. Understanding these changes is crucial for developing strategies for appropriate diagnosis, prevention, and treatment. In this section we will discuss some common pathological changes associated with cerebrovascular diseases (e.g., stroke, carotid stenosis, small vessel disease (SVD), intracranial atherosclerotic disease (ICAD)), with a deeper dive specifically into how dementia relates to cerebrovascular diseases.

Endothelial dysfunction is a common feature of cerebrovascular diseases, characterized by a reduced ability to produce vasodilators like nitric oxide, increased oxidative stress, and an enhanced inflammatory response. As in normal aging, this dysfunction can lead to altered cerebral blood flow, increased vascular permeability, and thrombosis, contributing to stroke and other cerebrovascular complications, however, in disease these present more acutely or severely.[19] Chronic inflammation is a hallmark of many cerebrovascular diseases, involving the activation of microglia and the infiltration of immune cells from the circulation. This inflammation can lead to further endothelial damage, contribute to the formation of atherosclerotic plaques, and

exacerbate brain injury following ischemic events.[26] Excessive production of reactive oxygen species leads to oxidative stress, damaging cellular components, including DNA, proteins, and lipids. In cerebrovascular diseases, oxidative stress is both a cause and a consequence of endothelial dysfunction and inflammation, perpetuating the cycle of vascular damage.[16]

Atherosclerosis, the buildup of plaques in the arterial walls, is another primary cause of cerebrovascular diseases. Plaque formation narrows and stiffens the arteries, impeding blood flow to the brain and increasing the risk of ischemic stroke. Plaque rupture can also lead to thrombosis and embolic strokes. Beyond atherosclerosis, the arteries can become stiff due to the loss of elastin and the accumulation of collagen in the vascular wall, a process that is accelerated by hypertension and diabetes. This stiffness reduces the arteries' ability to buffer the pulsatile blood flow from the heart, challenging the cerebral autoregulation mechanisms.[27] In cerebrovascular diseases, the brain's microvasculature undergoes excessive degeneration beyond that associated with normal aging, that result in reduced blood flow, impaired nutrient delivery, and increased susceptibility to toxins. These pathophysiological factors effectively reduce the tissue’s ability to obtain oxygen (i.e., decrease OEF), which causes neuronal damage and can eventually lead to cognitive dysfunction.

Advanced imaging techniques, like MRI, are instrumental in diagnosing cerebrovascular diseases by visualizing the brain's vascular structure and detecting regions of degeneration, ischemia, hemorrhage, or arterial blockage. These symptoms have various presentations in structural MRI, often as hypo- or hyperintensities, depending on the physiological phenomenon and the MRI technique being utilized as seen in **Figure 2.2**. These techniques can detect a wide variety of diseases and help differentiate degeneration or dysfunction associated with normal aging versus abnormal pathophysiology.

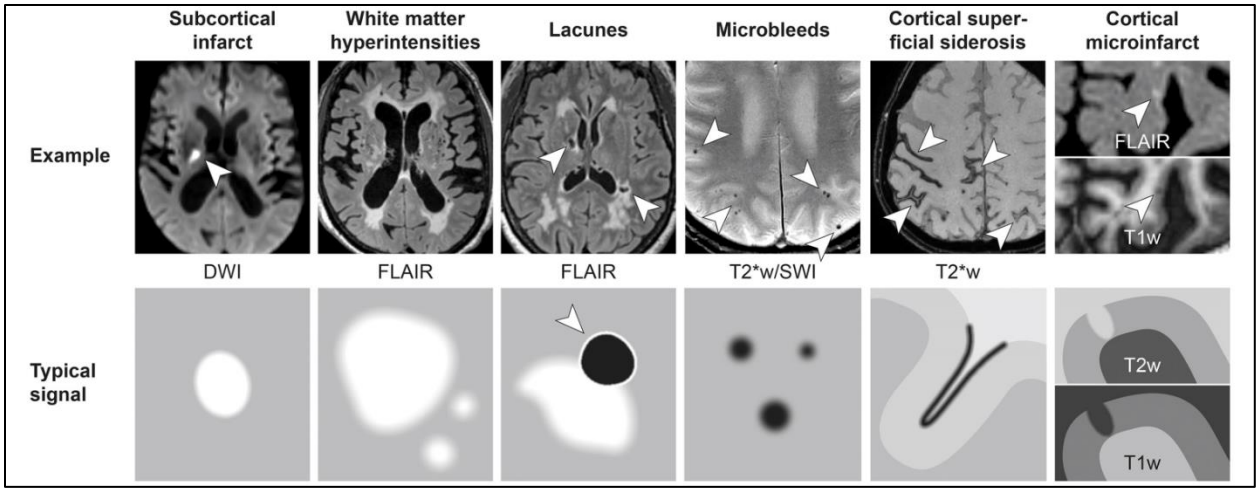


**Figure 2.2. MRI of Cerebrovascular Disease** (from Vemuri et al.[28]). Examples of various MRI contrasts, vascular disease presentations, and how those signals indicate disease in an image. Diffusion-weighted imaging (DWI) shows hyperintense subcortical infarcts. Fluid-attenuated inversion recovery (FLAIR) images display white matter hyperintensities and hypointense lacunes. Susceptibility-weighted imaging (SWI) exposes hypointense microbleeds. $T_2$*-weighted images can reveal superficial siderosis. Lastly, combining multiple co-localized contrasts can indicate and differentiate healthy tissue from abnormalities like microinfarcts.

Preventive strategies for cerebrovascular diseases focus on controlling vascular risk factors. These include managing hypertension, diabetes, and high cholesterol with medications, regular exercise and a balanced diet, and reducing smoking.[29] Treatments for cerebrovascular diseases vary depending on the specific condition but generally include medications to manage symptoms and prevent disease progression, interventions to restore blood flow, and rehabilitation to recover lost functions.[30] These treatments are critical to consider early before an individual experiences an event like a stroke that may cause irreversible damage.

The motivation of the work to follow aims to develop better tools for improving understanding and earlier diagnosis of cerebrovascular-linked dementia. Dementia is a neurological disorder in which there is a decline in cognitive function beyond what is associated with normal aging and may include deterioration of memory, cognition, and the ability to perform everyday activities.[2] The World Health Organization estimates that there are around 50 million people in the world currently living with dementia, and that there will be an as many as 82 million by the year 2030.[1] With these staggering numbers there are immense costs of care associated with dementia totaling an estimated $818 billion global cost in 2015 alone, which equates to ~1%

of the global gross domestic product (GDP).[1] In addition, there is a massive social and societal burden for the families and caregivers of those suffering from dementia.

There are a variety of different clinical presentations that can lead to a dementia diagnosis and multiple proposed pathobiological underpinnings for each type of dementia. While Alzheimer's Disease (AD) is generally considered to be the most common cause of dementia, accounting for about 60% of all dementia cases, vascular-related dementias are the second most common accounting for about 25%.[31] In addition, there is increasing evidence that mixed dementia, in which more than one clinical classification criteria are met, is much more prevalent than previous research has indicated, with some studies even suggesting that mixed dementia consisting of AD and vascular pathologies may be the single most prevalent form of age-related cognitive impairment.[32,33] This finding could be especially important as the vascular risk factors (e.g., atherosclerosis, hypertension, diabetes, etc.) associated with some dementias are currently the only preventable and treatable contributors. Improved understanding and early identification of the vascular contributors leading to dementia could therefore lead to fewer cases, better treatments, reduced speed of disease progression, and increased quality of life.

For vascular contributions to cognitive impairment and dementia (VCID), there are heterogenous clinical presentations that likely contribute to cognitive decline and the underlying mechanisms are not well understood. Observance of structural vascular indicators in MRI (**Figure 2.2**), such as recent stroke[34], microinfarcts[35], white matter hyperintensities (WMH)[3], or intracranial atherosclerosis[36], in conjunction with cognitive decline, can result in a diagnosis of VCID.

Currently, a diagnosis of VCID is given when a patient presents with cognitive impairment and some molecular or neuroradiological biomarker of cerebrovascular disease.[37] The most common neuroradiological modality utilized for this neuroimaging is MRI. MRI is prevalent in neurological care and research largely due to its ability to obtain non-invasive images of the whole brain with excellent soft tissue contrast and without ionizing radiation used in other imaging modalities, such as computed tomography (CT) and positron emission tomography (PET). MRI is

also quite flexible, and by adapting the acquisition sequence of an MRI, one can obtain images weighted to display contrast of specific brain structures of interest, such as grey matter, white matter, or cerebral vessels. The problem with most current MRI diagnostics, however, is that they depend on large structural changes (**Figure 2.2**) that are observable only after significant disease progression or injury, rather than the physiological changes that may precede them. The ability to accurately detect these early, sub-clinical changes in cerebrovascular physiology represents huge potential for better VCID care and outcomes.

### *2.4 | Cerebrovascular Reactivity*

One emerging imaging biomarker for detecting changes in cerebrovascular physiology responses is cerebrovascular reactivity (CVR).[38,39] CVR refers to the ability of cerebral blood vessels to dilate or constrict in response to a vasoactive stimulus, such as changes in blood pressure, metabolic demand, and blood carbon dioxide levels. CVR is a critical measure for understanding the functional integrity of the cerebrovascular system and reflects the health of the vascular endothelium, smooth muscle cells, and the NVU as a whole. Here we will briefly review the cellular mechanisms underpinning tissue-level CVR changes, the impact of normal aging and disease on CVR, and the methodologies for measuring CVR.

CVR is primarily mediated by the endothelial cells on the interior surface of blood vessels. These cells respond to stimuli by releasing vasodilators such as nitric oxide (NO), prostacyclin, and endothelium-derived hyperpolarizing factor, or vasoconstrictors like endothelin-1.[40] NO plays a pivotal role in CVR by diffusing to vascular smooth muscle cells and inducing relaxation through the activation of guanylate cyclase and the subsequent production of cyclic guanosine monophosphate (cGMP). Astrocytes also contribute to CVR by transmitting signals from neurons to the vasculature, thus linking neuronal activity with cerebral blood flow adjustments. Changes in intracellular calcium concentrations within astrocytes can trigger the release of vasoactive substances that influence vascular tone.[40] On a tissue level, CVR encompasses the coordinated

response of the entire cerebrovascular network, from large arteries to arterioles, ensuring adequate blood flow distribution throughout the brain. This is demonstrated in **Figure 2.3**, where the vessels go from a baseline state to dilated after the introduction of a hypercapnic stimulus, and then return to their baseline state after the vasodilatory stimulus is removed.[41]

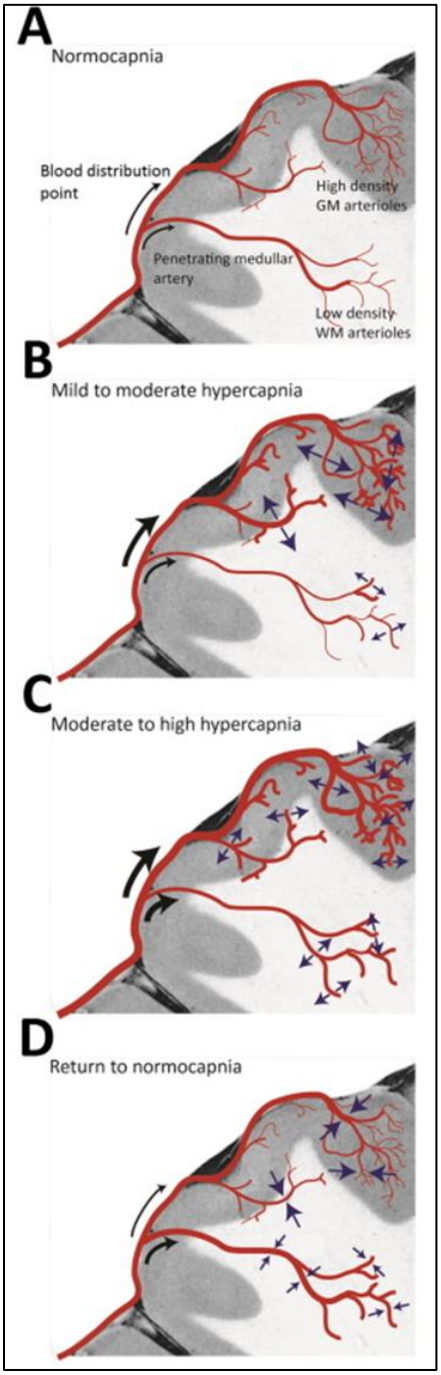


**Figure 2.3. Tissue Response to Hypercapnic Stimulus** (from Bhogal et al.[41]). Schematic of how cerebral vasculature responds to $CO_2$ stimulus. **A)** Normal blood distribution **(B)** increases with the introduction of hypercapnic gas **(C)** until reaching some maximal response and **(D)** returns to normal after hypercapnic gas is removed.

Normal aging is sometimes associated with a decline in CVR.[42] This decline is attributed to several factors, including increased arterial stiffness, reduced endothelial nitric oxide availability, and diminished smooth muscle cell responsiveness. These changes result in a decreased capacity of the cerebrovascular system to adequately adjust blood flow in response to metabolic demands and contribute to the increased risk of developing cerebrovascular diseases and cognitive decline observed in the elderly population.[43]

Pathological conditions that affect the vasculature, such as atherosclerosis, hypertension, and diabetes, can lead to structural changes like vessel stiffening, endothelial damage, and impaired autoregulation, ultimately reducing CVR.[42,44,45] In cerebrovascular diseases such as Alzheimer's disease[46–48] and small vessel disease[24], CVR is often significantly impaired. This impairment can be localized, affecting specific brain regions, or more global, impacting the entire cerebrovascular network. For instance, in stroke patients, the ischemic regions may exhibit reduced responses to vasodilatory stimuli[49], while in Alzheimer's disease, widespread endothelial dysfunction can lead to globally reduced CVR.[46]

MRI is a tool commonly used in research to measure CVR in a relatively non-invasive manner. MRI techniques that can detect changes in blood flow (**Figure 2.4A**) acquire images while a global stimulus, like $CO_2$ gas inhalation, breath modulation, or acetazolamide (**Figure 2.4B**), that actively induce a whole-brain cerebrovascular response. By comparing the images acquired at a baseline to the images acquired during the vascular response caused by stimulus administration, the extent of CVR can be determined.

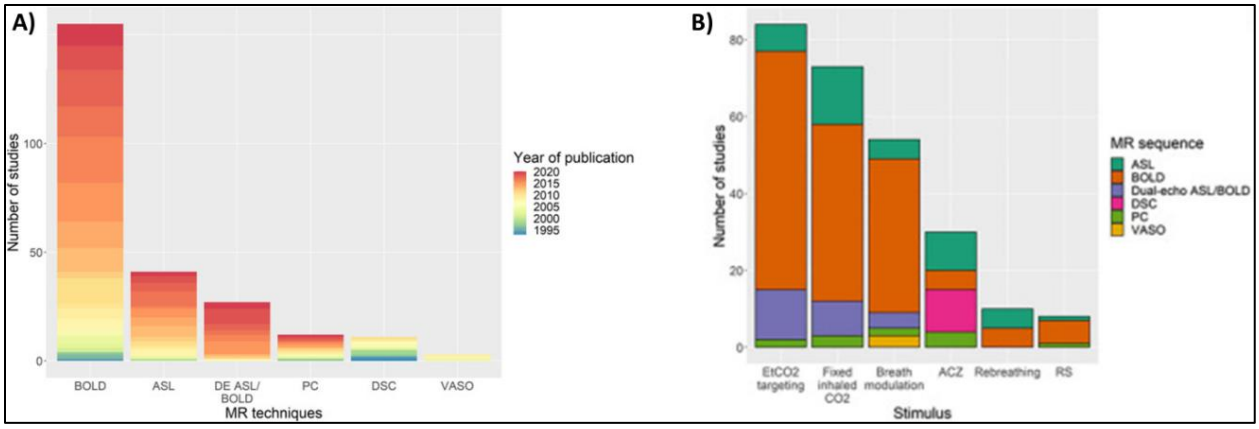


**Figure 2.4. Methods for Imaging Cerebrovascular Reactivity** (from Sleight et al.[39]). **A)** Prevalence of MR techniques used in cerebrovascular reactivity (CVR) studies. **B)** Prevalence of different stimuli used in CVR studies.

CVR is a fundamental aspect of cerebrovascular physiology, reflecting the health and functional integrity of the cerebrovascular system. Understanding the mechanisms underlying CVR, its alterations with aging and in disease, and the methods for its assessment are crucial for advancing our knowledge of cerebrovascular function and developing better diagnostics and targeted interventions to preserve cognitive health.

## *2.5 | Effects of Gas Inhalation on Vascular Physiology*

### *Hypoxia and Hyperoxia Effects on Hemodynamics*

The brain consumes 20% of the total oxygen we breathe, more than any other single organ, despite only making up 2% of total body weight, highlighting its strong dependence on consistent delivery of blood.[50] The oxygen dissociation curve describes how oxygen is transported by hemoglobin in the blood and how it is released to tissues, including the brain.[51] The curve plots the saturation of hemoglobin with oxygen against the partial pressure of oxygen ($PO_2$) in the blood. As hemoglobin becomes more saturated with oxygen, the curve plateaus, indicating that additional increases in $PO_2$ result in smaller increases in arterial oxygen saturation ($S_aO_2$).[51,52] This property allows hemoglobin to load oxygen efficiently in the high-oxygen environment of the lungs and to release it in the lower-oxygen environment of the tissues.

$PO_2$ and the partial pressure of carbon dioxide ($PCO_2$) are key determinants of this oxygen-hemoglobin binding and release process. $PO_2$ in arterial blood of ~100 mmHg allows for about 98% saturation of hemoglobin with oxygen.[53,54] As blood reaches tissues where $PO_2$ is lower due to ongoing oxygen metabolism, oxygen is released from hemoglobin. $PCO_2$ in the blood influences the carbonic acid-bicarbonate buffer system, which is pivotal in maintaining blood pH and facilitating $CO_2$ removal from the body.[55] An increase in $PCO_2$ in the blood from metabolism in brain tissues causes a decrease in blood pH and promotes the release of oxygen from hemoglobin. Conversely, in the lungs, where $CO_2$ is being expelled, the decrease in $PCO_2$ leads to an increase in pH, enhancing hemoglobin's oxygen-binding capacity, and saturating the blood with oxygen prior to being pumped to the rest of the body from the heart.[54,55]

If there are disruptions in normal oxygen delivery to the brain, like during hypoxia, there are compensatory mechanisms to offset the reduced blood oxygen content, like elevations in CBF. Increased CBF is made possible through dilation of intracranial vessels, therefore increasing the blood vessel radii and cerebral blood distribution. Some biological mechanisms that have been proposed to explain this vasodilation during hypoxia include increases in nitric oxide, prostaglandins, adenosine, and sympathetic nerve activity.[56] There has also been found to be impaired neurovascular coupling as a result of alterations in local hemodynamics from changes in oxygen availability.[57] Conversely, increases in blood oxygen content due to hyperoxia have yielded mixed conclusions. While hypoxia leads to a significant decrease in arterial oxygen saturation ($S_aO_2$), hyperoxia leads to a much smaller percent increase in $S_aO_2$, as the normal physiological range in healthy adults is already near 100%. Despite the small change, hyperoxia may benefit ischemic tissue and cause subtle changes in tissue oxygenation.[58]

These changes in hemodynamics have been studied in various pathologies of cerebrovascular disease in which there can be states of acute or chronic hypoxia. Lewis et al.[56] were able to induce significant decreases in $S_aO_2$ (-16-20%) and used ultrasound to observe significant increases in global CBF (+19-28%), arterial CBF (+18-45%), and arterial vessel

diameter (+7-13%) during hypoxia. Xu et al.[58] used MRI to find that when healthy subjects inhaled 14% $O_2$ gas, decreases in $S_aO_2$ (-11±0.8%) led to significant increases in CBF (+9.8±2.3%%). This study also looked at hyperoxia with a 98% $O_2$ gas inhalation condition and found that a modest increase in $S_aO_2$ (+1±0.05%) led to slight, but non-significant decreases in CBF. While these studies primarily looked at CBF, Christen et al.[59] previously looked at tissue oxygen saturation, blood volume fraction, and vessel radius under hypoxia and hyperoxia using MRI methods. They found significant changes in oxygen saturation of the brain when comparing images acquired during hypoxia against those during normoxia or hyperoxia.

*Hypercapnia Effects on Hemodynamics*

The state of high carbon dioxide intake is referred to as hypercapnia. During hypercapnia the vascular smooth muscle cells (SMCs) surrounding brain vessels relax due to the increased concentration of $CO_2$ in the extracellular space and endothelial cells.[60] This increased $CO_2$ content leads to a decrease in pH, SMC relaxation, and ultimately vasodilation. Specifically, increased interstitial $CO_2$ and decreased interstitial pH causes an increase of open SMC and endothelial cell potassium channels, leading to hyperpolarization of those cells. Hyperpolarization leads to decreased activity of voltage-dependent calcium channels and altered membrane potentials in SMCs and therefore vasodilation. Additionally, increased $CO_2$ and decreased pH can cause an increase in nitric oxide synthesis also contributing to SMC relaxation and vasodilation (**Figure 2.5**).[60] This physiological process of SMCs reacting to a $CO_2$ stimulus in the brain is a specific example of CVR as discussed in the prior section and shown previously in **Figure 2.3**.

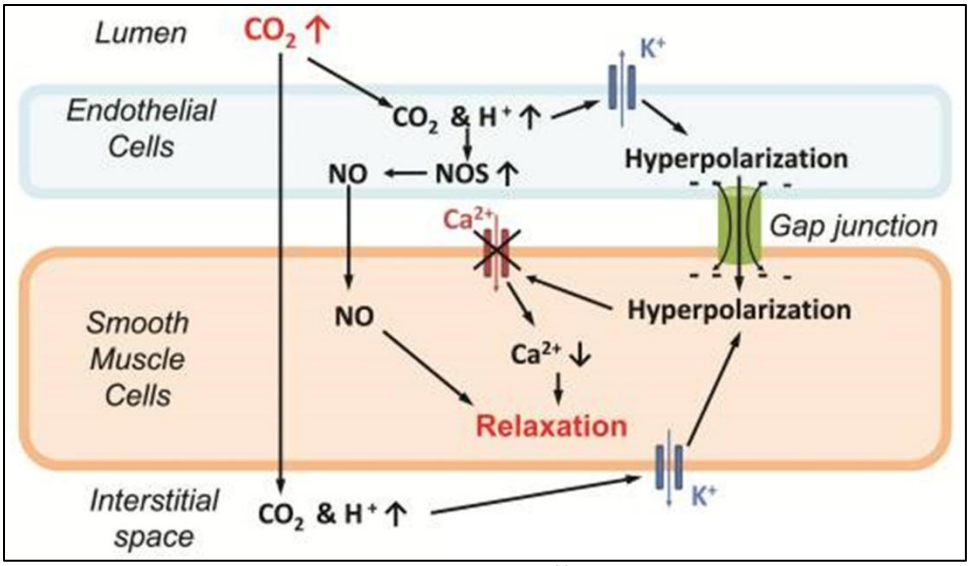


**Figure 2.5. Cellular Response to Hypercapnia** (from Liu et al.[60]). When $CO_2$ is introduced, there is an associated increase in $H^+$ that causes hyperpolarization of smooth muscle cells, relaxation of the adjacent endothelial cells, and a dilation of blood vessels.

Numerous studies have reported CVR changes in response to $CO_2$ gas which lay the foundation for expected CVR changes in healthy individuals and those with cerebrovascular diseases or cognitive impairment. Key methods and results from four of these studies are laid out in **Table 2.1** and will serve as partial reference to the results that are presented in later chapters of this work. In general, these studies demonstrated an ability to detect changes in CVR using MRI via the introduction of $CO_2$ inhalation. The specifics of the imaging methods and gas paradigms in **Table 2.1** will be expanded upon in later chapters.

**Table 2.1. Summary of Results from Previous MRI Hypercapnia CVR Studies**

| Authors | Subject Condition | Imaging Method | Gas Paradigm | Region-of-interest | CVR Response |
|---|---|---|---|---|---|
| Bhogal et al.[41] | Healthy | BOLD MRI | Targeted $EtCO_2$ | Gray Matter | 0.4 %ΔBOLD/mmHg |
| | | | Targeted $EtCO_2$ | White Matter | 0.21 %ΔBOLD/mmHg |
| Hare et al.[61] | Healthy | BOLD MRI | 5% $CO_2$ in air | Gray Matter | 0.11 %ΔBOLD/mmHg |
| | | ASL MRI | | | 4.46 %ΔCBF/mmHg |
| | | BOLD MRI | 5% $CO_2$ in oxygen | | 0.36 %ΔBOLD/mmHg |
| | | ASL MRI | | | 4.97 %ΔCBF/mmHg |
| Cantin et al.[47] | Healthy | BOLD MRI | 7% $CO_2$ in oxygen | Gray Matter | 0.62 %ΔBOLD/mmHg |
| | MCI | | 7% $CO_2$ in oxygen | Gray Matter | 0.36 %ΔBOLD/mmHg |
| | AD | | 7% $CO_2$ in oxygen | Gray Matter | 0.36 %ΔBOLD/mmHg |
| Liu et al.[62] | Healthy | BOLD MRI | 5% $CO_2$ in air | Gray Matter | 0.23 %ΔBOLD/mmHg |
| | | | | White Matter | 0.11 %ΔBOLD/mmHg |
| | Moyamoya | | | Proximal Gray Matter | 0.12 %ΔBOLD/mmHg |
| | | | | Distal Gray Matter | 0.21 %ΔBOLD/mmHg |

CVR = cerebrovascular reactivity, $EtCO_2$ = end-tidal carbon dioxide, BOLD = blood oxygen level dependent, ASL = arterial spin labeling, CBF = cerebral blood flow, MCI = mild cognitive impairment, AD = Alzheimer's disease

In this dissertation, we utilize modulations of both $O_2$ and $CO_2$ in healthy volunteers to develop new imaging tools and techniques to observe the associated physiological changes. These previous studies provide us a useful framework for which to compare the measures we observe and validate our new techniques.

## *2.6 | Conclusions*

This chapter lays the foundational anatomy and physiology knowledge necessary to understand and appreciate the studies and developments described later in this dissertation. By exploring critical structural and functional aspects of the cerebrovascular system, the changes it undergoes with aging, the alterations induced by diseases, and the mechanisms of CVR, this dissertation contextualizes the significance of quantifying cerebrovascular function. Finally, the cerebrovascular responses to hypoxia, hyperoxia, and hypercapnia represent useful indicators of the vascular system's adaptability and resilience and underscore the potential for gaining a better understanding of cerebrovascular function by advancing imaging capabilities.

# Chapter 3 – Neuroimaging of Cerebrovascular Function

## *3.1 | Imaging Background and Basics*

Neuroimaging is a pivotal tool in the study of cerebrovascular physiology, providing insights into the structural, functional, and metabolic aspects of the brain. In the context of cerebrovascular physiology, these techniques are instrumental in diagnosing diseases, understanding cerebral hemodynamics, and evaluating the effects of therapeutic interventions. Neuroimaging techniques utilize diverse physical principles that dictate the capabilities, limitations, and applications of each modality in studying cerebrovascular physiology. In this section, we discuss the physics and applications for the major neuroimaging modalities.

Computed Tomography (CT) is a rapid imaging technique that uses X-rays to create cross-sectional images. CT works by emitting X-rays from a source that pass through the body and are detected at various angles. The attenuation of the X-rays varies with the density of the materials they pass through, creating a map of tissue density. This information can be computationally reconstructed into cross-sectional images. CT is highly effective in detecting hemorrhages, skull fractures, and large brain lesions, making it a crucial tool in the acute assessment of stroke and head injuries.[63] However, its use is limited by low contrast resolution for soft tissues and the exposure to ionizing radiation. One specific type of CT, CT angiography, involves injecting a contrast into the blood to visualize cerebral vessels and assess for aneurysms, vascular malformations, and occlusions.[64]

Positron Emission Tomography (PET) is a molecularly-specific imaging modality that most commonly measures metabolic processes in the brain but can also be used to measure cerebral blood flow and oxygenation.[65,66] PET imaging is based on the detection of gamma rays produced by positron emission. A radioactively labeled tracer emits a positron as it decays that promptly annihilates with a nearby electron and produces pairs of photons traveling in opposite directions. The simultaneous detection of these photon pairs allows for the reconstruction of the tracer's

distribution, reflecting metabolic and molecular processes. Upon injection of radiotracers, PET can visualize cellular level activities and provide insights into brain function and the pathophysiology of diseases. Two prime examples of this are with the radiotracers [$^{18}$F]-fluorodeoxyglucose (FDG) and [$^{15}$O]-oxygen. FDG resembles a glucose substrate and when injected into the bloodstream is able to provide information on brain metabolism.[67] After inhalation, [$^{15}$O]-oxygen gas traverses the systemic physiology just as normal, unlabeled $O_2$, and is able to provide information related to brain OEF and $CMRO_2$.[68] With tracers like these, PET is particularly useful in identifying areas of the brain functionally affected by stroke, evaluating brain tumors, and studying metabolic change in neurodegenerative disorders.[69] Despite this high specificity for metabolic function, PET's use is limited by the need for ionizing radioactive tracers, low spatial resolution, high costs, and long scan times.

Similar to PET, Single Photon Emission Computed Tomography (SPECT) uses gamma rays emitted by injected radiotracers to create images of cerebral blood flow and metabolism.[70] In contrast to PET, SPECT tracers emit a single gamma photon directly, rather than through positron-electron annihilation. The use of a rotating gamma camera and collimators focuses on photons from specific directions, enabling the reconstruction of 3D images. Although SPECT typically has a lower spatial resolution than PET, it is more widely available and less expensive, making it a useful tool for assessing cerebral blood flow, especially in stroke and dementia.[71]

Magnetic Resonance Imaging (MRI) is a versatile imaging modality that uses strong magnetic fields and radio frequency waves to generate detailed images of the brain. MRI is based on the principles of nuclear magnetic resonance (NMR), a phenomenon where nuclei in a magnetic field respond to prescribed radiofrequency (RF) pulses. Hydrogen nuclei, primarily present in the body in water molecules, are aligned by a powerful external magnetic field, disturbed by an RF pulse, and then recorded as they return to their baseline state. The contrast in MRI images arises from differences in tissue properties that affect how quickly the transient excited magnetization signal decays and how quickly these nuclei return to their baseline

positions, allowing for detailed images of soft tissue structures. Unlike CT, PET, or SPECT, MRI does not employ ionizing radiation, making it a safer alternative for repeated imaging. MRI is particularly valuable in neuroimaging due to its high spatial resolution and contrast between different types of soft tissues, which enables detailed visualization of brain anatomy. Due to these inherent advantages, the next sections will explore the contrast mechanisms and quantification of MRI in more depth.

*3.2 | Magnetic Resonance Imaging*

Nuclear Magnetic Resonance (NMR) is the physical phenomenon central to MRI. NMR involves the interaction between atomic nuclei and external magnetic fields, along with the application of RF waves. This section will briefly lay out fundamental principles of NMR and how those are translated to MRI to form images.

NMR is based on the quantum mechanical properties of atomic nuclei. Certain nuclei possess a property known as spin, which makes them behave like tiny magnets. When placed in an external magnetic field ($B_0$), these spinning nuclei align with or against the direction of $B_0$. The net magnetization of these spins tends to align with the applied magnetic field, but because the difference in spins parallel and anti-parallel to $B_0$ is on the order of ppm, a very strong magnetic field is required. The nuclei primarily observed in MRI is the hydrogen nucleus, aka proton, due to its abundance in water and fat in the human body and its high sensitivity to magnetic fields.

The alignment of these protons with the external field is not exact as they precess around the direction of the magnetic field at a specific frequency known as the Larmor frequency (**Figure 3.1A**) This frequency is directly proportional to the strength of the magnetic field as in **Eq. 3.1**.

**Equation 3.1**: $$\omega = \gamma B_0$$

Where $\omega$ is the Larmor frequency, $\gamma$ is the gyromagnetic ratio ($\gamma$ = 42.58 MHz/T for $^1$H), and $B_0$ is the strength of the external magnetic field. By applying a RF pulse at the Larmor frequency, it is

possible to perturb the alignment of $^{1}H$ nuclei and cause them to absorb energy and move into a higher energy state (**Figure 3.1B**).

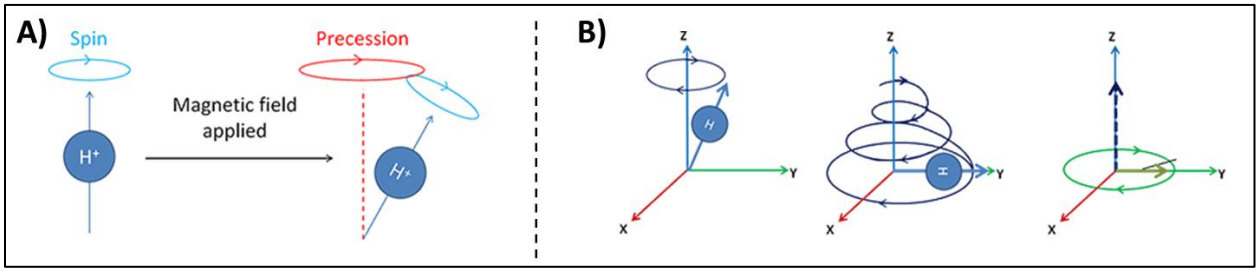


**Figure 3.1. Nuclear Magnetic Resonance** (from Radiology Café[72,73]). **A)** A hydrogen molecule with intrinsic spin and the same hydrogen molecule precessing about the axis of an applied magnetic field (red dotted line). **B)** When that molecule is precessing in a magnetic field in the z-direction and a 90° excitation radiofrequency pulse is played at its Larmor frequency, the molecule tips into a higher energy state in the xy-plane.

Once the RF pulse is turned off, these protons begin to relax back to their original state, during which their potential energy is released and RF signal can be detected by receive coils. There are two types of relaxation processes: $T_1$ (longitudinal recovery) relaxation, where protons realign with the magnetic field, and $T_2$ (transverse decay) relaxation, where protons lose phase coherence with one another. Additionally, while $T_2$ defines the transverse decay, in practice this transverse magnetization decays faster than what $T_2$ would indicate. This faster decay rate is described by $T_2$*, and is the result of magnetic field inhomogeneities, The evolutions of net magnetization due to relaxation were first described by Bloch in **Eq. 3.2**[74], where magnetization ***M(t)*** is affected by the $\gamma$, the total magnetic field ***B(t)***, $T_2$ in the transverse plane, and the equilibrium magnetization $M_0$ and $T_1$ in the direction of $B_0$.

**Equation 3.2a**: $$\frac{dM_x(t)}{dt} = \gamma\big(\boldsymbol{M}(t) \times \boldsymbol{B}(t)\big)_x - \frac{M_x(t)}{T_2}$$

**Equation 3.2b**: $$\frac{dM_y(t)}{dt} = \gamma\big(\boldsymbol{M}(t) \times \boldsymbol{B}(t)\big)_y - \frac{M_y(t)}{T_2}$$

**Equation 3.2c**: $$\frac{dM_z(t)}{dt} = \gamma\big(\boldsymbol{M}(t) \times \boldsymbol{B}(t)\big)_z - \frac{M_z(t) - M_0}{T_1}$$

The signals generated during these relaxation processes are influenced by their local environments, and thus, different tissues result in different relaxation rates and create the contrast seen in MRI. The ability to distinguish tissue contrasts is what enables MRI to produce detailed images of internal structures in the brain and provide insights into anatomy and pathology.

The transition from observing the NMR phenomena to generating MRI involves spatially encoding the NMR signals to create images. As mentioned, when the nuclei return to their equilibrium state, their emitted signals are detected by receive coils and used to reconstruct images. Without spatial encoding all protons in the body would have the same Larmor frequency, be excited by the same RF pulses, and then relax to equilibrium simultaneously, making it impossible to decipher where any signal recorded specifically originated. Spatial encoding in MRI is achieved using gradient magnetic fields, which are superimposed on the primary magnetic field. By varying the magnetic field strength linearly across the body, each slice (**Figure 3.2A**), row, and column within the body experiences a slightly different Larmor frequency. The gradients that cause these slight differences in total magnetic field are typically referred to as slice selection, phase encoding, and frequency encoding gradients, with each being turned on at prescribed times to enable 3D spatial encoding (**Figure 3.2B**). This variation allows for the localization of the NMR signal to specific regions within the body, enabling the reconstruction of detailed image volumes.

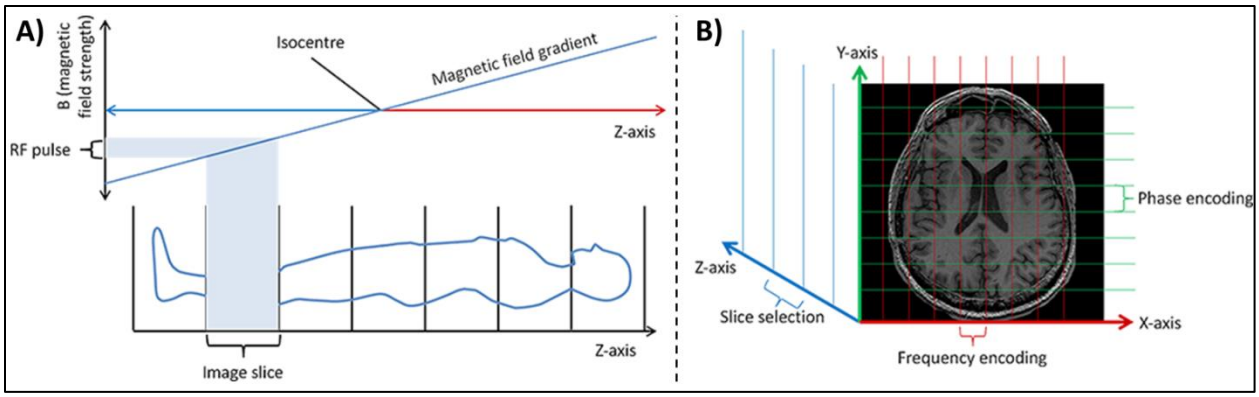


**Figure 3.2. NMR to MRI with Spatial Encoding** (from Radiology Café[73,75,76]). **A)** Schematic of how the slice selection gradient changes Larmor frequencies in space and the region that is excited by an applied RF. **B)** Visualization of how slice selection, phase encoding, and frequency encoding gradients relate to spatial positioning in image space.

The application of NMR principles in MRI revolutionized neuroimaging, offering a powerful and versatile tool for exploring cerebral physiology. Through the careful manipulation of magnetic fields and RF pulses, MRI provides an open and malleable canvas to investigate the brain.

*3.3 | Imaging Perfusion and Cerebrovascular Function*

In studying cerebrovascular physiology, MRI techniques leverage the sensitivity of NMR to measure blood flow and oxygenation. Imaging perfusion and cerebrovascular function is pivotal for understanding the complex dynamics of blood flow in the brain and is crucial for diagnosing and managing cerebrovascular diseases. This section explores common MRI techniques used for vascular imaging and each technique's specific physical principles, unique outputs, and tailored applications.

*Vascular Anatomy MRI*

Magnetic Resonance Angiography (MRA) is a technique that images the blood vessels using MRI. It can be performed with or without contrast agents. Non-contrast techniques, such as Time-of-Flight (TOF) MRA and Phase-Contrast (PC) MRA, rely on the inflow-related enhancement of moving blood spins and the signal phase shift induced by blood flow. Contrast-enhanced MRA uses gadolinium-based agents to increase the signal from blood, improving the visualization of the vascular structures.[77] TOF MRA sequences are sensitive to the flow of blood, making stationary tissue appear dark while enhancing flowing blood. PC MRA sequences are designed to measure the velocity of moving blood, creating images that can map the direction and speed of blood flow. Contrast-enhanced MRA involves the administration of a gadolinium-based contrast agent and the acquisition of $T_1$-weighted images to visualize the vascular system.[78] MRA provides high-resolution images of blood vessels, allowing for the assessment of vessel anatomy, integrity, and the detection of abnormalities. MRA is extensively used clinically in the evaluation of cerebrovascular diseases, including stroke, aneurysms, and vascular malformations.[77,78]

*Contrast-based Perfusion MRI*

Dynamic Susceptibility Contrast (DSC) MRI utilizes contrast agents (typically gadolinium-based) that cause a transient decrease in the MR signal due to $T_2$* relaxation effects when the contrast agents pass through the cerebral vasculature. This technique measures changes in blood volume and flow dynamics as the contrast agent passes through the brain to generate a signal intensity-time curve, from which cerebral blood volume (CBV), cerebral blood flow (CBF), and mean transit time (MTT; the average amount of time it takes blood to travel through a volume) maps can be extracted.[79] The technique employs rapid, $T_2$*-weighted gradient-echo sequences to capture the passage of the contrast agent through the brain's vasculature. DSC-MRI is widely used for stroke evaluation, assessing tumor vascularity, and guiding therapeutic interventions.[80]

Dynamic Contrast-Enhanced (DCE) MRI also involves the use of gadolinium-based contrast agents but focuses on $T_1$ relaxation effects. The contrast agent enhances the signal intensity in areas with increased perfusion and permeability, allowing for the quantification of these parameters over time. DCE-MRI yields information on tissue permeability, including the transfer constant ($K^{trans}$), which reflects the rate at which the contrast agent moves between the blood plasma and the extravascular space.[81] It employs $T_1$-weighted sequences that are sensitive to the contrast agent's presence, enabling detailed analysis of the contrast uptake and washout kinetics. DCE-MRI is particularly useful for assessing tumor blood supply, blood-brain barrier disruption, and the effects of anti-angiogenic treatments.[82]

*Non-contrast Vascular MRI*

Blood oxygen level dependent (BOLD) MRI is based on the magnetic properties of deoxyhemoglobin. Changes in the concentration of deoxyhemoglobin alter the local magnetic field, affecting the $T_2$* relaxation time, and thus the MR signal. BOLD imaging utilizes the relationship of the neurovascular unit that couples increased neuronal activity to increased blood delivery to that region of the brain. The BOLD effect can be imaged with MRI due to the unique

nature of oxyhemoglobin (Hb) and deoxyhemoglobin (dHb) in red blood cells. The conformational difference between the two forms causes only the deoxygenated state of Hb to be paramagnetic, which decreases the MRI signal in its local vicinity (**Figure 3.3**). As an active region of the brain consumes oxygen, it converts Hb to dHb. While this oxygen consumption decreases the MR signal in the active region of the brain, simultaneous blood flow into that region of the brain increases (to supply oxygenated blood) to a greater percentage than the change in oxygen consumption. This decreases the overall dHb fraction in that active area and increases the BOLD signal that can be imaged, indirectly reflecting changes in blood flow and oxygenation associated with neuronal activity. BOLD imaging typically employs $T_2$*-weighted gradient-echo sequences that are sensitive to the magnetic susceptibility effects of deoxyhemoglobin. While primarily known for its role in functional MRI (fMRI) to study neuronal activity, BOLD contrasts can also be used to assess cerebrovascular reactivity and oxygenation.[9]

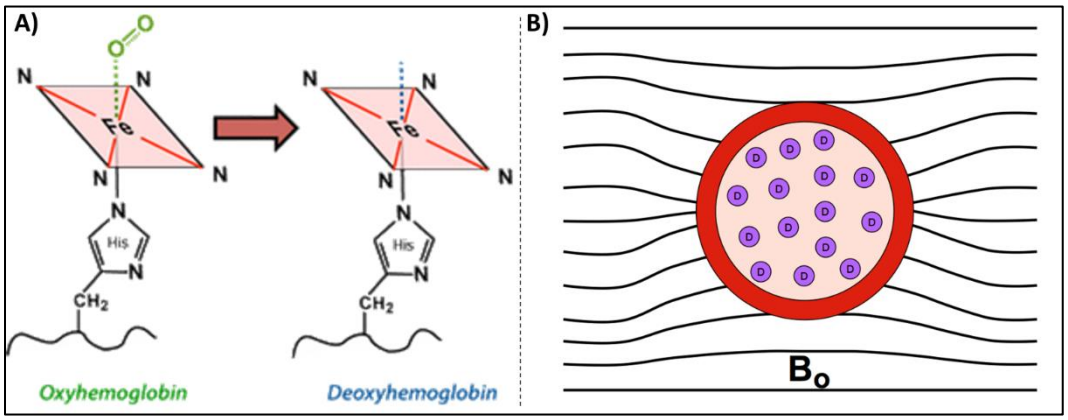


**Figure 3.3. Imaging the BOLD Effect with MRI** (from MRIquestions.com[83]). **A)** The conformational change that occurs when oxyhemoglobin (diamagnetic) is unbound from oxygen and becomes deoxyhemoglobin (paramagnetic). **B)** The paramagnetic deoxyhemoglobin (purple) causes a susceptibility difference in the micro-vessel (red) relative to the surrounding tissue and induces a change in local magnetic field.

While each of these methods can yield critical insights into cerebral hemodynamics, they all have unique limitations. These include only providing large structural cerebrovascular information as in MRA, reducing accessibility with the need for contrast agents as in DCE and DSC, or producing qualitative information as in BOLD. MRI techniques capable of generating a variety of vascular metrics quantitatively and without contrast have the potential to be important translational technical developments.

*3.4 | Quantitative MRI of Cerebrovascular Function*

Quantitative MRI (qMRI) of cerebrovascular function encompasses a range of techniques to measure the physical and functional properties of brain tissues in a quantitative manner. The ability to produce quantitative measures is critical for improved longitudinal monitoring, inter-subject comparisons, and standardization of imaging biomarkers.[84] Co-localized and individualized qMRI-derived maps of various parameters, like in **Figure 3.4**, have the potential to exponentially improve differential diagnoses with the increased prevalence of computational radiology and artificial intelligence in medical imaging.[85,86] This section delves into a few relevant qMRI methods, highlighting their physical principles, acquisition and processing protocols, analytical approaches, and clinical applications in cerebrovascular physiology.

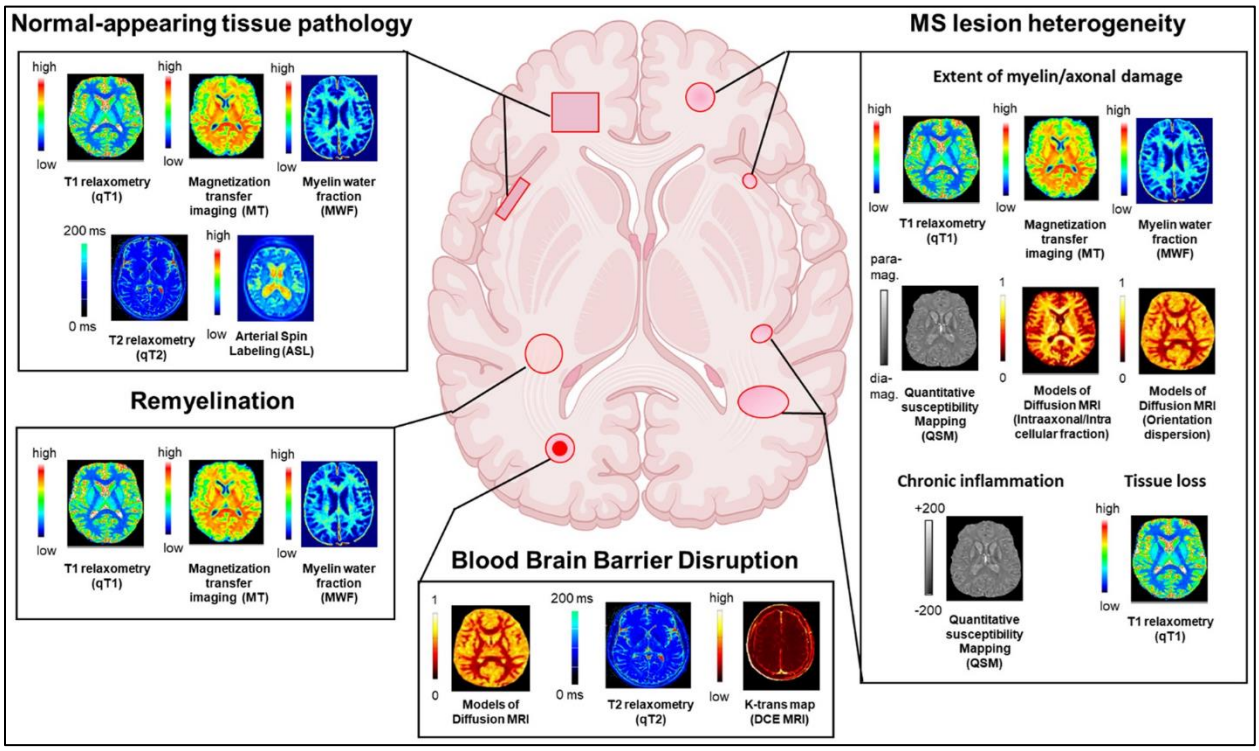


**Figure 3.4. Examples of Quantitative MRI** (from Granziera et al.[86]). An example of how quantitative MRI techniques have been used to study multiple sclerosis. The plethora of approaches and contrasts can provide information about healthy tissue (top left), structural changes (right), normal function (bottom left), and abnormal function (bottom middle).

Arterial Spin Labeling (ASL) MRI is a non-invasive MRI technique that uses magnetically labeled arterial blood as an endogenous tracer to measure CBF. The labeling is achieved by inverting the magnetization of incoming arterial blood upstream of the imaging slice and creating

a difference in magnetization between labeled blood and downstream tissue. This difference in magnetization results in a difference in signal intensity that can be incorporated into a kinetic model to directly measure CBF and provide quantitative maps of blood flow. ASL is used for evaluating cerebral perfusion in various pathologies, including stroke, dementia, and tumors, without the need for contrast agents, making it safe for patients with renal impairment.[87]

Vascular Space Occupancy (VASO) MRI is a technique that quantifies relative changes in CBV by utilizing inversion recovery sequences timed to null the signal from blood and highlight the signal from the extravascular tissue.[88] The difference in signal intensity corresponds to changes in blood volume and is used to generate CBV maps. VASO MRI has been used to map relative changes in blood volume associated with neuronal activity and respiratory challenges without the need for exogenous contrast agents, however, it still requires contrast agents to achieve absolute quantification.[89]

Quantitative Susceptibility Mapping (QSM) utilizes the magnetic susceptibility differences between tissues, which are influenced by their biochemical composition like iron and myelin content. Susceptibility differences lead to phase variations in the MRI signal, which QSM algorithms convert into quantitative maps of tissue magnetic susceptibility. This offers insights into localized susceptibility, which can be indicators of various neurodegenerative diseases, hemorrhages, and other pathologies.[90] The process involves acquiring gradient-echoes to capture phase information followed by mathematical dipole inversion to quantify the susceptibility contributions from different tissues. QSM is particularly valuable for quantifying brain iron levels, which can aid in the diagnosis and monitoring of neurodegenerative diseases like Parkinson's and Alzheimer's diseases. It's also used in identifying calcifications, microbleeds, and evaluating venous oxygen saturation.[90]

Quantitative blood oxygen level dependent (qBOLD) imaging extends the conventional BOLD technique by quantitatively assessing the oxygen saturation level in cerebral tissue via MRI. It relies on the same magnetic susceptibility differences between Hb and dHb as traditional

BOLD, which influence the relaxation rates of blood and surrounding tissues.[91] The qBOLD method requires a multi-echo acquisition, such as a gradient and spin echo or asymmetric spin echo sequence, to quantify both $T_2$* and $T_2$ decay which are then used to estimate the oxygenation level. Two-tissue compartment modeling is applied to separate the contributions of intravascular and extravascular signals. The analysis involves fitting the acquired data to a biophysical model that describes the relationship between transverse decay and blood oxygenation, yielding maps of OEF and deoxygenated blood volume. The qBOLD method has been able to provide valuable neurometabolic information to better understand cerebrovascular responses in diseases like ischemic stroke.[92,93]

qMRI offers significant value in diagnosing and monitoring cerebrovascular diseases by providing precise, objective measurements of tissue properties and enabling the detection of subtle changes that may not be visible with conventional qualitative MRI. Moreover, the qMRI techniques described in this section allow for repeated vascular measurements over time without exposing subjects to contrast agents, making them ideal for longitudinal studies. However, most current qMRI techniques also face limitations. The acquisition and processing of qMRI data can be time-consuming and require sophisticated software and technical expertise, which may limit accessibility and potential for clinical translation. Additionally, the interpretation of qMRI metrics can be complicated and influenced by a range of physiological and technical factors, illustrating the necessity for careful standardization and validation across different MRI systems and study protocols. Despite these challenges, the potential of qMRI to enhance our understanding of cerebrovascular diseases and improve the metrics used for diagnoses and treatments remains substantial.

## *3.5 | Magnetic Resonance Fingerprinting*

### *Principles of Magnetic Resonance Fingerprinting*

Another qMRI technique that can address some of these is magnetic resonance fingerprinting (MRF). MRF was introduced in 2013 by Ma et al.[8] as a novel approach to MRI acquisition and reconstruction with the capability to transform the way in which MRI is performed. MRF enables non-invasive, simultaneous, and quantitative mapping of multiple tissue properties from a single acquisition scan. This technique has potential to bring quantitative MRI to routine clinical use due to its inherent time efficiency, repeatability, and robustness to noise and motion.

Traditional MRI relies largely on qualitatively "weighted" images (e.g., $T_1$-weighted, $T_2$-weighted). This is done by playing a standard sequence with appropriate timings to achieve the contrast of interest before acquiring the image. These images are then examined, with many clinical diagnoses relying on hypo- or hyperintense regions relative to other surrounding tissues rather than a quantitative measure of the difference. This procedure has been the norm due to MR signal intensity not being quantitative itself, as it is a factor of the magnetic field strength, RF pulse profile, gradient strength and heterogeneity, noise, and many other factors aside from tissue properties. Additionally, existing quantitative MRI techniques provide information on a single parameter for each scan resulting in prohibitively long scan times and high sensitivity to external system characteristics.[5] MRF was therefore developed to overcome these shortcomings of conventional MRI and existing qMRI techniques.

MRF uses the assumption that unique tissue properties will generate a unique MRI signal evolution, akin to a fingerprint, when an adequately designed MR pulse sequence is utilized. By varying parameters such as flip angle, repetition time (TR), or echo time (TE), MRF acquires a series of signals that are sensitive to different tissue properties. Rather than using full resolution images of one contrast weighting, MRF compares the signal evolution of each voxel independently to simulated signal evolutions, which reveals the underlying parameters of interest. These simulated signal evolutions are the key aspect in allowing MRF to generate multiparametric

and quantitative metrics. The simulations are centered around the Bloch equations mentioned previously that describe magnetization and relaxation as shown in the combined form in **Eq. 3.3**.[74]

**Equation 3.3**: $$\frac{d\boldsymbol{M}}{dt} = \boldsymbol{M} \times \gamma \boldsymbol{B} - \frac{M_x \boldsymbol{i} + M_y \boldsymbol{j}}{T_2} - \frac{(M_z - M_o)\boldsymbol{k}}{T_1}$$

The change in magnetization (*d**M**/dt*) is dependent on system properties that affect magnetization (***M***) and magnetic fields (***B***) (i.e., flip angle, RF pulse profile, TR, magnetic field strength, etc.) and tissue properties of $T_2$ decay affecting transverse magnetization ($M_{xy}$) and $T_1$ recovery affecting longitudinal relaxation ($M_z$). While conventional MRI waits different amounts of time to acquire images that weight the $T_1$ or $T_2$ component more heavily, MRF uses the Bloch equation to prospectively model how various combinations of tissue properties affect signal decay over time. This also enables MRF to consider multiple parameters that affect signal decay simultaneously.

MRF has three key components: image acquisition (**Figure 3.5A**, **B**, and **C**), dictionary generation (**Figure 3.5D**), and pattern matching for reconstruction (**Figure 3.5E**, **F**, and **G**).[94] A specialized pulse sequence sensitive to changes in tissue parameters of interest is first developed and implemented in parallel into both numerical simulations for dictionary generation and image acquisition (**Figure 3.5A** and **B**). The pulse sequence is used on the scanner to acquire highly under sampled images at multiple timepoints with different signals intensities (**Figure 3.5C**). This allows the signal intensity of each individual voxel to be extracted over time for a unique voxel 'fingerprint' (**Figure 3.5F**). The pulse sequence is also used in parallel for the numerical simulations. With knowledge of the sequence parameters, simulated signal time courses can be calculated with varying values of parameters of interest that represent possible tissue voxels. The range and spacing of parameter values to use in simulations is set by the user and should be dictated by the expected physiological range of those parameters. The entire dictionary is generated by simulating every combination of varied parameters. **Figure 3.5D** shows an example of what four dictionary entries look like with parameters that could be expected in cerebrospinal fluid ($T_1$=5000 ms, $T_2$=500 ms), fat ($T_1$=400 ms, $T_2$=53 ms), white matter ($T_1$=850 ms, $T_2$=50 ms),

and gray matter ($T_1$=1300 ms, $T_2$=85 ms). The last of the three components of MRF is the matching algorithm. Each voxel fingerprint is compared to every dictionary entry, and the single dictionary entry that produces the closest fit as determined by the pattern matching algorithm is deemed that voxel's match (**Figure 3.5E**). This best match can then be traced back to how it was simulated, and the parameter values used for its simulation are then assigned spatially to that specific voxel. To illustrate this, in **Figure 3.5G** the specific $T_1$, $T_2$, $M_0$, and $B_0$ values used in the simulation of the yellow signal evolution are assigned to the corresponding voxel in the blue box of each map. This can then be repeated, matching every single voxel fingerprint to the entire dictionary, to find each fingerprint's best match, allowing for simultaneous, multiparametric, and quantitative reconstruction of the whole brain.

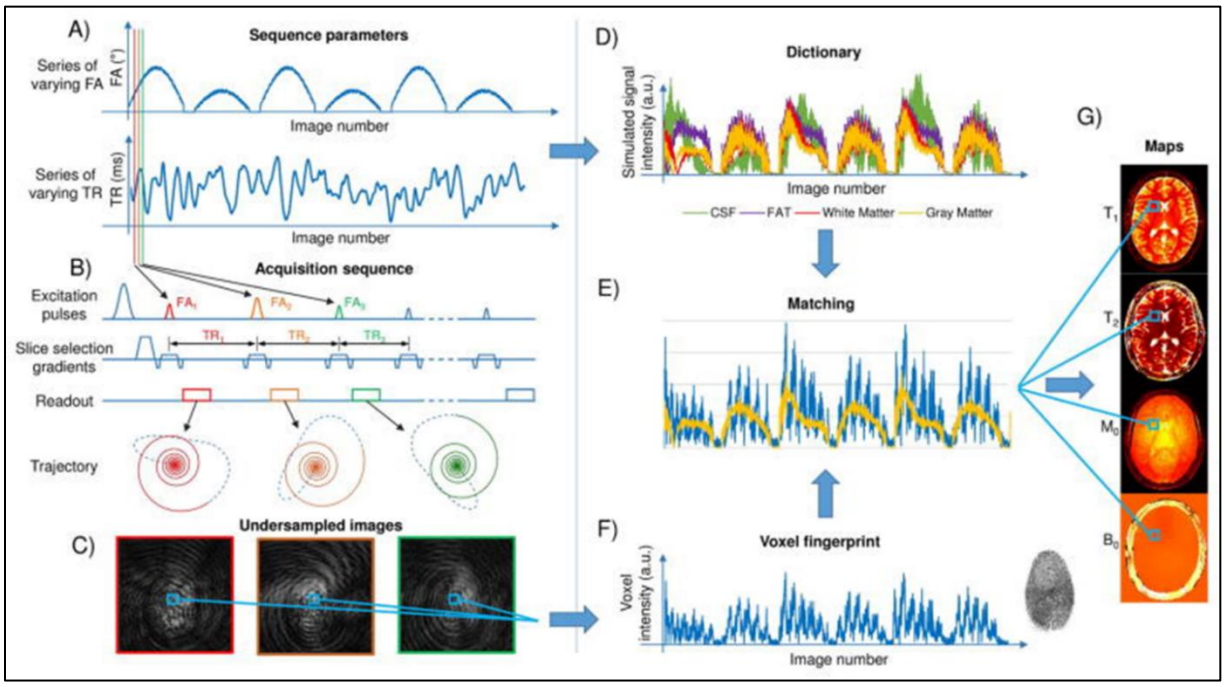


**Figure 3.5. Overview of Magnetic Resonance Fingerprinting** (from Panda et al.[94]). **(A)** The same, specialized pulse sequence is used in both the acquisition and the simulation framework. The sequence depicted here uses variable pseudo-random flip angles (FA) and repetition times (TR) to maximize parameter sensitivity. **(B)** This sequence is implemented onto the scanner for image acquisition with appropriate radiofrequency (RF) pulses, gradients, and readouts to traverse k-space for each TR and produce **(C)** under-sampled images at each of these TRs. **(D)** This sequence is also implemented into numerical simulations to generate a dictionary of signal evolutions with every combination of varied tissue parameters. The different colors here demonstrate how tissue types with different physical properties result in different simulated signal evolutions. **(E)** The entire dictionary (every possible parameter combination) is then compared to **(F)** the signal evolution of a single voxel (or voxel fingerprint) across all timepoints. The dictionary entry that most closely matches that voxel fingerprint based on a pattern matching algorithm is then selected as that voxel fingerprint's match. This is repeated for every voxel in the image so that there is a dictionary entry that best fits each voxel. **(G)** Since the underlying parameters used to generate the simulated dictionary are known, the multiple parameters for each voxel can be extracted to produce multiple quantitative parameter maps.

The key to MRF is the sensitivity of MRI signals to tissue-specific properties under varied acquisition parameters. The variations in the pulse sequences and parameters induces a wide range of signal evolutions that are dependent on the intrinsic properties of the tissue. The complexity of the sequences causes the signals from subtly different tissue types to evolve increasingly differently, making the resulting signal evolutions highly specific to the underlying tissue properties. This specificity is crucial for generating the fingerprints that can be identified in the matching process. Additionally, this framework of matching to signal progression makes MRF very insensitive to noise[8,95], motion[96,97], and under-sampling.[98,99]

Ultimately, the two primary advantages that MRF delivers are the ability to generate (1) multiple and (2) quantitative tissue parameter maps from a single MRI scan. These advantages make MRF a compelling candidate to translate quantitative MRI to the clinic and may allow for shorter scan times or more contrasts in the same amount of scan time previously required. Additionally, the quantitative component will allow for improved intra- and inter-patient comparisons across multiple timepoints, as well as improved comparisons across different sites and scanners[100] allowing for the development of imaging-based standards for clinical diagnoses, treatments, and research.

*Reliability, Repeatability, and Reproducibility with MRF*

Quantitative MRF measurements have been assessed for reliability and reproducibility across time, subjects, scanners, sites, field strengths, and vendors in many studies that have looked at one or more of these factors.[5–7,101–104] Significantly reducing or entirely eliminating the effect of these listed factors would benefit intra-subject comparisons across time, inter-subject comparisons across patient groups, and accessibility across scanners (i.e., sites, vendors, countries).

Konar et al.[101] performed an international, multisite, dual-field strength, reliability and repeatability study using the ISMRM/NIST system phantom. The key advantage of performing a

phantom study is that the ground truth values of relaxation time are known. The first method this study used to evaluate repeatability was calculating the mean $T_1$ and $T_2$ values imaged using MRF in each of the phantom's sections over 30 days at each scanner site. The second method they employed was calculating the coefficient-of-variation (CV) of the mean $T_1$ and $T_2$ values of each section of the phantom. Both methods provided strong indications of accurate, consistent, and high precision estimates of $T_1$ and $T_2$ with within-case CVs of less than 4% and 7% for $T_1$ and $T_2$, respectively.

Buoniconti et al.[102] and Fujita et al.[104] also published scan-rescan MRF repeatability studies looking at human subjects as opposed to a phantom. Both studies had a single "retest" scan. Buoniconti performed a "traveling head" study in which their healthy volunteers were scanned and rescanned on multiple scanners and sites. Test-retest MRF of $T_1$, $T_2$, and proton density (PD) resulted in gray and white matter regions with high repeatability ($T_1$ CVs from 0.7-1.3%, $T_2$ CVs from 2.0-7.8, and PD CVs from 1.4-2.5%) and reproducibility ($T_1$ CVs from 2.0-5.8%, $T_2$ CVs from 7.4-10.2, and PD CVs from 5.2-9.2%). Fujita focused on looking at the reliability of MRF parameters in smaller brain regions of interest (ROIs). The primary metric used in this study was also within-subject CV of $T_1$ and $T_2$, and their model also demonstrated more repeatable measures of $T_1$ than $T_2$ across all their ROIs.

In summary, MRF's capacity to non-invasively quantify multiple tissue properties simultaneously opens a wide array of applications, but prior to clinical adoption, ensuring the reliability of metrics is critical.

### *3.6 | Magnetic Resonance Vascular Fingerprinting*

*Overview of MRvF*

Another key advantage of MRF is its flexibility to be adapted to any physiological parameters of interest, if those parameters can be computationally modeled in such a way that influences net magnetization from the Bloch equations. One of the earliest demonstrations of that

flexibility was with Christen et al.[9] developing magnetic resonance vascular fingerprinting (MRvF). MRvF operates on the principle that the BOLD effect influences the local magnetization signal of tissue over time. Therefore, by prospectively biophysically modeling parameters that affect the magnetic susceptibility related to the BOLD signal in a voxel, you can then compare those modeled signals to acquired images and extract vascular parameters of interest using the MRF framework.

Vascular parameters that effect the BOLD signal modeled in MRvF are cerebral blood volume (CBV) which reflects the relative amount of blood in a voxel, microvascular vessel radius (R) reflecting the geometry and size of the vessels, and tissue oxygen saturation ($SO_2$). Variations in these parameters can provide significant information about cerebrovascular function and be indicators of diseases like stroke, epilepsy, and brain tumors.[105–107] More recent studies[108,109] have expanded MRvF to include additional parameter dimensions of $T_2$ and apparent diffusion coefficient (ADC). While $T_2$ and ADC are not directly related to the BOLD response, they contribute to the overall signal. By including these additional parameters into the dictionary simulations, variations to the signal can be better accounted for and provide even more metrics for characterizing tissue.

The ability of MRvF to simultaneously provide quantitative maps of CBV, R, $SO_2$, $T_2$, and ADC from a single scan has tremendous potential for improving the understanding of a wide variety of cerebrovascular phenomenon. Additionally, although still in early development, if a rapid scan that acquired multiple quantitative vascular metrics were possible, it could be used as a tool to better measure and understand cerebrovascular dysfunction at early stages of disease.

*Microvascular Biophysical Simulations and Dictionary Generation*

The biophysical simulation engine used to model signal evolutions for MRvF is the MRVox2D toolkit in MATLAB.[110] This toolbox allows for the user to define a voxel with a microstructure, set MR pulse sequence parameters, and then simulate the MR signal progression

considering the effect of susceptibility inclusions and water diffusion. The user can specifically control the geometry of the voxel (voxel size, size/number of blood vessels and cells, spacing, etc.), the MR-related properties of all compartments (i.e., $T_1$, $T_2$, $M_0$, and susceptibility of the blood, tissue, and cells), and the magnetic field and its variation ($B_0$ strength and orientation, linear gradients).

The algorithm of this toolbox is outlined in **Figure A3.1**. Specifically, MRVox first asks for the blood volume fraction, number of micro vessels, and radius of the micro vessels to generate the geometry of the virtual voxel on which the biophysical simulations will be performed. For cases where a contrast agent is considered, the user also sets the contrast agent's magnetic susceptibility, diffusivity, an arterial input function, blood flow, and permeability rate. In this work we sought to remove the need for contrast agents and thus excluded these portions of the model. Next, the vessel lattice generated from the first step incorporates the static magnetic field corresponding to the field of the scanner, the magnetic susceptibility difference between blood and tissue, and constant relaxation rates of blood and tissue. The magnetic susceptibility difference between blood and tissue ($\Delta\chi$) is given by the oxygen saturation level ($SO_2$) as described by **Eq. 3.4**:

**Equation 3.4**: $$\Delta\chi = \Delta\chi_0 \cdot Hct \cdot (1 - SO_2)$$

Where $\Delta\chi$ is also a factor of the susceptibility difference between fully deoxygenated and fully oxygenated red blood cells ($\Delta\chi_0$, assumed to be 0.264 ppm)[9] and Hct represents the microvascular hematocrit, which was set to 0.36.[9] Radiofrequency pulses corresponding to the timings, flip angles, and phase angles of the same sequence implemented on the scanner are played with respect to these relaxation lattices, resulting in longitudinal and transverse magnetization progression which leads to a description of signal evolution over time. In this work, we primarily focused on changing blood volume fraction, microvascular vessel radii, and oxygen saturation while holding all other simulated inputs constant.

The model uses a simplified 2D plane to represent the voxel being simulated and randomly disperses 2D disks in the plane to represent the magnetic inclusions from blood vessels. This results in a 2D square lattice with a specified side length (that matches the in-plane voxel size) containing vessels of uniform predefined radii. **Figure 3.6A** shows an example of a lattice with disks during a simulation with magnetic field perturbations surrounding each vessel.

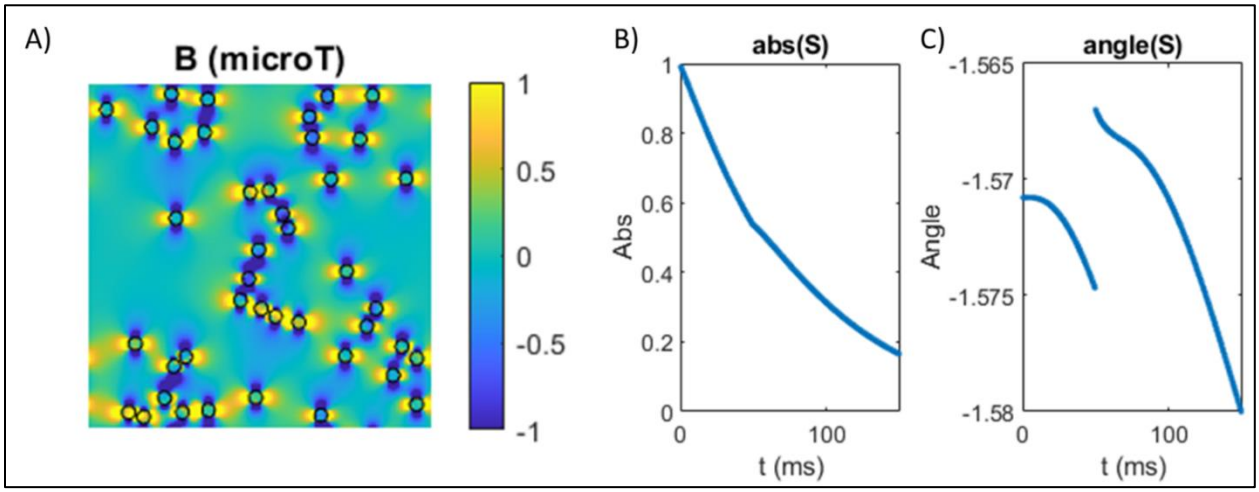


**Figure 3.6. Biophysical Simulations with MRVox**. Example outputs from the MRVox simulation engine. **(A)** A lattice of the change in local magnetic gradients outside of vessels perpendicular to $B_0$. This represents an example of a simulated 256 μm isotropic 2D voxel with a 256 by 256 lattice for numerical computations. A cerebral blood volume of 5%, 42 vessels with radii of 5 μm, and an oxygen saturation of 70% was used here. **(B)** The magnitude and **(C)** phase of the simulated signal over time with a sequence that has a 180° refocusing pulse at 50 ms.

This virtual voxel, in combination with the system parameters, can then be used to model the expected MR signal decay. **Eq. 3.5**[111] describes the magnetic field lattice (***ΔB***) induced by the virtual voxel where $B_0$ is the main magnetic field, $k_x$ and $k_y$ are the wave vectors in Fourier space,

**Equation 3.5**: $$\boldsymbol{\Delta B} = B_0 \times FT^{-1}\left\{\left(\frac{1}{3} - \frac{k_x^2 \sin^2\theta)}{k_x^2 + k_y^2}\right) FT\{\boldsymbol{\Delta\chi}\}\right\}$$

$\theta$ is the angle between the normal of the plane and $B_0$, and ***Δχ*** is the magnetic susceptibility lattice. *FT* and $FT^{-1}$ stand for Fourier transform and inverse Fourier transform, respectively. The ***ΔB*** lattice is then utilized as part of the deterministic approach to model magnetization changes[112] as illustrated in **Eq. 3.6**[111]:

**Equation 3.6**: $$\boldsymbol{M}(t + dt) = \boldsymbol{M}(t) \times e^{-i\gamma \boldsymbol{\Delta B} dt}$$

The transverse magnetization lattice, ***M(t)***, is iteratively calculated with the exponential dephasing factor across the lattice. From this, the signal at each time point can be determined and complex signal time course generated.

*Pulse Sequences for MRvF*

There are two primary pulse sequences we used for MRvF modeling and acquisition in this dissertation: a gradient-echo sampling of free induction decay and echo (GESFIDE) sequence and a spin- and gradient-echo (SAGE) sequence. The GESFIDE sequence was first introduced by Ma and Wehrli[113] as a means of measuring both reversible ($R_2$') and irreversible ($R_2$) relaxation rates in a single scan. Effective relaxation rate ($R_2$*) is described with **Eq. 3.7**:[114]

**Equation 3.7**: $$R_2^* = R_2 + R_2'$$

These relaxation rates are sensitive to sources of susceptibility, including the susceptibility effect of paramagnetic dHb. As a result, a sequence sensitive to these changes in brain oxygenation is a prime candidate for mapping vascular function with MRvF. Additionally, MRF requires an imaging scheme that acquires multiple images at different signal intensities in a single scan. The GESFIDE sequence typically acquires 30-40 brain volumes[9,115,116] with sampling during the free induction decay (FID), refocusing period after a 180° RF, and after the spin echo (**Figure A3.2**). These echoes are dispersed throughout the signal evolution to get portions of the sequence that are sensitive to each of the relaxation rates. The specific version of GESFIDE we used in this work has 14 TEs immediately after the initial 90° excitation RF pulse, 16 TEs during the refocusing period including the spin echo at 100 ms, and 10 TEs after the spin echo.[59,116]

GESFIDE also employs a fast-imaging technique known as echo planar imaging (EPI). With EPI, k-space is traversed multiple times within a single excitation, capturing several echoes to encode the different image contrasts associated with signal decay and refocusing. The way in which k-space is traversed in GESFIDE is illustrated in the pulse sequence diagram displayed in **Figure A3.2**. Concurrent with the 90° RF excitation pulse, a slice selection gradient is applied to

excite a specific slice of tissue. After this initial RF excitation, an EPI gradient scheme is employed. For multi-echo sequences, like GESFIDE, the scheme is adjusted to allow for the acquisition of multiple echoes within a single shot. Before each readout, a phase-encoding (PE) gradient is momentarily applied. The strength of this gradient is varied in a systematic way across successive excitations to fill different rows of k-space. The frequency-encoding (FE) gradient is applied during the acquisition of the echo, facilitating the rapid capture of data along rows of k-space. For each echo, the frequency encoding gradient is applied, allowing the MRI system to capture the signal and fill a line of k-space. Additionally, the GESFIDE sequence employs a crusher gradient around the 180° RF excitation pulse. In sequences like GESFIDE that involve multiple gradients, stimulated echoes can arise and contribute unwanted signal variations. Crusher gradients disrupt the phase coherence necessary for the formation of stimulated echoes, thereby minimizing their contribution to the overall MRI signal.

Overall, each echo fills k-space in a similar pattern but at different times relative to the excitation, capturing varying contrasts based on $T_2$* and $T_2$ properties. This allows for good in-plane spatial resolution (1-2 mm) with relatively short acquisition times (3-5 minutes). Additionally, by capturing multiple echoes, it's possible to use the GESFIDE sequence in an MRF paradigm.

The second sequence we utilized for MRvF is the SAGE sequence. The SAGE sequence was first introduced by Schmiedeskamp et al.[117] in an effort to estimate susceptibility-contrast perfusion-weighted brain imaging parameters from combined spin-echo (SE) and gradient-echo (GRE) acquisitions. Like GESFIDE, acquisition of both GRE and SE signals allows for measurements of $R_2$, $R_2$*, $R_2$' and their associated tissue susceptibility effects (**Figure A3.3**).[118] The SAGE sequence collects the full volume of the brain at fewer TEs, but with a much quicker total scan time than GESFIDE by acquiring all of k-space during a single TR.

An interleaved EPI readout with GRAPPA acceleration allows for all necessary PE lines of k-space in a slice to be captured during a single readout pass. Effectively, this is what allows all k-space data needed for reconstruction of all TEs to be collected in just a few seconds. With

GRAPPA[119], the MRI scanner acquires fewer lines of k-space than is typically necessary for the desired image resolution. This is achieved by undersampling which reduces the total scan time, however, undersampling also introduces aliasing artifacts. To accurately reconstruct the undersampled data, GRAPPA uses calibration scans, which are fully sampled central k-space regions. The calibration data gives the relationships between the signals received by different coils for the undersampled and the fully sampled lines in k-space. It then applies these relationships to predict and fill in the missing k-space lines for the undersampled data. Once the missing k-space data are reconstructed, a standard Fourier transform is used to convert the now-complete k-space data into image space. This accelerated acquisition with GRAPPA reconstruction can achieve reduced acquisition time but typically comes at the expense of lower SNR compared to full k-space acquisition.

The specific SAGE sequence used in the following work has two TEs after the initial 90° excitation RF pulse, a 180° refocusing RF, two TEs during this refocusing period, and a fifth TE near the spin echo.[120] The pulse sequence diagram for this SAGE is shown in **Figure A3.3**, and shows the EPI trains at each TE that traverse in-plane k-space, a similar crusher gradient to the GESFIDE, and a 90° spectral-spatial excitation pulse with associated oscillating slice-select gradients. Spectral-excitation pulses are highly selective in space and frequency making them selective for exciting only water protons in a given slice, effective at robustly suppressing signal contributions from lipids, and ideal for scans where many slices are acquired during a single TR, as each slice is only excited once per TR.[121] Previous uses of SAGE[117,118,120] have also used additional simultaneous multi-slice acceleration (SMS), which accelerate the sequence even more by a factor of the SMS. This method allows for rapid acquisition of images with different contrasts in a short time, making it highly effective for dynamic studies like contrast perfusion imaging, where changes over time are critical.

While multi-echo gradient and spin echo sequences like these have been used for nearly all previous MRvF studies thus far[9,107,109,115,122], most general MRF studies have been performed with

sequences designed specifically for MRF.[6,8,94,123,124] These MRF-specific sequences employ pseudorandom acquisitions with varied parameters, such as flip angles, TRs, and TEs, acquired with high undersampling for rapid collection of multiple time points. This acquisition scheme is meant to maximize sensitivity of fingerprints; however, they have been primarily designed for more traditional qMRI metrics like $T_1$, $T_2$, and $M_0$. Sequences like GESFIDE and SAGE are specifically designed for sensitivity of parameters related to oxygenation and vascular function while still acquiring the multiple time points necessary for fingerprinting analysis. The following chapters will investigate some of these tradeoffs of echo train length, undersampling, and sequence sensitivity with these two sequences for MRvF.

### *3.7 | Conclusions*

In this chapter, imaging modalities, techniques, physics, and applications were reviewed to provide background, context, and motivations for the work done in the rest of this dissertation. While numerous imaging modalities are used for neuroimaging applications, MRI has distinct advantages of being non-invasive, not requiring ionizing radiation, sensitivity to soft tissues (like those in the brain), and adaptability to various contrast mechanisms (like those utilized for vascular imaging with MRI). The two biggest limitations with MRI have historically been its qualitative nature and long scan times. Although many qMRI techniques have been developed to address the qualitative limitation, MRF enables both quantitative and fast imaging. Additionally, MRF is flexible to adaptation, like with MRvF, which has the potential to enable fast, multiparametric, quantitative measures of cerebrovascular function and disease. The rest of this dissertation presents studies we performed to advance this technique towards providing translationally and clinically relevant biomarkers of cerebrovascular function.

# Chapter 4 – Magnetic Resonance Fingerprinting of Oxygenation

## *4.1 | Introduction and Background*

Adequate tissue oxygenation is critically important for overall brain health and function, and inadequate oxygen delivery, saturation, extraction, and consumption are all indicators of cerebral pathophysiology.[69,125,126] As such, there have been several techniques developed to study brain oxygenation quantitatively and non-invasively with MRI.

MRI's sensitivity to tissue oxygenation stems from the magnetic properties of deoxyhemoglobin. Oxygenated hemoglobin (oxyhemoglobin) is weakly diamagnetic, meaning it does not distort the external magnetic field significantly. In contrast, deoxygenated hemoglobin (deoxyhemoglobin) is paramagnetic, creating local magnetic field inhomogeneities that can influence MRI signal characteristics, particularly affecting the transverse relaxation rates of water protons in surrounding tissues.

This blood oxygen level dependent (BOLD) phenomenon is the basis for functional MRI (fMRI) and has been used widely in neuroscience research for decades. In fMRI, the premise is that as a certain region of the brain is active, the local neurons consume more oxygen, and Hb is converted to dHb. This triggers an increase of oxygenated blood to flow that region, which outweighs the increase in oxygen consumption, leading to an overall decrease in the relative concentration of dHb in that region. This decreased dHb concentration causes an increased $T_2$*-weighted MRI signal in that local region, termed the BOLD effect, and thus provides an indirect measure of neuronal activity.

While fMRI is the most common imaging method that takes advantage of the BOLD effect, significant work has been done to use baseline BOLD scans to extract oxygenation information quantitatively. This is referred to as quantitative BOLD (qBOLD) and takes advantage of the local susceptibility effects that dHb has on transverse relaxation rates. By utilizing a multi-echo sequence with gradient and spin echoes, $R_2$*, $R_2$, and $R_2$' can be determined and used to

retrospectively calculate various physiological measures like deoxygenated blood volume and oxygen extraction fraction.

Magnetic resonance vascular fingerprinting (MRvF) is a relatively new approach that uses the magnetic resonance fingerprinting (MRF) framework first introduced by Ma et al.[8] to prospectively model qBOLD signals that would result from deoxygenated cerebral vasculature with a specific MR pulse sequence. These prospectively generated signals can be compared to actual images acquired with the same sequence, and then vascular measures like cerebral blood volume (CBV), microvascular vessel radii (R), and oxygen saturation ($SO_2$) can be estimated per voxel. These MRvF metrics offer an alternative to the analytical qBOLD models, with related vascular measures.

Both MRvF and qBOLD offer enticing techniques to produce quantitative measures of oxygenation that can provide better understating and diagnoses of cerebrovascular function and diseases. This chapter describes our work to: (1) investigate different modeling and matching approaches for MRvF, (2) compare MRvF- and qBOLD-derived measures of oxygenation, and (3) validate both methods through retrospective analysis of scans collected during a controlled hypoxic and hyperoxic respiratory gas challenge.

### *4.2 | Signal Evolution Modeling and Pattern Matching Considerations*

MRvF relies on biophysically simulating how MR signal is affected by a virtual voxel, and understanding how the vasculature influences MR signal is important for selecting an appropriate sequence and matching algorithm. When a voxel in the brain has a higher CBV, there will be more dHb in that voxel and a faster decay of signal magnitude (**Figure 4.1**; top left). Similarly, a voxel with lower $SO_2$ will have more dHb relative to Hb and a faster signal magnitude decay (**Figure 4.1**; top right). Variations in signal magnitude decay due to vessel radii (R) has been shown to effect transverse relaxation rates ($R_2$ and $R_2$*) and the ratio of $\Delta R_2^*/\Delta R_2$ is indicative of average vessel size in the voxel.[105,127] This can be visualized particularly after the refocusing pulse (**Figure**

**4.1**; top middle). The signal phase evolution can also be used in the pattern matching step of MRvF. The phase shift in a voxel is dependent on the magnetic field in that voxel which is affected by the local magnetic susceptibility of the tissue. The difference in magnetic susceptibility between Hb and dHb leads to differences in signal phase[126] that may help disentangle the similar signal magnitude effects of increasing CBV and decreasing $SO_2$. Higher CBV values result in much greater signal phase changes relative to the signal phase changes observed when varying R or $SO_2$ (**Figure 4.1**, bottom).

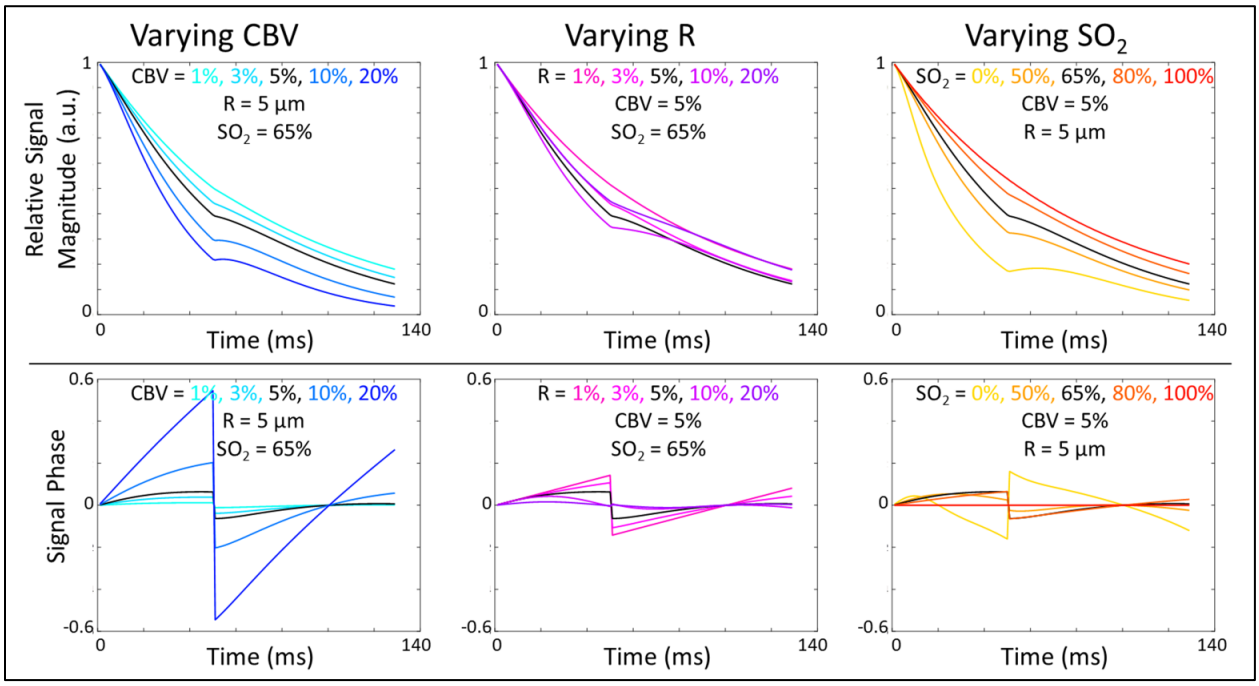


**Figure 4.1. Signal Magnitude and Phase Progression**. Magnitude (top) and phase (bottom) signal time-courses from an MRvF dictionary generated with biophysical simulations using different combinations of vascular parameters. Varying cerebral blood volume (CBV; left), vessel radius (R; middle), and oxygen saturation ($SO_2$; right) result in signal evolution differences that enable the sensitivity of MRvF.

The new premise here is then to utilize this phase information that is acquired innately as part of the complex-valued MRI signals to increase sensitivity of MRvF. This approach requires a different matching algorithm, as the coefficient-of-determination ($R^2$) method used in previous MRvF[9,107] studies utilizes only the magnitude of the signal to determine a best match between the voxel fingerprint and dictionary. A common method for other non-vascular MRF studies that incorporates both magnitude and phase components into matching is inner product (IP).[8,128–130] Simply, the vector dot product (**Eq. 4.1**) between every dictionary ($M$) entry ($j$) and an image ($s$)

voxel ($x_i$) is computed at corresponding time points ($t_n$). The dictionary entry that produces the highest sum across timepoints ($n$) is selected as the best fit ($IP_{match}$) for that voxel and the multiple parameters used to generate that entry are extracted. Repeating this for every voxel results in full brain mapping.

**Equation 4.1**: $$IP_{match} = max_j \left| \sum_n M_j(t_n) \cdot s(x_i, t_n) \right|$$

While the flexibility of MRF to be adapted to the physiological range of any parameter that can be biophysically modeled is great for examining different tissue properties and processes, one significant drawback is that anything that is not modeled in the simulations cannot be reconstructed. If the tissue properties of a certain disease are not simulated, then MRF will not be able to accurately detect those abnormalities. This can be mitigated through expansion of the dictionary with greater parameter ranges and diversity of virtual voxels, however, increasing dictionary size and complexity increases computational time required to both generate the dictionary and perform matching. Another mitigation strategy is to expand the dimensionality of the dictionary by increasing the number and type of parameters that are varied. Recent MRvF work has shown that adding $T_2$ and ADC as modifiable parameters in the dictionary produces more accurate physiology, alters the signal evolutions to be more representative of tissues, and improves parameter mapping accuracy.[108]

The simulation model used previously for MRvF has previously been validated through simulation studies[9,105,110], phantom studies[111], comparison to alternative quantitative parameter mapping MRI[59,107,131], and through expected in vivo physiological tissue changes.[59,107,108,131] There are two different ways that the virtual voxels have been previously designed for modeling. The first method has the user specify the number ($N$) of vessels in the virtual voxel and then the field-of-view ($FOV$) is determined based on $N$ in combination with the vessel radius ($R$) and cerebral blood volume ($CBV$) in that simulation as shown in **Eq. 4.2.**[105]

**Equation 4.2**: $$FOV = R\sqrt{\frac{\pi N}{CBV}}$$

A limitation with performing the biophysical simulations with this method is that the *FOV*, which is in essence the voxel size, varies with every unique combination of *R* and *N*. Therefore, a second method was developed that has the user specify their *FOV* to match the in-plane voxel size of their acquired image, and then *N* in the virtual voxel is automatically calculated based on the *R* and *CBV* specified as shown in **Eq. 4.3**.[105]

**Equation 4.3**: $$N = \frac{CBV \cdot FOV^2}{\pi R^2}$$

While this method is more representative of the image voxel size; it has its own potential issues. Modeling only small vessels in a large piece of tissue is unrealistic and there are failed cases when trying to simulate large CBV with small R or large R with small CBV. Additionally, when utilizing the method based off **Eq. 4.3**, the simulation software only provides magnitude signal progression and no phase information. In this work we perform both methods of biophysical modeling and compare the results obtained.

### *4.3 | Noise Considerations for Simulations*

The MRI simulation studies conducted here require the addition of noise to idealized signals to evaluate MRvF modeling and matching implementations across different SNR settings. Before adding this noise, it is important to understand contributors to noise in an MRI and how to appropriately model it. Noise in an MRI system can come from the system hardware, the participant in the scanner, and outside interfering contributors. System hardware induced noise include thermal noise due to motion of free electrons in the system, gradient and magnetic field instability, and resistance of the RF receive coils. Subject induced noise can be the result of movements interacting with the magnetic field or physiological effects.[132] While some these contributors are more readily addressed prior to and during scan acquisition, it is impossible to eliminate all sources of noise in an image.

The statistical characteristics of noise in MRI have been extensively investigated and mathematically modeled with the general conclusion that thermal noise can be statistically modeled as a zero-mean Gaussian distribution that is independent with equal variance in real and imaginary components.[132–135] This is simplified in **Eq. 4.4** where the MR signal acquired,

**Equation 4.4**: $$S(f) = S_R(f) + N_R(f) + i\big(S_I(f) + N_I(f)\big), \quad i = \sqrt{-1}$$

*S(f)*, is dependent on uncorrelated complex noise, *N(f)*, in the real and imaginary domains. Therefore $S_R(f)$ and $S_I(f)$ represent the real and imaginary true (noise-free) signals respectively, and $N_R(f)$ and $N_I(f)$ represent the real and imaginary Gaussian noise contributions. An inverse discrete Fourier transform of *S(f)* converts the signal to image-space. Since the Fourier transform of a Gaussian is another Gaussian, the noise in the image can continue to be described with independent normal distributions in the real and imaginary parts with equal variances.

While this is helpful for describing noise in real and imaginary images, the typical MRI is displayed as a magnitude image, and for this work it is also vital to understand noise properties in the phase image as well. It has been previously derived then that the distribution of pixel intensities observed in magnitude images with noise can be described with a Rician probability density function.[133–135] Additionally, it has been shown that in the presence of no magnitude signal, this Rician distribution reduces to the Rayleigh distribution, and with high SNR (>2) the distribution can be approximated as Gaussian.[133–135] The deviation of the phase angle due to noise has been derived and demonstrated to be represented by a random distribution of all angles when there is no underlying signal and a Gaussian distribution when the signal is significantly higher than the standard deviation of the noise.[133]

Here, simulations in which noise is introduced must closely consider the target SNR and the components (real/imaginary or magnitude/phase) to which the noise will be added to appropriately model the noisy MR signal. Since the noise in areas where there is no tissue is not relevant in the simulation framework, the Rayleigh distribution for signal magnitude can be

ignored. Additionally, images acquired with the GESFIDE sequence that is utilized here have demonstrated high SNR (~80-100) and therefore the pixel intensities and phases are expected to fall into the Gaussian distribution.

Many initial implementations of MRF have used highly under sampled images across the signal evolution timepoints which can result in very poor SNR and parallel imaging techniques that complicate the derivation of the noise distribution functions.[8,95,136] The GESFIDE sequence retrospectively analyzed here, however, acquires fully sampled data and does not utilize multiband techniques, therefore not introducing these additional noise considerations. Another concern with MRF is intra-scan subject motion that causes voxels in the brain to move relative to their initial position.[96,97] While MRF is robust to a random movement and return to initial position, it is not impervious to a mid-scan or gradual movement by the subject. Mitigation of the influence of noise on images and parameter maps can be addressed at multiple levels: prospectively through scanner quality control, appropriate sequence design, and minimizing subject movement, and retrospectively, if necessary, through spatial or temporal signal filtering, denoising algorithms, or other preprocessing steps.

*4.4 | Testing Model and Algorithm Combinations*

To explore various modeling and matching strategies as laid out in *Section 4.2*, we performed Monte Carlo simulations on noisy signals. First we generated four vascular fingerprinting dictionaries for the simulated sequence using the MRVox[110,111] toolkit in MATLAB with 2D virtual voxels. The first dictionary used the model from **Eq 4.2** and the second used **Eq 4.3**. The third and fourth dictionary were identical to the first two, but with an added $T_2$ dimension. Matching was performed on the complex or magnitude signal, and with a typical inner product algorithm (**Eq 4.1**) or a 2-step iterative inner product. All ten of these various model/matching combinations are detailed in **Table A4.1**. The sequence used in simulations was the multi-echo sequence with both gradient and spin echo sampling, GESFIDE, described previously.

Biophysical simulations used combinations of 40 values of $SO_2$ from 0 to 100%, 40 values of CBV from 0.1 to 25%, 40 values of R from 2 to 24 µm, and when applicable, 40 values of $T_2$ from 40-140 ms for a total of 64,000 unique signal evolutions for the first two dictionaries and 2,560,000 unique signal evolutions for the last two dictionaries.

We added Gaussian noise at an SNR of 100 (based off the first TE) independently to the real and imaginary components of a randomly selected dictionary entry to create a test signal before matching it against the entire dictionary. We calculated the root-mean-squared error (RMSE) between the estimated parameters from the best match and the true underlying parameters and repeated this with a random dictionary entry 1,000 times, for each of the 10 modeling/matching combinations.

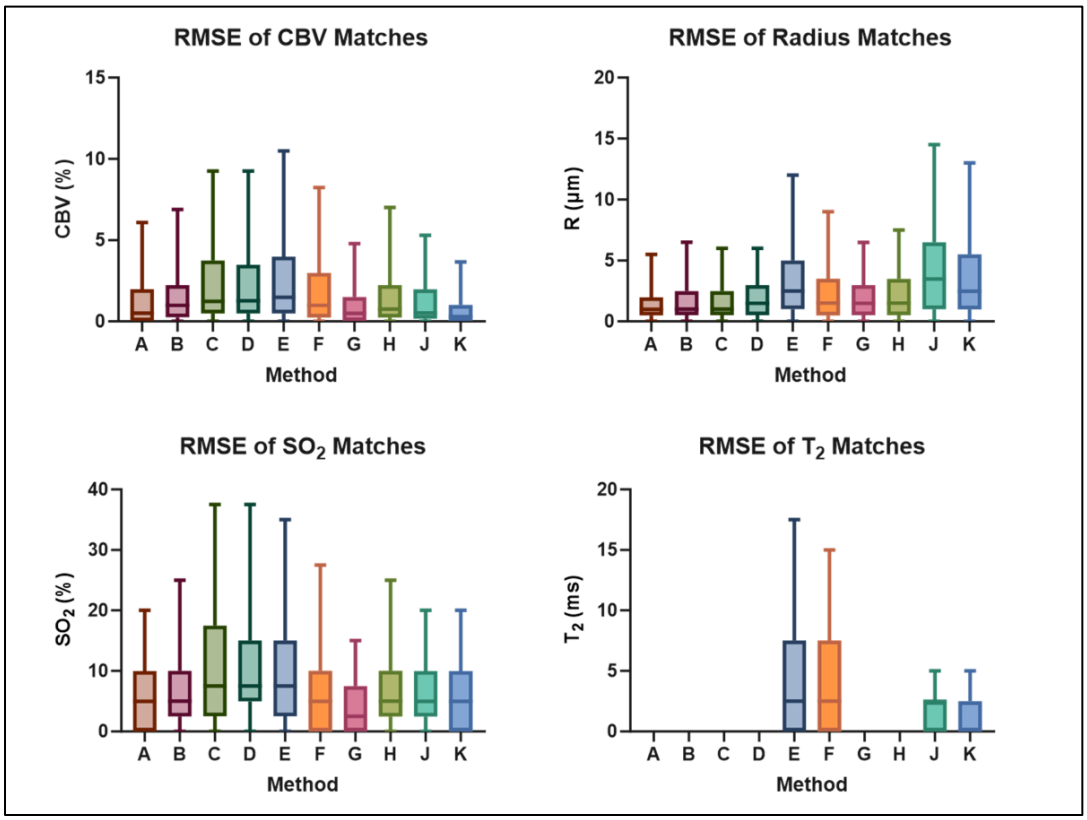


**Figure 4.2. GESFIDE Simulations with Varying Models and Matching Strategies**. Root-mean-square error (RMSE) between the actual parameter values and the predicted values from the noisy signal using each of the ten methods described in Table A4.1. Each boxplot represents 1,000 Monte Carlo simulations with Gaussian noise added to simulated signals at a signal-to-noise ratio of 100. Outliers were removed with the ROUT method and Q set to 1%.

The most noticeable observations from these simulations (**Figure 4.2**) were that the methods based on **Eq. 4.3** (G-K) had lower average error for CBV and significantly lower

estimation errors of $T_2$. In contrast, the methods based on **Eq. 4.2** without the additional $T_2$ dimension (A-D) had lower average error for R.

After simulations, we performed retrospective MRvF analysis on 12 healthy volunteers (33±6 years) that had been scanned at 3T (MR 750, GE Healthcare Systems) with the GESFIDE sequence (TR=2000 ms, 40 TEs, spin echo=100 ms, in-plane resolution=1.5×1.5 mm, slice thickness=2.5 mm, matrix=128×128, 12 slices, scan time=4 min). In addition to the GESFIDE imaging for oxygenation measurements, a $T_1$-weighted image for structural information and registration was also collected. GESFIDE acquisitions were acquired while participants inhaled hypoxic gas (14% $O_2$), normal air (21% $O_2$), and hyperoxic gas (100% $O_2$) using a custom gas delivery setup (**Figure A4.1**) with the goal of measuring the effects of inhaled oxygen with MRvF. Each of the GESFIDE images was used in MRvF with each of the ten different methods from **Table A4.1** to reconstruct CBV, R, $SO_2$, and $T_2$ parameter maps.

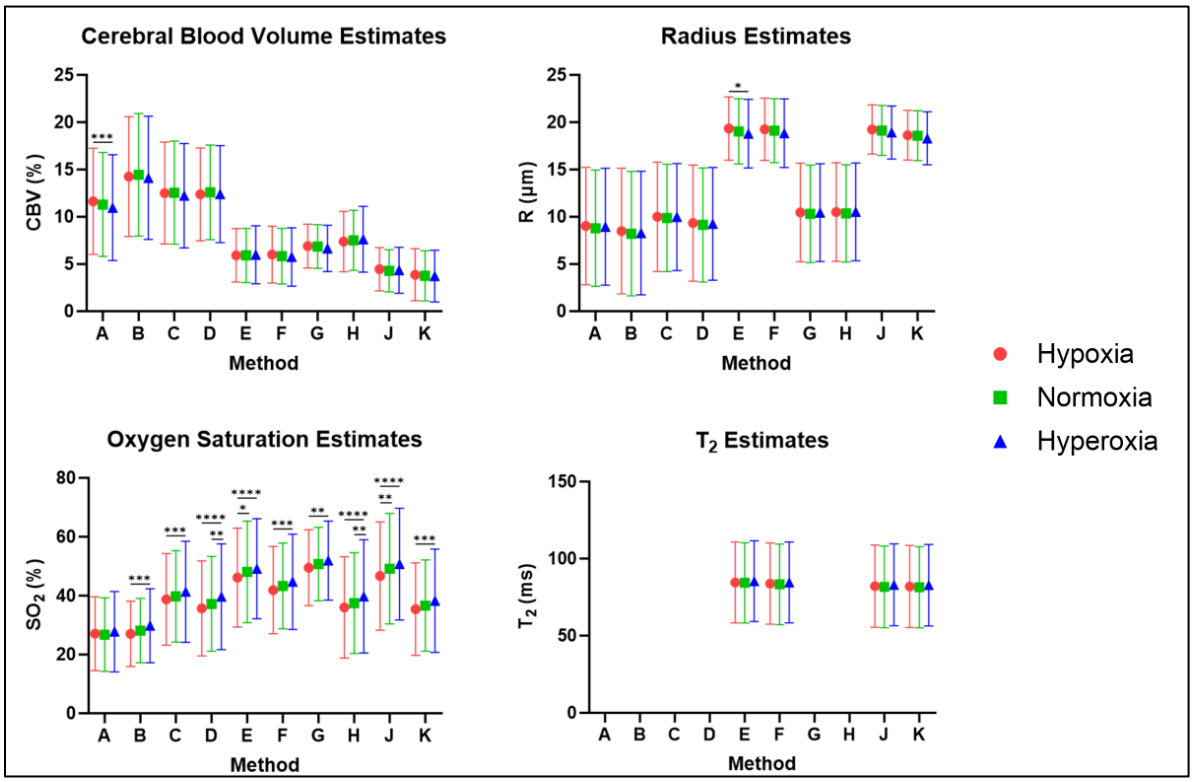


**Figure 4.3. Average Parameter Values in Gray Matter Across Conditions and Methods**. Group average maps across each method and inhalation condition were created for each parameter. One-way ANOVA with Bonferroni correction was performed independently within each method to observe significant differences between inhalation conditions (*=p<0.05, **=p<0.01, ***=p<0.001, ****=p<0.0001). Shapes and error bars represent mean and standard deviation, respectively.

We linearly registered the first echo of the GESFIDE image for each breathing condition to each subject's $T_1$-weighted image (FLIRT[137,138]), and nonlinearly registered each $T_1$-weighted image to the MNI structural atlas (FNIRT[139]). These two transformations were applied to all MRvF parameters to get all subjects' maps into the same standard space. We then averaged those maps in MNI space across parameter, oxygen condition, and method to create group averages of CBV (**Figure A4.2**), R (**Figure A4.3**), $SO_2$ (**Figure A4.4**), and $T_2$ (**Figure A4.5**). With just 12 slices and limited brain coverage in the z-direction, we used the frontal and parietal cortical gray matter as the region-of-interest (ROI), since it was where the most subjects had overlapping volumes. Finally, we calculated the mean and standard deviation from each group average in this ROI (**Figure 4.3**).

We compared the ability to detect the changes in brain physiology due to different oxygen inhalation conditions across MRvF methods using one-way ANOVA within each method for each parameter. We found minimal differences due to gas breathing across any of CBV, R, or $T_2$, but most MRvF methods showed significance for $SO_2$ changes with different gas conditions. Group average MRvF-derived $SO_2$ was significantly different between hyperoxia and hypoxia for methods B-J, hyperoxia and normoxia for methods D and H, and normoxia and hypoxia for methods E and J (**Figure 4.3**).

*4.5 | Comparison of MRvF and Quantitative BOLD*

Several different MRI methods to measure brain oxygenation (specifically oxygen extraction fraction) have been demonstrated and compared.[50,126] Both qBOLD[91,140,141] and MRvF[9] represent promising approaches, so next we directly compared these oxygenation methods in the same healthy, young participants described in the previous section during the various oxygen inhalation conditions.

For MRvF analysis, method F was used for comparison as it was the best performing method using **Eq. 4.2** based on numerical simulations in the previous section. For qBOLD

analysis, GESFIDE data were first motion corrected with MCFLIRT[138] and smoothed with a Gaussian kernel (σ=1.5mm) to mitigate the effect of noisy voxels (**Figure 4.4**). $R_2$' was calculated by using the free induction decay (FID) denoted as regime A of signal evolution, with decay rate of $R_{2,}{}^*_A$, and refocusing echoes (regime B) with decay rate $R_{2,}{}^*_B$ (**Eq. 4.5**).

**Equation 4.5**: $$R_2' = \frac{R^*_{2,A} - R^*_{2,B}}{2}$$

We implemented the linear qBOLD model[142] in MATLAB to apply a linear fit of the GESFIDE signal echoes after a spin echo displacement time of τ > 15ms (total of 5 data points). Deoxygenated blood volume (DBV) was then estimated directly from the linear model, where DBV is the offset between the linear intercept and the spin echo data.

**Equation 4.6**: $$OEF = \frac{3 \cdot R_2'}{DBV \cdot \gamma \cdot 4\pi \cdot \Delta\chi_0 \cdot Hct \cdot B_0}$$

OEF was calculated by known constant of proportionality (**Eq. 4.6**), where $\gamma$ is the proton gyromagnetic ratio, $\Delta\chi_0$ is the susceptibility difference between Hb and dHb, *Hct* is the hematocrit, and $B_0$ is the external magnetic field strength.

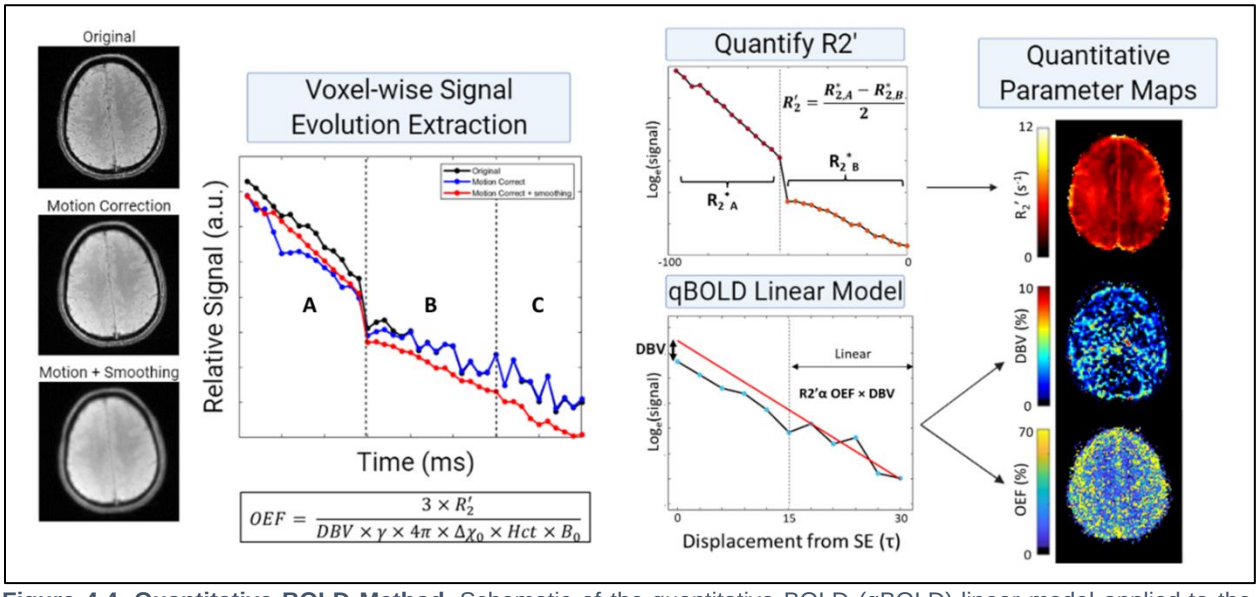


**Figure 4.4. Quantitative BOLD Method**. Schematic of the quantitative BOLD (qBOLD) linear model applied to the GESFIDE sequence. After preprocessing involving motion correction and smoothing, oxygen extraction fraction (OEF) is calculated by known constants of proportionality from deoxygenated blood volume (DBV) and $R_2$'.

When comparing linear qBOLD and MRvF, qBOLD $R_2$' is calculated from the free induction decay and refocusing echoes, while DBV is calculated from the post-spin echo TEs. These are

then combined to calculate OEF using **Eq. 4.6**. In contrast, for MRvF the entire signal (all TEs) is used to calculate all parameters simultaneously (**Figure 4.5**). While both qBOLD and MRvF generate parameter values for each voxel independently, the parameters themselves differ as qBOLD produces maps of $R_2$', DBV, and OEF while MRvF generates maps of CBV, R, and $SO_2$. OEF reflects the relative difference in the oxygen saturation of arterial and venous blood, whereas $SO_2$ reflects the oxygenation in the tissue. Therefore, these two metrics are very closely related, as the level of tissue oxygenation is dependent on the OEF from the capillaries and can be converted to one another for direct comparison.

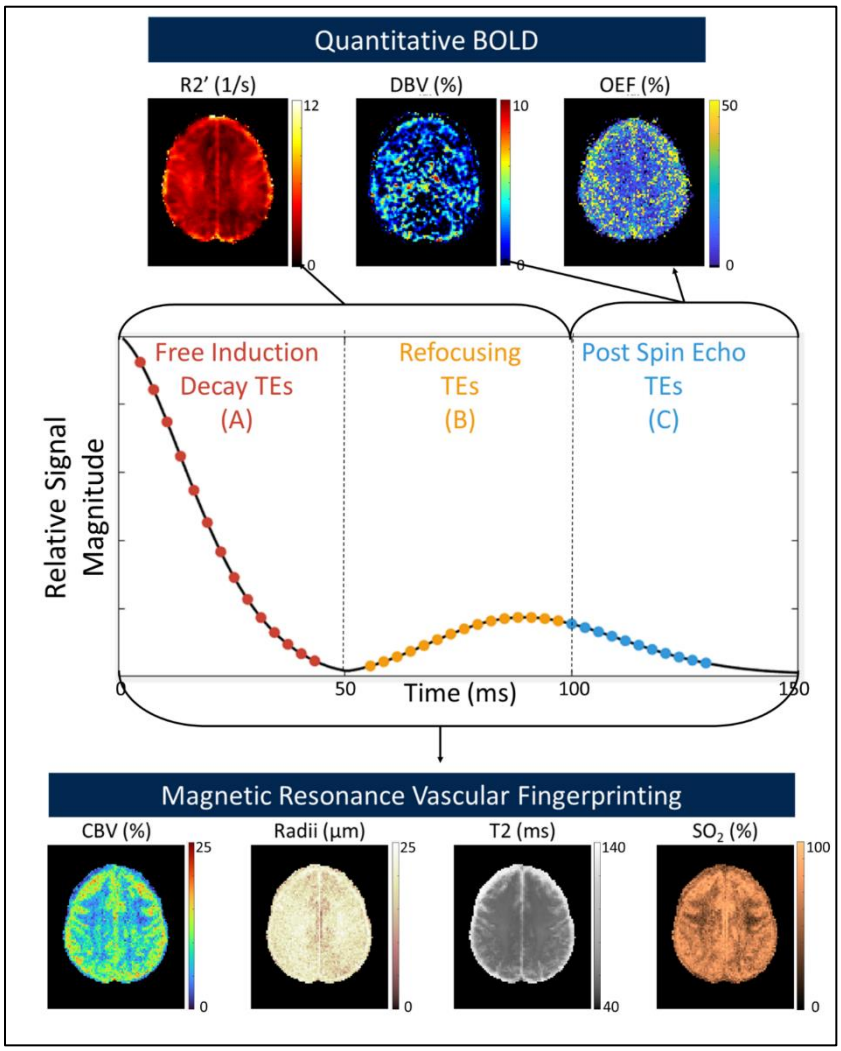


**Figure 4.5. Comparison of MRvF and qBOLD Signals and Outputs**. The GESFIDE sequence (middle) with example group average parameter maps generated from two different approaches, MRvF (bottom) and qBOLD (top). MRvF uses all 40 echoes available in the imaging data to reconstruct its four parameter maps, while the qBOLD method here uses the free induction decay and refocusing signal to produce $R_2$' maps, and the post spin echo signal to produce deoxygenated blood volume (DBV) and oxygen extraction fraction (OEF) maps.

*4.6 | Validating Oxygenation Measurements with Hypo-, Norm-, and Hyperoxia*

For this direct comparison of MRvF and qBOLD metrics, we converted $SO_2$ measurements acquired using MRvF to OEF using **Eq. 4.7**:

**Equation 4.7**: $$OEF = \frac{S_aO_2 - S_vO_2}{S_aO_2}$$

Here, $S_vO_2$ stands for venous oxygen saturation and represents the measurements obtained from $SO_2$ from MRvF for each voxel, and $S_aO_2$ is the average arterial oxygen saturation recorded via pulse oximeter throughout each scan. OEF maps from both MRvF and qBOLD were transformed into MNI space as in the previous section, to create group average maps. A linear mixed-effects model adjusted for subject clustering was generated for the OEF for each subject and oxygen condition using the same ROI as in the previous section. Values of OEF from qBOLD and MRvF were demonstrated to be directly correlated, although MRvF tended to estimate slightly higher results (**Figure 4.6**).

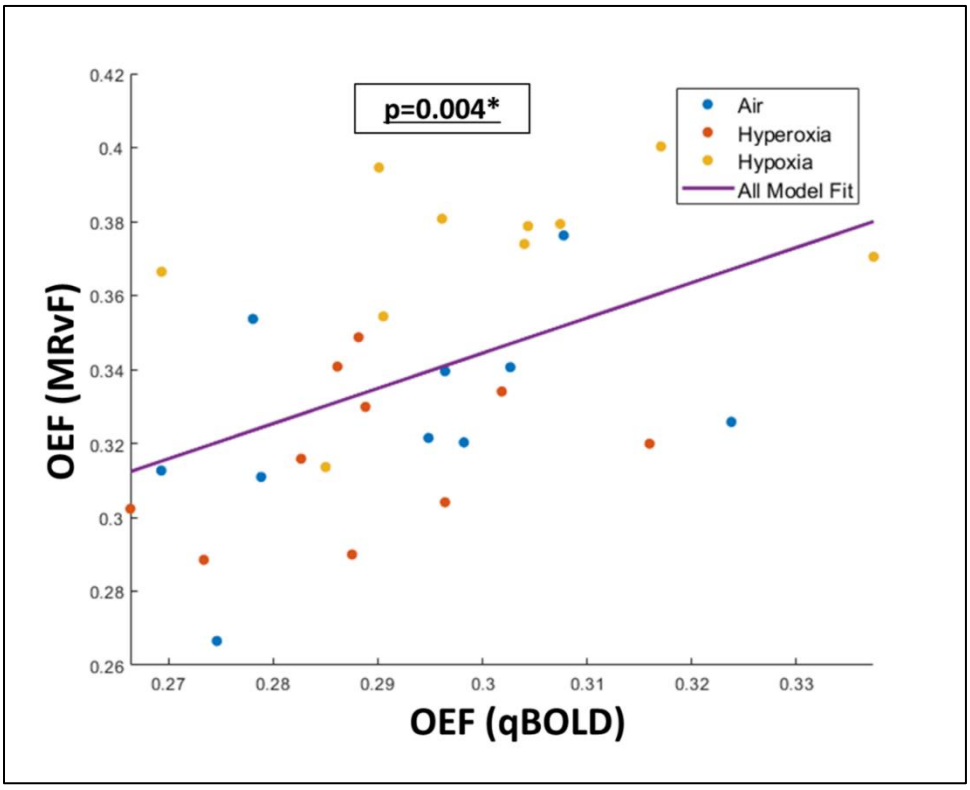


**Figure 4.6. Correlation Between MRvF- and qBOLD-derived OEF Measurements**. The correlation between MRvF-derived OEF and qBOLD-derived OEF during different oxygen inhalation conditions in gray matter of the frontal and parietal lobes. A linear mixed-effects model adjusted for subject clustering was fit to all participants across all conditions (purple line).

To verify the physiological effect of the induced hyperoxia and hypoxia conditions, arterial blood oxygenation was measured via pulse oximeter throughout scans. We calculated the change in OEF from normal air to hypoxia and hyperoxia in relation to the change in average $S_aO_2$ from the pulse oximeter during normal air compared to hyperoxia and hypoxia with another linear mixed effects model adjusted for subject clustering. Both qBOLD and MRvF showed significant increases in OEF as the arterial blood oxygenation decreased as expected (**Figure 4.7**).

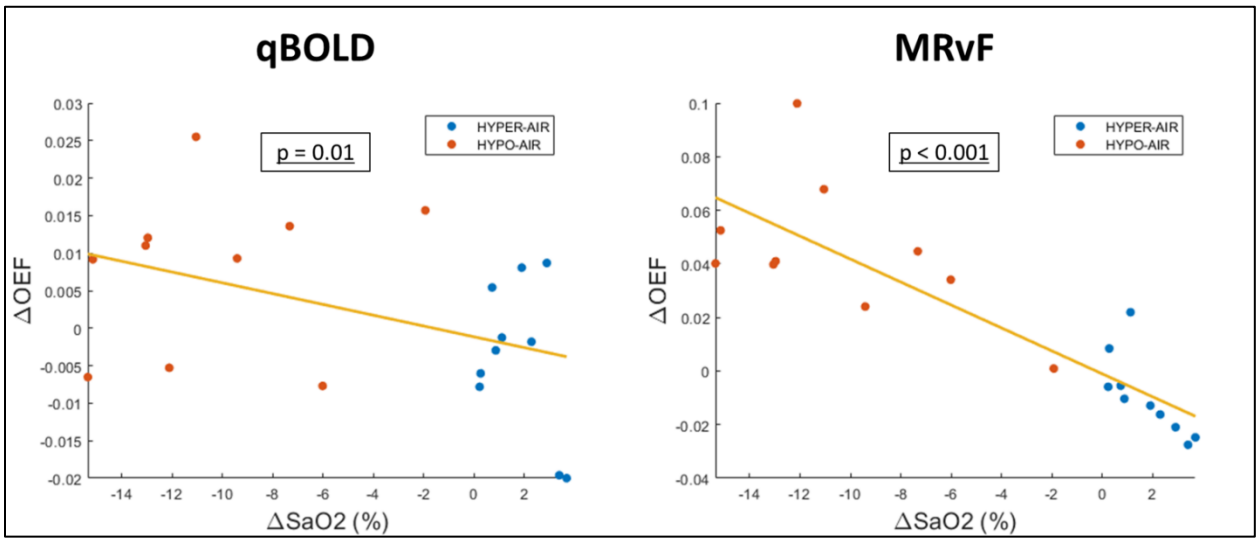


**Figure 4.7. Validation of OEF Measures from MRvF and qBOLD Against Pulse Oximeter**. A linear mixed effects model adjusted for subject clustering was fit to the change in OEF (measured with either MRvF or qBOLD) in gray matter and the change in arterial oxygen saturation ($S_aO_2$) measured by pulse oximetry. ΔOEF and $\Delta S_aO_2$ refer to the change from normoxia for each participant independently.

While there is not a "gold-standard" MRI method to measure oxygen extraction fraction in the brain, the ability to detect expected changes during controlled physiological experiments can be a useful validator for a new technique. Therefore, the average regional OEF measurements using both techniques were compared. Both qBOLD and MRvF showed significant changes in OEF during hypoxia compared to the normal air and hyperoxia conditions (**Figure 4.8**). However, the OEF values from MRvF under all three conditions were higher, and OEF during hypoxia compared to normoxia or hyperoxia was much more elevated using MRvF (**Figure 4.8**).

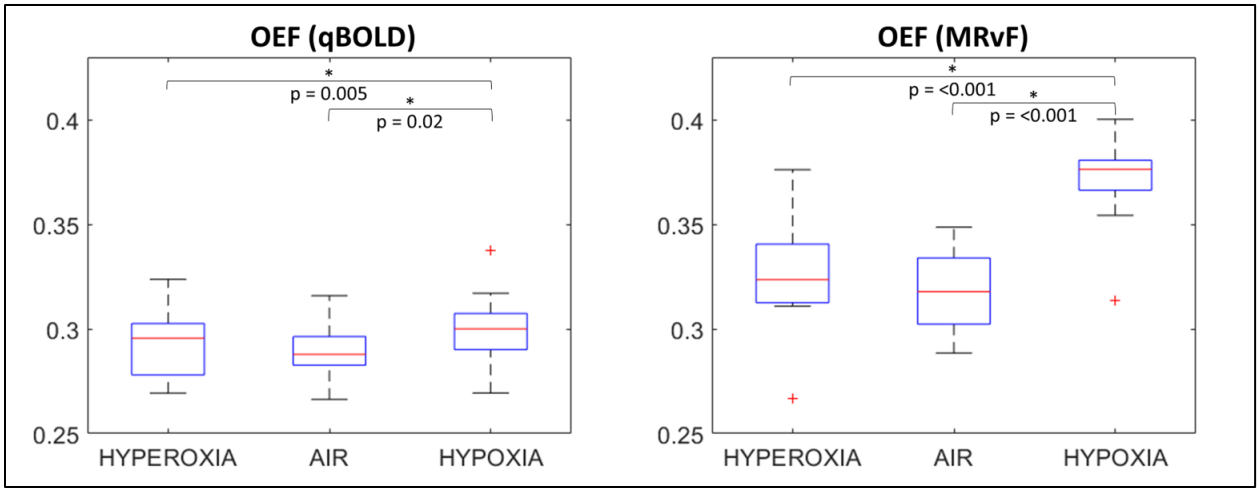


**Figure 4.8. Oxygen Extraction Fraction Across Oxygen Conditions with MRvF and qBOLD**. OEF values derived using MRvF and qBOLD during different oxygen inhalation conditions in gray matter of the frontal and parietal lobes for all subjects.

## *4.7 | Discussion and Conclusions*

The findings of this study reveal that brain OEF measurements from both qBOLD and MRvF provide sensitivity to physiological changes across hypoxic and hyperoxic inhalation conditions. OEF maps from MRvF visually showed higher SNR and more significant changes during different gas conditions, potentially reflecting the robustness of fingerprint matching to noise. Another possible reason the MRvF OEF has more significant changes in relation to changes in $S_aO_2$ could be due to the way we indirectly calculated OEF from MRvF using **Eq. 4.7**. By including $S_aO_2$ in the calculation, we may bias MRvF OEF to be related to $S_aO_2$. Theoretically, the $SO_2$ measurement from MRvF should be almost exclusively driven by venous blood, however, during hypoxia the $S_aO_2$ decreases significantly, likely also influencing the $SO_2$ measurements, and in turn making **Eq. 4.7** more biased.

For this work, a linear qBOLD model was utilized due to its simplicity of implementation and the GESFIDE sequence containing just five usable echoes after the spin echo for DBV calculations. However, more sophisticated qBOLD analytical models with 2-tissue compartments and Bayesian priors have been introduced and showed increased accuracy and reliability.[142] This limitation is especially noticeable in the group average OEF map (**Figure 4.5**) where we observe

considerable noise and unphysiological values. Recent studies have shown these Bayesian approaches to qBOLD mapping reduce inhomogeneity in OEF maps while providing more physiologically reasonable measures.[143]

A consistent limitation for this work, and the field of MRI-based oxygenation measures, is the lack of an easily accessible baseline validator for measures of cerebral oxygenation and oxygen consumption. The "gold-standard" for these experiments would be $^{15}$O-PET imaging, but practically this is rarely performed as PET imaging uses ionizing radiation and the $^{15}$O isotope has a half-life of only 2 minutes, which requires a very close cyclotron.[50] In the absence of an available "gold standard", a common practice is to induce a respiratory challenge to see if an expected change can be observed as we did here. Specifically, given the proportional relationships between CBF, $CMRO_2$, and OEF[144], during hypoxia less oxygenated blood is delivered[58,145] and therefore the proportion extracted from the blood increases. This is consistent with our results in **Figure 4.7** for both MRvF and qBOLD.

To summarize, in this chapter we investigated the effects of MRvF modeling and matching on parameter accuracy and reliability in silico and in vivo. Through a comparison with qBOLD, we demonstrated consistency between the techniques, reliable brain OEF measurements when compared against changes in $S_aO_2$ from a pulse oximeter, and expected changes in OEF in relation to hypoxia, normal air, and hyperoxia breathing conditions during scanning. Future studies can utilize these MRvF models to assess oxygenation changes in pathologies that affect neurovascular physiology. Finally, MRvF techniques effectively map brain hemodynamic parameters, including OEF, and are sensitive to changes in hypoxic and hyperoxic gas inhalation.

# Chapter 5 – Development and Optimization of Dynamic, Contrast-free Magnetic Resonance Vascular Fingerprinting

## *5.1 | Introduction and Background*

Advanced MRI techniques continue to be developed to measure brain perfusion[146], oxygenation[126], oxygen metabolism[147], and vascular reactivity[39] to better understand normal cerebrovascular function and indicate dysfunction. Magnetic resonance fingerprinting (MRF) is a relatively new technique that innovatively leverages MRI acquisition and reconstruction in order to overcome limitations of existing MRI techniques for quantitative, and multiparametric mapping.[8] MRF can also improve reproducibility[101–104] while being more robust to motion[96,97], noise[95,148], and under-sampling.[148–151] MRF is flexible to different biophysical models and ideally suited for quantification of parameters that are otherwise subtle or hard to measure, such as physiology corresponding to a small blood compartment. MRF has been performed with ASL sequences to produce maps of cerebral blood flow (CBF) and arterial transit time[152–154], and other fingerprinting studies have used combined gradient- and spin-echo sequences to simultaneously measure cerebral blood volume (CBV), microvascular radius (R), and oxygen saturation ($SO_2$).[9]

The latter has been referred to as MR vascular fingerprinting (MRvF) and leverages this framework to extract vascular parameters from BOLD signals using the fingerprinting method.[9] By varying microvascular parameters in a voxel tissue model, a dictionary containing the signal evolution of every combination of CBV, R, and $SO_2$ can be generated. A pattern-matching algorithm matches the closest virtual voxel in the dictionary to the measured signal time-course (obtained from each voxel in the images) and allows the underlying parameters from the closest simulation to be extracted to produce multiple quantitative vascular maps (**Figure 5.1**).

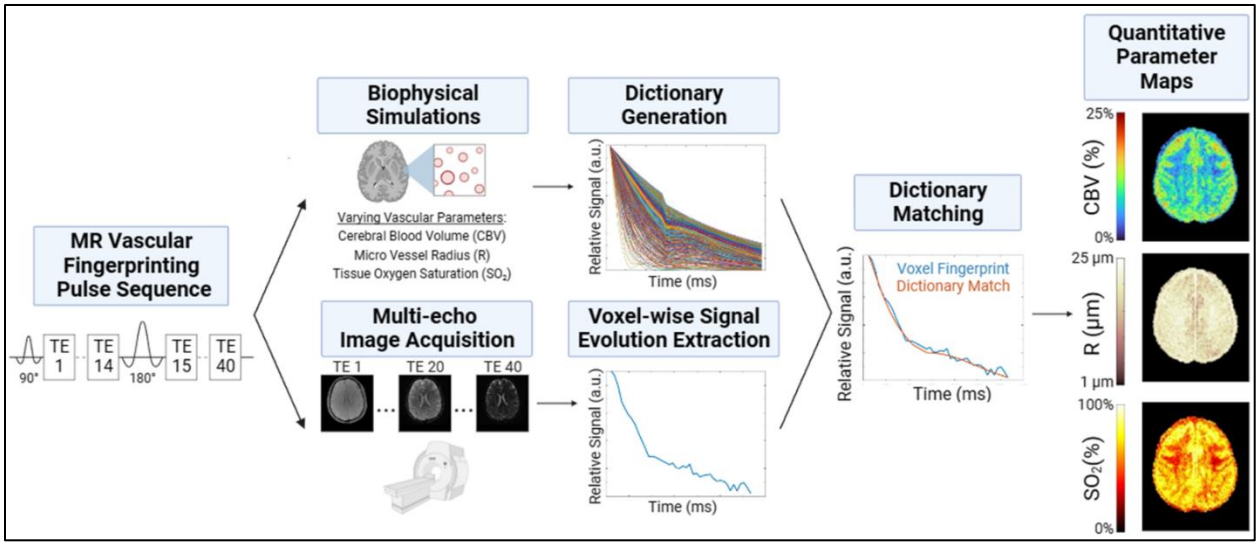


**Figure 5.1. Magnetic Resonance Vascular Fingerprinting Schematic**. A pulse sequence that samples both gradient and spin echoes and is sensitive to the vascular parameters of interest is utilized for both imaging and MR physics simulations. Physiological ranges of cerebral blood volume (CBV), micro vessel radius (R), and tissue oxygen saturation ($SO_2$) are used to simulate the MR signal in a 2D or 3D virtual voxel with each combination of those parameters. After the images are acquired, the time-course signal evolution of each voxel is compared to all dictionary entries. The closest match between the fingerprint and dictionary, as determined by the maximum inner product, allows for the extraction of the underlying parameters for quantitative parameter mapping.

Thus far, MRvF techniques have been utilized to examine stroke and brain tumors and produced vascular parameter maps similar to those produced with existing, validated methods.[9,107] Initial MRvF studies have all utilized either gadolinium or superparamagnetic iron oxide (USPIO) nanoparticle contrast agents to enhance the sensitivity of parameter matching. While often helpful for the visualization of vasculature and perfusion, exogenous contrast agents like gadolinium exclude patients that are allergic or have renal failure, and there is concern about the long-term deposition and toxicity of using such agents.[155] Contrast agents also prevent dynamic, repeated studies from being possible as once the agent is injected, the patient cannot be imaged at baseline until the agent is cleared. Accurate brain mapping of vascular parameters using MRvF methods has not yet been achieved in the absence of exogenous contrast agents.

Due to the paradigm shift of using signal progression to reconstruct images in MRF, pseudo-random and fast, under-sampled imaging has been used to generate reliable signal time courses for sensitive and accurate matching. Many of the first MRF studies[8,129,156] for relaxometry used thousands of consecutive images to generate these time courses, but recent studies[9,157] have shown that using fewer, fully sampled images with longer TR and higher signal-to-noise ratio

(SNR) can achieve comparable accuracy with similar scan time. In the context of vascular parameters, sequences that are known to be sensitive to vascular tissue properties can be adopted and accelerated. A recent fast spin- and gradient-echo (SAGE) pulse sequence provides entire brain volumes at five echo times (TEs), is sensitive to quantitative perfusion metrics[118,120], and could allow for dynamic vascular parameter mapping on the order of seconds. Like the gradient-echo sampling of the free induction decay and echo (GESFIDE) sequence used in the previous section and previous MRvF studies, the SAGE sequence samples signal during both the gradient and spin echoes, making it appropriate for qBOLD models of tissue oxygenation and blood volume. The SAGE sequence utilized in this work uses single shot echo planar imaging (EPI) readouts to allow for the full volume of the brain to be captured about every five seconds with five echoes collected per volume. While five TEs provide limited timepoints for an MRF pattern matching algorithm, a sequence with multiple TEs and very short acquisition time would be highly desirable for investigating rapid cerebrovascular processes and would represent a significant advancement from previous MRvF and MRF-ASL techniques that acquired the full brain on the order of 3-6 minutes.[9,107,152,153,158,159]

Overall, the recent introduction of MRF advances the capabilities of MRI and can be specifically used to probe vascular tissue properties of interest with MRvF. This chapter describes our work to advance dynamic MRvF by: (1) developing contrast-free MRvF using a novel matching algorithm and (2) optimizing a fast combined gradient- and spin-echo acquisition specifically for MRvF through numerical simulations and retrospective subsampling of a longer GESFIDE acquisition to ultimately enable future dynamic MRvF studies.

### *5.2 | Contrast-free Matching Algorithms for Gradient and Spin Echo Signal Curves*

A key component of MRvF is to identify a suitable algorithm to match the simulated dictionary to each voxel in the acquired signals. Previous studies with contrast found that certain vascular parameters have better sensitivity pre-contrast at certain TEs and post-contrast at other

TEs.[9,108,131] Similarly to what was demonstrated in *Chapter 4*, here we proposed two ideas to increase the contrast-free sensitivity and accuracy of fingerprint matching: (1) using phase information from the signals and (2) performing multistep matching. Previous MRvF methods have relied entirely on the signal magnitude of the images, but the complex-valued MRI signal also includes relevant signal phase information that has not been exploited. The difference in magnetic susceptibility between hemoglobin and deoxyhemoglobin could, for instance, lead to physiologically meaningful differences in signal phase and improve contrast-free sensitivity.[126] Alternatively, these same studies have also demonstrated that the earlier gradient echoes are most sensitive to bulk tissue oxygenation and could therefore be weighted more heavily to estimate $SO_2$ in MRvF. The key distinction between this matching optimization and *Chapter 4's* is the focus here on using fewer TEs for matching to enable accelerated, dynamic acquisitions as will be discussed later in this chapter.

These matching approaches were directly compared with the 40-echo GESFIDE sequence framework previously used for MRvF. We generated vascular fingerprinting dictionaries for the simulated GESFIDE sequence using the MRVox[110,111] toolkit in MATLAB with 2D virtual voxels. The dictionary contained 64,000 signal entries through simulating combinations of 40 values of $SO_2$ from 0 to 100%, 40 values of CBV from 0.1 to 25%, and 40 values of R from 2 to 24 microns (**Table A5.1**).

Matching, and subsequent parameter extraction were determined by selecting the simulated dictionary entry that had the maximum inner product with each acquired signal. Four matching algorithms (**Figure 5.2**) were implemented utilizing the magnitude or complex signal, and a 1-step or 2-step matching algorithm. The first step of the 2-step methods uses only the gradient echoes to identify an initial range of $SO_2$, as this signal regime is most sensitive to $SO_2$. The second step uses all echoes but limits the dictionary range in the $SO_2$ dimension to ±5% of the best match from the first step. We performed Monte Carlo simulations by randomly selecting a dictionary entry, adding Gaussian noise at a SNR of 160 independently to the real and imaginary

components, and then matching it against the entire dictionary. SNR was calculated using the first echo. We calculated the root-mean-squared error (RMSE) between the estimated parameters from the best match and the true underlying parameters. This was repeated 1,000 times, with a random dictionary entry (i.e., different vascular parameter values) each time, using each of the four matching algorithms on every noisy simulation.

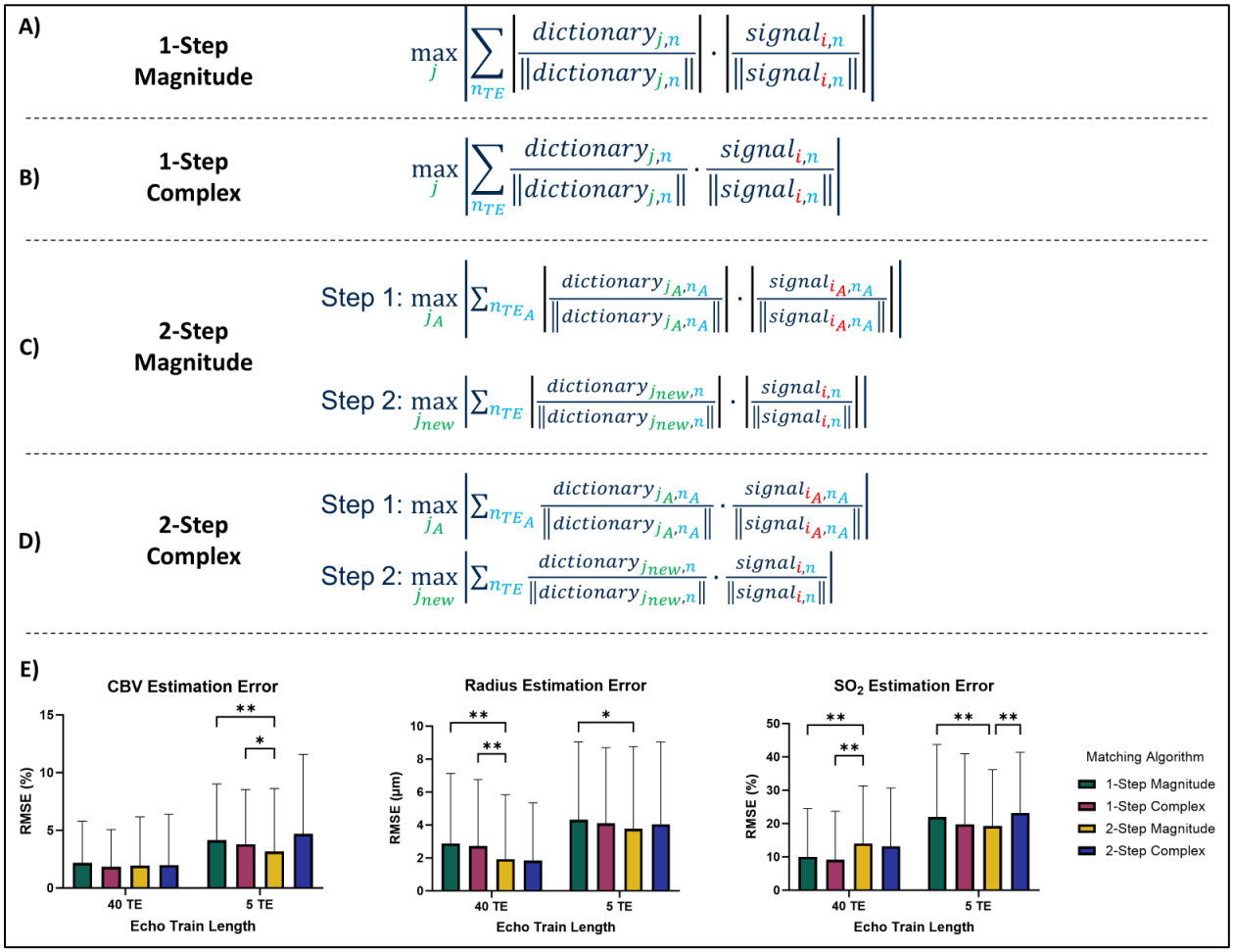


**Figure 5.2. Matching Algorithms and Simulation Estimation Error**. The 1-step algorithm includes Euclidean normalization of each dictionary entry (j) and each voxel (i) before taking the dot product between the two across all echoes ($n_{TE}$) using **(A)** the magnitude of the signal or **(B)** the complex signal. The 2-step iterative method first uses the free induction decay regime ($n_{TEA}$) and takes the dot product between the Euclidean normalized dictionary entries ($j_A$) and each voxel ($i_A$). The second step considers all echoes but limits the dictionary ($j_{new}$) to ±5% the $SO_2$ match determined from the first step. Both steps use either **(C)** just the magnitude of the signal or **(D)** the complex signal. **E)** Numerical simulation results: The root-mean-square error (RMSE) between the actual parameter values and the estimated values using each of the four matching algorithms. Each bar represents 1,000 Monte Carlo simulations with Gaussian noise added to simulated signals at a signal-to-noise ratio of 160. RMSE was calculated by simulating the 40-echo GESFIDE sequence and a subsampled 5-echo GESFIDE sequence. One-way ANOVA was performed to compare algorithm performance for 40- and 5-echoes independently.

We then retrospectively evaluated the four matching algorithms on an in vivo GESFIDE acquisition in a young, healthy volunteer. The GESFIDE sequence (TR=2000 ms, 40 TEs, spin

echo=100 ms, field-of-view=20×20 $cm^2$, slice thickness=2.5 mm, matrix=128×128, 12 slices, scan time=4 min) was acquired on a 3T scanner (MR 750, GE Healthcare Systems). We performed phase unwrapping and background phase removal[160,161] on the GESFIDE images and then matched the signal time course of each voxel to the GESFIDE dictionary described above, which was consistent with the imaging parameters from this in vivo acquisition.

*5.3 | Noise Levels and Retrospective Subsampling of Echoes*

We aimed to improve the temporal resolution for vascular fingerprint mapping by decreasing the number of TEs acquired. MRF utilizes the signal evolution across multiple TEs, therefore the tradeoff between mapping accuracy and number of TEs was investigated through a retrospective subsampling of the GESFIDE dataset.

We first took the previously simulated GESFIDE dictionary and subsampled in the TE dimension to generate new dictionaries with 20, 10, and 5 TE signal progressions. The purpose of this was to examine the effect of echo train length at various SNRs, as the target SAGE sequence has 5 TEs. Therefore, we subsampled the simulated GESFIDE dictionary signal curves to most closely mirror the SAGE sequence (**Figure 5.3**). We again randomly selected a dictionary entry, added Gaussian noise at SNRs of 160, 80, 40, 20, and 10, and matched it against each of the four dictionaries using the 2-step magnitude method. We calculated the RMSE between the estimated parameters and the true underlying parameters and repeated this with 1,000 random dictionary entries for each SNR/TE combination.

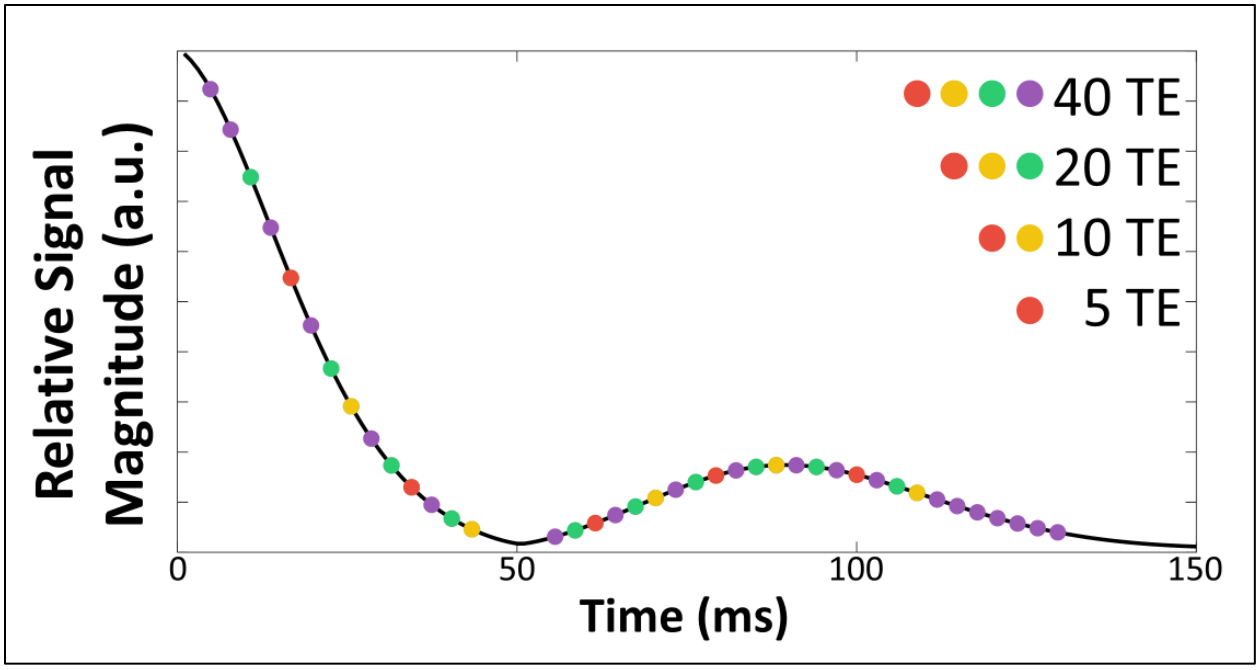


**Figure 5.3. Schematic of GESFIDE Subsampling**. GESFIDE scan and dictionary simulations with 40 echo times (TE) were subsampled to produce signals with 20, 10, and 5 TE, respectively.

The retrospective in vivo GESFIDE acquisition containing 40 TEs from the same subject as in *Section 5.2* was also subsampled to include only 20, 10, and 5 TEs. We matched the subsampled imaging datasets to their equivalently subsampled GESFIDE dictionaries and reconstructed the MRvF parameter maps with the 2-step magnitude method. The first echo of the GESFIDE images were registered to the subject's $T_1$-weighted structural scan (FSL FLIRT[137,138]), and these transforms were applied to the corresponding MRvF parameter maps from the same data. We segmented gray and white matter masks (FSL FAST[162]) from the $T_1$-weighted image for calculating tissue-specific parameter averages.

## *5.4 | Optimization of SAGE Sequence Parameters for Vascular Fingerprinting*

Our next goal was to optimize the SAGE sequence for prospective acquisition with only five echoes. Biophysical signal simulations were again performed using the MRVox toolkit in MATLAB but this time with the SAGE imaging sequence. An example of a simulated SAGE signal is shown in **Figure 5.4**, illustrating the free induction decay after the initial 90° RF pulse, the

refocusing after the 180° RF, and the signal dephasing after the spin echo. Eight TE patterns and imaging parameters were evaluated for both simulations and in vivo imaging (**Figure 5.4**).

A)

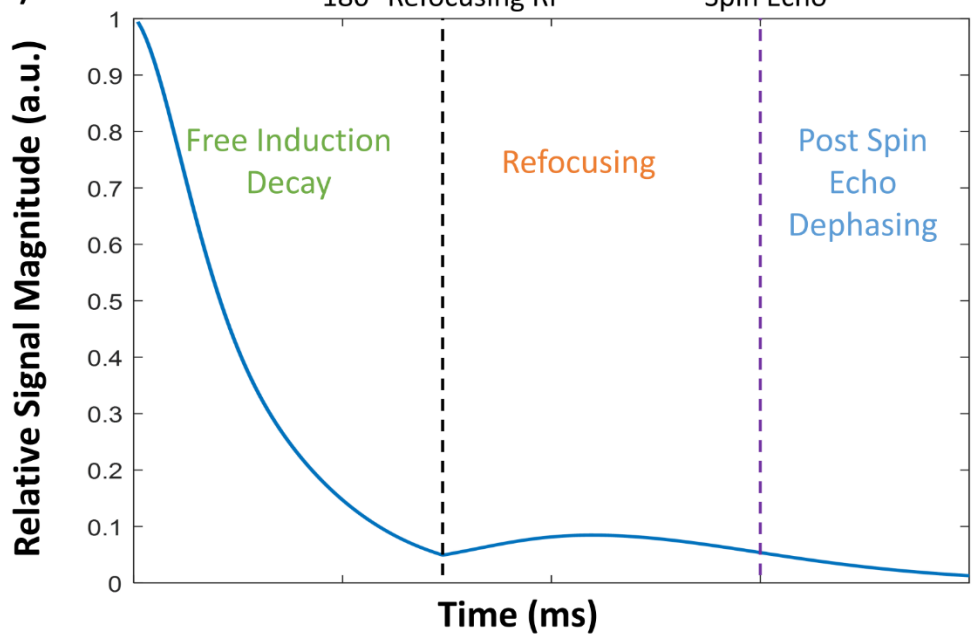


B)

| | 180° Refocusing RF | Spin Echo | $TE_1$ | $TE_2$ | $TE_3$ | $TE_4$ | $TE_5$ |
|---|---|---|---|---|---|---|---|
| A | 71 | 142 | 21 | 51 | 90 | 120 | 150 |
| B | 75 | 150 | 25 | 55 | 94 | 124 | 154 |
| SE | 79 | 158 | 29 | 59 | 98 | 128 | 158 |
| C | 80 | 160 | 30 | 60 | 99 | 129 | 159 |
| D | 85 | 170 | 35 | 65 | 104 | 134 | 164 |
| E | 90 | 180 | 40 | 70 | 109 | 139 | 169 |
| F | 95 | 190 | 45 | 75 | 114 | 144 | 174 |
| G | 100 | 200 | 50 | 80 | 119 | 149 | 179 |

*all times in table are in milliseconds

**Figure 5.4. Optimization of SAGE Sequence Imaging Parameters**. **A)** An example simulated signal from the spin and gradient echo (SAGE) sequence with the 180° refocusing pulse at 75 ms. **B)** Imaging parameters implemented in simulations and in vivo with colors indicating whether the sampled echo time is in the free induction decay (green), refocusing (orange), or post spin echo dephasing (blue) portion.

We generated eight simulated dictionaries, one for each set of imaging parameters, using the same vascular parameter ranges as described above for a total of 64,000 entries per dictionary. We selected the same random combination of vascular parameters from each

dictionary, added Gaussian noise at an SNR of 160, and then matched the noisy signals to their appropriate dictionary. This was repeated with 1,000 random parameter combinations, and the average RMSE was calculated for each of the eight imaging TE patterns.

To assess these SAGE imaging parameters in vivo, we scanned a healthy subject at 3T (Siemens Skyra) with each of the eight TE patterns in the same session. All other sequence parameters were kept the same (TR=4500 ms, 5 TEs, in-plane resolution=2×2 mm, slice thickness=5 mm, matrix size=110×110, 24 slices, in-plane GRAPPA acceleration=3). We matched the images from each TE pattern to the appropriate dictionary using the 2-step magnitude method to reconstruct CBV, R, and $SO_2$ maps. With the optimized SAGE parameters, we then used numerical simulations to perform an analogous SNR analysis to what was described for the GESFIDE simulations.

### *5.5 | Temporal Resolution and Noise Evaluation*

With an increase in acquisition speed and temporal resolution, there can be limitations in SNR. If the SNR achieved from one TR were deemed inadequate for good MRvF reconstruction, the sequence could be repeated, and multiple scans averaged to produce a single, higher SNR image. Therefore, the number of averages to reach this SNR threshold for accurate fingerprint matching dictates the achievable time resolution with this sequence and, ultimately, the types of rapid physiological changes in the brain that could be observed.

To examine whether the SNR achieved with the optimized SAGE sequence would be adequate for vascular fingerprinting, we collected SAGE images from the same healthy subject as in the previous section and performed signal averaging on 4, 16, and 64 consecutive repetitions of the sequence (TR=4.5s) to achieve relative SNR (rSNR) of 2x, 4x, and 8x respectively prior to fingerprint matching. The total acquisition time for each of these levels of rSNR were 18, 72, and 288 seconds, respectively. These higher rSNR images, in comparison to a single-TR image with no averaging, were matched to the SAGE dictionary to produce vascular parameter maps.

*5.6 | Contrast-free Matching Accuracy, Sensitivity, and Subsampling*

The average RMSE between the estimates from the noisy signal and the true underlying parameters were calculated for simulated GESFIDE signals with 40 and 5 TEs (**Figure 5.2**). For the 5 TE simulations, the 2-step magnitude method had significantly lower RMSE than at least one other method for all three MRvF parameters. Parameter maps generated using the single step matching methods show unphysiologically high estimates of CBV and low estimates for $SO_2$, which were improved using our iterative method (**Figure 5.5**).

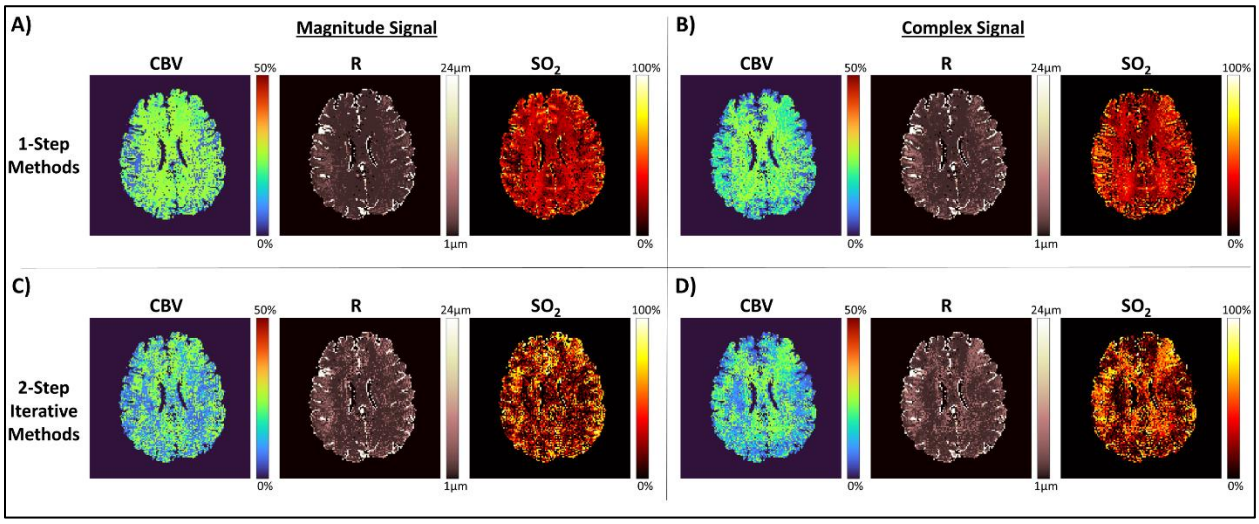


**Figure 5.5. Matching Algorithms with GESFIDE Images**. Parameter maps reconstructed from fingerprint matching a representative GESFIDE scan to the same dictionary using each matching algorithm in Figure 5.2. Maps were generated using **(A)** the 1-step magnitude method, **(B)** the 1-step complex method, **(C)** the 2-step magnitude method, and **(D)** the 2-step complex method.

The ability of the 2-step magnitude algorithm to distinguish the best match at different levels of SNR and number of TEs was assessed further for each of CBV, R, and $SO_2$ (**Figure 5.6**). Twenty combinations of SNR level (160, 80, 40, 20, and 10) and echo train length (40, 20, 10, and 5) were compared. The average RMSE for all parameters increased with decreasing SNR. With decreasing number of TEs, the highest RMSE was found for the 10-TE sequence for the majority of the simulations.

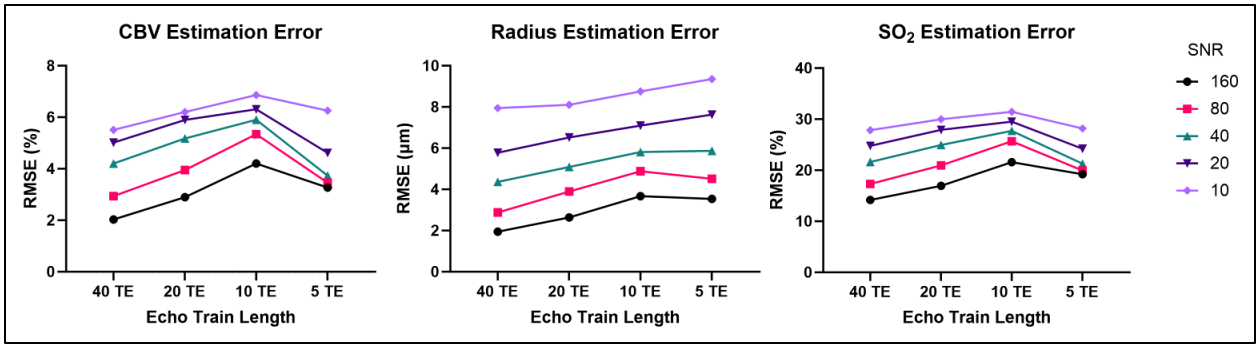


**Figure 5.6. Effects of Signal-to-noise Ratio and Echo Train Length on GESFIDE Simulations**. Mean root-mean-squared-error (RMSE) of vascular parameters predicted from matching noisy signals and the simulated signals true underlying parameter values at five signal-to-noise ratios (SNR) and with five echo train lengths (TE). A random parameter combination was independently taken 1,000 times, and the RMSE at each SNR/TE combination was calculated and then averaged.

The sensitivity of the technique was evaluated by showing the inner product matching metric for an example parameter combination (CBV=5%, R=5 μm, $SO_2$=65%) and all dictionary entries at varying levels of SNR (**Figure A5.1**). In this sensitivity plot, the matching metric after the first step of the magnitude matching method is displayed to show the entire range of the dictionary. The ability to localize good potential matches (i.e., dark bands in the figures) decreases sharply with decreasing SNR. This was also done with the same example parameter combination and varying the number of TEs, but only at an SNR of 160 (**Figure A5.2**). Unlike with the varying levels of SNR, decreasing the number of TEs did not substantially change the ability to match to a general region of the dictionary.

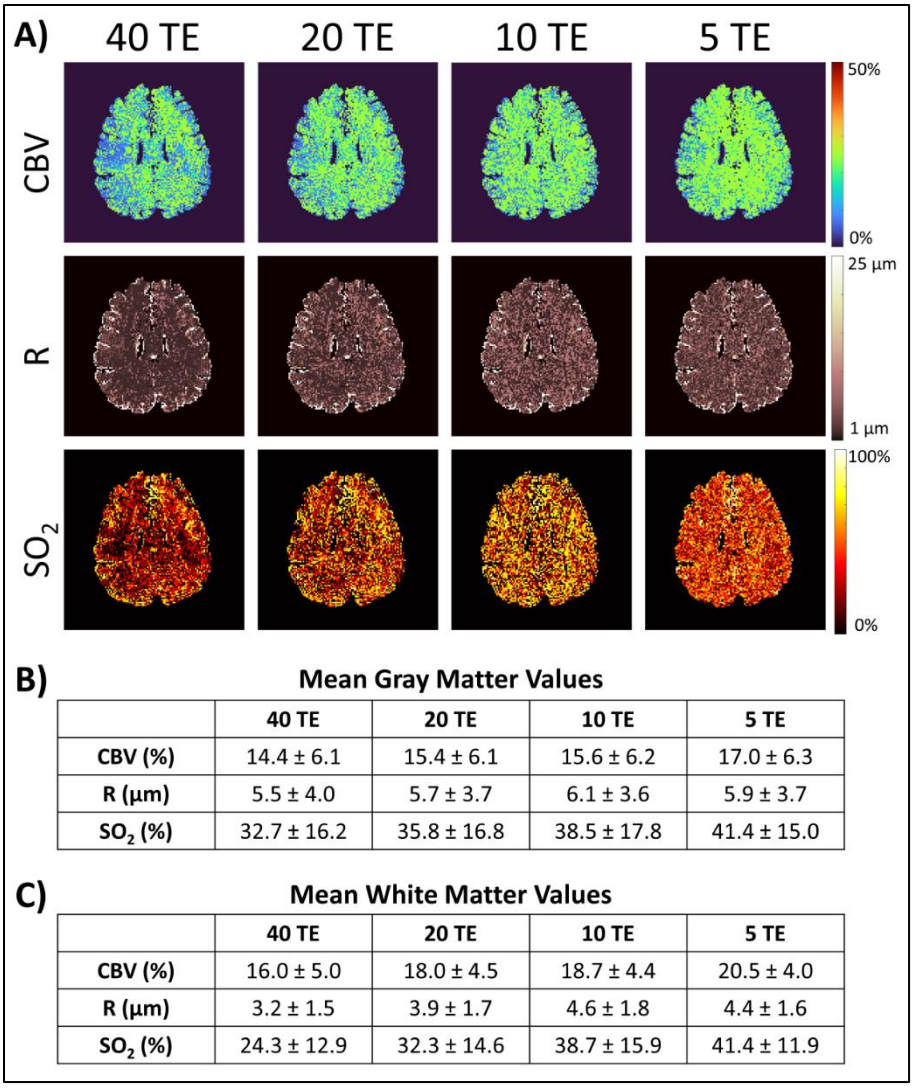


**B) Mean Gray Matter Values**

| | 40 TE | 20 TE | 10 TE | 5 TE |
|---|---|---|---|---|
| **CBV (%)** | 14.4 ± 6.1 | 15.4 ± 6.1 | 15.6 ± 6.2 | 17.0 ± 6.3 |
| **R (µm)** | 5.5 ± 4.0 | 5.7 ± 3.7 | 6.1 ± 3.6 | 5.9 ± 3.7 |
| **$SO_2$ (%)** | 32.7 ± 16.2 | 35.8 ± 16.8 | 38.5 ± 17.8 | 41.4 ± 15.0 |

**C) Mean White Matter Values**

| | 40 TE | 20 TE | 10 TE | 5 TE |
|---|---|---|---|---|
| **CBV (%)** | 16.0 ± 5.0 | 18.0 ± 4.5 | 18.7 ± 4.4 | 20.5 ± 4.0 |
| **R (µm)** | 3.2 ± 1.5 | 3.9 ± 1.7 | 4.6 ± 1.8 | 4.4 ± 1.6 |
| **$SO_2$ (%)** | 24.3 ± 12.9 | 32.3 ± 14.6 | 38.7 ± 15.9 | 41.4 ± 11.9 |

**Figure 5.7. Parameter Mapping of Subsampled GESFIDE Images**. **A)** Cerebral blood volume (CBV), vessel radius (R), and tissue oxygen saturation ($SO_2$) maps that were generated from a representative GESFIDE scan in a healthy volunteer. Matching was performed using all 40 echoes or to retrospective subsampled data with 20, 10, or 5 echoes for matching. Parameter values were averaged in the gray matter **(B)** and white matter **(C)** for maps with each number of acquired echoes.

For the retrospective in vivo TE subsampling of the GESFIDE acquisition (**Figure 5.7A**), R remains visually consistent, while CBV and $SO_2$ values overall appear to increase with fewer TEs. In this representative participant, quantitative regional analysis also shows that CBV and $SO_2$ estimates had an increasing trend with decreasing number of TEs in both gray (**Figure 5.7B**) and white matter (**Figure 5.7C**).

*5.7 | Sensitivity, Accuracy, and Temporal Resolution with SAGE Sequence*

Simulations with the eight SAGE echo patterns (**Figure 5.4**) generally saw reduced RMSE for R and $SO_2$ matching using the sequences with the shortest first TE (patterns A, B, and SE). The lowest RMSE for both R and $SO_2$ parameters was the SE pattern, which had the fifth TE occurring exactly at the spin echo (**Figure 5.8**). The in vivo parameter maps reconstructed from these different SAGE echo patterns showed minimal visual differences (**Figure 5.8**).

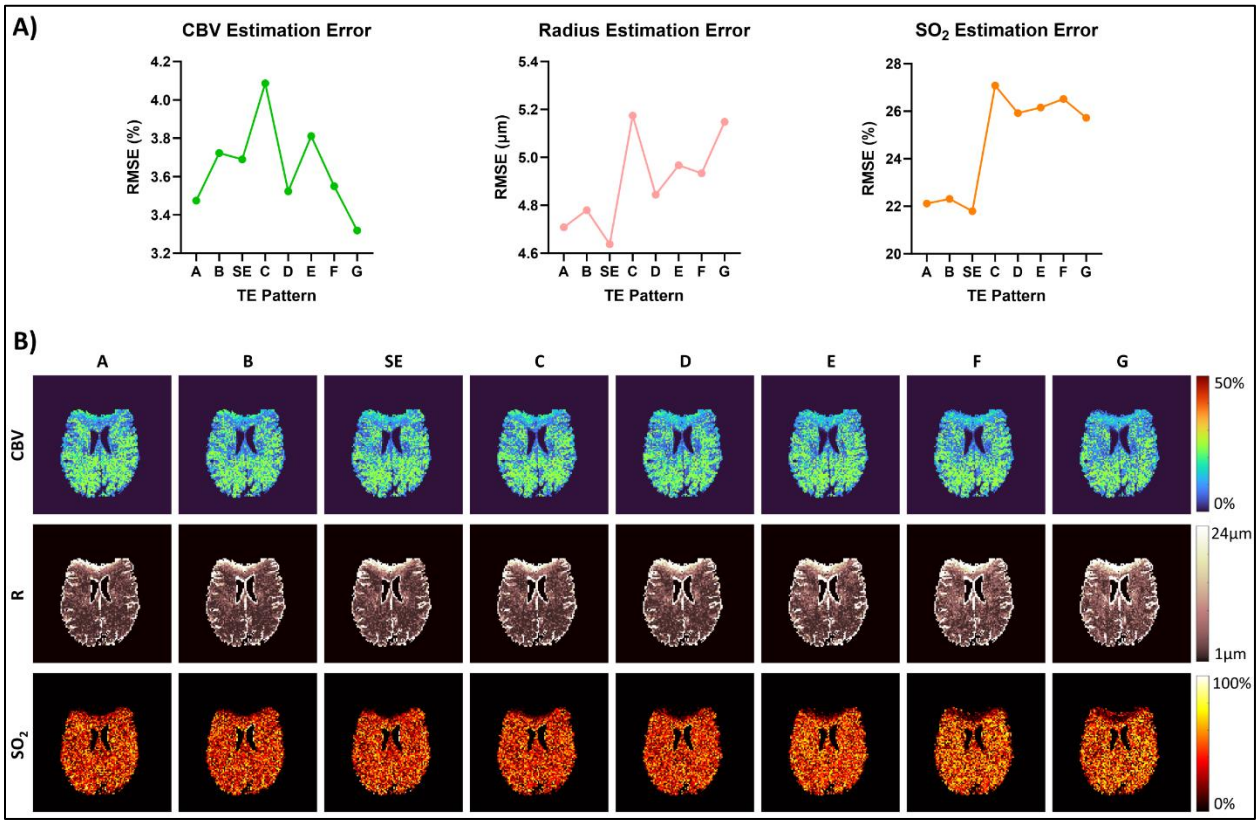


**Figure 5.8. Optimization of SAGE Sequence**. **A)** The average root-mean-square error (RMSE) between the actual cerebral blood volume (CBV), microvascular vessel radius (R), and tissue oxygen saturation ($SO_2$) values and the estimated values for each of the eight echo-time (TE) patterns as outlined in Figure 5.4. Gaussian noise was added independently to simulated signals at a signal-to-noise ratio of 160 for 1,000 Monte Carlo simulations. **B)** CBV, R, and $SO_2$ maps generated with the different sequence parameters used in dictionary simulations and image acquisition.

Given these results, the SE pattern was chosen as the optimal echo pattern and used in the next set of analyses. For SAGE simulations with varying levels of SNR, the RMSE was found to be significantly higher for SNRs below 80 for CBV and R estimates, and significantly higher for SNRs below 160 for $SO_2$ estimates (**Figure 5.9**). Similarly to the GESFIDE plots, the SAGE

sensitivity plots show a sharp decline in the ability to distinguish adjacent dictionary entries as SNR decreases (**Figure A5.3**).

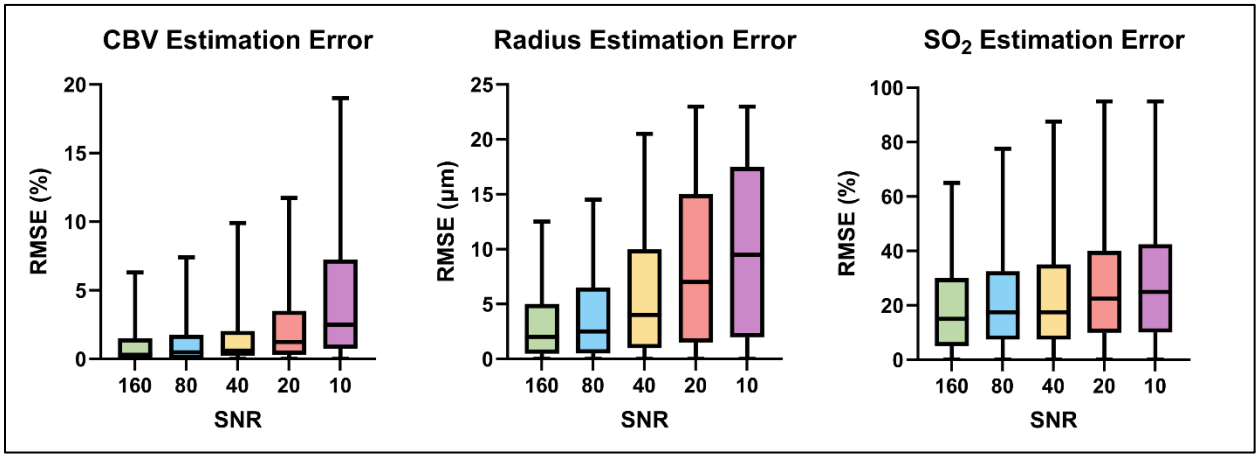


**Figure 5.9. Effect of Signal-to-noise Ratio on Optimized SAGE Simulations**. Root-mean-squared-error (RMSE) of vascular parameters predicted from matching noisy signals and the simulated signals true underlying parameter values at five signal-to-noise ratios (SNR) with the optimized SAGE sequence. Random parameter combinations were independently taken 1,000 times, and the RMSE with each SNR was calculated. Outliers were removed with the ROUT method, and Q was set to 1% prior to one-way ANOVA with multiple comparisons and Dunnett correction.

The tradeoff between SNR and temporal resolution was investigated in vivo by generating parameter maps from signal-averaged images. There were minimal observable differences regardless of rSNR, and the inner product matching metric remained consistently high for all rSNR levels (**Figure 5.10A**). Quantitative regional analysis showed no differences between average CBV, R, or $SO_2$ values in either the gray (**Figure 5.10B**) or white matter (**Figure 5.10C**) at different rSNR levels and were consistent with the values and regional trends in **Figure 5.7**.

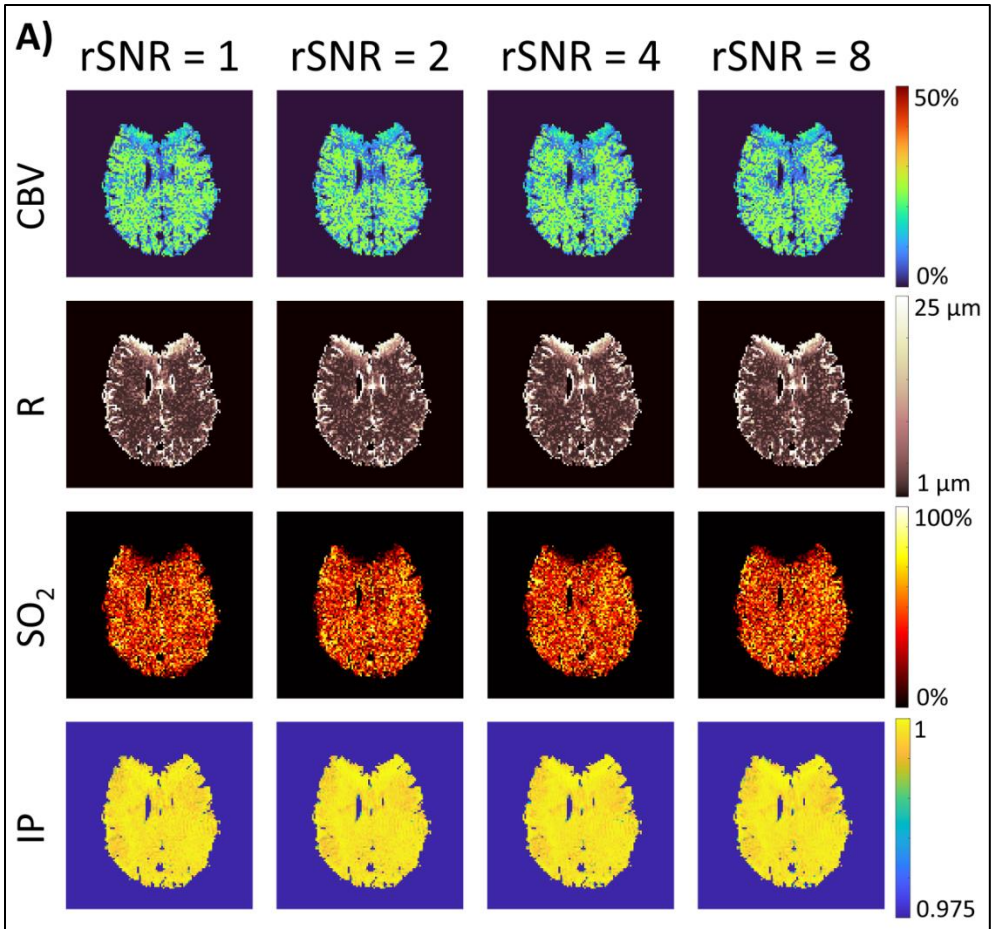


**B)** **Mean Gray Matter Values**

| | rSNR = 1 | rSNR = 2 | rSNR = 4 | rSNR = 8 |
|---|---|---|---|---|
| **CBV (%)** | 13.4 ± 6.5 | 13.4 ± 6.5 | 13.4 ± 6.5 | 13.3 ± 6.6 |
| **R (m)** | 8.2 ± 5.7 | 8.2 ± 5.7 | 8.2 ± 5.7 | 8.3 ± 5.8 |
| **$SO_2$ (%)** | 32.6 ± 17.1 | 32.8 ± 17.1 | 32.8 ± 17.1 | 33.1 ± 17.3 |

**C)** **Mean White Matter Values**

| | rSNR = 1 | rSNR = 2 | rSNR = 4 | rSNR = 8 |
|---|---|---|---|---|
| **CBV (%)** | 17.1 ± 5.5 | 17.2 ± 5.6 | 17.2 ± 5.6 | 17.0 ± 5.7 |
| **R (m)** | 5.9 ± 4.7 | 5.8 ± 4.7 | 5.8 ± 4.6 | 5.8 ± 4.7 |
| **$SO_2$ (%)** | 36.0 ± 14.7 | 35.8 ± 14.8 | 36.0 ± 14.7 | 36.1 ± 14.7 |

**Figure 5.10. Relative SNR and Temporal Resolution of SAGE Sequence**. **A)** Images were consecutively acquired with the SAGE sequence for 110 repetitions during free breathing. The first 4, 16, and 64 images were averaged to produce relative signal-to-noise ratio (rSNR) images of 2x, 4x, and 8x, respectively. The SAGE images with different levels of signal averaging then underwent MRvF matching to produce the cerebral blood volume (CBV), vessel radius (R), and tissue oxygen saturation ($SO_2$) shown. The inner product (IP) maps indicate the value of the matching metric for each voxel. Average parameter values are shown for the gray matter **(B)** and white matter **(C)** at each rSNR for the representative participant.

*5.8 | Discussion and Conclusions*

In this work, we extended existing MRvF methods to enable dynamic and quantitative mapping of cerebrovascular physiology and demonstrated the ability to produce robust vascular parameter maps in the absence of contrast agents, further increasing the techniques' accessibility and translatability. While we demonstrated good accuracy (**Figure 5.6**) at high levels of SNR in simulations, in vivo parameter estimations generally had higher CBV and lower $SO_2$ values than we would anticipate (CBV from 1-10%[163,164] and $SO_2$ from 50-80%[125,165]) in healthy individuals. The sensitivity plots (**Figures A5.1**, **A5.2**, **A5.3**) illustrate the relationship between the matching metric and all dictionary entries, highlighting the difficulty in disentangling CBV and $SO_2$, as increasing CBV and decreasing $SO_2$ have similar effects on the qBOLD signal. This relationship between CBV and $SO_2$ likely contributes to our estimations being higher and lower, respectively, than we expected and is a key reason contrast agents have been used in previous MRvF studies. Additionally, using more echoes like previous studies with the GESFIDE sequence could have mitigated, but not eliminated these biases. While introducing 2-step iterative matching (**Figure 5.5**) improved the $SO_2$ maps by more heavily weighting the gradient echo portion of the sequence for extracting oxygenation values, adding the phase component of the signal showed limited effect. The limited benefit of phase may be partially related to difficulties with phase unwrapping and background phase removal of images prior to MRvF matching, which will be optimized in future work.

While MRF has been shown to be quite robust to noise, when considering dynamic MRF, the minimum SNR necessary to generate accurate maps is of critical importance. Our results (**Figure 5.10**) demonstrated no meaningful differences in parameter matching after signal averaging, indicating that a single TR of the SAGE sequence has adequate SNR for parameter matching. This aligns with SNR simulation results as the in vivo images had an SNR of ~160 at the first echo and simulations found significantly less error at SNRs above 80 for CBV and R, and above 160 for $SO_2$. These findings are relevant for dynamic mapping as one SAGE repetition with

this protocol took 4.5 seconds, whereas if the 4, 16, or 64 averages were necessary, each repetition would take 18, 72, or 288 seconds respectively, decreasing temporal resolution and the physiological processes these techniques could observe. This sequence could be accelerated even further with the incorporation of simultaneous-multi-slice (SMS) techniques used with SAGE previously.[120] Reducing the TR of the sequence from 4.5 seconds to <2 seconds could have significant applications for simultaneously investigating resting-state BOLD fluctuations in parallel to CBV, R, and $SO_2$ from MRvF.

While it is positive that the SNR of this SAGE sequence was not a limiting factor of MRvF matching, it leads to the question of why our estimates of CBV and $SO_2$ are higher and lower than we would anticipate regardless of increasing rSNR. This likely points to an issue with sensitivity of our dictionary as opposed to SNR of our signal. The broad inner product maxima, as seen in our sensitivity plots (**Figure A5.1**, **A5.2**, **A5.3**), illustrate this lack of sensitivity and major limitation of this approach. As discussed previously, contrast agents improve this sensitivity but introduce their own problems and limit the ability to perform dynamic studies. Therefore, a few other approaches to improve sensitivity could be developing new, fast sequences specifically for dynamic MRvF that maximize sensitivity of CBV and $SO_2$, using a more sophisticated matching algorithm for distinguishing between dictionary entries, or adding additional information to the matching process like another parameter or phase as in *Chapter 4*.

In the optimization of the SAGE sequence for MRvF, the lowest error was observed in the three TE patterns with the earliest first echo. These are the only three patterns that sample at the spin echo or later and, therefore, may have increased sensitivity to signal contributions from the microvasculature. Additionally, the earlier the first TE, the higher the signal and therefore better SNR, compared to patterns with later TEs. While adapting an existing sequence like SAGE for MRvF methods increases the ease of access, developing a new sequence that intentionally maximizes sensitivity of the three MRvF parameters is an active area of research[166] and could increase sensitivity, accuracy, and temporal resolution.

Another interesting observation was that the 5-echo subsampled simulations on average had lower RMSE than the 10-echo subsampled simulations (**Figure 5.6**). Including more time points for fingerprint matching would seem like it should improve accuracy, so these results were slightly counterintuitive. However, there may be a few explanations of this phenomenon. Like the SAGE optimization mentioned above, the earliest TEs have drastically higher SNR than later TEs. With the 10-echo subsampling, we are including five additional TEs for matching, with four of those TEs expected to be at very low SNR portions of the signal and the fifth one still lower SNR than the first TE of the 5-echo subsampled sequence (**Figure 5.3**). The 20-echo and 40-echo simulations both had at least one TE earlier than the 5-echo simulations. The addition of these low SNR TEs may introduce significant additional noise into the matching component, negating the benefit of having additional timepoints. Performing the 10-echo subsampling with an earlier, higher SNR TE would likely result in lower RMSE for those simulations. Similarly, if we performed the 5-echo subsampling with the additional echoes that were added in the 10-echo subsampling we would expect increased RMSE due to the significantly worse SNR. The subsampling was conducted to most closely reflect the TE sampling we have with the SAGE sequence, however, additional subsampling at other timepoints could be done to investigate the optimal sampling for MRvF sequences in general. Both the SAGE optimization and this GESFIDE subsampling indicate the importance of sampling timepoints, highlight by improved accuracy with earlier TEs that have higher SNR.

In this chapter we advanced MR vascular fingerprinting through pattern matching without contrast agents, investigating the tradeoffs between SNR, sensitivity, number of echoes, and temporal resolution, and optimizing an accelerated spin- and gradient-echo sequence for future dynamic MRvF. These techniques demonstrated improved parameter mapping with an iterative matching algorithm and adequate SNR with the SAGE sequence from just one repetition for robust vascular parameter matching on the order of seconds. This optimized, dynamic MRvF

framework enabled the next set of studies that look at dynamic cerebrovascular function using MRvF and will be discussed in the next chapter.

# Chapter 6 – Application of Dynamic Magnetic Resonance Vascular Fingerprinting During Hypercapnia

## *6.1 | Introduction and Background*

Accurate vascular parameter map reconstruction with MRvF is dependent on using a pulse sequence that is sensitive to changes in blood oxygenation. Previous MRvF studies[9,107] have used time-consuming, sequences and contrast agents to increase this sensitivity, at the expense of temporal resolution. In *Chapter 5* we demonstrated how contrast-free MRvF reconstruction, in combination with a rapid acquisition, could allow for dynamic mapping of multiple vascular parameters and enable new investigations of dynamic vascular function in the brain. By utilizing a fast spin- and gradient-echo (SAGE) pulse sequence with only five echo times (TE) that is sensitive to quantitative perfusion metrics[120], we can dynamically reconstruct vascular parameter maps in seconds (<5 s) rather than minutes. While five TEs provides limited timepoints for the pattern matching algorithm, we showed in *Chapter 5* that SAGE has an adequate echo train length and signal-to-noise ratio for MRvF while also providing high temporal resolution and accuracy.

MRvF with these advantages allows for its utilization to look at rapid physiological processes in the brain. One such process is cerebrovascular reactivity (CVR), which is the ability of the vessels in the brain to respond (constrict or dilate) in response to vasoactive stimuli, like carbon dioxide ($CO_2$) gas. Due to this response, $CO_2$ inhalation has been shown to significantly increase cerebral blood flow in healthy individuals, but significantly less in normal aging[42,167] and dementia.[48,168] Hypercapnia therefore is expected to also cause changes in other vascular parameters of interest, like those measured with MRvF. By introducing $CO_2$ gas inhalation (hypercapnia) during MR acquisition, we can quantitatively measure how CBV, vessel radius, and $SO_2$ change in relation to fluctuations in the stimulus. CVR has been primarily measured using BOLD sequences[39], but with MRvF and the SAGE sequence, changes in CBV, R, and $SO_2$ in

response to a vasoactive stimulus could be obtained simultaneously to BOLD for parallel comparison and validation of the new metrics. Insights into how the magnitude and rate of these parameters change may be able to provide information on disease progression and provide additional diagnostic value.

The significant strides towards dynamic MRvF made in *Chapter 5* of improving contrast-free matching with a novel algorithm and optimizing a SAGE acquisition specifically for MRvF enable further studies to probe dynamic vascular physiology. This chapter describes our work to apply this advanced dynamic MRvF imaging platform in prospective scans during a controlled hypercapnic respiratory gas challenge. Ultimately, this work could lead to rapid, quantitative, and multiparametric functional imaging biomarkers of cerebrovascular physiology.

### *6.2 | Acquisition of MR Vascular Fingerprinting During Hypercapnia*

To assess the sensitivity of MRvF-derived vascular parameters to observe rapid, expected changes in physiology, we set up an experiment to observe subjects' responses to hypercapnic stimulus. All MRI images were acquired on a 3T scanner (Siemens Skyra). Four separate participants (ages 25±0.7 years, 2 female) underwent imaging that included a T1-weighted magnetization prepared rapid gradient echo (MPRAGE) and two separate SAGE acquisitions with the optimized imaging parameters (TR=4500 ms, 5 TEs [29 59 98 128 158 ms], in-plane resolution=2×2 mm, slice thickness=5 mm, matrix size=110×110, 24 slices, in-plane GRAPPA acceleration=3), one during hypercapnia and one during free-breathing. For each of the two SAGE acquisitions, we repeated the sequence 110 times consecutively for an acquisition time of ~8.5 minutes.

Throughout imaging, participants were connected to a gas breathing apparatus (**Figure 6.1**[169]). The breathing apparatus was connected to a Douglas bag filled with medical grade hypercapnic gas (5% $CO_2$, 21% $O_2$, 74% $N_2$) and contained a switch to control whether the participant would be breathing the gas or normal room air. The apparatus also contained a line

that ran out of the scanner room to a capnograph (Nonin, RespSense II) that recorded end-tidal $CO_2$ ($EtCO_2$) values from the participant. A nose plug was used to ensure that the participant exclusively breathed through the apparatus. Respiratory rate, heart rate, and pulse oxygen saturation were monitored throughout the scan to ensure participant safety and compliance.

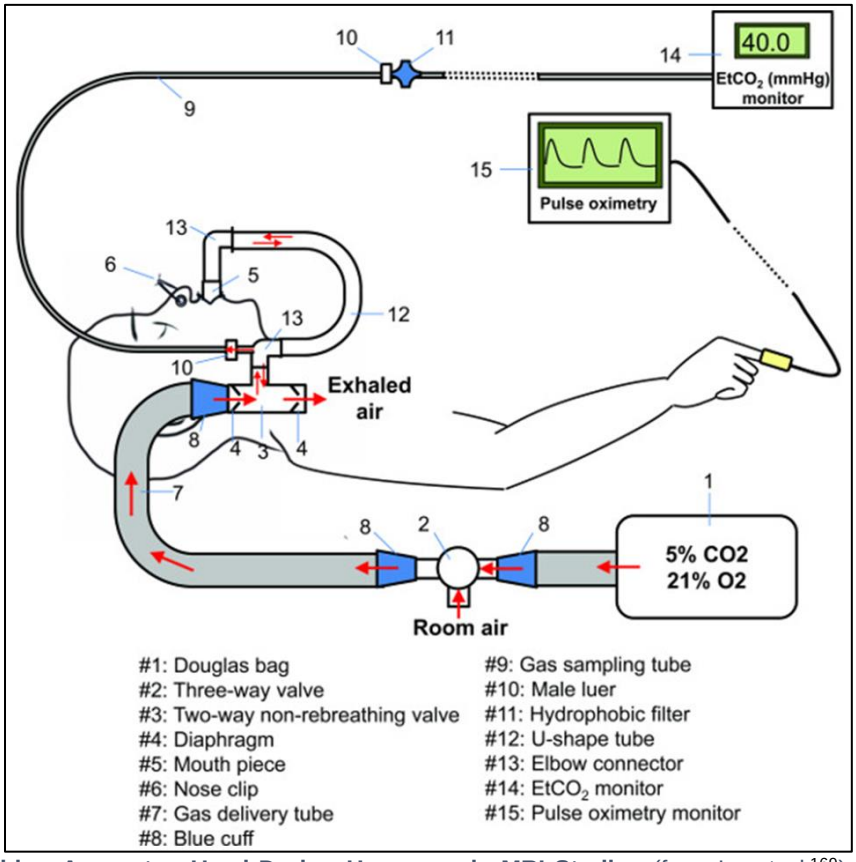


**Figure 6.1. Breathing Apparatus Used During Hypercapnia MRI Studies** (from Lu et al.[169]). 5% $CO_2$ gas was delivered in 1-minute blocks that were controlled by flipping the switch (#2) between room air and the hypercapnic gas filled Douglas bag (#1). Each participant's nose was clipped shut (#6) and forced to breathe through the scuba-like mouthpiece (#5) while in the scanner. End-tidal $CO_2$ ($EtCO_2$) from exhalations was monitored via a capnograph (#14) located outside of the scanner room.

During $CO_2$ inhalation, CVR takes about 30 to 60 seconds to reach near maximal response.[170] Therefore, a gas-inhalation paradigm with four 1-minute blocks each of gas-delivery and rest was utilized while the first set of SAGE images were acquired (**Figure 6.2A**). With this design, 13 to 14 SAGE volumes are captured during each block. This sampling rate during each block will be an important consideration for future work investigating the speed of reactivity to reach maximal response.

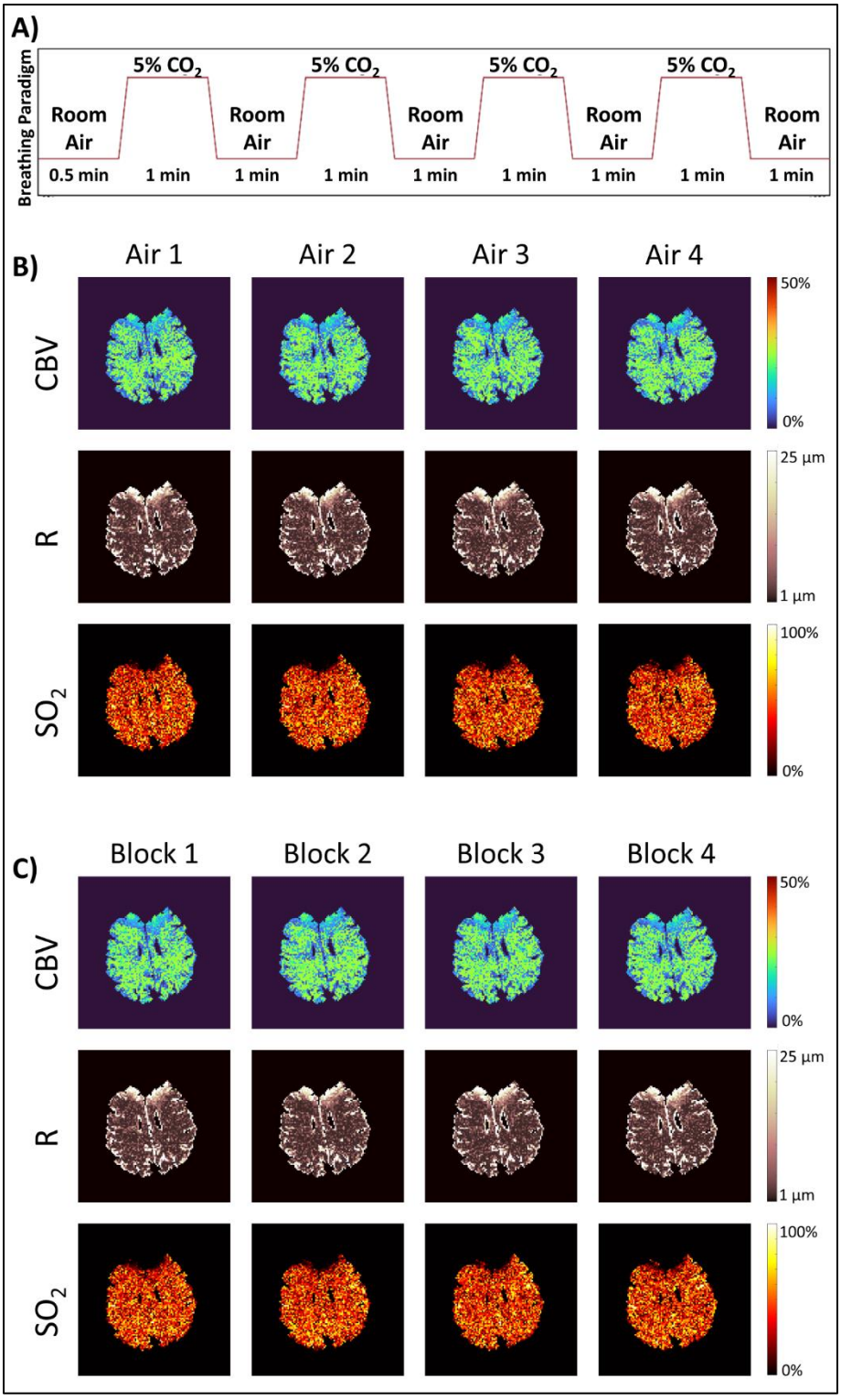


**Figure 6.2. Breathing Paradigm and Stability of Parameter Mapping**. Images were continuously acquired with the SAGE sequence for 110 repetitions times (TR) for a scan time of ~8.5 minutes. **A)** During the scan, the participant experienced four 1-minute blocks of hypercapnic gas (5% $CO_2$) inhalation. The cerebral blood volume (CBV), vessel radius (R), and tissue oxygen saturation ($SO_2$) were matched using MRvF independently at each TR. **B)** The parameter maps reconstructed from the same slice of the representative at TRs 3, 35, 62, and 87, each during periods of normal air breathing with typical $EtCO_2$. **C)** The parameter maps reconstructed from the same slice at TRs 22, 50, 76, and 104, each during separate periods of hypercapnic gas breathing with elevated $EtCO_2$.

*6.3 | Analysis of MR Vascular Fingerprinting During Hypercapnia*

The first gradient echo (TE = 29 ms) of the SAGE sequence was extracted as a BOLD-weighted image for each TR to directly compare our MRvF-derived metrics during gas breathing to BOLD responses in the same individuals. We utilized the optimal SAGE dictionary generated in *Chapter 5*, along with the 2-step magnitude matching algorithm, to reconstruct vascular parameter maps for the four participants. This was repeated for every TR to generate CBV, R, and $SO_2$ maps at every time-point.

Using FLIRT in FSL[137,138], we registered the spin echo of the SAGE sequence to each participant's T1-weighted image and then applied this transform to their BOLD, CBV, R, and $SO_2$ maps. We segmented gray and white matter regions-of-interest (ROIs) on each participant's T1-weighted image using FAST in FSL.[162] The BOLD signal and MRvF-derived CBV, R, and $SO_2$ values were spatially averaged to produce a single time course per parameter in each ROI for each participant. This was done for both gray and white matter during the hypercapnic and free-breathing SAGE acquisitions. We then manually aligned each participant's $EtCO_2$ time course to their whole-brain BOLD time course and applied this temporal alignment to the MRvF parameter time courses.

To test that the BOLD, CBV, R, and $SO_2$ curves showed cerebrovascular modulation in response to the block-design gas stimulus, we took the ROI time courses acquired during the hypercapnic SAGE acquisition and performed linear regression to the $EtCO_2$ response[60]:

**Equation 6.1**: $$Parameter = \beta_0 + \beta_1 EtCO_2 + \beta_2 t + \varepsilon$$

where *Parameter* is any of BOLD, CBV, R, or $SO_2$; $t$ is time, included to account for signal drift; $\beta_0$, $\beta_1$, and $\beta_2$ are the coefficients being estimated; and $\varepsilon$ is residual error. With these coefficients, we were then able to calculate the unit percent change in our parameter relative to the unit change (mmHg) in $EtCO_2$, or CVR[60]:

**Equation 6.2**: $$CVR_{par} = \frac{\beta_1}{\beta_0 + \min(ETCO_2)\beta_1}$$

This reactivity calculation was repeated for BOLD and each of the three MRvF parameters in both gray matter and white matter.

*6.4 | Vascular Fingerprinting Parameter Responses to Hypercapnic Stimulus*

The participants exhibited an average increase of approximately 10 mmHg in $EtCO_2$ recordings during periods of hypercapnic gas delivery compared to free breathing. The $EtCO_2$ trace, the BOLD signal (from the first SAGE echo), and vascular fingerprinting derived measures (CBV, R, and $SO_2$) in response to the block vascular stimulus from a representative subject's gray matter are shown in the top half of **Figure 6.3**. The bottom half of **Figure 6.3** shows the same recordings during the second SAGE scan with free-breathing and does not show the same large periodic fluctuations. Example parameter maps reconstructed during periods of free-breathing and hypercapnia are shown in **Figure 6.2**. These maps also demonstrate the consistency of MRvF through similar parameter maps being independently reconstructed for hypercapnic and normal breathing conditions despite being collected minutes apart.

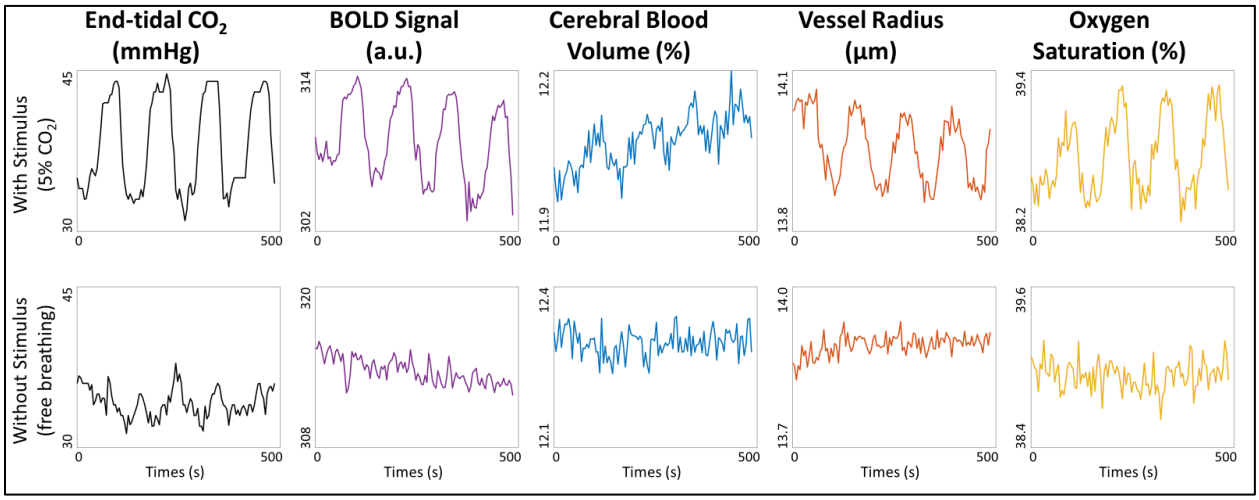


**Figure 6.3. Representative Gray Matter Signal Time Courses During Hypercapnia Study**. Gray matter averaged time-courses of end-tidal $CO_2$, blood oxygen level dependent (BOLD) signal, cerebral blood volume (CBV), microvascular vessel radius (R), and tissue oxygen saturation ($SO_2$) acquired during hypercapnic stimulus blocks (top row) and during free breathing (bottom row) from a single participant. BOLD, CBV, R, and $SO_2$ values represent gray matter averages.

Linear regression (**Eq. 6.1**) was performed for BOLD, CBV, R, and $SO_2$ against $EtCO_2$ during the hypercapnic acquisition for all four subjects in both gray matter (**Figure 6.3**, **Figure A6.2**) and white matter (**Figure A6.3**). This regression analysis showed that the BOLD, $SO_2$, and CBV time curves significantly ($p<0.01$) correlated with $EtCO_2$ fluctuations in all participants, whereas R negatively correlated with $EtCO_2$ ($p<0.01$). The normalized regression coefficients for gray matter (**Table A6.1**) and white matter (**Table A6.2**) were then used to determine the reactivity (CVR) of each parameter (**Eq. 6.2**) and averaged across subjects. BOLD-CVR and $SO_2$-CVR showed similar regional differences with higher CVR in gray matter than white matter, while R-CVR showed the opposite trend (**Table 6.1**).

**Table 6.1. Regional CVR from BOLD and MRvF Parameters During Hypercapnic Stimulus**

| | Gray Matter | White Matter |
|---|---|---|
| $CVR_{BOLD}\left(\frac{\%\Delta BOLD}{mmHg}\right)$ | 0.21 ± 0.083 | 0.14 ± 0.049 |
| $CVR_{CBV}\left(\frac{\%\Delta CBV}{mmHg}\right)$ | 0.041 ± 0.027 | 0.050 ± 0.011 |
| $CVR_{Radius}\left(\frac{\%\Delta Radius}{mmHg}\right)$ | -0.10 ± 0.046 | -0.13 ± 0.029 |
| $CVR_{SO2}\left(\frac{\%\Delta SO_2}{mmHg}\right)$ | 0.17 ± 0.075 | 0.12 ± 0.058 |

Table displays the mean ± standard deviation of the CVR measurements across all four participants.

## *6.5 | Discussion and Conclusions*

Here, we demonstrated the ability to generate CBV, R, and $SO_2$ maps on the order of seconds, opening the possibility to measure brain physiology with these parameters dynamically. We demonstrated this ability of the MRvF paradigm to detect changes in cerebrovascular function, observing MRvF-derived physiological changes temporally aligned with induced changes in $EtCO_2$ during delivery of hypercapnic gas.

Significant susceptibility distortions can be seen throughout the SAGE parameter maps in **Figures 5.8**, **5.10**, and **6.2** caused by the sensitivity of EPI readout to field inhomogeneity. The effect of these distortions was mitigated in this work by masking out those regions of the brain with a matching metric threshold. If the inner product was below the threshold, such as in areas outside the brain, regions without vascular structures like the ventricles, or areas with distortion artifacts, they were not included in analyses. Future studies will include scans with reversed phase-encode direction or field map acquisitions to allow for distortion correction of raw SAGE images prior to fingerprint matching.

The utilization of the SAGE sequence and administration of $CO_2$ resulted in temporally aligned $EtCO_2$ and BOLD changes and BOLD-CVR values similar to those previously reported.[60,171] The gray matter signal traces for the MRvF parameters (**Figure 6.3**) show the $SO_2$ values experiencing the largest fluctuations and most temporal similarity to the $EtCO_2$, while the R values experience fluctuations inversely correlated to $EtCO_2$. While CVR can be defined as the ability of vessels to dilate in response to $CO_2$, this dilation largely occurs in arteries, arterioles, veins, and venules that are larger in scale than the micro vessels being modeled here.[172,173] Still, it is curious that a decrease in radius was observed, albeit on the order of tenths of a micron, rather than no change or a slight increase, which warrants further investigation. Alternatively, since the dilation is primarily expected in the larger vessels, another approach could be to hold microvascular radii constant, and then observe how just CBV and $SO_2$ fluctuate in response to the stimulus. This could mitigate any undue influences that the confounding radius response may be having on the estimates of those two parameters.

Another limitation of the hypercapnia results is that the $SO_2$ changes, while statistically significant and in the expected direction, are small in amplitude. Most hypercapnic challenges that would increase $EtCO_2$ by 10 mmHg likely increase CBF by 25% or more, so the concomitant $SO_2$ change (assuming constant oxygen metabolism) may be expected to be

larger. Future studies will acquire separate baseline and hypercapnic perfusion scans to directly measure the increase in CBF each participant experiences during $CO_2$ inhalation.

One of the disadvantages of analytical MRvF matching is that only vasculature that is simulated can then be reconstructed, as those are the only configurations present in the dictionary for matching. For the study performed here, we only scanned healthy individuals and the ranges of our vascular parameters were appropriate for the changes we expected to see in the microvasculature from 5% $CO_2$ inhalation. However, these dictionaries did only contain very small micro vessels, and our acquired voxels are quite large and likely heterogenous, with some including larger vessels with CBV and R greater than our simulated range. For future studies with different anticipated cerebrovascular response or pathology, it will be important to generate a dictionary with ranges to accommodate that. Significant advancements have also been made in the biophysical modeling component used for MRvF[105,108,174], and realistic vascular models derived from high-resolution optical imaging may more accurately represent the complexity of brain tissue. Additionally, the use of a continuous reconstruction algorithm, like a machine learning implementation,[175–177] could allow us to perform more accurate parameter estimation (particularly with so few time points for matching) without the discrete restrictions of the simulated dictionary. Additionally, a machine learning approach would significantly reduce the reconstruction time required for dynamic parameter mapping and allow for the inclusion of additional varied MRvF parameters, like $T_2$ or ADC, that could provide more physiological relevant measures that contribute to signal progression but are currently not possible due to prohibitively big dictionaries with analytical matching.

To improve sensitivity of parameter time courses, we regionally averaged parameters prior to $EtCO_2$ regression. This was done to maximize the observable effect of $CO_2$ on our MRvF parameters due to their higher noise and heterogeneity compared to the BOLD signal; however, it precluded the ability to produce voxelwise CVR maps that could identify regional changes in vascular function. Lastly, as **Table 6.1** shows, the highest CVR is observed in the

gray matter of the brain, which is consistent with literature, and as such, has been a primary region utilized for previous CVR studies. Relatedly, our gray matter regions produced more robust and more physiologically reasonable MRvF values compared to white matter regions, likely due to higher blood volume, and therefore better sensitivity in gray matter. In addition to reduced signal in white matter, the biophysical model we used in this study does not capture microstructure orientation and other susceptibility effects, like myelin, which causes qBOLD analytical models to be challenging in white matter.

To summarize, in this chapter we applied dynamic MR vascular fingerprinting to a hypercapnic imaging design. These results demonstrated parameter consistency over time and regional changes in BOLD and quantitative vascular fingerprinting estimates of CBV, R, and $SO_2$ in response to an induced hypercapnic stimulus. This validated MRvF framework and breathing paradigm enabled exploratory studies to investigate both the magnitude and rate of reactivity during aging as discussed in the next chapter and could be applied to study cerebrovascular disease progression.

# Chapter 7 – Magnetic Resonance Vascular Fingerprinting Measures of Cerebrovascular Reactivity with Aging

## *7.1 | Introduction and Background*

The cerebral vascular system undergoes normal changes with aging that affect brain health and function. One such change involves cerebral vascular reactivity (CVR), which is a critical parameter that reflects the capacity of cerebral blood vessels to dilate or constrict in response to stimuli and serves as an indicator of vascular health and the brain's ability to regulate blood flow according to metabolic demand. With normal aging there is altered neuronal activity, decreased cerebral metabolism, and increased arterial stiffness that can all contribute to gradual decline in ability to regulate blood flow and respond to stimuli.[42,178,179] Significant decreases in CVR with aging are associated with impaired neurovascular coupling[180,181], increased risks of cerebrovascular diseases[45,49,182], and cognitive decline[44,168], highlighting the need for precise, non-invasive methods to assess these changes.

Blood oxygen level dependent (BOLD) imaging and arterial spin labeling (ASL) have been the primary MRI techniques used to measure CVR, but they each face their own limitations. BOLD imaging uses the inherent magnetic differences between Hb and dHb to detect the increase in oxygenated blood to the brain while ASL magnetically labels blood inferior to the brain and is able to capture increases in blood flow as the increased volume of labelled blood travels to the brain. While BOLD has high spatial and temporal resolution for capturing the intricate dynamics of the vascular response, BOLD signal itself is qualitative in nature and therefore has limitations related to its interpretability and reliability. ASL, on the other hand, produces quantitative maps of cerebral blood flow, but is limited due to its poorer spatial resolution and long scans times limiting its ability to observe rapid dynamic processes.

Dynamic magnetic resonance vascular fingerprinting (MRvF) offers another potential way to obtain CVR measures from MRI during vasoactive stimulus administration. Dynamic MRvF has

the advantage of using fast sequences like BOLD imaging, but results in quantitative parameters like ASL. Additionally, since it generates multiple quantitative parameter maps simultaneously, each of these maps can be independently measured over time for multiple metrics of vascular changes in response to the same vasoactive stimulus. Finally, as demonstrated in *Chapter 6*, the accelerated spin- and gradient echo (SAGE) sequence that has been optimized for dynamic MRvF inherently captures a BOLD contrast image and therefore can provide co-localized supplemental quantitative parameters of cerebral blood volume (CBV), microvascular vessel radius (R), and tissue oxygen saturation ($SO_2$) to this widely studied BOLD response.

In this chapter we compare the CVR measurements obtained from BOLD, ASL, and each of the three MRvF parameters (CBV, R, and $SO_2$) to one another and to previously reported studies. We also explore the application of MRvF for measuring differences in CVR in healthy young and healthy old cohorts and discuss how these results can inform future dynamic MRvF study design.

### *7.2 | Hypercapnic MRI Acquisition and Analysis with Young and Old Cohorts*

We recruited 11 healthy older subjects (69.2±5.1 years old, 5 female) and 11 healthy younger subjects (24.3±2.9 years old, 6 female) to undergo imaging for this study. All MRI images were acquired on a 3T scanner (Siemens Skyra). Subjects with a history of cerebrovascular disease or breathing disorders were excluded from this study and all recruited subjects were asked to not consume anything with caffeine for 6 hours prior to the imaging session. Scans acquired included an MPRAGE for a $T_1$-weighted anatomical reference and the optimized SAGE acquisition determined in *Chapter 6* during four 1-minute blocks of hypercapnic stimulus. SAGE images were acquired with 5 TEs (29, 59, 98, 128, and 158 ms), a 4.5 second repetition time (TR), a 2×2×5 mm voxel size, a 220×220 mm in-plane FOV, 24 slices, and GRAPPA in-plane acceleration of 3. The sequence was repeated 125 times consecutively during a block hypercapnic gas inhalation paradigm for an acquisition time of about 9 minutes (**Figure 7.1**). The

first TE of the SAGE sequence was also extracted as the BOLD image (**Figure 7.2A**) and repeated for every TR (**Figure 7.2B**).

We also acquired a pulsed ASL (pASL) acquisition while the subject breathed normal air for 4 minutes and a pASL acquisition during a 4-minute step of hypercapnic stimulus inhalation (**Figure 7.1**). The ASL scans were acquired at baseline and during hypercapnia to calculate cerebral blood flow (CBF) change for comparison to the changes in the MRvF parameters. The pASL images were collected with settings in line with the ASL white paper[183] recommendations for pASL: 800 ms bolus duration, 1800 ms inversion time, 35 label/control pairs, 15 ms TE, 3.5 second TR, 3.5 mm isotropic voxel size, 224×224 mm in-plane FOV, and 35 slices. The acquisition time for each pASL scan was just over 4 minutes (**Figure 7.1**).

Throughout imaging, participants were connected to the gas breathing apparatus described previously (**Figure 6.1**[169]). The breathing apparatus allowed for controlled breathing of normal room air or of gas from the connected Douglas bag (5% $CO_2$, 21% $O_2$, 74% $N_2$). End-tidal $CO_2$ ($EtCO_2$) measurements from the participants were recorded throughout all scans via tubing that ran from the breathing apparatus out of the MRI room to a capnograph (Nonin, RespSense II) in the scanner operating room. The participants wore a nose plug throughout the duration of the imaging to force breathing exclusively through the scuba-like mouthpiece of the apparatus and to ensure appropriate gas inhalation and accurate, continuous $EtCO_2$ recordings. Respiratory rate, heart rate, and pulse oxygen saturation were also monitored throughout the scan to ensure participant safety and compliance.

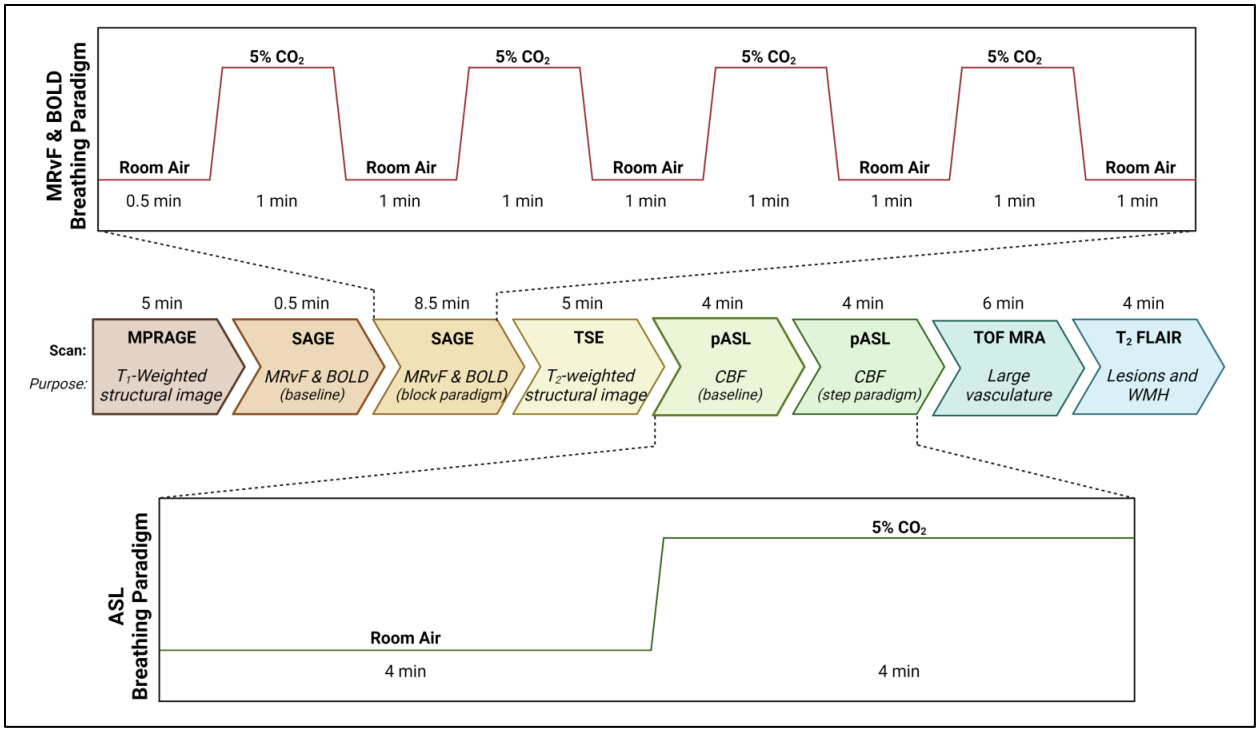


**Figure 7.1. Breathing Paradigms and Imaging Protocol Schematic**. Scans acquired for this study included a magnetization prepared rapid gradient echo (MPRAGE) for a $T_1$-weighted anatomical reference, spin- and gradient-echo (SAGE) scans for magnetic resonance vascular fingerprinting (MRvF) and blood oxygen level dependent (BOLD) measures, a turbo spin echo (TSE) for $T_2$-weighted anatomical information, pulsed arterial spin labeling (pASL) scans for cerebral blood flow (CBF) measures, a time-of-flight magnetic resonance angiography (TOF MRA) for examination of large vasculature, and a $T_2$ fluid-attenuated inversion recovery ($T_2$-FLAIR) for possible identification of lesions and white matter hyperintensities (WMH). Participants were delivered 5% $CO_2$ gas via four one-minute blocks during the SAGE acquisition, and 5% $CO_2$ gas via a four-minute step paradigm during the second pASL acquisition.

In preparation for MRvF analysis, biophysical signal simulations were performed using the SAGE sequence implemented into the MRVox toolkit in MATLAB.[111] Simulated SAGE time courses were generated for all combinations of CBV (0-24%), R (2-50 μm), and $SO_2$ (0-100%) with evenly spaced parameter sampling (**Table A7.1**), resulting in a simulated dictionary with 61,500 entries. An iterative, magnitude-based matching algorithm (**Figure 5.2C**) was performed to find the simulated signal that resulted in the highest inner product with each voxel's signal evolution. This was repeated for every TR to generate CBV, R, and $SO_2$ maps at every time point (**Figure 7.2B**).

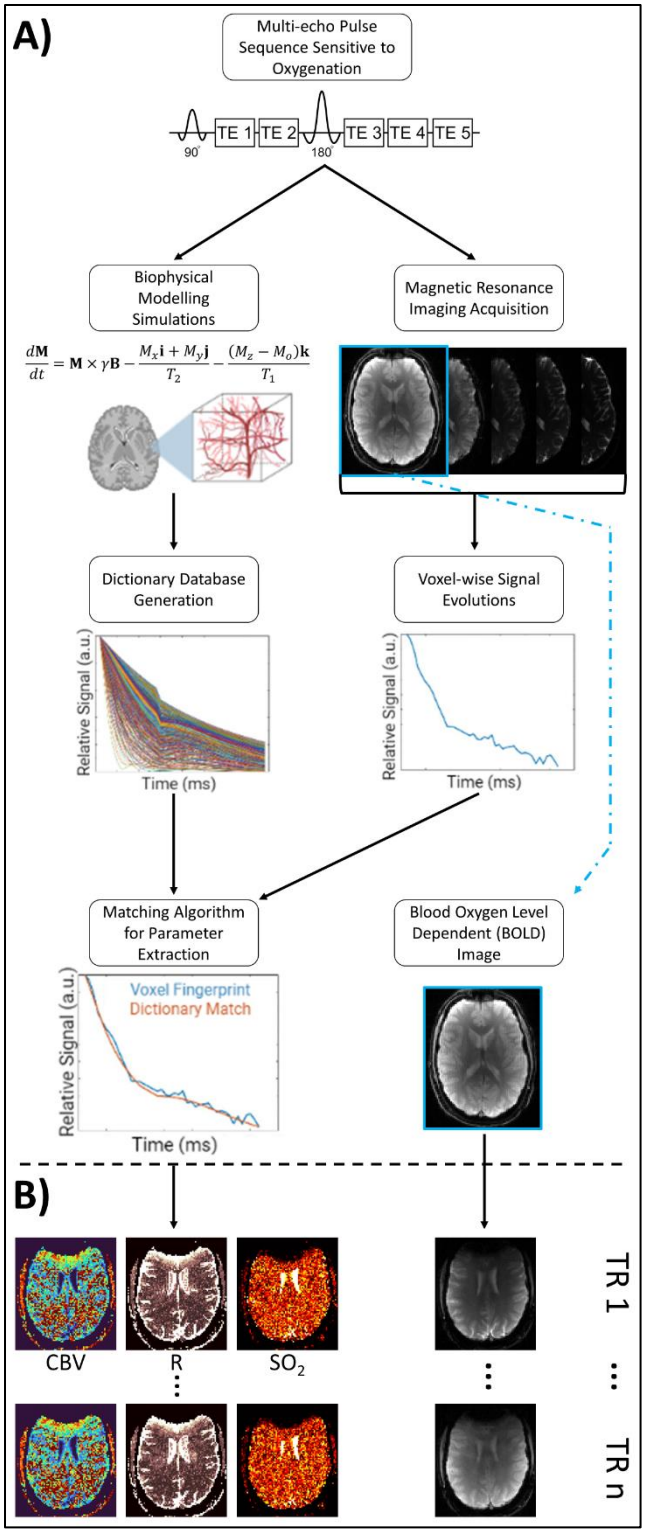


**Figure 7.2. Diagram of Simultaneous BOLD and MRvF Acquisition**. **A)** A specialized MRI pulse sequence is used in parallel for biophysical simulations and image acquisitions. The acquired signals are matched to a database of simulated ones, allowing for the underlying parameters of the best simulated fit to be extracted. The first echo time (TE) image is also separately isolated as the blood oxygen level dependent (BOLD) image. **B)** These underlying parameters can be produced for the whole brain to generate cerebral blood volume (CBV), microvascular vessel radius (R), and tissue oxygen saturation ($SO_2$) maps. This process is repeated for every repetition time (TR) to monitor how the MRvF parameters and BOLD values fluctuate over time.

We performed linear registration using FLIRT in FSL[137,138], to align the spin echo of the SAGE sequence to the $T_1$-weighted image for each subject and then non-linearly registered each $T_1$-weighted image to an atlas in MNI space using FNIRT in FSL.[139] The BOLD, CBV, R, and $SO_2$ maps for each subject were warped to MNI space using these subject-specific transformations. White matter (WM) and cortical gray matter (GM) regions of interest (ROIs) were segmented using the Harvard-Oxford Subcortical Atlas in the same standard space. BOLD, CBV, R, and $SO_2$ values were spatially averaged in each of the GM and WM ROIs at every TR to produce mean time courses per parameter for each participant.

The partial pressure of $CO_2$ in the subject's exhaled breath that we recorded with the capnograph was processed by extracting the peaks of each breathing cycle as the $EtCO_2$ measurements and performing 5-point moving average smoothing. We manually aligned each participant's $EtCO_2$ time course to their whole-brain BOLD time course and applied this temporal alignment to the MRvF parameter time courses. CVR was calculated for each of BOLD, CBV, R, and $SO_2$ for every subject and ROI using **Eq. 6.1** and **6.2**. We also performed voxelwise CVR mapping by using these same two equations and temporal alignments but using the signal progression for each voxel independently rather than the ROI averages.

We generated CBF maps for the normal air and hypercapnic ASL scans independently using BASIL[184] with the recommended settings from the ASL white paper.[183] We calculated the percent change CBF per voxel by subtracting the resting CBF from the hypercapnic CBF and dividing that difference by the resting CBF. The $EtCO_2$ throughout the resting and hypercapnic ASL scans were extracted and averaged across each ~4-minute scan for separate $EtCO_2$ values for each of the two scans. We then found the difference between these two $EtCO_2$ values and used them in combination with the previously calculated percent change in CBF in **Eq. 7.1** to calculate the CBF-derived CVR.

**Equation 7.1**: $$CVR_{CBF} = \frac{\%\Delta\mathrm{CBF}}{\Delta EtCO_2}$$

We again performed linear registration using FLIRT in FSL[137,138], to align the $M_0$ of the hypercapnic pASL acquisition to the $M_0$ of the resting pASL acquisition. Then the $M_0$ of the resting acquisitions were registered to the $T_1$-weighted image for each subject. The resting CBF, hypercapnic CBF, percent change in CBF, and $CVR_{CBF}$ maps for each subject were warped to MNI space using these subject-specific transformations and the previously computed $T_1$-to-MNI nonlinear transformations. The same GM and WM ROIs in MNI space were used to spatially average the CBF metrics. Finally, we averaged resting CBF, hypercapnic CBF, percent change in CBF, and $CVR_{CBF}$ values to create group average maps.

*7.3 | BOLD, MRvF, and ASL Responses to Hypercapnia*

All 22 participants were able to complete the imaging without interruption or complication. There were no complaints of discomfort due to inhaling the hypercapnic gas mixture, however, a few participants commented on the scuba-like mouthpiece being moderately uncomfortable. One participant in the older group did not experience significant changes in $EtCO_2$ (less than 3 mmHg increase) during periods of hypercapnic stimulus so their data was excluded from analyses and group comparisons. The BOLD, CBV, R, and $SO_2$ time courses were first detrended and smoothed via 5-point moving average. Z-scores were calculated at each time point of every subject's time courses to normalize signal progression relative to their mean of each parameter. These Z-score time courses were then averaged across the two age groups to produce the parameter evolutions in **Figure 7.3**.

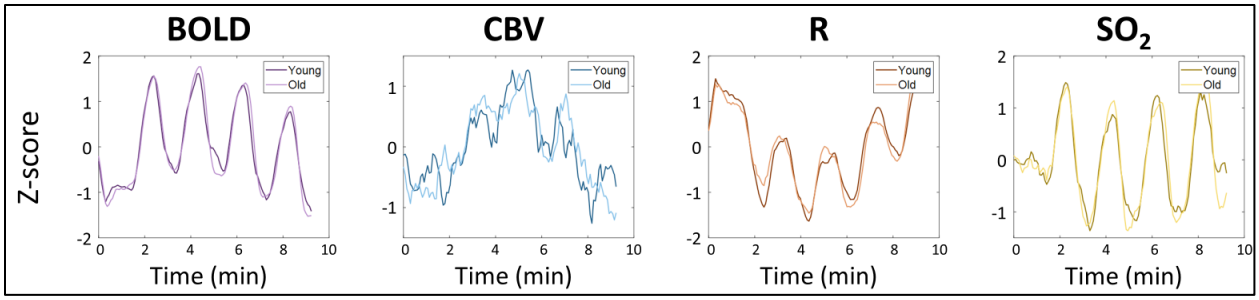


**Figure 7.3. Average Gray Matter Time Courses of BOLD, CBV, R, and $SO_2$ for Young and Old Cohorts**. The gray matter parameter Z-scores averaged across all participants after detrending and temporal smoothing for the young (darker lines) and old (lighter lines) cohorts. Fluctuations of blood oxygen level dependent (BOLD) signal, cerebral blood volume (CBV), microvascular vessel radius (R), and tissue oxygen saturation ($SO_2$) acquired during hypercapnic stimulus blocks are shown.

The GM BOLD and $SO_2$ and time courses (**Figure 7.3**) positively fluctuate in a temporally aligned way with the $EtCO_2$ time courses (**Figure A7.1**), whereas the R time courses negatively fluctuate at the same times. Visually, there is little perceivable difference between BOLD, CBV, R, or $SO_2$ when comparing the young and old group time courses for these GM signal averages. This continues to hold true for all parameter time courses when looking at the WM (**Figure A7.2**) and whole-brain averages (**Figure A7.3**).

Group average perfusion maps computed from the ASL scans with normal air and hypercapnic gas are shown in **Figure A7.5**. The percent change in CBF from rest to hypercapnia generally shows an increase in CBF in the GM, whereas the WM appears more inhomogeneous.

## *7.4 | Cerebrovascular Reactivity from BOLD, MRvF, and ASL*

ROI CVR values for BOLD, CBV, R, and $SO_2$ for every subject show similar $CVR_{BOLD}$, $CVR_{CBV}$, $CVR_R$, and $CVR_{SO2}$ between the young and old groups across the GM, WM, and whole brain (**Figure 7.4**). Notably, $CVR_{BOLD}$ and $CVR_{SO2}$ averages were slightly higher and $CVR_R$ averages were slightly lower for the young group in GM (**Table 7.1**), but none of these differences were determined to be significant upon statistical analysis with Welch's t-test. The WM had reduced $CVR_{BOLD}$, $CVR_{SO2}$, and $CVR_R$ compared to the GM, but neither the WM (**Table A7.2**) nor whole-brain (**Table A7.3**) ROIs showed significant differences between the young and old groups for any of the BOLD or MRvF metrics.

CVR maps for each subject were also produced via voxelwise CVR regressions and averaged across the two groups for each of BOLD, CBV, R, and $SO_2$ (**Figure A7.4**). The $CVR_{BOLD}$ maps are visually anatomically similar and have values within the range of previous literature.[60,171] CVR maps for the three MRvF parameters are visually much noisier with notably more negative values, particularly for $CVR_R$, which is consistent with ROI CVR calculations.

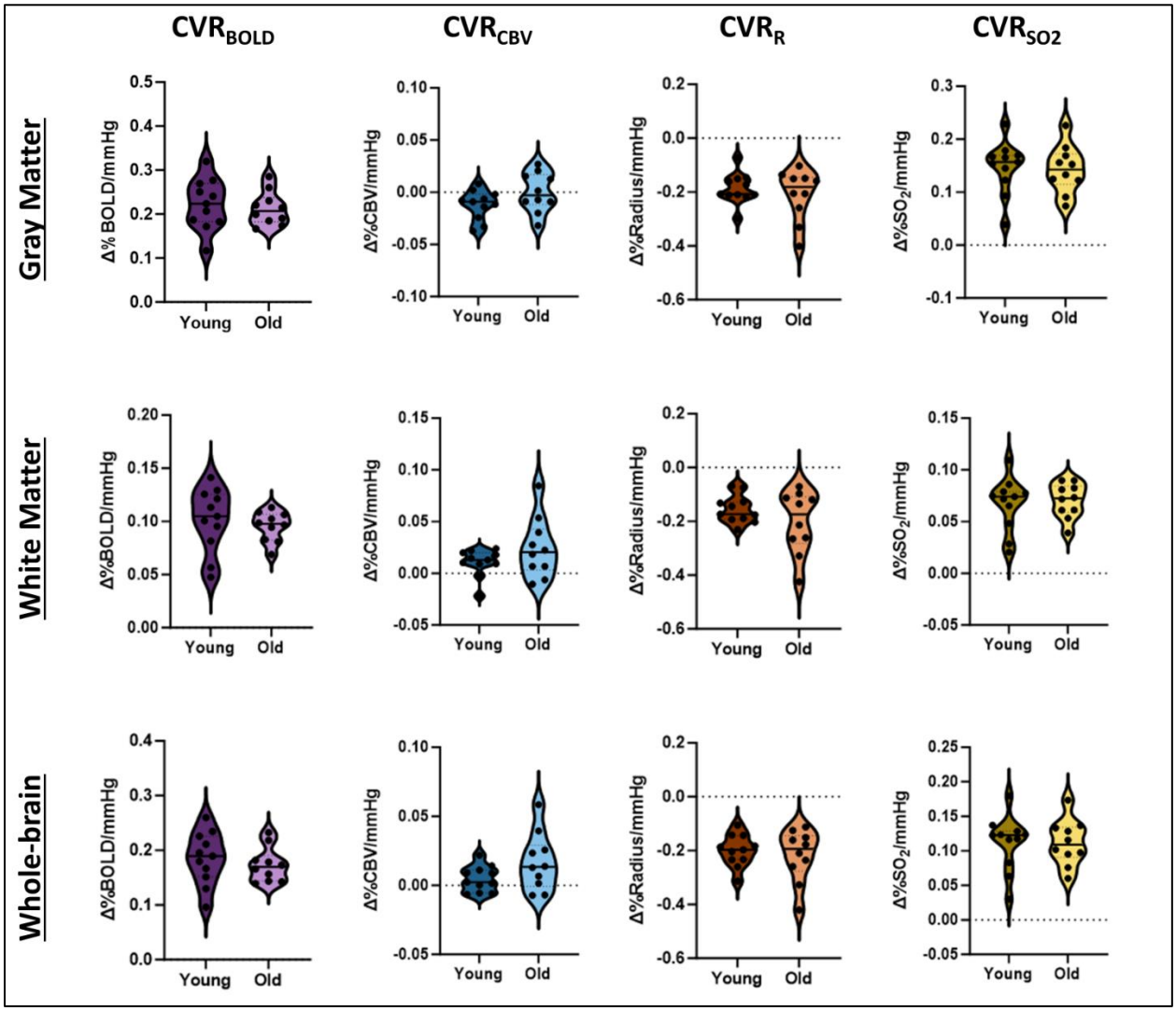


**Figure 7.4. Comparing Regional CVR Values Across Young and Old Cohorts**. Violin plots showing the CVR values of all participants for the young and old groups. Parameters derived from MRvF were averaged in gray matter, white matter, and whole-brain ROIs for each subject and individually regressed against that subject's end-tidal $CO_2$ to compute each parameter-specific CVR.

CBF maps for each subject were averaged across the two age groups for the resting ASL scan and the ASL scan during 5% $CO_2$ inhalation (**Figure A7.5**, top). The percent change in CBF was calculated for each individual and then combined for group average maps (**Figure A7.5**,

middle). This CBF fluctuation was normalized to each subject's change in average $EtCO_2$ (mmHg) from the normal air to the hypercapnic breathing for $CVR_{CBF}$, and then averaged for the group (**Figure A7.5**, bottom).

The group level average GM, WM, and whole-brain CVR values for each parameter are shown in **Table 7.1**, **Table A7.2**, and **Table A7.3**, respectively. The GM $CVR_{CBF}$ is about an order of magnitude greater than $CVR_{BOLD}$ and is in the range between 1.5-6%Δ/mmHg matching previous literature in which similar changes in $EtCO_2$ were achieved.[43,167]

**Table 7.1. Gray Matter CVR Measures from BOLD, MRvF, and CBF Parameters During Hypercapnic Stimuli**

| | Young | Old |
|---|---|---|
| $CVR_{BOLD}\left(\frac{\%\Delta BOLD}{mmHg}\right)$ | 0.22 ± 0.057 | 0.21 ± 0.038 |
| $CVR_{CBV}\left(\frac{\%\Delta CBV}{mmHg}\right)$ | -0.012 ± 0.014 | 1.5e-5 ± 0.018 |
| $CVR_{R}\left(\frac{\%\Delta Radius}{mmHg}\right)$ | -0.19 ± 0.057 | -0.21 ± 0.095 |
| $CVR_{SO2}\left(\frac{\%\Delta SO_2}{mmHg}\right)$ | 0.15 ± 0.049 | 0.14 ± 0.044 |
| $CVR_{CBF}\left(\frac{\%\Delta CBF}{mmHg}\right)$ | 2.8 ± 9.9 | 2.7 ± 9.3 |

Table displays the mean ± standard deviation of the CVR measurements across all participants in each group

*7.5 | Discussion and Conclusions*

In this study we demonstrated our novel imaging and MRvF protocol to measure BOLD, CBV, R, and $SO_2$ as well as their associated CVR derivatives in two groups that significantly varied in age. All 22 scans were completed from start to finish with no adverse responses to the administration of the hypercapnic gas and with 21 of the subjects experiencing significant and expected changes in $EtCO_2$. BOLD and CBF changes that resulted from hypercapnia were

consistent with literature, validating protocol design and allowing for reassurance that physiology was being appropriately modulated when assessing the new MRvF parameter responses.

There were no significant differences in $CVR_{BOLD}$, $CVR_{CBV}$, $CVR_R$, and $CVR_{SO2}$ between young and old groups. While there have been many studies that have found significantly reduced $CVR_{BOLD}$ in groups with specific cerebrovascular diseases like AD[46,47], Moyamoya disease[62,185], and cerebral steno-occlusive disease[186], studies looking at healthy aging have gleaned more mixed results. Some studies[23,42,178] have found a decrease in $CVR_{BOLD}$ with healthy aging while others[167,179] have found no significant differences. Some of these differences in significance can likely be contributed to common factors like sample size, but one significant limitation within CVR literature is the wide variability in practices for acquisition, processing, and analysis.[39] CVR can not only be acquired using different types of sequences like BOLD, ASL, PC, and DSC (**Figure 2.4A**), but regardless of sequence, CVR can be induced with a wide variety of strategies like $CO_2$ inhalation, breath modulation, and acetazolamide (**Figure 2.4B**). Even if only $CO_2$ is considered for the stimulus, it can be administered at various fixed percentages with normal oxygen and nitrogen, at various fixed percentages with only oxygen added (carbogen), or it can be administered with more sophisticated breathing equipment to reach a specific $EtCO_2$ target. Some recent publications have started to raise these concerns with the aim of creating some standards for acquisition and CVR induction, as well as best practices for pre-processing and analyzing CVR data for improved comparisons across research studies.[187–190]

Targeted $EtCO_2$ via computer-controlled $CO_2$ gas delivery is a compelling option for future MRvF hypercapnia studies due its ability to ensure every participant experiences the same change in $EtCO_2$, and therefore more similar changes in physiological modulation, as $EtCO_2$ acts as a proxy for arterial partial pressure of $CO_2$. For the subjects analyzed in this study, the older participants had a $\Delta EtCO_2$ range of +5.7-14.7 mmHg from rest to hypercapnia and the young participants had a $\Delta EtCO_2$ range of +4.9-12.2 mmHg from rest to hypercapnia. This is significant because CBF and BOLD signal, and therefore CVR, have been found to have nonlinear

relationships to change in $EtCO_2$.[171,191] Targeted $EtCO_2$ would eliminate this variation of $EtCO_2$ response seen in hypercapnia studies like ours that use fixed percent $CO_2$ delivery. What remains an obstacle even with the use of a targeted $EtCO_2$ gas delivery system is that there is variability in baseline $EtCO_2$ within the population. The same $\Delta EtCO_2$ will lead to greater CVR measures in individuals with lower baseline $EtCO_2$ if using targeted $EtCO_2$ gas delivery. Conversely, with individuals that start at the same baseline, greater $\Delta EtCO_2$ will actually typically lead to lesser CVR values with fixed gas delivery protocols due to this nonlinear response and the normalization by $\Delta EtCO_2$ used to calculate CVR (**Eq. 7.1**).[171] These same studies have also suggested that CVR can vary within the same subject from one imaging session to the next, further increasing the difficulty of observing significant results comparing healthy individuals.[171] While some of these factors may be able to be mitigated with targeted $EtCO_2$ gas delivery, averaging across repeated imaging sessions, or an increase in the number of subjects for a study, they are important considerations for the interpretability of CVR studies.

When looking at the ASL-derived CBF results from this study, we achieved CBF and $CVR_{CBF}$ values consistent with literature,[43,43,167] but the corresponding maps present evidence for future improvements. In particular, the percent change in CBF and $CVR_{CBF}$ maps show significant variability in the WM with unphysiologically high and negative values (**Figure A7.5**). Similarly to a limitation of MRvF discussed earlier, ASL has less signal from CBF in the WM due to decreased vascular density and therefore reduced SNR[192] leading to the noisy maps and unrealistic values in **Figure A7.5**. For this reason, spatial smoothing is often implemented as a pre-processing step for CBF mapping and could be performed in future analysis with this data. Additionally, with the large voxels used for ASL there is concern about partial volume effects confounding CBF quantification. Future work will employ partial volume correction and compare the difference in results between corrected and uncorrected maps.

Since this is the first study to introduce generating CVR maps from MRvF-derived values of CBV, R, and $SO_2$, spatial smoothing is also a step we could consider in our MRvF processing

pipeline to improve the quality and reliability of MRvF parameter maps. Performing smoothing on the SAGE images prior to pattern matching would allow for denoising and averaging of spatial information but could bias how the biophysical simulations match to signals assumed to be unmodified. Smoothing after MRvF matching is another possible option but would lose out on the benefits of averaging signal from neighboring voxels with similar structural and functional tissue for the matching process.

When considering the MRvF responses to hypercapnia (**Table 7.1**), there are very minimal changes detected in CBV, despite BOLD and CBF showing increases in blood flow. With an increase in blood flow from hypercapnia, we would expect both $SO_2$ and CBV to increase, however, a decreased deoxyhemoglobin fraction with increased CBF could contribute to decreased sensitivity in the ability of MRvF to disentangle $SO_2$ and CBV. Additionally, previous PET studies[193] have shown that the increase in CBF in response to hypercapnia is greater than the increase in CBV (indicating an increase in blood velocity), and therefore better sensitivity may be required to accurately measure the more subtle changes in CBV.

Finally, the ability to produce CBV, R, and $SO_2$ maps in a dynamic fashion may provide insights into the temporal dynamics of cerebrovascular function and how those change with age and disease. In addition to possible differences in the magnitude of CVR response between these groups, there may also be differences in the rate of response. A few recent studies[194–196] have started to consider this temporal aspect of CVR. They take similar approaches where they essentially measue the slope of the CVR signal evolution and the rate at which it increases after the introduction of a hypercapnic stimulus. Furthermore, this rate of change of CVR has shown to be significantly different between subjects with Alzheimer's disease (AD) compared to healthy controls, indicating its potential value for diagnosis, differentiation, or understanding of disease.[197] These previous rate of CVR studies used BOLD MRI with TRs between 1 and 2.5 seconds[194–196], whereas with the SAGE we had a temporal resolution of 4.5 seconds. However, Richardi et al.[168] found that on average it took healthy individuals 33 seconds and a group of mild cognitively

impaired and AD patients 59 seconds to reach 90% of peak CVR response. This would allow for 7 to 8 SAGE volumes to be collected during the average healthy participant, which should be enough for measuring rate of response despite decreased temporal resolution. Additionally, the SAGE sequence could be accelerated through the use of simultaneous multi-slice (SMS) techniques to reduce its TR to as low as 1.5 seconds without changing other imaging parameters as has been shown previously.[120] Ultimately, incorporating this additional temporal metric in future studies and analysis may provide insight into how our three MRvF parameters dynamically differ from each another and how they differ between healthy individuals and those with vascular dysfunction.

In conclusion, in this chapter we applied our novel approach of dynamic MRvF with a hypercapnic imaging design to examine the responses of young and old healthy volunteers. Both groups experienced changes in BOLD, CBV, R, $SO_2$, and CBF in response to the introduced hypercapnic stimuli. Although the groups' responses themselves were not significantly different from each other, both $CVR_{BOLD}$ and $CVR_{CBF}$ were consistent with previous literature using similar hypercapnic breathing paradigms. Further analysis will examine whether the rate of reactivity for the young and old groups are significantly different for BOLD or any of the MRvF parameters.

# Chapter 8 – Discussion, Perspectives, Future Work, and Conclusions

## *8.1 | Discussion*

Our overarching goal was to design imaging technologies, tools, and techniques to improve understanding, diagnosis, and treatment of cerebrovascular diseases. Throughout this dissertation we discussed the development and application of new magnetic resonance vascular fingerprinting (MRvF) techniques. Through our studies we were able to use MRvF to measure cerebral blood volume (CBV), microvascular vessel radius (R), and tissue oxygen saturation ($SO_2$), investigate how these changed in response to different inhaled gas challenges, and compare the response of these metrics in a study of healthy aging. This final chapter aims to synthesize the insights gained from our studies, discuss the broader implications of our findings, and lay out possible directions of future research and development in the field.

### *Summary of Main Findings*

In the first study laid out in *Chapter 4*, we performed retrospective MRvF analysis of GESFIDE images collected during hypoxia, normoxia, and hyperoxia and compared those results to results obtained using a quantitative blood oxygen level dependent (qBOLD) method. We found that MRvF-derived measures of oxygen extraction fraction (OEF) significantly correlated with OEF measures from analytical qBOLD analysis. Furthermore, average OEF measured with MRvF during hyperoxia and normoxia were significantly lower than OEF during hypoxia. The ability to detect this expected change in OEF with MRvF helped build confidence in the sensitivity of the MRvF parameters to detect cerebrovascular changes across different physiological conditions.

In *Chapter 5*, we described the simulation, retrospective, and prospective experiments we conducted to investigate and optimize the accuracy, sensitivity, and temporal resolution of MRvF. An iterative, pattern-matching algorithm was developed to improve reconstruction in the absence of contrast agents. Subsampling of a 40-echo GESFIDE sequence in silico and in vivo

demonstrated the feasibility of MRvF with only 5 echoes. It also showed that SNR effected matching accuracy and sensitivity more significantly than echo train length. Finally, we optimized and collected preliminary images with a 5-echo SAGE sequence and found that a single repetition had adequate SNR for MRvF reconstruction with a 4.5 second temporal resolution.

We followed this up in *Chapter 6* with an initial application of this optimized SAGE sequence in four young, healthy volunteers. Given the rapid acquisition, we introduced a hypercapnic breathing paradigm during imaging for assessment of how CBV, R, and $SO_2$ fluctuated relative to induced fluctuations in $EtCO_2$. Through this pilot study, we observed expected regional brain changes in BOLD and fluctuations in each of the three MRvF parameters that significantly correlated with changes in $EtCO_2$.

Our last study outlined in *Chapter 7* built off the hypercapnic pilot study, this time recruiting 11 young and 11 old healthy participants for hypercapnic MRvF imaging. It also included the inclusion of an ASL scan for CBF measures of CVR for an additional comparator. The average BOLD, CBV, R, and $SO_2$ time-courses from both the young and old groups correlated significantly with changes in hypercapnia. The CVRs calculated using BOLD, the MRvF parameters, and CBF were not significantly different between the two groups, but gray matter CVR values for BOLD and CBF were in line with literature and the CVR values calculated using the MRvF parameters were comparable to those from the pilot study.

*Contributions to the Field*

This dissertation represents six primary contributions to the fields of MR vascular fingerprinting and dynamic, quantitative measurements of cerebrovascular vascular reactivity:

1) We developed an iterative pattern matching algorithm for improved MRvF reconstruction without exogenous contrast agents.
2) We validated the ability of MRvF to detect changes in cerebral oxygenation during hypoxia.

3) We demonstrated the limited effect of echo train length on MRvF sensitivity when using fully sampled images.
4) We optimized a rapid, 5-echo, spin- and gradient echo pulse sequence for MRvF mapping on the order of seconds.
5) We introduced an imaging protocol with a hypercapnic breathing paradigm that enabled co-localized, simultaneously acquired reactivity maps of BOLD, CBV, R, and $SO_2$ and demonstrated that each parameter's fluctuations in response to a 5% $CO_2$ hypercapnic correlated with $EtCO_2$ fluctuations.
6) We showed how CBV, R, and $SO_2$ changes varied relative to changes in BOLD and CBF from hypercapnic gas inhalation and compared those changes between a young and old group of healthy subjects.

This work sets up framework that will provide insights into how different cerebrovascular parameters react to vasoactive stimuli. Ideally, these techniques and ideas will continue to be improved and inspire us and others to carry on the work of developing imaging biomarkers to better understand cerebrovascular function and dysfunction.

## *8.2 | Perspectives and Future Directions*

In this section we will briefly give some thoughts on the directions and application of MRvF in cerebrovascular research. The aim is to offer a candid and thoughtful examination of what will allow for the most significant improvements of MRvF, how it could have the greatest impacts, and what it would take for adoption more widely in research and clinical settings.

### *Biophysical Modeling for MRvF*

While the flexibility of MRF to look at any parameter that can be modeled is a key benefit, a key related limitation of MRF is that it can only reconstruct elements that are computationally modeled. Therefore, if the biophysical model does not include characteristics present in the real

tissue, then it will not be able to accurately detect those characteristics. For MRvF, this means that advancing the virtual vascular tissue model to be more realistic, tunable, and representative of possible abnormal microvasculature could allow for more accurate parameter mapping.

Many studies have already expanded computational microvascular tissue models, including a few MRvF ones[115,122], pushing biophysical simulations to three dimensions and using images of vasculature from high-resolution microscopy to inform vessel network design. An example of one of these recent studies is shown in **Figure 8.1**, in which the entirety of a mouse brain was imaged via microscopy slides prior to the vascular network of the brain being re-combined digitally. This new, full model of the mouse brain was then re-divided into voxel-sized sections prior to implementation into the MRVox biophysical modeling software. While it would be on a much larger scale, developing a similar model for the human brain would mitigate limitations of current MRvF implementations that do 2D simulations on homogenous tissue with constant vessel radius, often lack larger vascular structures representative of arteries and veins, and do not account for different vessel orientations that are in certain regions of the brain, like near white matter fiber tracts.

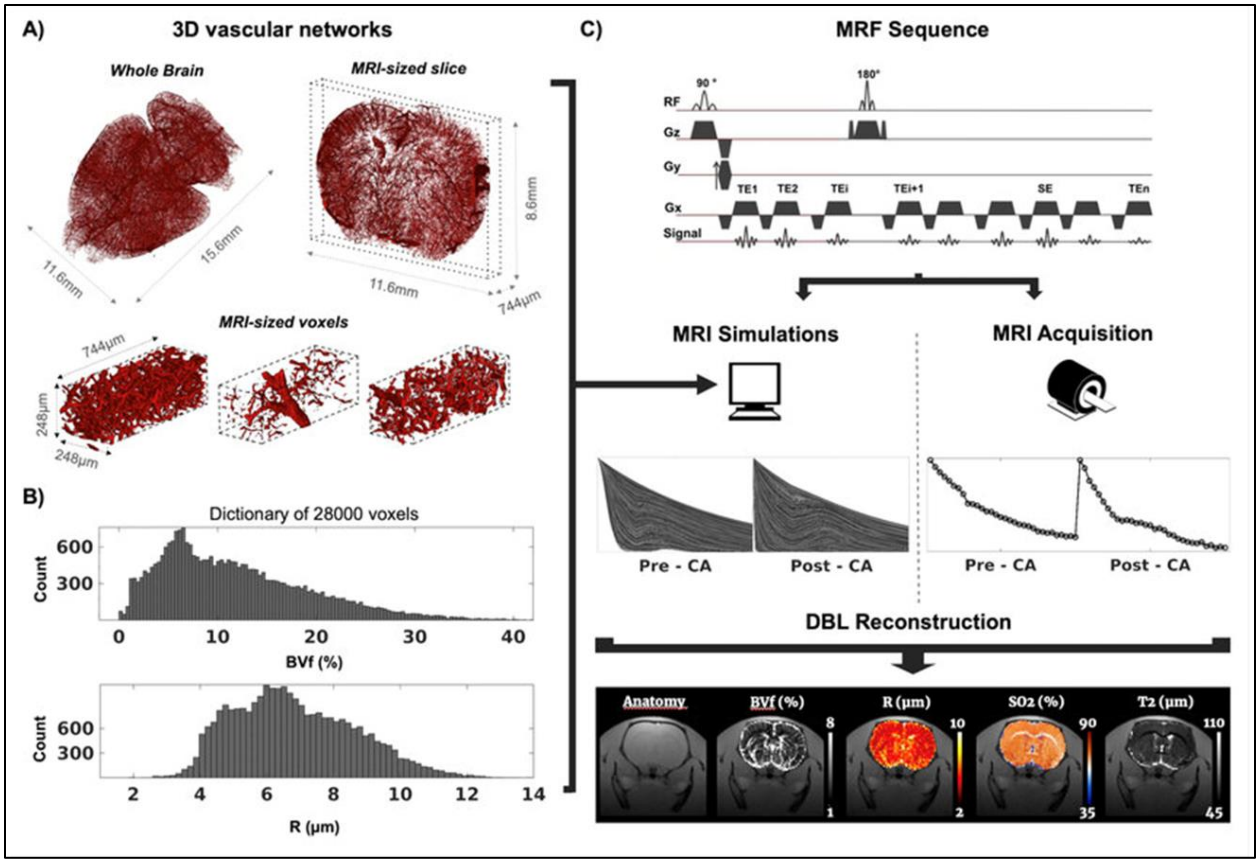


**Figure 8.1. Microscopy-derived Vasculature Models for MRvF Biophysical Simulations** (from Delphin et al.[122]). **A)** The MRvF framework has been adapted to utilize vascular architecture from high-resolution microscopy images for more representative virtual voxel design. **B)** In these realistic voxels, the cerebral blood volume and radius are distributed around typically occurring values within a physiological range and can be averaged throughout the volume for extraction and parameter map reconstruction. **C)** Once set up, these physiological virtual voxels can be used in simulations, with the same sequence used in imaging, for simultaneous multiparametric reconstruction of the vascular parameters of interest.

These realistic biophysical models could be extended even further with intentional inclusion of pathological tissues. Cerebrovascular diseases with structural microvascular abnormalities, like small vessel disease and microvascular ischemic disease, could be directly included into the biophysical model and have dictionary entries that would specifically represent the anatomy and physiology seen in those diseases.

*Machine Learning in MRF*

An increasingly prevalent technique that can help improve both accuracy and computational speed for MRF is machine learning (ML).[198] MRF matching is readily adaptable for ML, as the simulations with known parameters can be directly implemented into ML frameworks

as training data. Numerous MRF studies have begun utilizing ML for both dictionary generation and signal matching.[159,175–177,198–201] Future incorporation of ML into an MRvF framework could allow for more complicated tissue models to be efficiently simulated, and for faster and more accurate parameter map reconstruction. The majority of machine learning approaches applied to MRF thus far have utilized a subset of ML known as deep learning (DL), specifically with a feedforward neural network architecture, similar to the basic diagram shown in the middle of **Figure 8.2**.[175–177] These methods have shown great promise with more accurate parameter mapping than traditional MRF matching, increases in computational speed from 300-5000 fold faster[177], enhanced robustness to noise, and improved reproducibility.[175]

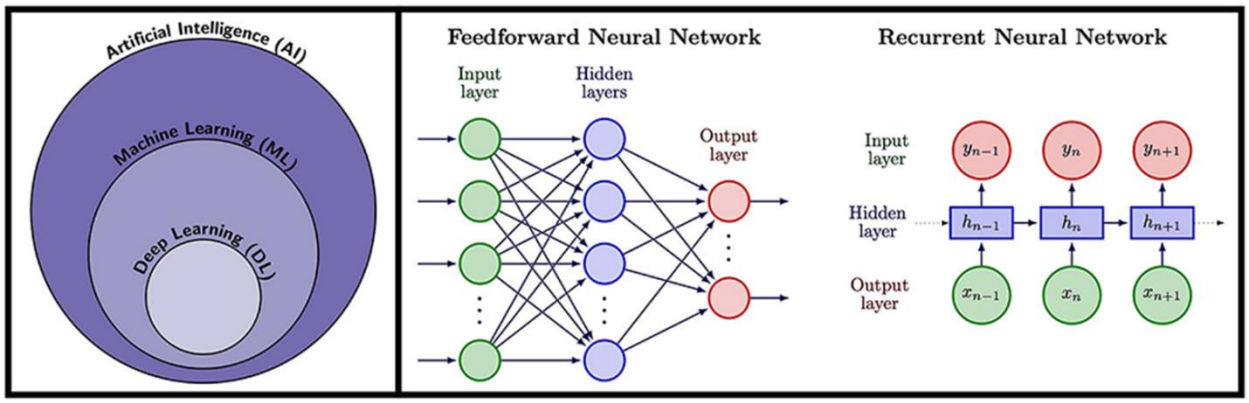


**Figure 8.2. AI, Machine Learning, and Deep Learning** (from Velasco et al.[202]). Artificial intelligence (AI) is a general term to describe a computer performing a task automatically while machine learning (ML) is a specific subset of AI in which a computer program or algorithm is trained to perform a task. Deep learning (DL) is a subset of ML that trains artificial neural networks (NNs) to perform the task. The two broad types of DL are feedforward NNs and recurrent NNs. Feedforwards NNs take input and are unidirectional to the final output, whereas recurrent NNs take input and are bi-directional, with the ability to take intermediate outputs and input those back into the same nodes prior to final output.

The other main type of DL algorithm uses recurrent neural networks (**Figure 8.2**, right), which allow bi-directional flow of outputs into previous nodes of the neural network as inputs. While their use in MRF applications have been limited thus far, they are well suited for predicting time series data like you may have with an MRF fingerprint with many time points.[203,204] Dynamic MRF, like we described throughout this dissertation, may also represent a compelling application of RNNs where the maps from one volume could be used as prior information on the next TR or to improve the previous TR.

Possibly the most significant effect of implementing machine learning into our dynamic MRvF framework would be the computational time savings. With dynamic MRvF, an entire volume of the brain is captured at five echo times every 4.5 seconds and repeated for ~9 minutes. With traditional pattern matching each of these repetitions requires independent MRvF reconstruction in which hundreds of thousands of voxels are individually compared against the entire dictionary with tens of thousands of entries to determine the best match. For the matching done in this dissertation, one of these volumes would generally take about two minutes to complete, and the whole times series would then take about four hours to complete. This severely limits the size of the dictionary that can be used due to practical time constraints. With DL, the network would only need to be trained on the entire dictionary a single time. After training, rather than comparing each voxel to every entry in the large dictionary, you could simply input each voxel's signal evolution into the single network and drastically reduce reconstruction times. Ultimately, these ML reconstruction techniques may enable MRF to be more widely adopted. The significantly reduced computational times could allow for reconstruction directly on the MR scanner and massively increase accessibility of MRF for those who do not have the technical expertise or time to perform sophisticated offline reconstructions.

*Transforming the Clinical MRI Workflow*

While not yet used clinically, the advantages of MRF over traditional MRI are substantial and could change how MRI is viewed as an imaging tool in clinical practice. However, before any of these evolutions occur, MRF needs to mature into a user-friendly product that is as easy to use as any other MR sequence for an MR technologist and provides useful information to the physician reading the images. Clinical practice and research have revolved exclusively around qualitative MRI techniques until recently, and quantitative MRI has very few clinical applications at this point. Therefore, new quantitative maps from MRF may not initially be seen as particularly useful to radiologists who were trained on and have been reading qualitatively weighted images

for decades. One recent, and especially compelling, development in MRF are sequences and reconstruction techniques that provide quantitative parameter maps and classic qualitatively weighted images from the same scan. One exemplary illustration of this was recently published by Cao et al.[205] They use a DTI-MRF approach with a specially tailored pulse sequence and very sophisticated reconstruction pipeline to generate five quantitative parameter maps of $T_1$, $T_2$, proton density, apparent diffusion coefficient, and fractional anisotropy (**Figure 8.3A**) and synthesize six clinical contrasts (**Figure 8.3B**) with 1-mm isotropic resolution from a single 10 minute scan. Schauman et al.[206] from the same group have pushed it even further to produce three quantitative parameter maps of $T_1$, $T_2$, proton density and five clinical contrasts with 1-mm isotropic resolution from a scan that is only 1-minute long. Development of an imaging protocol similar to this DTI-MRF one, but with vascular parameters like those in MRvF, could radically change the ubiquity of MRI, allow for more frequent scans during normal clinical visits, and ultimately lead to detection of vascular dysfunction before severe vascular complications or cognitive decline.

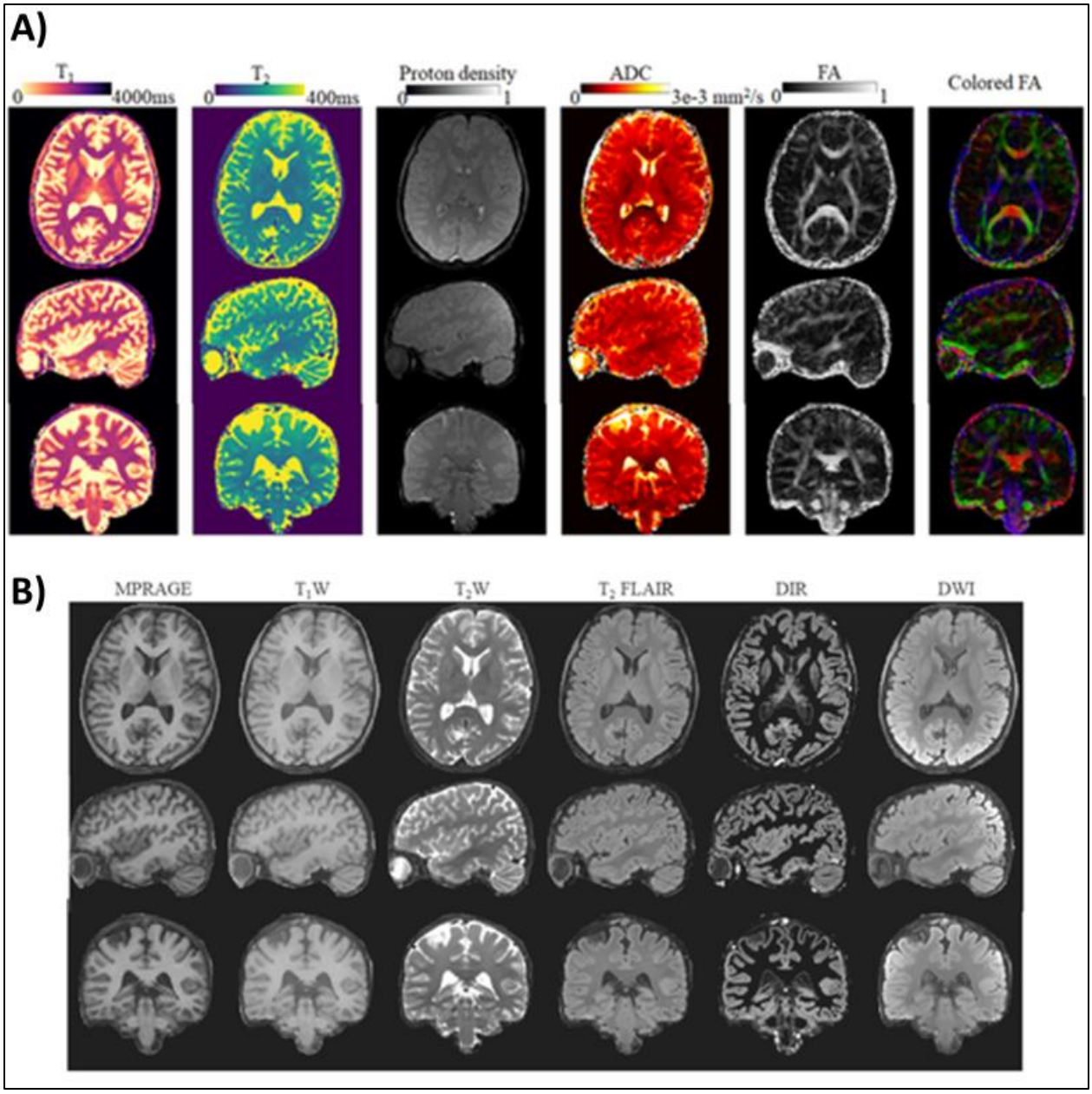


**Figure 8.3. Fast, Comprehensive MRI with Quantitative Maps and Traditional Contrasts** (from Cao et al.[205]). **A)** Orthogonal views of $T_1$, $T_2$, proton density, apparent diffusion coefficient (ADC), fractional anisotropy (FA), and colored-FA parameter maps from diffusion tensor imaging (DTI) MR fingerprinting with 1-mm isotropic resolution and 10-min acquisition time. **B)** Synthesized clinical contrast images produced from the same acquisition using the quantitative results obtained with DTI-MRF.

In addition to the acceleration of multiparametric image acquisition with MRF, the ability of MRF to be robust to noise, under sampling, and motion artifacts could transform MRI in another way. MRI systems are expensive to maintain and operate, necessitate substantial infrastructure, and require very strong magnetic fields to produce quality images. These factors increase the cost of MRI scans and limit the accessibility for patients to get an MRI and for healthcare settings

to have a scanner on site. One growing field to address these particular limitations is low field MRI, which are considered as scanners with a field strength 0.5T or lower. MRI scanners face challenges related to lower SNR and reduced contrast between different tissue types at these field strengths, however, MRF is better suited to deal with these issues than traditional reconstruction techniques.[207] The pattern-recognition approach of MRF allows it to extract valuable quantitative information even from the relatively noisy data produced by low-field scanners.[208] With further improvements, MRF could open up the possibility for lower field MR scanners to be practically useful, and enable more hospitals and clinics to purchase less expensive scanners and increase the accessibility of MRI. Additionally, MRF has been shown to be effective at producing meaningful quantitative parameter maps for MR scanners with as low as 50mT field strength, potentially opening the door for point-of-care devices based on MR principles.[209,210] While there is still substantial progress to be made before translating low-field scanners to widespread use, MRF will likely be one of the driving forces in the effort to make MRI more accessible.

### *8.3 | Conclusions*

Throughout this dissertation we presented a series of techniques we developed and studies we performed that demonstrate the capabilities of dynamic, contrast-free MR vascular fingerprinting. Initial studies presented here discussed matching algorithms to improve sensitivity in the absence of contrast agents, accuracy of parameter mapping with varying levels of SNR, and temporal resolution achievable from an accelerated sequence with a short echo train length. We optimized an accelerated SAGE sequence to enable continuous MRvF reconstruction of quantitative, multiparametric vascular parameter maps. This allowed us to validate our MRvF parameter fluctuations during hypercapnia induced changes of cerebral vasculature, which we then utilized in a study to compare vascular responses of healthy young and healthy old cohorts. In conclusion, the dynamic MRvF studies presented in this work lay the foundation for future

research into imaging rapid cerebrovascular processes and provide a step forward in developing novel functional imaging biomarkers of vascular function for early identification and treatment of cerebrovascular diseases and vascular-linked dementias.

# References


1. Dementia. World Health Orgnaization. https://www.who.int/news-room/fact-sheets/detail/dementia
2. Corriveau RA, Bosetti F, Emr M, et al. The Science of Vascular Contributions to Cognitive Impairment and Dementia (VCID): A Framework for Advancing Research Priorities in the Cerebrovascular Biology of Cognitive Decline. *Cell Mol Neurobiol*. 2016;36(2):281-288. doi:10.1007/s10571-016-0334-7
3. Alber J, Alladi S, Bae H, et al. White matter hyperintensities in vascular contributions to cognitive impairment and dementia (VCID): Knowledge gaps and opportunities. *Alzheimers Dement Transl Res Clin Interv*. 2019;5(1):107-117. doi:10.1016/j.trci.2019.02.001
4. Banerjee G, Wilson D, Jäger HR, Werring DJ. Novel imaging techniques in cerebral small vessel diseases and vascular cognitive impairment. *Biochim Biophys Acta BBA - Mol Basis Dis*. 2016;1862(5):926-938. doi:10.1016/j.bbadis.2015.12.010
5. European Society of Radiology (ESR). Magnetic Resonance Fingerprinting - a promising new approach to obtain standardized imaging biomarkers from MRI. *Insights Imaging*. 2015;6(2):163-165. doi:10.1007/s13244-015-0403-3
6. Hsieh JJL, Svalbe I. Magnetic resonance fingerprinting: from evolution to clinical applications. *J Med Radiat Sci*. 2020;67(4):333-344. doi:10.1002/jmrs.413
7. Poorman ME, Martin MN, Ma D, et al. Magnetic resonance fingerprinting Part 1: Potential uses, current challenges, and recommendations. *J Magn Reson Imaging*. 2020;51(3):675-692. doi:10.1002/jmri.26836
8. Ma D, Gulani V, Seiberlich N, et al. Magnetic resonance fingerprinting. *Nature*. 2013;495(7440):187-192. doi:10.1038/nature11971
9. Christen T, Pannetier N, Ni W, et al. MR vascular fingerprinting: A new approach to compute cerebral blood volume, mean vessel radius, and oxygenation maps in the human brain. *NeuroImage*. 2014;(89):262-270. doi:10.1016/j.neuroimage.2013.11.052
10. An H, Lin W, Celik A, Lee YZ. Quantitative measurements of cerebral metabolic rate of oxygen utilization using MRI: a volunteer study. *NMR Biomed*. 2001;14(7-8):441-447. doi:10.1002/nbm.717
11. Vazquez A, Masamoto K, Fukuda M, Kim SG. Cerebral oxygen delivery and consumption during evoked neural activity. *Front Neuroenergetics*. 2010;2. https://www.frontiersin.org/articles/10.3389/fnene.2010.00011
12. Watts ME, Pocock R, Claudianos C. Brain Energy and Oxygen Metabolism: Emerging Role in Normal Function and Disease. *Front Mol Neurosci*. 2018;11. https://www.frontiersin.org/articles/10.3389/fnmol.2018.00216
13. Fantini S, Sassaroli A, Tgavalekos KT, Kornbluth J. Cerebral blood flow and autoregulation: current measurement techniques and prospects for noninvasive optical methods. *Neurophotonics*. 2016;3(3):031411. doi:10.1117/1.NPh.3.3.031411
14. Tomoto T, Lu M, Khan AM, et al. Cerebral blood flow and cerebrovascular resistance across the adult lifespan: A multimodality approach. *J Cereb Blood Flow Metab*. 2023;43(6):962-976. doi:10.1177/0271678X231153741
15. Quick S, Moss J, Rajani RM, Williams A. A Vessel for Change: Endothelial Dysfunction in Cerebral Small Vessel Disease. *Trends Neurosci*. 2021;44(4):289-305. doi:10.1016/j.tins.2020.11.003
16. Herrera MD, Mingorance C, Rodríguez-Rodríguez R, Alvarez De Sotomayor M. Endothelial dysfunction and aging: An update. *Ageing Res Rev*. 2010;9(2):142-152. doi:10.1016/j.arr.2009.07.002
17. Toth P, Tarantini S, Csiszar A, Ungvari Z. Functional vascular contributions to cognitive impairment and dementia: mechanisms and consequences of cerebral autoregulatory dysfunction, endothelial

impairment, and neurovascular uncoupling in aging. *Am J Physiol-Heart Circ Physiol*. 2017;312(1):H1-H20. doi:10.1152/ajpheart.00581.2016

18. Ungvari Z, Tarantini S, Donato AJ, Galvan V, Csiszar A. Mechanisms of Vascular Aging. *Circ Res*. 2018;123(7):849-867. doi:10.1161/CIRCRESAHA.118.311378

19. Kohn JC, Lampi MC, Reinhart-King CA. Age-related vascular stiffening: causes and consequences. *Front Genet*. 2015;06. doi:10.3389/fgene.2015.00112

20. Smith EE, Greenberg SM. β-Amyloid, Blood Vessels, and Brain Function. *Stroke*. 2009;40(7):2601-2606. doi:10.1161/STROKEAHA.108.536839

21. Zhao MY, Woodward A, Fan AP, et al. Reproducibility of cerebrovascular reactivity measurements: A systematic review of neuroimaging techniques *. *J Cereb Blood Flow Metab*. Published online November 22, 2021:0271678X2110567. doi:10.1177/0271678X211056702

22. Mokhber N, Shariatzadeh A, Avan A, et al. Cerebral blood flow changes during aging process and in cognitive disorders: A review. *Neuroradiol J*. 2021;34(4):300-307. doi:10.1177/19714009211002778

23. Peng SL, Chen X, Li Y, Rodrigue KM, Park DC, Lu H. Age-related changes in cerebrovascular reactivity and their relationship to cognition: A four-year longitudinal study. *NeuroImage*. 2018;174:257-262. doi:10.1016/j.neuroimage.2018.03.033

24. Lee BC, Tsai HH, Huang APH, et al. Arterial Spin Labeling Imaging Assessment of Cerebrovascular Reactivity in Hypertensive Small Vessel Disease. *Front Neurol*. 2021;12:640069. doi:10.3389/fneur.2021.640069

25. Deery HA, Di Paolo R, Moran C, Egan GF, Jamadar SD. Lower brain glucose metabolism in normal ageing is predominantly frontal and temporal: A systematic review and pooled effect size and activation likelihood estimates meta-analyses. *Hum Brain Mapp*. 2023;44(3):1251-1277. doi:10.1002/hbm.26119

26. Liberale L, Badimon L, Montecucco F, Lüscher TF, Libby P, Camici GG. Inflammation, Aging, and Cardiovascular Disease. *J Am Coll Cardiol*. 2022;79(8):837-847. doi:10.1016/j.jacc.2021.12.017

27. Saji N, Toba K, Sakurai T. Cerebral Small Vessel Disease and Arterial Stiffness: Tsunami Effect in the Brain. *Pulse*. 2015;3(3-4):182-189. doi:10.1159/000443614

28. Vemuri P, Decarli C, Duering M. Imaging Markers of Vascular Brain Health: Quantification, Clinical Implications, and Future Directions. *Stroke*. 2022;53(2):416-426. doi:10.1161/STROKEAHA.120.032611

29. Boehme AK, Esenwa C, Elkind MSV. Stroke Risk Factors, Genetics, and Prevention. *Circ Res*. 2017;120(3):472-495. doi:10.1161/CIRCRESAHA.116.308398

30. Kuriakose D, Xiao Z. Pathophysiology and Treatment of Stroke: Present Status and Future Perspectives. *Int J Mol Sci*. 2020;21(20):7609. doi:10.3390/ijms21207609

31. Kalaria RN. The pathology and pathophysiology of vascular dementia. *Neuropharmacology*. 2018;134:226-239. doi:10.1016/j.neuropharm.2017.12.030

32. Schneider JA, Arvanitakis Z, Bang W, Bennett DA. Mixed brain pathologies account for most dementia cases in community-dwelling older persons. *Neurology*. 2007;69(24):2197-2204. doi:10.1212/01.wnl.0000271090.28148.24

33. White L, Small BJ, Petrovitch H, et al. Recent Clinical-Pathologic Research on the Causes of Dementia in Late Life: Update From the Honolulu-Asia Aging Study. *J Geriatr Psychiatry Neurol*. 2005;18(4):224-227. doi:10.1177/0891988705281872

34. Guermazi A, Miaux Y, Rovira-Cañellas A, et al. Neuroradiological findings in vascular dementia. *Neuroradiology*. 2007;49(1):1-22. doi:10.1007/s00234-006-0156-2

35. Razek AAKA, Elsebaie NA. Imaging of vascular cognitive impairment. *Clin Imaging*. 2021;74:45-54. doi:10.1016/j.clinimag.2020.12.038

36. Smith EE. Clinical presentations and epidemiology of vascular dementia. *Clin Sci*. 2017;131(11):1059-1068. doi:10.1042/CS20160607

37. Zlokovic BV, Gottesman RF, Bernstein KE, et al. Vascular contributions to cognitive impairment and dementia (VCID): A report from the 2018 National Heart, Lung, and Blood Institute and National Institute of Neurological Disorders and Stroke Workshop. *Alzheimers Dement*. 2020;16(12):1714-1733. doi:10.1002/alz.12157

38. Catchlove SJ, Pipingas A, Hughes ME, Macpherson H. Magnetic resonance imaging for assessment of cerebrovascular reactivity and its relationship to cognition: a systematic review. *BMC Neurosci*. 2018;19(1):21. doi:10.1186/s12868-018-0421-4

39. Sleight E, Stringer MS, Marshall I, Wardlaw JM, Thrippleton MJ. Cerebrovascular Reactivity Measurement Using Magnetic Resonance Imaging: A Systematic Review. *Front Physiol*. 2021;12:643468. doi:10.3389/fphys.2021.643468

40. Carr JMJR, Caldwell HG, Ainslie PN. Cerebral blood flow, cerebrovascular reactivity and their influence on ventilatory sensitivity. *Exp Physiol*. 2021;106(7):1425-1448. doi:10.1113/EP089446

41. Bhogal AA, Philippens MEP, Siero JCW, et al. Examining the regional and cerebral depth-dependent BOLD cerebrovascular reactivity response at 7 T. *NeuroImage*. 2015;114:239-248. doi:10.1016/j.neuroimage.2015.04.014

42. Catchlove SJ, Parrish TB, Chen Y, Macpherson H, Hughes ME, Pipingas A. Regional Cerebrovascular Reactivity and Cognitive Performance in Healthy Aging. *J Exp Neurosci*. 2018;12:117906951878515. doi:10.1177/1179069518785151

43. Kim D, Hughes TM, Lipford ME, et al. Relationship Between Cerebrovascular Reactivity and Cognition Among People With Risk of Cognitive Decline. *Front Physiol*. 2021;12:645342. doi:10.3389/fphys.2021.645342

44. Aslanyan V, Mack WJ, Ortega NE, et al. Cerebrovascular reactivity in Alzheimer's disease signature regions is associated with mild cognitive impairment in adults with hypertension. *Alzheimers Dement*. Published online December 18, 2023:alz.13572. doi:10.1002/alz.13572

45. Mandell DM, Han JS, Poublanc J, et al. Mapping Cerebrovascular Reactivity Using Blood Oxygen Level-Dependent MRI in Patients With Arterial Steno-occlusive Disease: Comparison With Arterial Spin Labeling MRI. *Stroke*. 2008;39(7):2021-2028. doi:10.1161/STROKEAHA.107.506709

46. Yezhuvath US, Uh J, Cheng Y, et al. Forebrain-dominant deficit in cerebrovascular reactivity in Alzheimer's disease. *Neurobiol Aging*. 2012;33(1):75-82. doi:10.1016/j.neurobiolaging.2010.02.005

47. Cantin S, Villien M, Moreaud O, et al. Impaired cerebral vasoreactivity to CO2 in Alzheimer's disease using BOLD fMRI. *NeuroImage*. 2011;58(2):579-587. doi:10.1016/j.neuroimage.2011.06.070

48. Glodzik L, Randall C, Rusinek H, de Leon MJ. Cerebrovascular Reactivity to Carbon Dioxide in Alzheimer's Disease. *J Alzheimers Dis*. 2013;35(3):427-440. doi:10.3233/JAD-122011

49. Bellomo J, Sebök M, Stumpo V, et al. Blood Oxygenation Level–Dependent Cerebrovascular Reactivity–Derived Steal Phenomenon May Indicate Tissue Reperfusion Failure After Successful Endovascular Thrombectomy. *Transl Stroke Res*. Published online October 25, 2023. doi:10.1007/s12975-023-01203-y

50. Jiang D, Lu H. Cerebral oxygen extraction fraction MRI : Techniques and applications. *Magn Reson Med*. 2022;88(2):575-600. doi:10.1002/mrm.29272

51. Barcroft J, Hill AV. The nature of oxyhæmoglobin, with a note on its molecular weight. *J Physiol*. 1910;39(6):411-428. doi:10.1113/jphysiol.1910.sp001350

52. Hill AV. The Combinations of Haemoglobin with Oxygen and with Carbon Monoxide. I. *Biochem J*. 1913;7(5):471-480. doi:10.1042/bj0070471

53. Kaufman DP, Kandle PF, Murray IV, Dhamoon AS. Physiology, Oxyhemoglobin Dissociation Curve. In: *StatPearls*. StatPearls Publishing; 2024. http://www.ncbi.nlm.nih.gov/books/NBK499818/

54. Patel S, Jose A, Mohiuddin SS. Physiology, Oxygen Transport And Carbon Dioxide Dissociation Curve. In: *StatPearls*. StatPearls Publishing; 2024. http://www.ncbi.nlm.nih.gov/books/NBK539815/

55. Komoda T, Matsunaga T. Chapter 5 - Biochemistry of Internal Organs. In: Komoda T, Matsunaga T, eds. *Biochemistry for Medical Professionals*. Academic Press; 2015:65-73. doi:10.1016/B978-0-12-801918-4.00005-0

56. Lewis NCS, Messinger L, Monteleone B, Ainslie PN. Effect of acute hypoxia on regional cerebral blood flow: effect of sympathetic nerve activity. *J Appl Physiol*. 2014;116(9):1189-1196. doi:10.1152/japplphysiol.00114.2014

57. Stadlbauer A, Kinfe TM, Zimmermann M, et al. Association between tissue hypoxia, perfusion restrictions, and microvascular architecture alterations with lesion-induced impairment of neurovascular coupling. *J Cereb Blood Flow Metab*. Published online August 12, 2020:0271678X2094754. doi:10.1177/0271678X20947546

58. Xu F, Liu P, Pascual JM, Xiao G, Lu H. Effect of Hypoxia and Hyperoxia on Cerebral Blood Flow, Blood Oxygenation, and Oxidative Metabolism. *J Cereb Blood Flow Metab*. 2012;32(10):1909-1918. doi:10.1038/jcbfm.2012.93

59. Christen T, Ni W, Fan A, Moseley M, Zaharchuk G. MR Vascular Fingerprinting During Gas Challenges. Presented at: Proc. Intl. Soc. Mag. Reson. Med. 26; 2018. https://cds.ismrm.org/protected/18MProceedings/PDFfiles/0678.html

60. Liu P, De Vis JB, Lu H. Cerebrovascular reactivity (CVR) MRI with CO2 challenge: A technical review. *NeuroImage*. 2019;187:104-115. doi:10.1016/j.neuroimage.2018.03.047

61. Hare HV, Germuska M, Kelly ME, Bulte DP. Comparison of $CO_2$ in Air Versus Carbogen for the Measurement of Cerebrovascular Reactivity with Magnetic Resonance Imaging. *J Cereb Blood Flow Metab*. 2013;33(11):1799-1805. doi:10.1038/jcbfm.2013.131

62. Liu P, Welch BG, Li Y, et al. Multiparametric imaging of brain hemodynamics and function using gas-inhalation MRI. *NeuroImage*. 2017;146:715-723. doi:10.1016/j.neuroimage.2016.09.063

63. Gibney B, Redmond CE, Byrne D, Mathur S, Murray N. A Review of the Applications of Dual-Energy CT in Acute Neuroimaging. *Can Assoc Radiol J*. 2020;71(3):253-265. doi:10.1177/0846537120904347

64. Heiss WD, Rosenberg GA, Thiel A, Berlot R, de Reuck J. Neuroimaging in vascular cognitive impairment: a state-of-the-art review. *BMC Med*. 2016;14(1):174. doi:10.1186/s12916-016-0725-0

65. Ito H, Kanno I, Ibaraki M, Hatazawa J. Effect of Aging on Cerebral Vascular Response to $Paco_2$ Changes in Humans as Measured by Positron Emission Tomography. *J Cereb Blood Flow Metab*. 2002;22(8):997-1003. doi:10.1097/00004647-200208000-00011

66. Ito H, Ibaraki M, Yamakuni R, et al. Oxygen extraction fraction is not uniform in human brain: a positron emission tomography study. *J Physiol Sci*. 2023;73(1):25. doi:10.1186/s12576-023-00880-6

67. Hoh CK. Clinical use of FDG PET. *Nucl Med Biol*. 2007;34(7):737-742. doi:10.1016/j.nucmedbio.2007.07.001

68. Fan AP, An H, Moradi F, et al. Quantification of brain oxygen extraction and metabolism with [15O]-gas PET: A technical review in the era of PET/MRI. *NeuroImage*. 2020;220:117136. doi:10.1016/j.neuroimage.2020.117136

69. Donahue MJ, Achten E, Cogswell PM, et al. Consensus statement on current and emerging methods for the diagnosis and evaluation of cerebrovascular disease. *J Cereb Blood Flow Metab*. 2018;38(9):1391-1417. doi:10.1177/0271678X17721830

70. Matsuda H. Role of Neuroimaging in Alzheimer's Disease, with Emphasis on Brain Perfusion SPECT. *J Nucl Med*. 2007;48(8):1289-1300. doi:10.2967/jnumed.106.037218

71. Ferrando R, Damian A. Brain SPECT as a Biomarker of Neurodegeneration in Dementia in the Era of Molecular Imaging: Still a Valid Option? *Front Neurol*. 2021;12:629442. doi:10.3389/fneur.2021.629442

72. Introduction to MRI. Radiology Café. Published March 28, 2017. https://www.radiologycafe.com/frcr-physics-notes/mr-imaging/introduction-to-mri/

73. Abdulla S, Clarke C. *FRCR Physics Notes: Medical Imaging Physics for the First FRCR Examination*. 3rd ed. Radiology Cafe Publishing; 2020.

74. Bloch F. Nuclear Induction. *Phys Rev*. 1946;70(7-8):460-474. doi:10.1103/PhysRev.70.460

75. Slice selection. Radiology Café. Published March 28, 2017. https://www.radiologycafe.com/frcr-physics-notes/mr-imaging/slice-selection/

76. Spatial encoding. Radiology Café. Published March 28, 2017. https://www.radiologycafe.com/frcr-physics-notes/mr-imaging/spatial-encoding/

77. Hartung MP, Grist TM, François CJ. Magnetic resonance angiography: current status and future directions. *J Cardiovasc Magn Reson*. 2011;13(1):19. doi:10.1186/1532-429X-13-19

78. Kuo AH, Nagpal P, Ghoshhajra BB, Hedgire SS. Vascular magnetic resonance angiography techniques. *Cardiovasc Diagn Ther*. 2019;9(S1):S28-S36. doi:10.21037/cdt.2019.06.07

79. Calamante F. Perfusion MRI Using Dynamic-Susceptibility Contrast MRI: Quantification Issues in Patient Studies. *Top Magn Reson Imaging*. 2010;21(2):75-85. doi:10.1097/RMR.0b013e31821e53f5

80. Peret A, Capel KW, Jen ML, et al. Perfusion MRI Techniques: Beyond DSC. *Neurographics*. 2023;13(3):210-229. doi:10.3174/ng.2100041

81. Khalifa F, Soliman A, El-Baz A, et al. Models and methods for analyzing DCE-MRI: A review. *Med Phys*. 2014;41(12):124301. doi:10.1118/1.4898202

82. Bergamino M, Bonzano L, Levrero F, Mancardi GL, Roccatagliata L. A review of technical aspects of T1-weighted dynamic contrast-enhanced magnetic resonance imaging (DCE-MRI) in human brain tumors. *Phys Med*. 2014;30(6):635-643. doi:10.1016/j.ejmp.2014.04.005

83. BOLD Contrast Mechanism. MRIquestions.com. http://mriquestions.com/bold-contrast.html

84. Cashmore MT, McCann AJ, Wastling SJ, McGrath C, Thornton J, Hall MG. Clinical quantitative MRI and the need for metrology. *Br J Radiol*. 2021;94(1120):20201215. doi:10.1259/bjr.20201215

85. Weiskopf N, Edwards LJ, Helms G, Mohammadi S, Kirilina E. Quantitative magnetic resonance imaging of brain anatomy and in vivo histology. *Nat Rev Phys*. 2021;3(8):570-588. doi:10.1038/s42254-021-00326-1

86. Granziera C, Wuerfel J, Barkhof F, et al. Quantitative magnetic resonance imaging towards clinical application in multiple sclerosis. *Brain*. 2021;144(5):1296-1311. doi:10.1093/brain/awab029

87. Detre JA, Rao H, Wang DJJ, Chen YF, Wang Z. Applications of arterial spin labeled MRI in the brain. *J Magn Reson Imaging*. 2012;35(5):1026-1037. doi:10.1002/jmri.23581

88. Donahue MJ, Jan Van Laar P, Van Zijl PCM, Stevens RD, Hendrikse J. Vascular space occupancy (VASO) cerebral blood volume-weighted MRI identifies hemodynamic impairment in patients with carotid artery disease. *J Magn Reson Imaging*. 2009;29(3):718-724. doi:10.1002/jmri.21667

89. Lu H, Hua J, Van Zijl PCM. Noninvasive functional imaging of cerebral blood volume with vascular-space-occupancy (VASO) MRI. *NMR Biomed*. 2013;26(8):932-948. doi:10.1002/nbm.2905

90. Ruetten PPR, Gillard JH, Graves MJ. Introduction to Quantitative Susceptibility Mapping and Susceptibility Weighted Imaging. *Br J Radiol*. 2019;92(1101):20181016. doi:10.1259/bjr.20181016

91. Yablonskiy DA, Haacke EM. Theory of NMR signal behavior in magnetically inhomogeneous tissues: The static dephasing regime. *Magn Reson Med*. 1994;32(6):749-763. doi:10.1002/mrm.1910320610

92. Stone AJ, Harston GWJ, Carone D, Okell TW, Kennedy J, Blockley NP. Prospects for investigating brain oxygenation in acute stroke: Experience with a non-contrast quantitative BOLD based approach. *Hum Brain Mapp*. 2019;40(10):2853-2866. doi:10.1002/hbm.24564

93. Lee H, Englund EK, Wehrli FW. Interleaved quantitative BOLD: Combining extravascular R2' - and intravascular R2-measurements for estimation of deoxygenated blood volume and hemoglobin oxygen saturation. *NeuroImage*. 2018;174:420-431. doi:10.1016/j.neuroimage.2018.03.043

94. Panda A, Mehta BB, Coppo S, et al. Magnetic resonance fingerprinting – An overview. *Curr Opin Biomed Eng*. 2017;3:56-66. doi:10.1016/j.cobme.2017.11.001

95. Kara D, Fan M, Hamilton J, Griswold M, Seiberlich N, Brown R. Parameter map error due to normal noise and aliasing artifacts in MR fingerprinting. *Magn Reson Med*. 2019;81(5):3108-3123. doi:10.1002/mrm.27638

96. Yu Z, Zhao T, Assländer J, Lattanzi R, Sodickson DK, Cloos MA. Exploring the sensitivity of magnetic resonance fingerprinting to motion. *Magn Reson Imaging*. 2018;54:241-248. doi:10.1016/j.mri.2018.09.002

97. Mehta BB, Ma D, Pierre EY, Jiang Y, Coppo S, Griswold MA. Image reconstruction algorithm for motion insensitive MR Fingerprinting (MRF): MORF. *Magn Reson Med*. 2018;80(6):2485-2500. doi:10.1002/mrm.27227

98. Ye H, Ma D, Jiang Y, et al. Accelerating magnetic resonance fingerprinting (MRF) using t-blipped simultaneous multislice (SMS) acquisition: Accelerating MRF Using t-Blipped SMS. *Magn Reson Med*. 2016;75(5):2078-2085. doi:10.1002/mrm.25799

99. Ye H, Cauley SF, Gagoski B, et al. Simultaneous multislice magnetic resonance fingerprinting (SMS-MRF) with direct-spiral slice-GRAPPA (ds-SG) reconstruction. *Magn Reson Med*. 2017;77(5):1966-1974. doi:10.1002/mrm.26271

100. Fujita S, Cencini M, Buonincontri G, et al. Simultaneous relaxometry and morphometry of human brain structures with 3D magnetic resonance fingerprinting: a multicenter, multiplatform, multifield-strength study. *Cereb Cortex*. 2023;33(3):729-739. doi:10.1093/cercor/bhac096

101. Shridhar Konar A, Qian E, Geethanath S, et al. Quantitative imaging metrics derived from magnetic resonance fingerprinting using ISMRM/NIST MRI system phantom: An international multicenter repeatability and reproducibility study. *Med Phys*. 2021;48(5):2438-2447. doi:10.1002/mp.14833

102. Buonincontri G, Kurzawski JW, Kaggie JD, et al. Three dimensional MRF obtains highly repeatable and reproducible multi-parametric estimations in the healthy human brain at 1.5T and 3T. *NeuroImage*. 2021;226:117573. doi:10.1016/j.neuroimage.2020.117573

103. Sushentsev N, Kaggie JD, Slough RA, Carmo B, Barrett T. Reproducibility of magnetic resonance fingerprinting-based T1 mapping of the healthy prostate at 1.5 and 3.0 T: A proof-of-concept study. *PLOS ONE*. 2021;16(1):e0245970. doi:10.1371/journal.pone.0245970

104. Fujita S, Buonincontri G, Cencini M, et al. Repeatability and reproducibility of human brain morphometry using three-dimensional magnetic resonance fingerprinting. *Hum Brain Mapp*. 2021;42(2):275-285. doi:10.1002/hbm.25232

105. Delphin A. *MRI Signals Simulation for Validation of a New Microvascular Characterization*. KTH Royal Institute of Technology; 2019.

106. Boux F. *Statistical Methods for Vascular Magnetic Resonance Fingerprinting : Application to the Epileptic Brain*. University of Grenoble Alpes; 2020.

107. Lemasson B, Pannetier N, Coquery N, et al. MR Vascular Fingerprinting in Stroke and Brain Tumors Models. *Sci Rep*. 2016;6(1):37071. doi:10.1038/srep37071

108. Delphin A, Boux F, Brossard C, et al. Towards optimizing MR vascular fingerprinting. Presented at: Proc. Intl. Soc. Mag. Reson. Med. 29; 2021. https://cds.ismrm.org/protected/21MProceedings/PDFfiles/0172.html

109. Venugopal K, Arzanforoosh F, Van Dorth D, et al. MR Vascular Fingerprinting with Hybrid Gradient–Spin Echo Dynamic Susceptibility Contrast MRI for Characterization of Microvasculature in Gliomas. *Cancers*. 2023;15(7):2180. doi:10.3390/cancers15072180

110. Pannetier NA, Debacker CS, Mauconduit F, Christen T, Barbier EL. A Simulation Tool for Dynamic Contrast Enhanced MRI. *PLoS ONE*. 2013;8(3):e57636. doi:10.1371/journal.pone.0057636

111. Pannetier NA, Sohlin M, Christen T, Schad L, Schuff N. Numerical modeling of susceptibility-related MR signal dephasing with vessel size measurement: Phantom validation at 3T: Susceptibility-Related Dephasing with Vessel Size Measurement. *Magn Reson Med*. 2014;72(3):646-658. doi:10.1002/mrm.24968

112. Klassen LM, Menon RS. NMR Simulation Analysis of Statistical Effects on Quantifying Cerebrovascular Parameters. *Biophys J*. 2007;92(3):1014-1021. doi:10.1529/biophysj.106.087965

113. Ma J, Wehrli FW. Method for Image-Based Measurement of the Reversible and Irreversible Contribution to the Transverse-Relaxation Rate. *J Magn Reson B*. 1996;111(1):61-69. doi:10.1006/jmrb.1996.0060

114. Ni W, Christen T, Zun Z, Zaharchuk G. Comparison of R2′ measurement methods in the normal brain at 3 tesla: Comparison of R2′ Measurement Methods in Brain at 3T. *Magn Reson Med*. 2015;73(3):1228-1236. doi:10.1002/mrm.25232

115. Pouliot P, Gagnon L, Lam T, et al. Magnetic resonance fingerprinting based on realistic vasculature in mice. *NeuroImage*. 2017;149:436-445. doi:10.1016/j.neuroimage.2016.12.060

116. Ni WW, Christen T, Zaharchuk G. Benchmarking transverse spin relaxation based oxygenation measurements in the brain during hypercapnia and hypoxia: Mapping R2'/R2*/R2 With Gas Challenges. *J Magn Reson Imaging*. 2017;46(3):704-714. doi:10.1002/jmri.25582

117. Schmiedeskamp H, Straka M, Newbould RD, et al. Combined spin- and gradient-echo perfusion-weighted imaging: Spin- and Gradient-Echo PWI. *Magn Reson Med*. 2012;68(1):30-40. doi:10.1002/mrm.23195

118. Schmiedeskamp H, Andre JB, Straka M, et al. Simultaneous Perfusion and Permeability Measurements Using Combined Spin- and Gradient-Echo MRI. *J Cereb Blood Flow Metab*. 2013;33(5):732-743. doi:10.1038/jcbfm.2013.10

119. Griswold MA, Jakob PM, Heidemann RM, et al. Generalized autocalibrating partially parallel acquisitions (GRAPPA). *Magn Reson Med*. 2002;47(6):1202-1210. doi:10.1002/mrm.10171

120. Manhard MK, Bilgic B, Liao C, et al. Accelerated whole-brain perfusion imaging using a simultaneous multislice spin-echo and gradient-echo sequence with joint virtual coil reconstruction. *Magn Reson Med*. 2019;82(3):973-983. doi:10.1002/mrm.27784

121. Zur Y. Design of improved spectral-spatial pulses for routine clinical use. *Magn Reson Med*. 2000;43(3):410-420. doi:10.1002/(SICI)1522-2594(200003)43:3<410::AID-MRM13>3.0.CO;2-3

122. Delphin A, Boux F, Brossard C, et al. Enhancing MR vascular Fingerprinting through realistic microvascular geometries. Published online May 26, 2023. doi:10.48550/arXiv.2305.17092

123. Chen Y, Lu L, Zhu T, Ma D. Technical overview of magnetic resonance fingerprinting and its applications in radiation therapy. *Med Phys*. Published online October 11, 2021:mp.15254. doi:10.1002/mp.15254

124. Ding H, Velasco C, Ye H, et al. Current Applications and Future Development of Magnetic Resonance Fingerprinting in Diagnosis, Characterization, and Response Monitoring in Cancer. *Cancers*. 2021;13(19):4742. doi:10.3390/cancers13194742

125. Christen T, Bouzat P, Pannetier N, et al. Tissue Oxygen Saturation Mapping with Magnetic Resonance Imaging. *J Cereb Blood Flow Metab*. 2014;34(9):1550-1557. doi:10.1038/jcbfm.2014.116

126. Christen T, Bolar DS, Zaharchuk G. Imaging Brain Oxygenation with MRI Using Blood Oxygenation Approaches: Methods, Validation, and Clinical Applications. *Am J Neuroradiol*. 2013;34(6):1113-1123. doi:10.3174/ajnr.A3070

127. Boxerman JL, Hamberg LM, Rosen BR, Weisskoff RM. Mr contrast due to intravascular magnetic susceptibility perturbations. *Magn Reson Med*. 1995;34(4):555-566. doi:10.1002/mrm.1910340412

128. Gu Y, Wang CY, Anderson CE, et al. Fast magnetic resonance fingerprinting for dynamic contrast-enhanced studies in mice: Gu et al. *Magn Reson Med*. 2018;80(6):2681-2690. doi:10.1002/mrm.27345

129. Ma D, Jiang Y, Chen Y, et al. Fast 3D magnetic resonance fingerprinting for a whole-brain coverage. *Magn Reson Med*. 2018;79(4):2190-2197. doi:10.1002/mrm.26886

130. McGivney DF, Boyacıoğlu R, Jiang Y, et al. Magnetic resonance fingerprinting review part 2: Technique and directions. *J Magn Reson Imaging*. 2020;51(4):993-1007. doi:10.1002/jmri.26877

131. Delphin A, Boux F, Brossard C, et al. Optimizing signal patterns for MR vascular fingerprinting. Presented at: Proc. Intl. Soc. Mag. Reson. Med. 28; 2020. https://cds.ismrm.org/protected/20MProceedings/PDFfiles/3743.html

132. McVeigh ER, Henkelman RM, Bronskill MJ. Noise and filtration in magnetic resonance imaging: Noise and filtration in magnetic resonance imaging. *Med Phys*. 1985;12(5):586-591. doi:10.1118/1.595679

133. Gudbjartsson H, Patz S. The rician distribution of noisy mri data. *Mag Res Med*. 1995;(34):910-914.

134. Cardenas-Blanco A, Tejos C, Irarrazaval P, Cameron I. Noise in magnitude magnetic resonance images. *Concepts Magn Reson Part A*. 2008;32A(6):409-416.

135. Aja-Fernández S, Vegas-Sánchez-Ferrero G. *Statistical Analysis of Noise in MRI*. Springer International Publishing; 2016. doi:10.1007/978-3-319-39934-8

136. Dietrich O, Raya JG, Reeder SB, Ingrisch M, Reiser MF, Schoenberg SO. Influence of multichannel combination, parallel imaging and other reconstruction techniques on MRI noise characteristics. *Magn Reson Imaging*. Published online 2008:9.

137. Jenkinson M, Smith S. A global optimisation method for robust affine registration of brain images. *Med Image Anal*. 2001;5(2):143-156. doi:10.1016/S1361-8415(01)00036-6

138. Jenkinson M, Bannister P, Brady M, Smith S. Improved Optimization for the Robust and Accurate Linear Registration and Motion Correction of Brain Images. *NeuroImage*. 2002;17(2):825-841. doi:10.1006/nimg.2002.1132

139. Andersson J, Jenkinson M, Smith S. *Non-Linear Registration Aka Spatial Normalisation*. FMRIB Centre; 2007.

140. Stone AJ, Blockley NP. A streamlined acquisition for mapping baseline brain oxygenation using quantitative BOLD. *NeuroImage*. 2017;147:79-88. doi:10.1016/j.neuroimage.2016.11.057

141. Yablonskiy DA. Quantitation of intrinsic magnetic susceptibility-related effects in a tissue matrix. Phantom study. *Magn Reson Med*. 1998;39(3):417-428. doi:10.1002/mrm.1910390312

142. Cherukara MT, Stone AJ, Chappell MA, Blockley NP. Model-based Bayesian inference of brain oxygenation using quantitative BOLD. *NeuroImage*. 2019;202:116106. doi:10.1016/j.neuroimage.2019.116106

143. Le LNN, Wheeler GJ, Holy EN, et al. Cortical oxygen extraction fraction using quantitative BOLD MRI and cerebral blood flow during vasodilation. *Front Physiol*. 2023;14:1231793. doi:10.3389/fphys.2023.1231793

144. Kety SS, Schmidt CF. The Nitrous Oxide Method for the Quantitative Determination of Cerebral Blood Flow in Man: Theory, Procedure and Normal Values. *J Clin Invest*. 1948;27(4):476-483. doi:10.1172/JCI101994

145. Duffin J, Mikulis DJ, Fisher JA. Control of Cerebral Blood Flow by Blood Gases. *Front Physiol*. 2021;12:640075. doi:10.3389/fphys.2021.640075

146. Smeeing DPJ, Hendrikse J, Petersen ET, Donahue MJ, De Vis JB. Arterial Spin Labeling and Blood Oxygen Level-Dependent MRI Cerebrovascular Reactivity in Cerebrovascular Disease: A Systematic Review and Meta-Analysis. *Cerebrovasc Dis*. 2016;42(3-4):288-307. doi:10.1159/000446081

147. Rodgers ZB, Detre JA, Wehrli FW. MRI-based methods for quantification of the cerebral metabolic rate of oxygen. *J Cereb Blood Flow Metab*. 2016;36(7):1165-1185. doi:10.1177/0271678X16643090

148. Sommer K, Amthor T, Doneva M, Koken P, Meineke J, Börnert P. Towards predicting the encoding capability of MR fingerprinting sequences. *Magn Reson Imaging*. 2017;41:7-14. doi:10.1016/j.mri.2017.06.015

149. Zhao B, Setsompop K, Adalsteinsson E, et al. Improved magnetic resonance fingerprinting reconstruction with low-rank and subspace modeling: A Subspace Approach to Improved MRF Reconstruction. *Magn Reson Med*. 2018;79(2):933-942. doi:10.1002/mrm.26701

150. Lima da Cruz G, Bustin A, Jaubert O, Schneider T, Botnar RM, Prieto C. Sparsity and locally low rank regularization for MR fingerprinting. *Magn Reson Med*. 2019;81(6):3530-3543. doi:10.1002/mrm.27665

151. Dikaios N, Protonotarios NE, Fokas AS, Kastis GA. Quantification of T1, T2 relaxation times from Magnetic Resonance Fingerprinting radially undersampled data using analytical transformations. *Magn Reson Imaging*. 2021;80:81-89. doi:10.1016/j.mri.2021.04.013

152. Su P, Mao D, Liu P, et al. Multiparametric estimation of brain hemodynamics with MR fingerprinting ASL. *Magn Reson Med*. 2017;78(5):1812-1823. doi:10.1002/mrm.26587

153. Wright KL, Jiang Y, Ma D, et al. Estimation of perfusion properties with MR Fingerprinting Arterial Spin Labeling. *Magn Reson Imaging*. 2018;50:68-77. doi:10.1016/j.mri.2018.03.011

154. Lahiri A, Fessler JA, Hernandez-Garcia L. Optimizing MRF-ASL scan design for precise quantification of brain hemodynamics using neural network regression. *Magn Reson Med*. 2020;83(6):1979-1991. doi:10.1002/mrm.28051

155. Fraum TJ, Ludwig DR, Bashir MR, Fowler KJ. Gadolinium-based contrast agents: A comprehensive risk assessment: Gadolinium Risk Assessment. *J Magn Reson Imaging*. 2017;46(2):338-353. doi:10.1002/jmri.25625

156. Ma D, Pierre EY, Jiang Y, et al. Music-based magnetic resonance fingerprinting to improve patient comfort during MRI examinations: MRF-Music. *Magn Reson Med*. 2016;75(6):2303-2314. doi:10.1002/mrm.25818

157. Rieger B, Akçakaya M, Pariente JC, et al. Time efficient whole-brain coverage with MR Fingerprinting using slice-interleaved echo-planar-imaging. *Sci Rep*. 2018;8(1):6667. doi:10.1038/s41598-018-24920-z

158. Su P, Fan H, Liu P, et al. MR fingerprinting ASL: Sequence characterization and comparison with dynamic susceptibility contrast (DSC) MRI. *NMR Biomed*. 2020;33(1). doi:10.1002/nbm.4202

159. Fan H, Su P, Huang J, Liu P, Lu H. Multi-band MR fingerprinting (MRF) ASL imaging using artificial-neural-network trained with high-fidelity experimental data. *Magn Reson Med*. 2021;85(4):1974-1985. doi:10.1002/mrm.28560

160. Li W, Wu B, Liu C. Quantitative susceptibility mapping of human brain reflects spatial variation in tissue composition. *NeuroImage*. 2011;55(4):1645-1656. doi:10.1016/j.neuroimage.2010.11.088

161. Wu B, Li W, Guidon A, Liu C. Whole brain susceptibility mapping using compressed sensing. *Magn Reson Med*. 2012;67(1):137-147. doi:10.1002/mrm.23000

162. Zhang Y, Brady M, Smith S. Segmentation of brain MR images through a hidden Markov random field model and the expectation-maximization algorithm. *IEEE Trans Med Imaging*. 2001;20(1):45-57. doi:10.1109/42.906424

163. Ciris PA, Qiu M, Constable RT. Noninvasive MRI measurement of the absolute cerebral blood volume-cerebral blood flow relationship during visual stimulation in healthy humans: Absolute CBV-CBF Relationship. *Magn Reson Med*. 2014;72(3):864-875. doi:10.1002/mrm.24984

164. Hua J, Liu P, Kim T, et al. MRI techniques to measure arterial and venous cerebral blood volume. *NeuroImage*. 2019;187:17-31. doi:10.1016/j.neuroimage.2018.02.027

165. Baas KPA, Vu C, Shen J, et al. Venous Blood Oxygenation Measurements Using TRUST and T2-TRIR MRI During Hypoxic and Hypercapnic Gas Challenges. *J Magn Reson Imaging*. Published online April 24, 2023:jmri.28744. doi:10.1002/jmri.28744

166. Coudert T, Delphin A, Warnking J, Lemasson B, Barbier EL, Christen T. Searching for an MR Fingerprinting sequence to measure brain oxygenation without contrast agent. Presented at: Proc. Intl. Soc. Mag. Reson. Med. 30; 2022. https://index.mirasmart.com/ISMRM2022/PDFfiles/2591.html

167. Taneja K, Liu P, Xu C, et al. Quantitative Cerebrovascular Reactivity in Normal Aging: Comparison Between Phase-Contrast and Arterial Spin Labeling MRI. *Front Neurol*. 2020;11:758. doi:10.3389/fneur.2020.00758

168. Richiardi J, Monsch AU, Haas T, et al. Altered cerebrovascular reactivity velocity in mild cognitive impairment and Alzheimer's disease. *Neurobiol Aging*. 2015;36(1):33-41. doi:10.1016/j.neurobiolaging.2014.07.020

169. Lu H, Liu P, Yezhuvath U, Cheng Y, Marshall O, Ge Y. MRI Mapping of Cerebrovascular Reactivity via Gas Inhalation Challenges. *J Vis Exp*. 2014;(94):52306. doi:10.3791/52306

170. Poublanc J, Crawley AP, Sobczyk O, et al. Measuring Cerebrovascular Reactivity: The Dynamic Response to a Step Hypercapnic Stimulus. *J Cereb Blood Flow Metab*. 2015;35(11):1746-1756. doi:10.1038/jcbfm.2015.114

171. Hou X, Liu P, Li Y, et al. The association between BOLD-based cerebrovascular reactivity (CVR) and end-tidal CO2 in healthy subjects. *NeuroImage*. 2020;207:116365. doi:10.1016/j.neuroimage.2019.116365

172. Hutchinson EB, Stefanovic B, Koretsky AP, Silva AC. Spatial flow-volume dissociation of the cerebral microcirculatory response to mild hypercapnia. *NeuroImage*. 2006;32(2):520-530. doi:10.1016/j.neuroimage.2006.03.033

173. Masamoto K, Vazquez A. Optical imaging and modulation of neurovascular responses. *J Cereb Blood Flow Metab*. 2018;38(12):2057-2072. doi:10.1177/0271678X18803372

174. Delphin A, Boux F, Brossard C, et al. Using 3D realistic blood vessel structures and machine learning for MR vascular Fingerprinting. Presented at: Proc. Intl. Soc. Mag. Reson. Med. 30; 2022. https://index.mirasmart.com/ISMRM2022/PDFfiles/2592.html

175. Zhang Q, Su P, Chen Z, et al. Deep learning–based MR fingerprinting ASL ReconStruction (DeepMARS). *Magn Reson Med*. 2020;84(2):1024-1034. doi:10.1002/mrm.28166

176. Boux F, Forbes F, Arbel J, Lemasson B, Barbier EL. Bayesian Inverse Regression for Vascular Magnetic Resonance Fingerprinting. *IEEE Trans Med Imaging*. 2021;40(7):1827-1837. doi:10.1109/TMI.2021.3066781

177. Cohen O, Zhu B, Rosen MS. MR fingerprinting Deep RecOnstruction NEtwork (DRONE). *Magn Reson Med*. 2018;80(3):885-894. doi:10.1002/mrm.27198

178. Bhogal AA, De Vis JB, Siero JCW, et al. The BOLD cerebrovascular reactivity response to progressive hypercapnia in young and elderly. *NeuroImage*. 2016;139:94-102. doi:10.1016/j.neuroimage.2016.06.010

179. McKetton L, Sobczyk O, Duffin J, et al. The aging brain and cerebrovascular reactivity. *NeuroImage*. 2018;181:132-141. doi:10.1016/j.neuroimage.2018.07.007

180. Fisher JA, Mikulis DJ. Cerebrovascular Reactivity: Purpose, Optimizing Methods, and Limitations to Interpretation – A Personal 20-Year Odyssey of (Re)searching. *Front Physiol*. 2021;12:629651. doi:10.3389/fphys.2021.629651

181. Pinto J, Bright MG, Bulte DP, Figueiredo P. Cerebrovascular Reactivity Mapping Without Gas Challenges: A Methodological Guide. *Front Physiol*. 2021;11:608475. doi:10.3389/fphys.2020.608475

182. Siero JCW, Hartkamp NS, Donahue MJ, et al. Neuronal activation induced BOLD and CBF responses upon acetazolamide administration in patients with steno-occlusive artery disease. *NeuroImage*. 2015;105:276-285. doi:10.1016/j.neuroimage.2014.09.033

183. Alsop DC, Detre JA, Golay X, et al. Recommended implementation of arterial spin-labeled perfusion MRI for clinical applications: A consensus of the ISMRM perfusion study group and the European consortium for ASL in dementia. *Magn Reson Med*. 2015;73(1):102-116. doi:10.1002/mrm.25197

184. Chappell MA, Groves AR, Whitcher B, Woolrich MW. Variational Bayesian Inference for a Nonlinear Forward Model. *IEEE Trans Signal Process*. 2009;57(1):223-236. doi:10.1109/TSP.2008.2005752

185. Liu P, Liu G, Pinho MC, et al. Cerebrovascular Reactivity Mapping Using Resting-State BOLD Functional MRI in Healthy Adults and Patients with Moyamoya Disease. *Radiology*. 2021;299(2):419-425. doi:10.1148/radiol.2021203568

186. Liu P, Li Y, Pinho M, Park DC, Welch BG, Lu H. Cerebrovascular reactivity mapping without gas challenges. *NeuroImage*. 2017;146:320-326. doi:10.1016/j.neuroimage.2016.11.054

187. Sobczyk O, Sayin ES, Sam K, et al. The Reproducibility of Cerebrovascular Reactivity Across MRI Scanners. *Front Physiol*. 2021;12:668662. doi:10.3389/fphys.2021.668662

188. Sobczyk O. *Standardization of a Cerebrovascular Stress Test Using Carbon Dioxide and BOLD-MRI for Clinical Application*. University of Toronto; 2018.

189. Liu P, Baker Z, Li Y, et al. CVR-MRICloud: An online processing tool for CO2-inhalation and resting-state cerebrovascular reactivity (CVR) MRI data. Shih YYI, ed. *PLOS ONE*. 2022;17(9):e0274220. doi:10.1371/journal.pone.0274220

190. Sleight E, Stringer MS, Mitchell I, et al. Cerebrovascular reactivity measurements using 3T BOLD MRI and a fixed inhaled CO2 gas challenge: Repeatability and impact of processing strategy. *Front Physiol*. 2023;14:1070233. doi:10.3389/fphys.2023.1070233

191. Sobczyk O, Battisti-Charbonney A, Fierstra J, et al. A conceptual model for CO2-induced redistribution of cerebral blood flow with experimental confirmation using BOLD MRI. *NeuroImage*. 2014;92:56-68. doi:10.1016/j.neuroimage.2014.01.051

192. Haller S, Zaharchuk G, Thomas DL, Lovblad KO, Barkhof F, Golay X. Arterial Spin Labeling Perfusion of the Brain: Emerging Clinical Applications. *Radiology*. 2016;281(2):337-356. doi:10.1148/radiol.2016150789

193. Ito H, Kanno I, Ibaraki M, Hatazawa J, Miura S. Changes in Human Cerebral Blood Flow and Cerebral Blood Volume during Hypercapnia and Hypocapnia Measured by Positron Emission Tomography. *J Cereb Blood Flow Metab*. 2003;23(6):665-670. doi:10.1097/01.WCB.0000067721.64998.F5

194. Yao J (Fiona), Yang HC (Shawn), Wang JH, et al. A novel method of quantifying hemodynamic delays to improve hemodynamic response, and CVR estimates in CO2 challenge fMRI. *J Cereb Blood Flow Metab*. 2021;41(8):1886-1898. doi:10.1177/0271678X20978582

195. Poublanc J, Shafi R, Sobczyk O, et al. Normal BOLD Response to a Step CO2 Stimulus After Correction for Partial Volume Averaging. *Front Physiol*. 2021;12:639360. doi:10.3389/fphys.2021.639360

196. Duffin J, Sobczyk O, Crawley AP, Poublanc J, Mikulis DJ, Fisher JA. The dynamics of cerebrovascular reactivity shown with transfer function analysis. *NeuroImage*. 2015;114:207-216. doi:10.1016/j.neuroimage.2015.04.029

197. Holmes KR, Tang-Wai D, Sam K, et al. Slowed Temporal and Parietal Cerebrovascular Response in Patients with Alzheimer's Disease. *Can J Neurol Sci J Can Sci Neurol*. 2020;47(3):366-373. doi:10.1017/cjn.2020.30

198. Hamilton JI, Seiberlich N. Machine Learning for Rapid Magnetic Resonance Fingerprinting Tissue Property Quantification. *Proc IEEE*. 2020;108(1):69-85. doi:10.1109/JPROC.2019.2936998

199. Chen Y, Fang Z, Hung SC, Chang WT, Shen D, Lin W. High-resolution 3D MR Fingerprinting using parallel imaging and deep learning. *NeuroImage*. 2020;206:116329. doi:10.1016/j.neuroimage.2019.116329

200. Cao P, Cui D, Vardhanabhuti V, Hui ES. Development of fast deep learning quantification for magnetic resonance fingerprinting in vivo. *Magn Reson Imaging*. 2020;70:81-90. doi:10.1016/j.mri.2020.03.009

201. Cao P, Cui D, Ming Y, Vardhanabhuti V, Lee E, Hui E. Accelerating Magnetic Resonance Fingerprinting Using Hybrid Deep Learning and Iterative Reconstruction. *Investig Magn Reson Imaging*. 2021;25(4):293. doi:10.13104/imri.2021.25.4.293

202. Velasco C, Fletcher TJ, Botnar RM, Prieto C. Artificial intelligence in cardiac magnetic resonance fingerprinting. *Front Cardiovasc Med*. 2022;9:1009131. doi:10.3389/fcvm.2022.1009131

203. Oksuz I, Cruz G, Clough J, et al. Magnetic Resonance Fingerprinting Using Recurrent Neural Networks. In: *2019 IEEE 16th International Symposium on Biomedical Imaging (ISBI 2019)*. IEEE; 2019:1537-1540. doi:10.1109/ISBI.2019.8759502

204. Hoppe E, Thamm F, K&#246, et al. Magnetic Resonance Fingerprinting Reconstruction Using Recurrent Neural Networks. In: *German Medical Data Sciences: Shaping Change – Creative Solutions for Innovative Medicine*. IOS Press; 2019:126-133. doi:10.3233/SHTI190816

205. Cao X, Liao C, Zhou Z, et al. DTI-MR fingerprinting for rapid high-resolution whole-brain $T_1$, $T_2$, proton density, ADC, and fractional anisotropy mapping. *Magn Reson Med*. 2024;91(3):987-1001. doi:10.1002/mrm.29916

206. Schauman S, Iyer S, Yurt M, et al. Toward a 1-minute high-resolution brain exam - MR Fingerprinting with fast reconstruction and ML-synthesized contrasts. In: ; :0053. doi:10.58530/2022/0053

207. Campbell-Washburn AE, Jiang Y, Körzdörfer G, Nittka M, Griswold MA. Feasibility of MR fingerprinting using a high-performance 0.55 T MRI system. *Magn Reson Imaging*. 2021;81:88-93. doi:10.1016/j.mri.2021.06.002

208. Mickevicius NJ, Glide-Hurst CK. LOW-RANK inversion reconstruction for THROUGH-PLANE accelerated radial MR fingerprinting applied to relaxometry at 0. 35 T. *Magn Reson Med*. 2022;88(2):840-848. doi:10.1002/mrm.29244

209. Xuan L, Zhang Y, Wu J, He Y, Xu Z. Quantitative brain mapping using magnetic resonance fingerprinting on a 50-mT portable MRI scanner. *NMR Biomed*. Published online December 6, 2023:e5077. doi:10.1002/nbm.5077

210. O'Reilly T, Börnert P, Liu H, Webb A, Koolstra K. 3D magnetic resonance fingerprinting on a low-field 50 mT point-of-care system prototype: evaluation of muscle and lipid relaxation time mapping and comparison with standard techniques. *Magn Reson Mater Phys Biol Med*. 2023;36(3):499-512. doi:10.1007/s10334-023-01092-0

# Appendix

## A | Publications Related to Dissertation

*Peer-reviewed journal articles*

1. **Wheeler G**, Lee Q, Fan A. *Dynamic Magnetic Resonance Vascular Fingerprinting During Hypercapnia for Quantitative and Multiparametric Cerebrovascular Reactivity Measures*. IEEE Engineering in Medicine and Biology Society (EMBC); December 2023. DOI: 10.1109/EMBC40787.2023.1033996

*Journal articles in review or preparation for submission*

1. **Wheeler G**, Le L, Lee Q, Bilgic B, Delphin A, Christen T, Manhard MK, Fan A. *Development, Optimization, and Application of Dynamic, Contrast-free Magnetic Resonance Vascular Fingerprinting*. In preparation.
2. **Wheeler G**, Lee Q, Lin C, Linh L, Korte J, Fan A. M*agnetic Resonance Vascular Fingerprinting Measures of Cerebral Vascular Reactivity with Aging*. In preparation.

*Conference abstracts*

1. **Wheeler G**, Lee Q, Fan A. *Dynamic Magnetic Resonance Vascular Fingerprinting During Hypercapnia for Quantitative and Multiparametric Cerebrovascular Reactivity Measures*. Presented at IEEE Engineering in Medicine and Biology Conference (EMBC); July 26, 2023; Sydney, Australia.
2. **Wheeler G**, Le L, Lee Q, Fan A. *Optimizing an Accelerated Spin- and Gradient-Echo Sequence for Dynamic MR Vascular Fingerprinting*. Presented at International Society for Magnetic Resonance in Medicine (ISMRM) Annual Meeting; June 6, 2023; Toronto, Canada.
3. **Wheeler G**, Lee Q, Manhard MK, Bilgic B, Fan A. *Feasibility of Dynamic Contrast-free Vascular Magnetic Resonance Fingerprinting*. Presented at International Society for Magnetic Resonance in Medicine (ISMRM) Annual Meeting; May 12, 2022; London, United Kingdom.
4. **Wheeler G**, Fan A. *Noise Considerations for Accelerated MR Vascular Fingerprinting*. Presented at International Society for Magnetic Resonance in Medicine (ISMRM) Annual Meeting; May 7, 2021; Virtual conference.

*Peer-reviewed journal article contributions*

1. Lee Q, Chen J, **Wheeler G**, Fan A. *Characterizing systemic physiological effects on the blood oxygen level dependent signal of resting-state fMRI in time-frequency space using wavelets*. Human Brain Mapping. November 2023. DOI: 10.1002/hbm.26533
2. Le L, **Wheeler G**, Holy E, Donnay C, Blockley N, Yee A, Ng K, Fan, A. *Cortical oxygen extraction fraction using quantitative BOLD MRI and cerebral blood flow during vasodilation*. Frontiers in Physiology. October 2023. DOI: 10.3389/fphys.2023.1231793A.

*Conference abstract contributions*

1. Hsu C, Lee Q, **Wheeler G**, Fan A. *White Matter Hyperintensity Burden is Related to White Matter Cerebrovascular Reactivity in Aging*. Accepted to Organization for Human Brain Mapping (OHBM) Annual Meeting; June 2024; Seoul, South Korea.

2. Lin C, **Wheeler G**, Fan A. *MR Vascular Fingerprinting with Deep Learning to Estimate Brain Physiological Parameters*. Accepted to International Society for Magnetic Resonance in Medicine (ISMRM) Annual Meeting; May 2024; Singapore.
3. Hsu C, Lee Q, **Wheeler G**, Fan A. *Evaluating the Relationship between White Matter Hyperintensities and Cerebrovascular Reactivity in White Matter Regions of Elderly Participants*. Poster presented at Biomedical Engineering Society (BMES) Annual Meeting; October 14, 2023; Seattle, WA.
4. Le L, **Wheeler G**, Blockley N, Fan A. *Quantitative BOLD with Variational Bayesian inference: model comparisons with Monte Carlo simulations and in an elderly cohort*. Presented at International Society for Magnetic Resonance in Medicine (ISMRM) Annual Meeting; June 6, 2023; Toronto, Canada.
5. Le L, **Wheeler G**, Fletcher E, Blockley N, Fan A. *Assessment of Oxygen Extraction Fraction mapping between normal cognition and mild cognitive impairment in an elderly cohort using quantitative BOLD*. Presented at International Society for Magnetic Resonance in Medicine (ISMRM) Annual Meeting; June 6, 2023; Toronto, Canada.
6. Tavakoli A, Le L, **Wheeler G**, Fan A. *Measuring Brain Hemodynamics with Quantitative BOLD imaging: Accuracy and Mean Squared Error*. Poster presented at Biomedical Engineering Society (BMES) Annual Meeting; October 15, 2022; San Antonio, TX.
7. Lee Q, Chen J, **Wheeler G**, Fan A. *Characterizing systemic physiological effects on rsfMRI signals in time and frequency using wavelets*. Presented at Organization for Human Brain Mapping (OHBM) Annual Meeting; June 20, 2022; Glasgow, United Kingdom.
8. Le L, **Wheeler G**, Christen T, Zaharchuk G, Fan A. *Comparison of Quantitative BOLD and Vascular MRF for Mapping Brain Oxygenation*. Presented at International Society for Magnetic Resonance in Medicine (ISMRM) Annual Meeting; May 12, 2022; London, United Kingdom.
9. Le L, **Wheeler G**, Momjian A, Donnay C, Blockley N, Fan A. *Oxygen Extraction Fraction Using Quantitative BOLD and Cerebral Blood Flow During Vasodilation*. Presented at International Society for Magnetic Resonance in Medicine (ISMRM) Annual Meeting; May 12, 2022; London, United Kingdom.
10. Lee Q, Chen J, **Wheeler G**, Fan A. *Characterizing spectral and temporal effects of heart rate variability on resting-state BOLD signals using wavelet transform coherence*. Presented at International Society for Magnetic Resonance in Medicine (ISMRM) Annual Meeting; May 9, 2022; London, United Kingdom.
11. Zhong D, Kim M, **Wheeler G**, Fan A. *Reproducibility of R2' Measurement for Oxygen Saturation in the Human Brain*. Poster presented at Biomedical Engineering Society (BMES) Annual Meeting; October 17, 2020; Virtual conference.

## B | Supplementary Figures

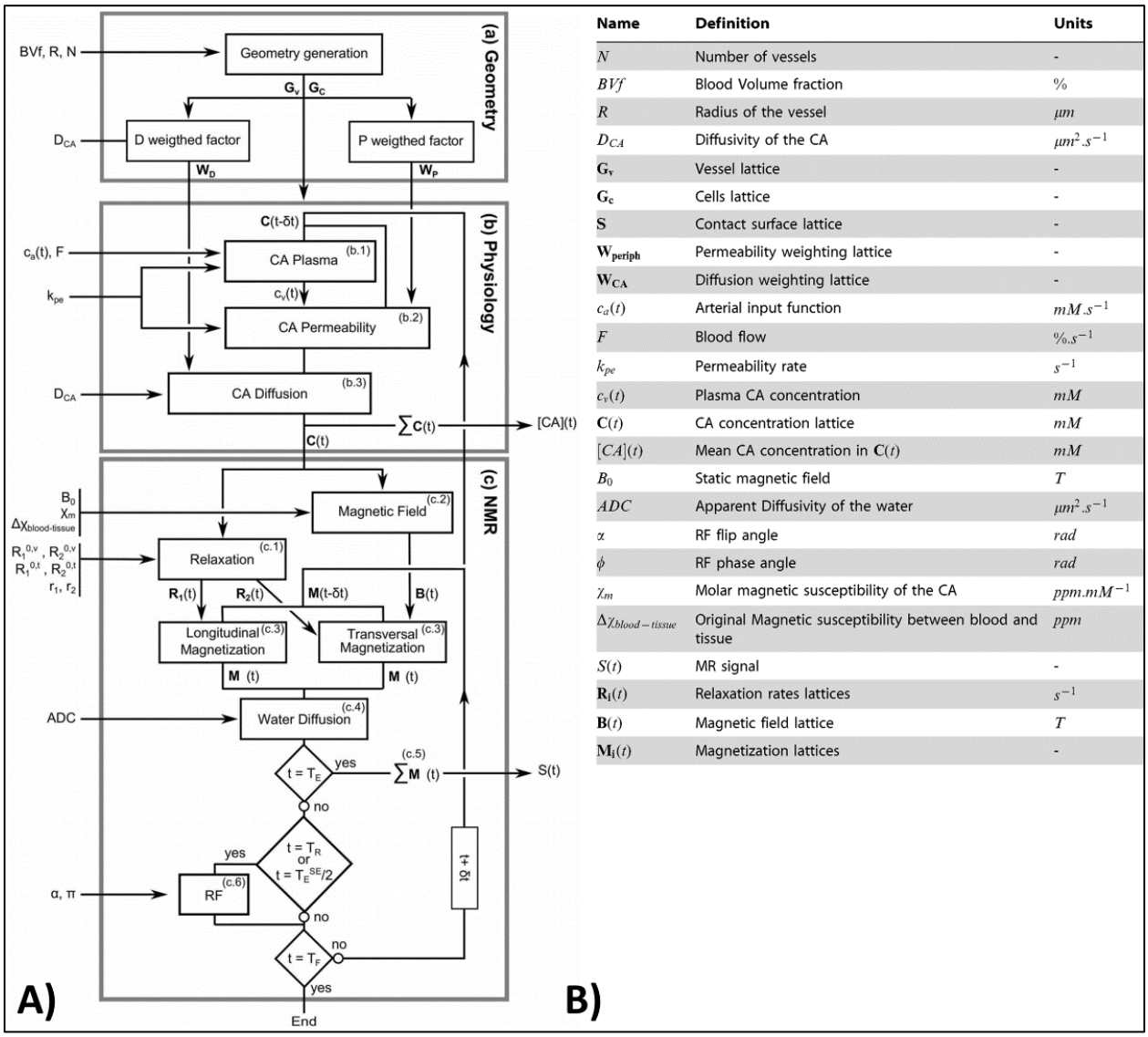


| Name | Definition | Units |
|---|---|---|
| $N$ | Number of vessels | - |
| $BVf$ | Blood Volume fraction | % |
| $R$ | Radius of the vessel | $\mu m$ |
| $D_{CA}$ | Diffusivity of the CA | $\mu m^2.s^{-1}$ |
| $\mathbf{G_v}$ | Vessel lattice | - |
| $\mathbf{G_c}$ | Cells lattice | - |
| $\mathbf{S}$ | Contact surface lattice | - |
| $\mathbf{W_{periph}}$ | Permeability weighting lattice | - |
| $\mathbf{W_{CA}}$ | Diffusion weighting lattice | - |
| $c_a(t)$ | Arterial input function | $mM.s^{-1}$ |
| $F$ | Blood flow | $\%.s^{-1}$ |
| $k_{pe}$ | Permeability rate | $s^{-1}$ |
| $c_v(t)$ | Plasma CA concentration | $mM$ |
| $\mathbf{C}(t)$ | CA concentration lattice | $mM$ |
| $[CA](t)$ | Mean CA concentration in $\mathbf{C}(t)$ | $mM$ |
| $B_0$ | Static magnetic field | $T$ |
| $ADC$ | Apparent Diffusivity of the water | $\mu m^2.s^{-1}$ |
| $\alpha$ | RF flip angle | $rad$ |
| $\phi$ | RF phase angle | $rad$ |
| $\chi_m$ | Molar magnetic susceptibility of the CA | $ppm.mM^{-1}$ |
| $\Delta\chi_{blood-tissue}$ | Original Magnetic susceptibility between blood and tissue | $ppm$ |
| $S(t)$ | MR signal | - |
| $\mathbf{R_i}(t)$ | Relaxation rates lattices | $s^{-1}$ |
| $\mathbf{B}(t)$ | Magnetic field lattice | $T$ |
| $\mathbf{M_i}(t)$ | Magnetization lattices | - |

**Figure A3.1. MRVox Algorithm, Inputs, and Outputs** (from Pannetier et al.[110]) **A)** Variables on the left of the boxes are inputs to the model that can be modified. Data on the right are outputs after the simulation. The simulation is organized in three blocks. Block (a) initializes the geometry, block (b) describes the contrast agent (CA) behavior over time, and block (c) estimates the MR signal. **B)** List of main parameters used in the algorithm with definitions of acronyms.

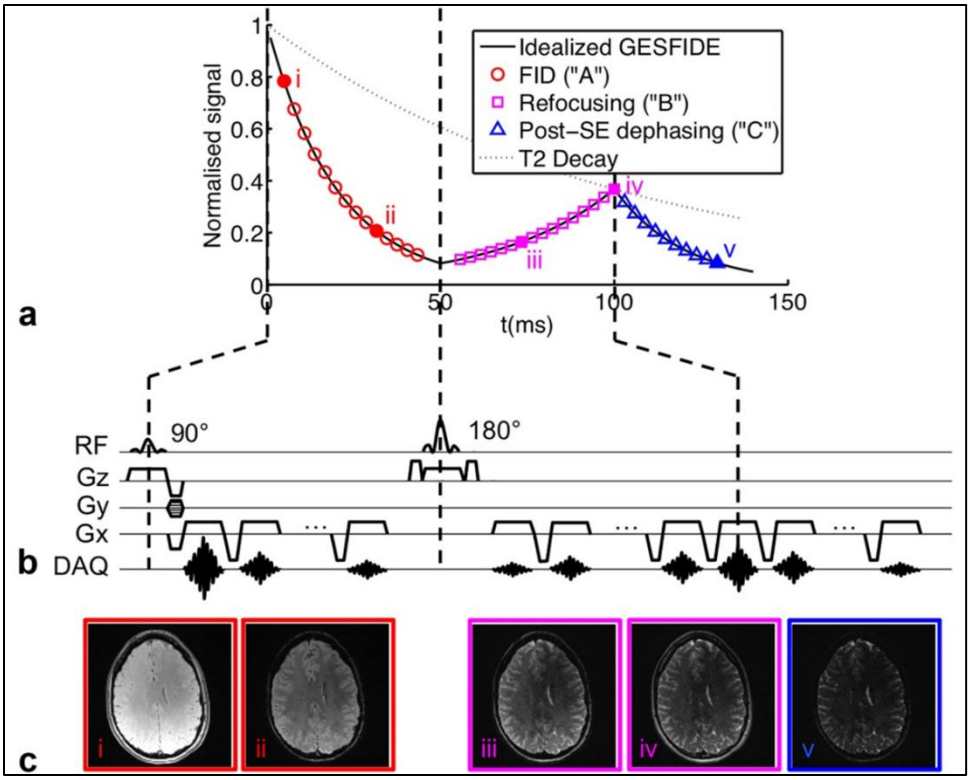


**Figure A3.2. The GESFIDE Sequence** (from Ni et al.[116]) **A)** Schematic of the GESFIDE sequence showing echo sampling in the free-induction decay (FID), refocusing, and post spin echo (SE) dephasing signal regimes. **B)** The pulse sequence diagram illustrating the acquisition of multiple echoes. **C)** Representative images of the same slice corresponding to different echo times in the signal.

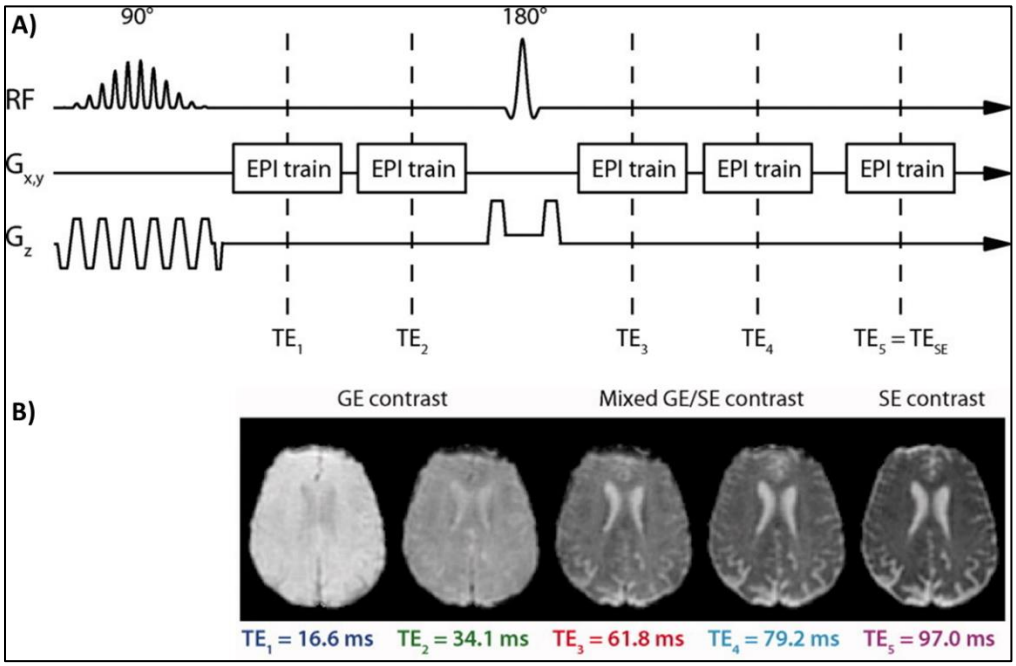


**Figure A3.3. The SAGE Sequence** (from Schmiedeskamp et al.[117]). **A)** Schematic of the SAGE sequence showing echo planar imaging (EPI) acquisition of two gradient echoes, a 180° refocusing pulse, and three more EPI readouts. **B)** Representative images of the same slice corresponding to each echo time acquired with the sequence.

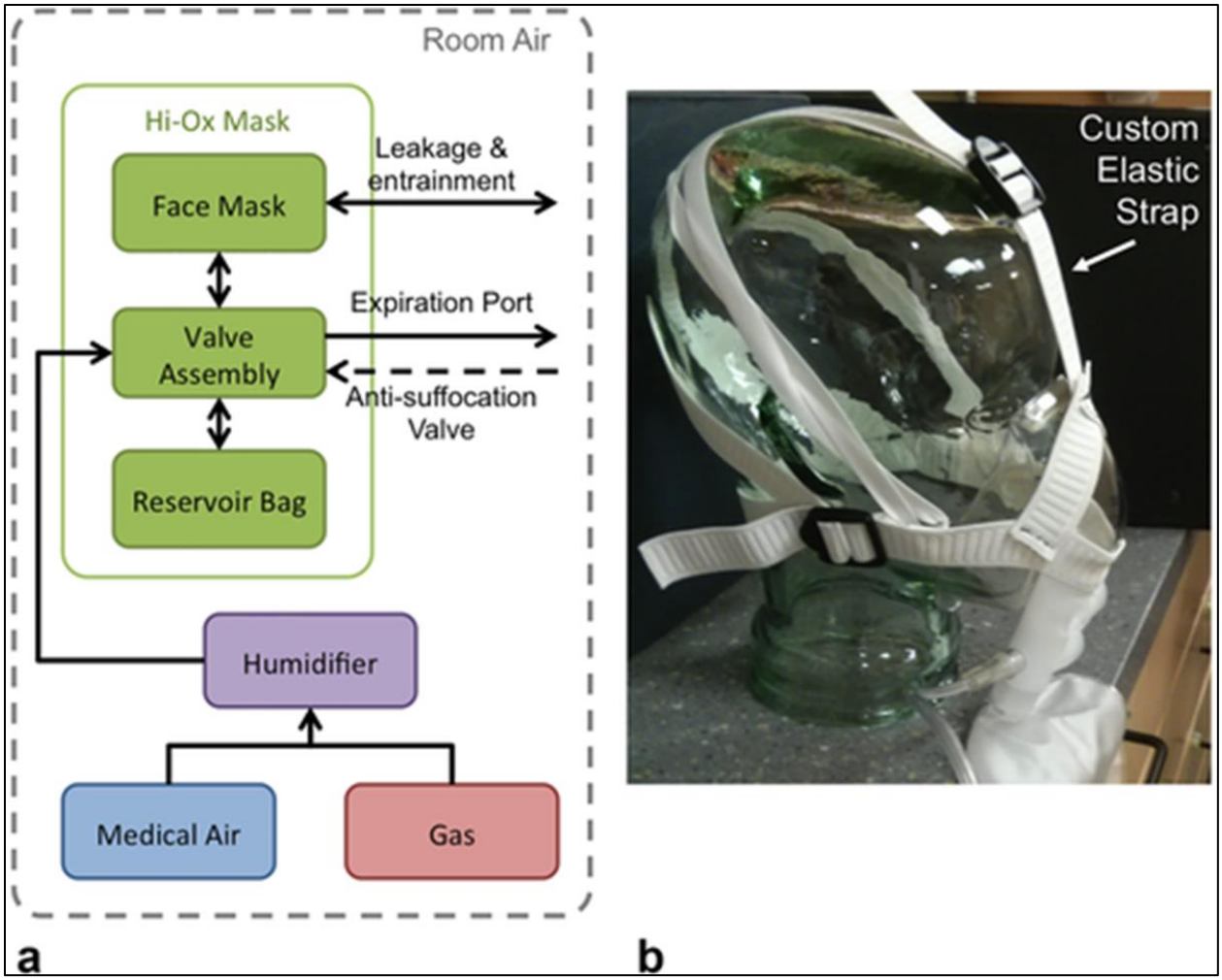


**Figure A4.1. Breathing Apparatus Used During Hypoxia and Hyperoxia Study** (from Ni et al.[116]) **A)** Schematic of gas inhalation set up with a Certec Hi-Ox mask (green box) and arrows indicating direction of airflow. **B)** Photo of the set up on a mannequin head showing straps that keep the facemask seal tight.

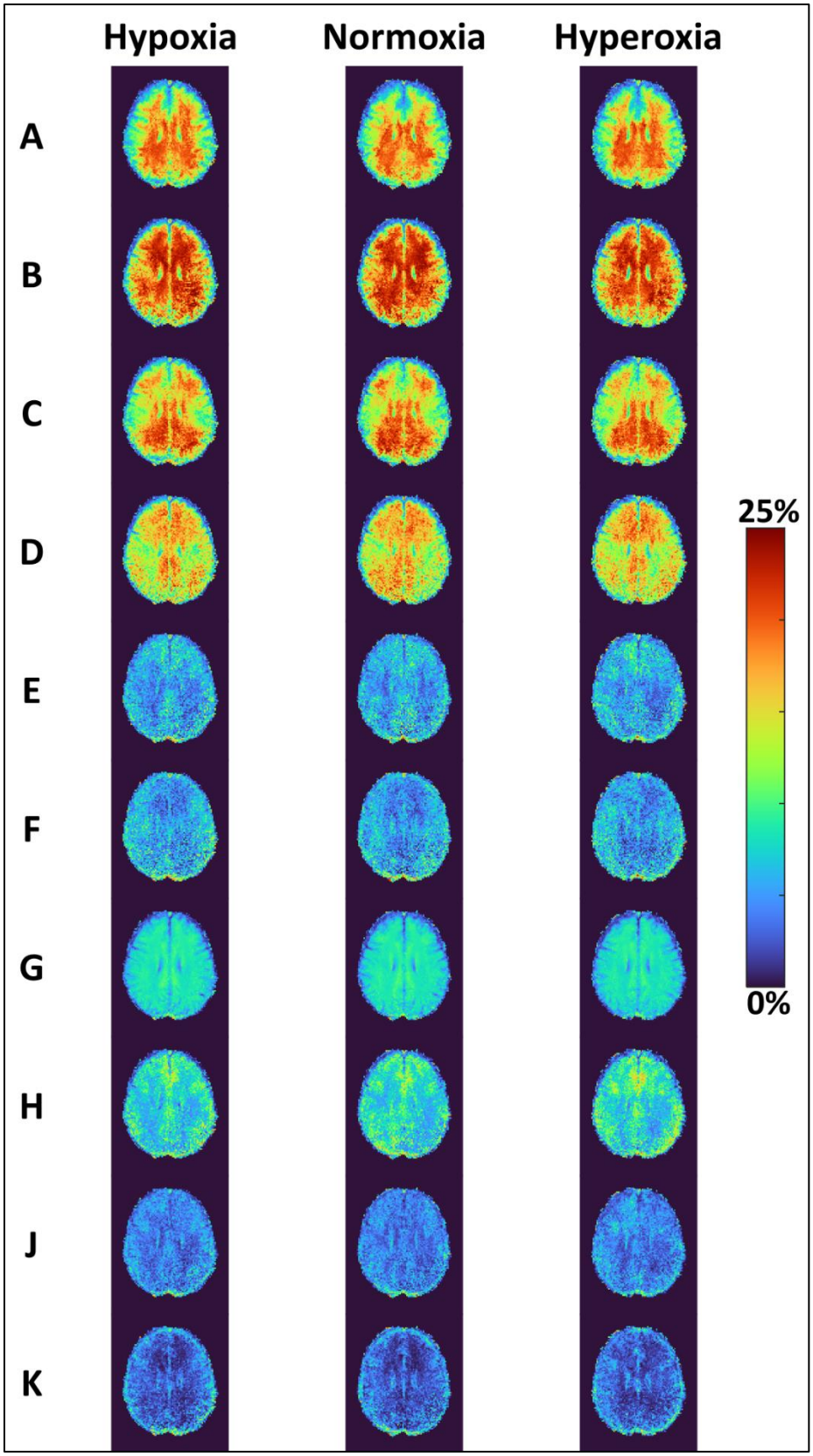


**Figure A4.2. Average CBV Maps with Different Methods Across Oxygen Conditions**. Group average CBV maps generated with each of the 10 methods from Table A4.1 for each gas inhalation condition.

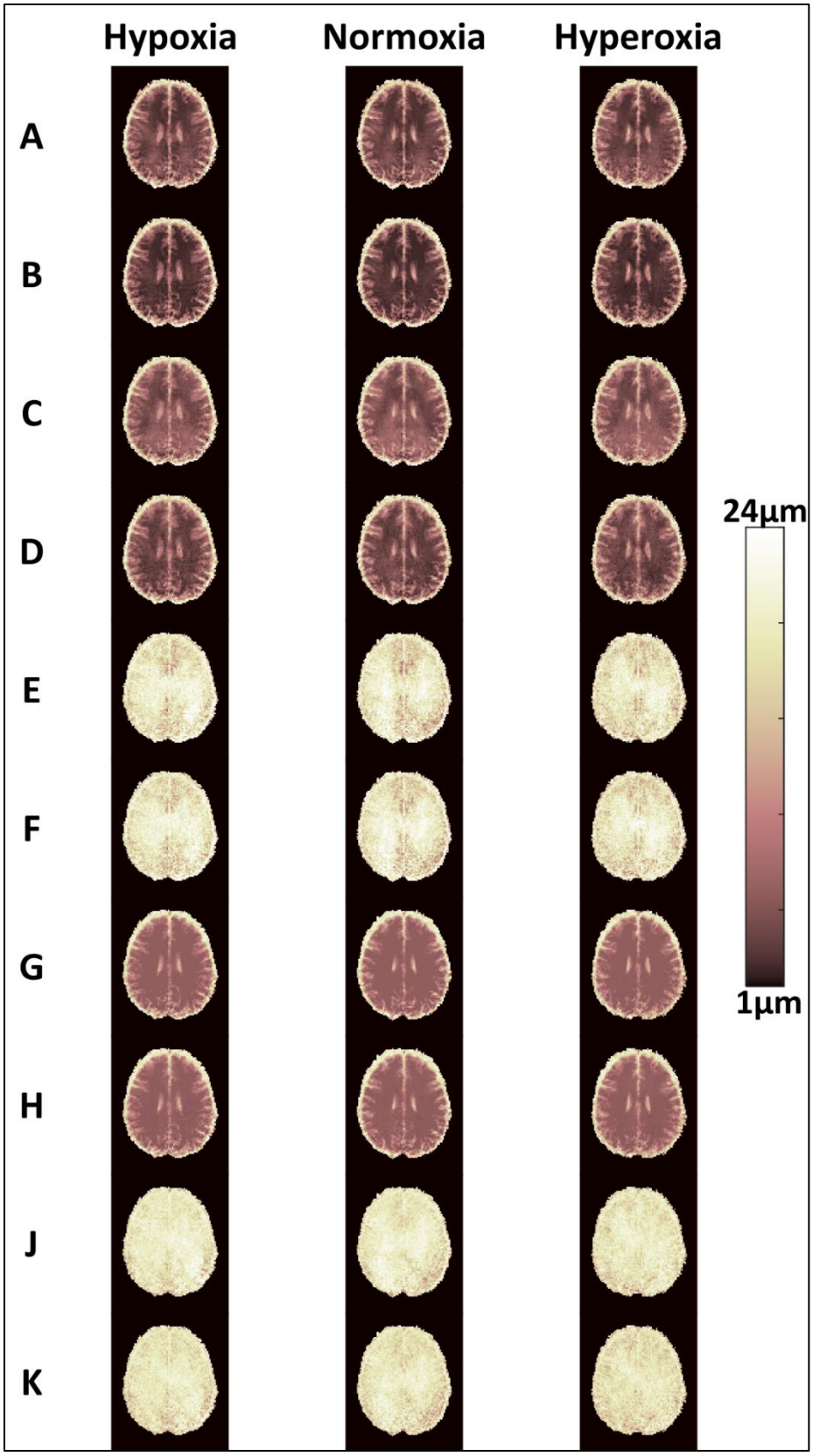


**Figure A4.3. Average Radius Maps with Different Methods Across Oxygen Conditions**. Group average radius maps generated with each of the 10 methods from Table A4.1 for each gas inhalation condition.

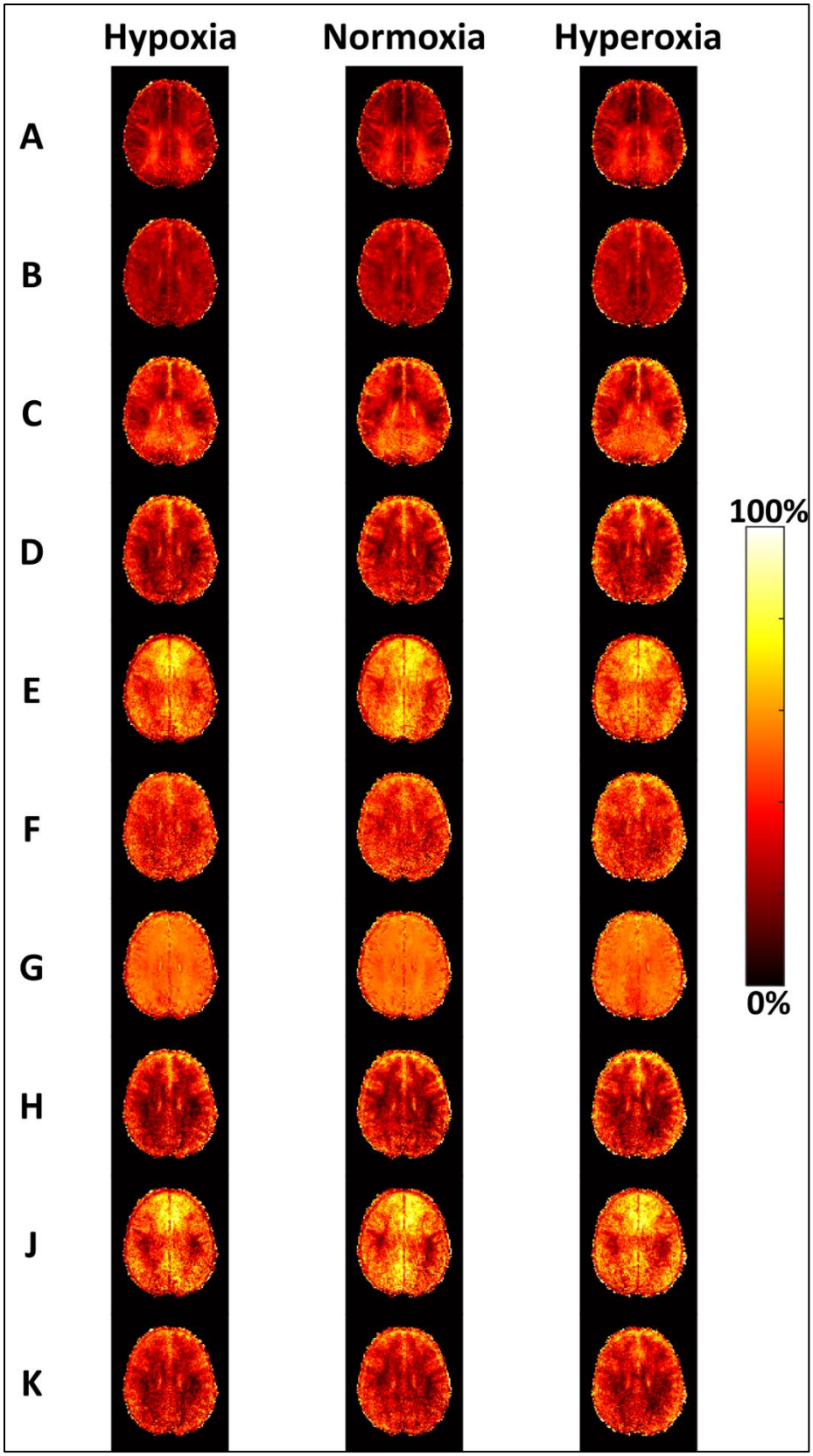


**Figure A4.4. Average $SO_2$ Maps with Different Methods Across Oxygen Conditions**. Group average $SO_2$ maps generated with each of the 10 methods from Table A4.1 for each gas inhalation condition.

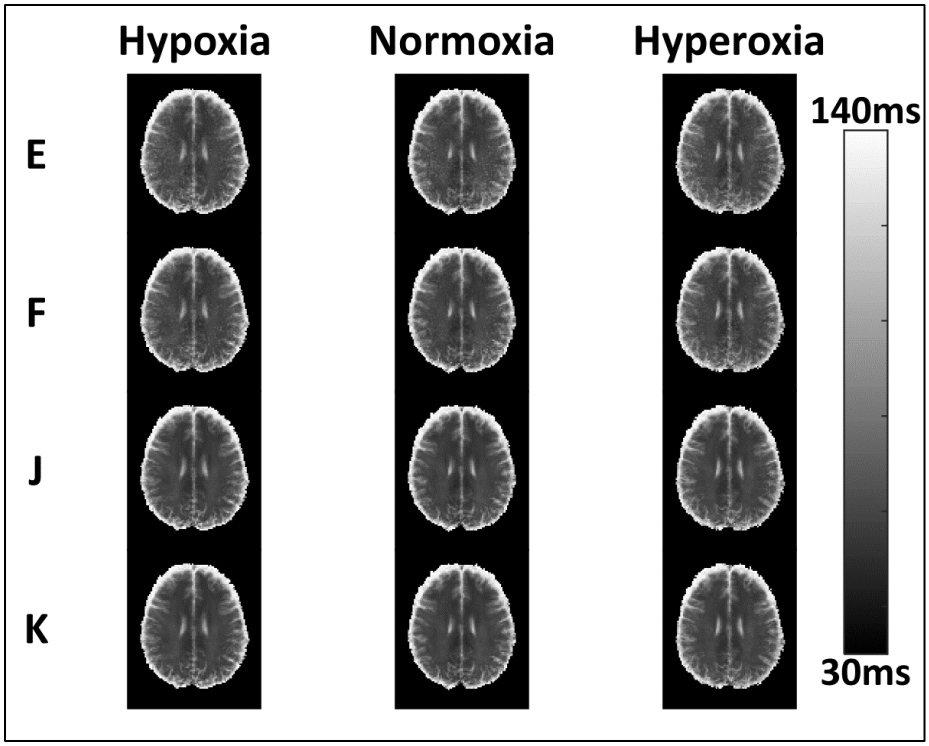


**Figure A4.5. Average $T_2$ Maps with Different Methods Across Oxygen Conditions**. Group average $T_2$ maps generated with each of the four methods from Table A4.1 that use $T_2$ for each gas inhalation condition.

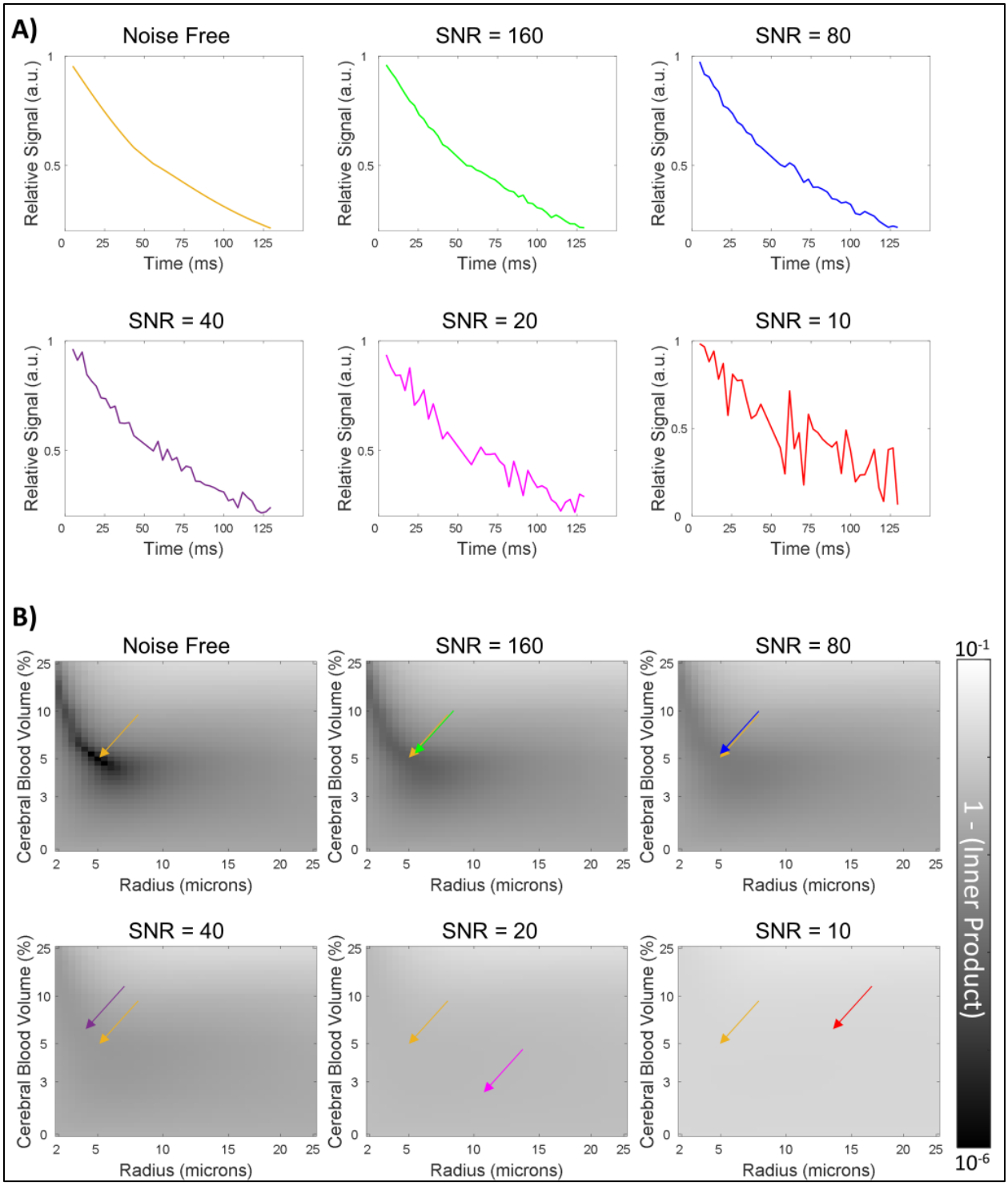


**Figure A5.1. Signal-to-noise Ratio GESFIDE Sensitivity Simulations**. **A)** The noise-free signal evolution of a GESFIDE sequence simulation with 5% CBV, 5 µm R, and 65% $SO_2$ (orange), as well as the same parameter combination with added Gaussian noise at signal-to-noise ratios (SNR) of 160 (green), 80 (blue), 40 (purple), 20 (pink), and 10 (red). **B)** The sensitivity plots obtained by matching each dictionary entry to the example noise-free and noisy signals, repeated 100 times, and averaged. The plots show where $SO_2$ = 65% with all combinations of CBV and radius. The orange arrows indicate the true parameters underlying the signal and each colored arrow shows the predicted parameters from the corresponding noisy signal in **A**.

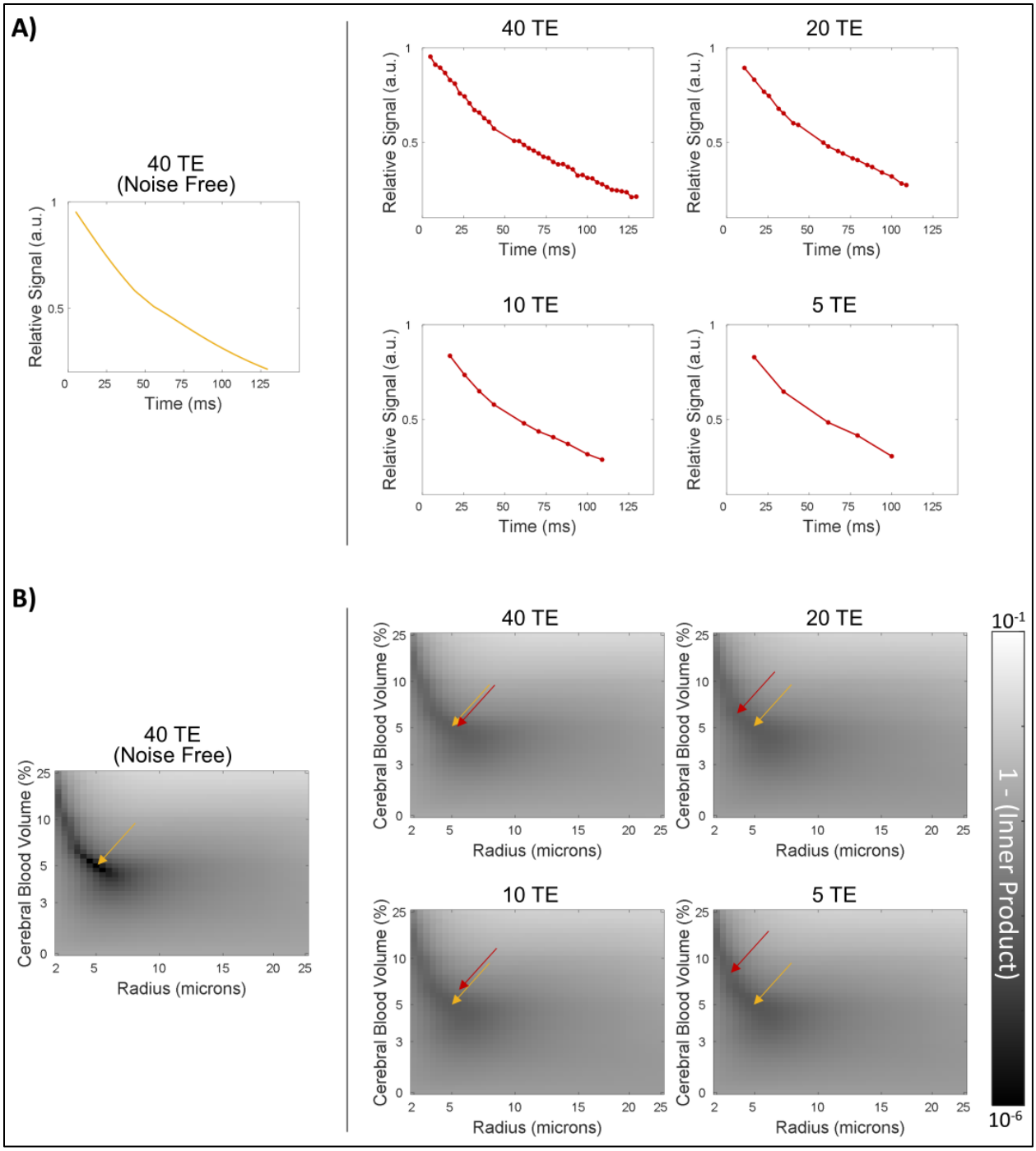


**Figure A5.2. Echo Train Length Sensitivity Simulations**. **A)** The noise-free signal evolution of a single GESFIDE sequence simulation with 5% CBV, 5 µm R, and 65% $SO_2$ and the same parameter combination with added Gaussian noise at a signal-to-noise ratio (SNR) of 160 with 40, 20, 10, or 5 subsampled echo times (TE). Each red dot represents where the noisy signal was subsampled. **B)** Sensitivity plots of the inner product values obtained by matching all dictionary entries to the example signal (5% CBV, 5 µm R, and 65% $SO_2$) with the various number of echoes, repeated 100 times and averaged. The plots show where $SO_2$ = 65% with all combinations of CBV and radius. The orange arrows indicate the true parameters of the signal, and the red arrows show the predicted parameters from the corresponding noisy signal in **A**.

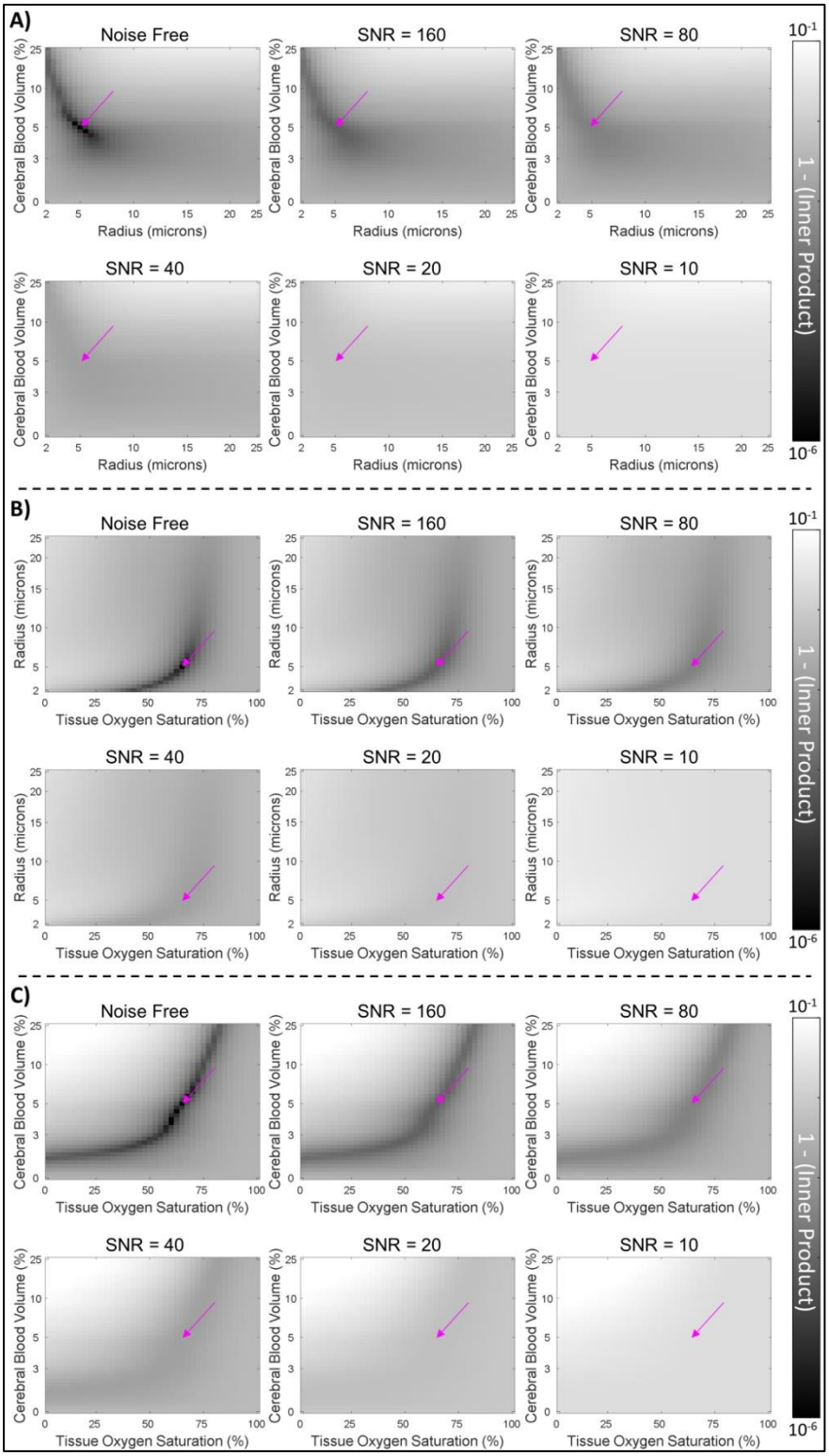


**Figure A5.3. Signal-to-noise Ratio SAGE Sensitivity Simulations**. Average sensitivity plots obtained by matching a simulated noise-free and simulated noisy signals with known underlying parameters (5% CBV, 5 µm R, and 65% $SO_2$) to every signal in the dictionary and repeated 100 times. **A)** Plots where $SO_2$ = 65% with all combinations of CBV and R. **B)** Plots where CBV = 5% with all combinations of R and $SO_2$. **C)** Plots where R = 5 µm with all combinations of CBV and $SO_2$. The pink arrows indicate the true parameters underlying the signal. Parameter combinations in the dictionary that match the noisy signal better (higher inner product) are signified by darker regions in the plot.

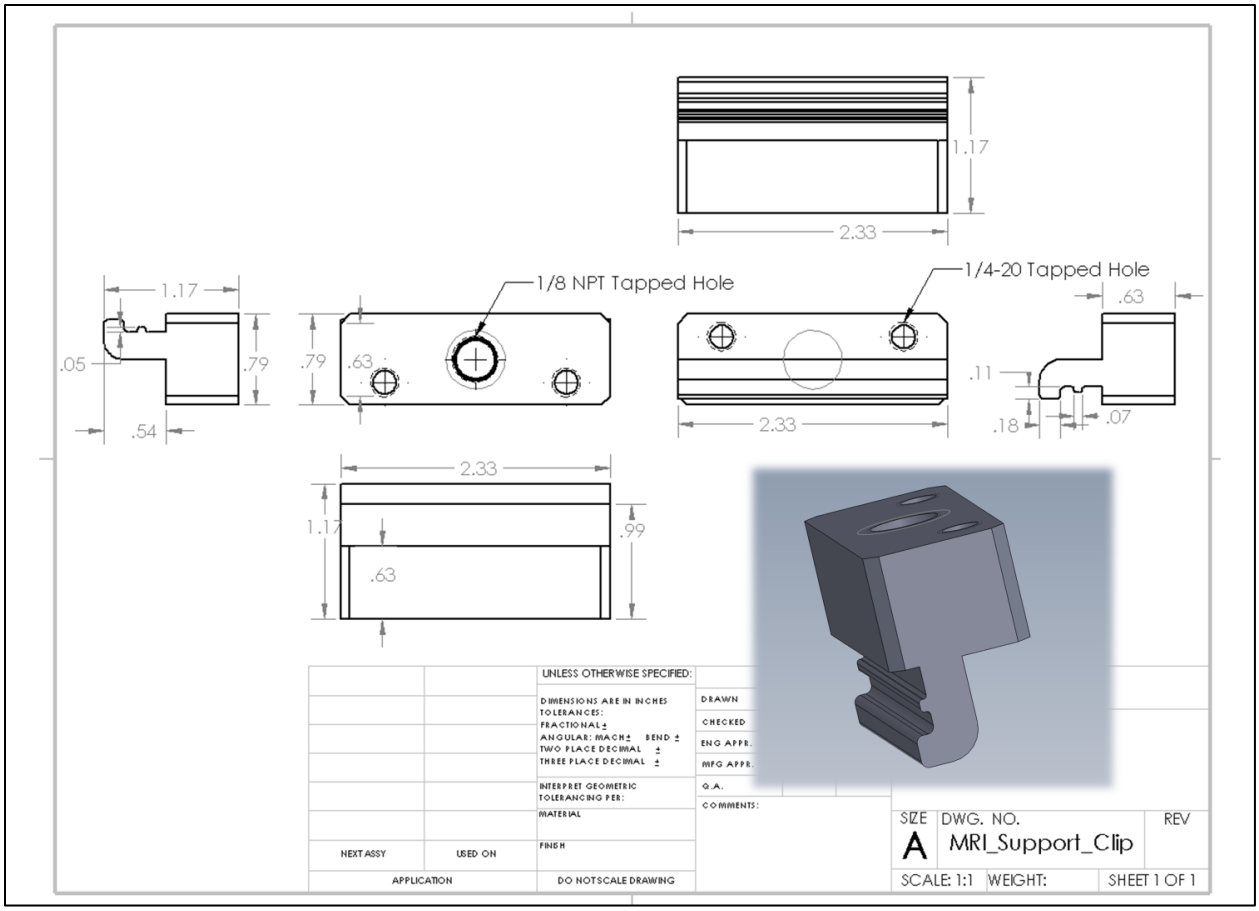


**Figure A6.1. Mounting Clip for Breathing Apparatus**. Dimensions and virtual model of custom designed and 3D printed clip to mount the support arm to the rail of the MRI scanner. This support connects via plastic bracket and plastic screws to the two-way non-rebreathing valve (#3) in Figure 6.1 and ensures the breathing apparatus remains in place throughout each scan.

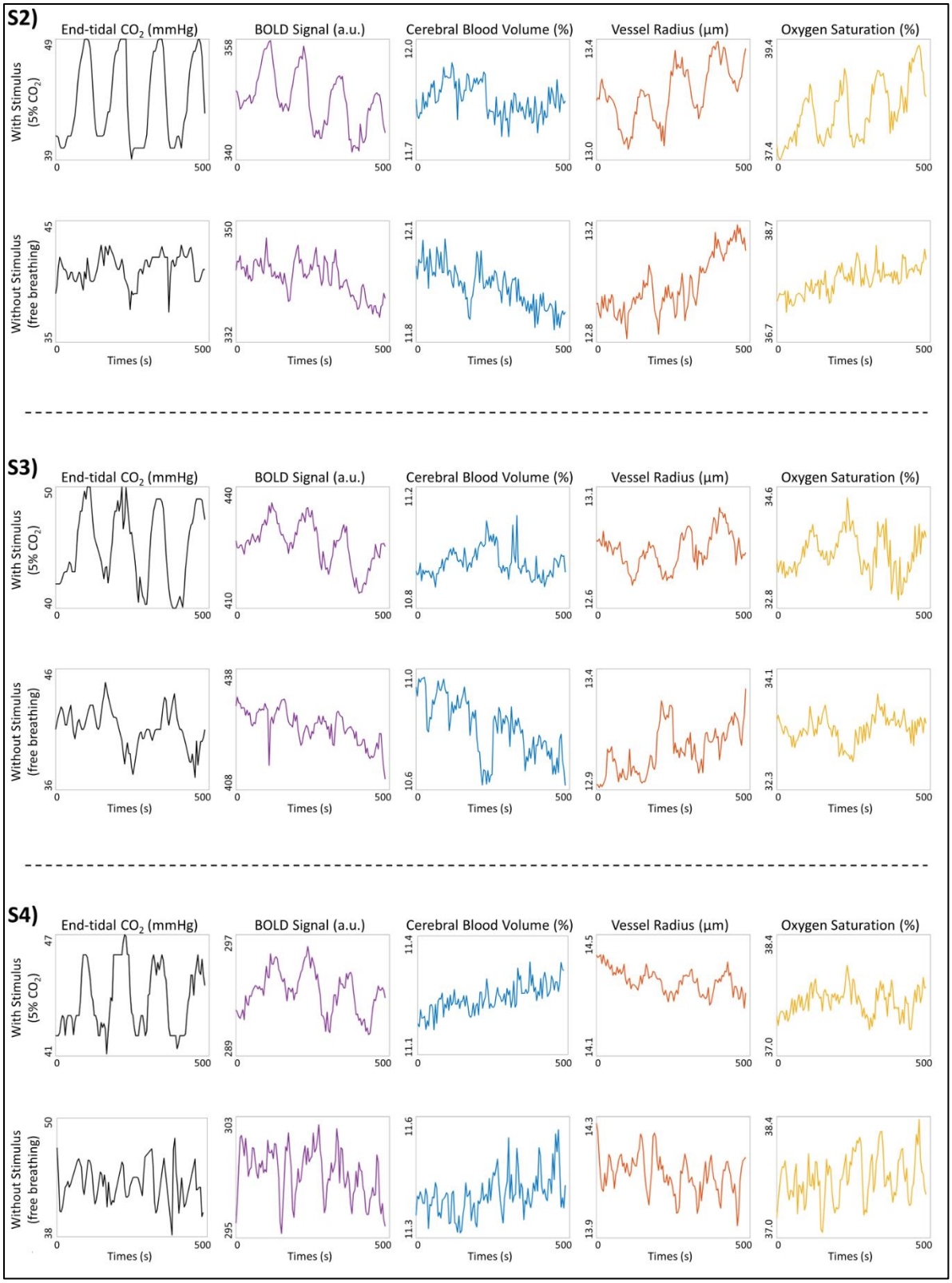


**Figure A6.2. Gray Matter Signal Time Courses During Hypercapnic Study**. Averaged time-courses of end-tidal $CO_2$, blood oxygen level dependent (BOLD) signal, cerebral blood volume (CBV), microvascular vessel radius (R), and tissue oxygen saturation ($SO_2$) acquired during hypercapnic stimulus blocks and during free breathing from three other pilot participants (S2, S3, and S4). BOLD, CBV, R, and $SO_2$ values represent gray matter averages.

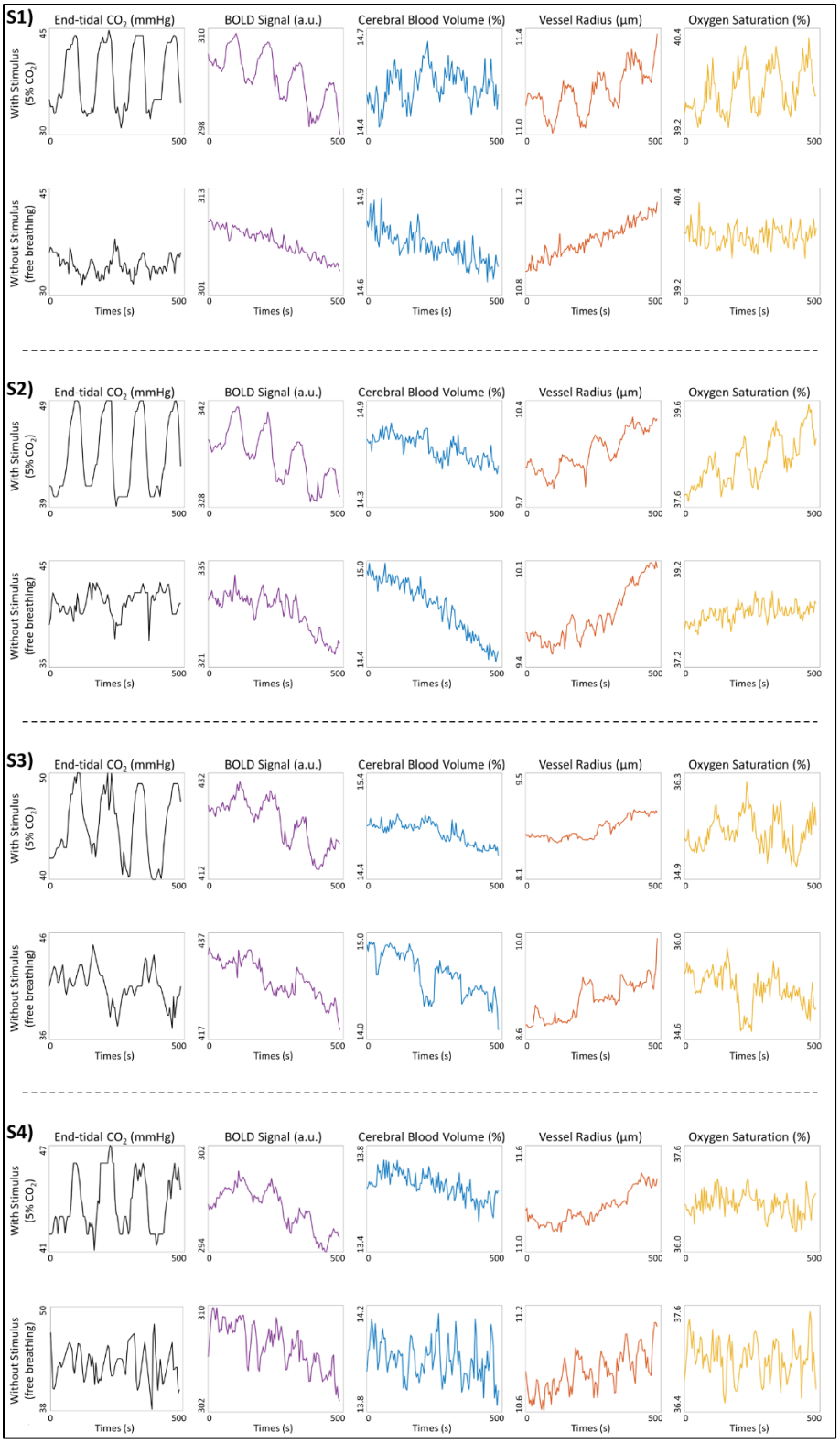


**Figure A6.3. White Matter Signal Time Courses During Hypercapnic Study**. End-tidal $CO_2$, and white matter averaged time-courses of blood oxygen level dependent (BOLD) signal, cerebral blood volume (CBV), microvascular vessel radius (R), and tissue oxygen saturation ($SO_2$) acquired during hypercapnic stimulus blocks and during free breathing from all four participants.

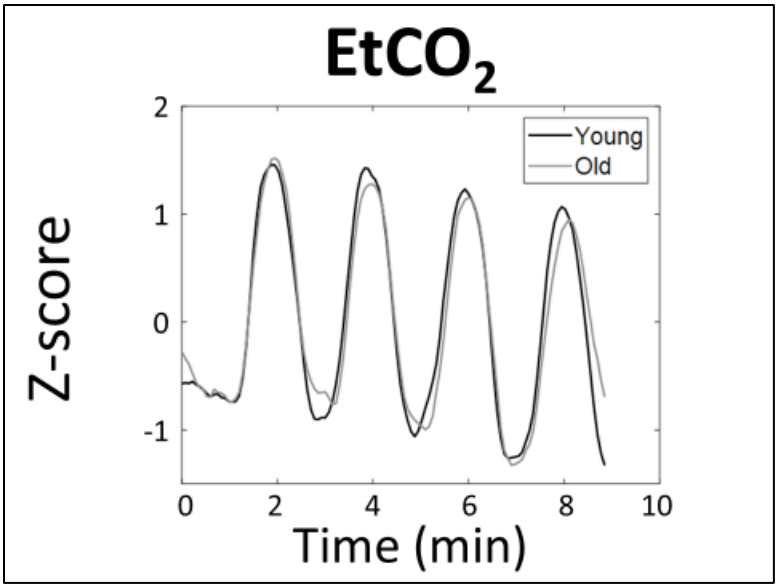


**Figure A7.1. Average End-Tidal $CO_2$ Changes for Young and Old Cohorts**. The end-tidal $CO_2$ ($EtCO_2$) time courses averaged across all participants after detrending and normalization for the young (black line) and old (gray line) cohorts during hypercapnic stimulus blocks block acquisition.

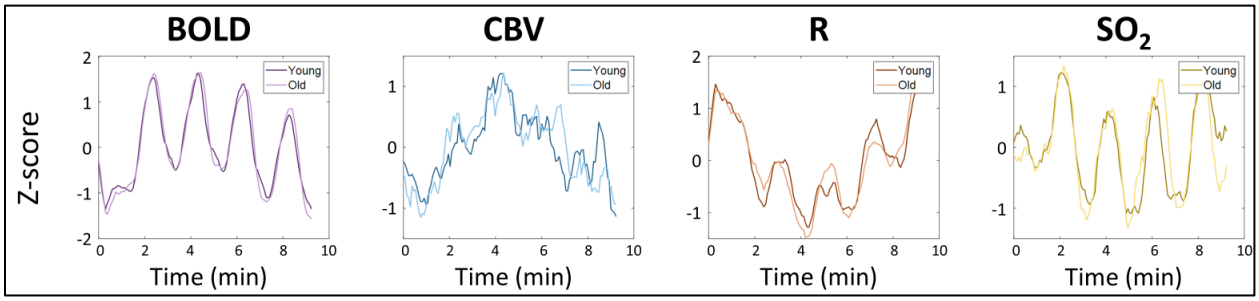


**Figure A7.2. Average White Matter Time Courses of BOLD, CBV, R, and $SO_2$ for Young and Old Cohorts**. The white matter parameter Z-scores averaged across all participants in the young (darker lines) and old (lighter lines) cohorts. Fluctuations of blood oxygen level dependent (BOLD) signal, cerebral blood volume (CBV), microvascular vessel radius (R), and tissue oxygen saturation ($SO_2$) acquired during hypercapnic stimulus blocks are shown.

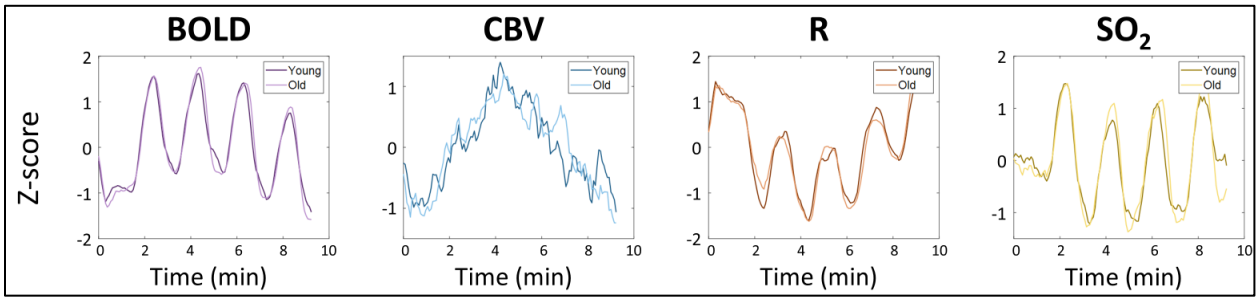


**Figure A7.3. Average Whole-brain Time Courses of BOLD, CBV, R, and $SO_2$ for Young and Old Cohorts**. The whole-brain parameter Z-scores averaged across all participants in the young (darker lines) and old (lighter lines) cohorts. Fluctuations of blood oxygen level dependent (BOLD) signal, cerebral blood volume (CBV), microvascular vessel radius (R), and tissue oxygen saturation ($SO_2$) acquired during hypercapnic stimulus blocks are shown.

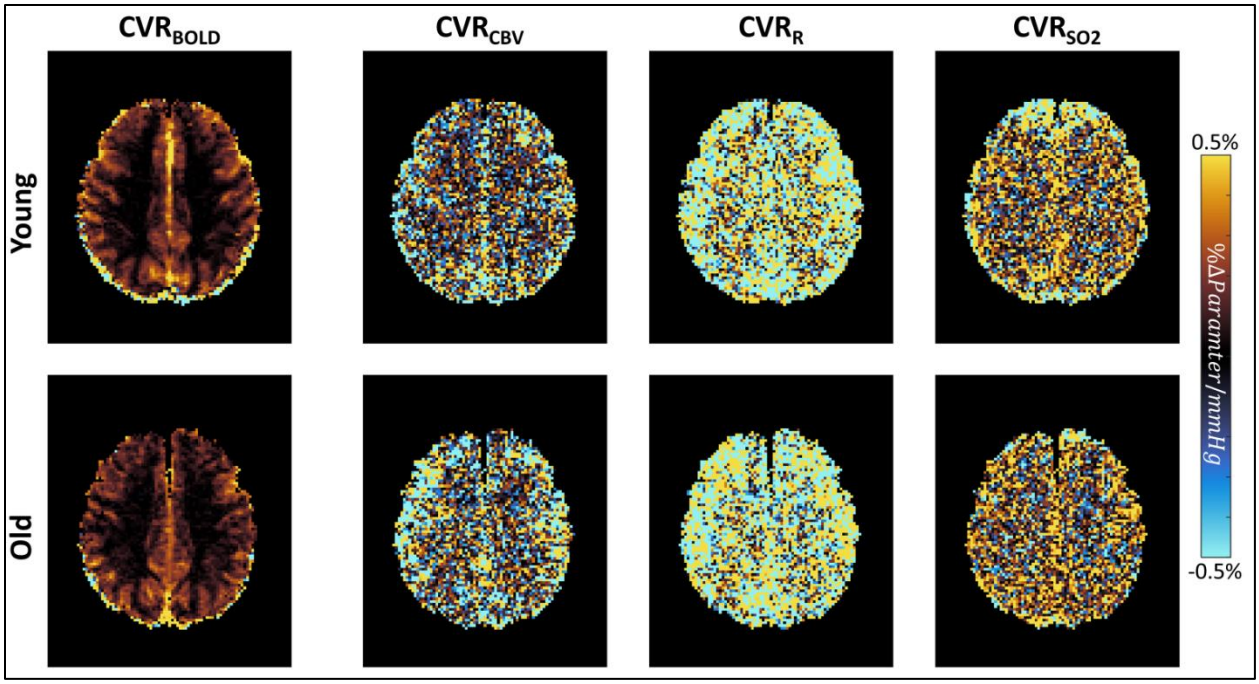


**Figure A7.4. Average CVR Maps Derived from MRvF Imaging for Young and Old Cohorts**. To generate these, voxelwise cerebrovascular reactivity (CVR) maps were generated for each subject by regressing the time-course of blood oxygen level dependent (BOLD) signal, cerebral blood volume (CBV), vessel radius (R), and oxygen saturation ($SO_2$) of each voxel independently against the subject's end-tidal $CO_2$ time-course. These subject CVR maps were then averaged across parameter and age group.

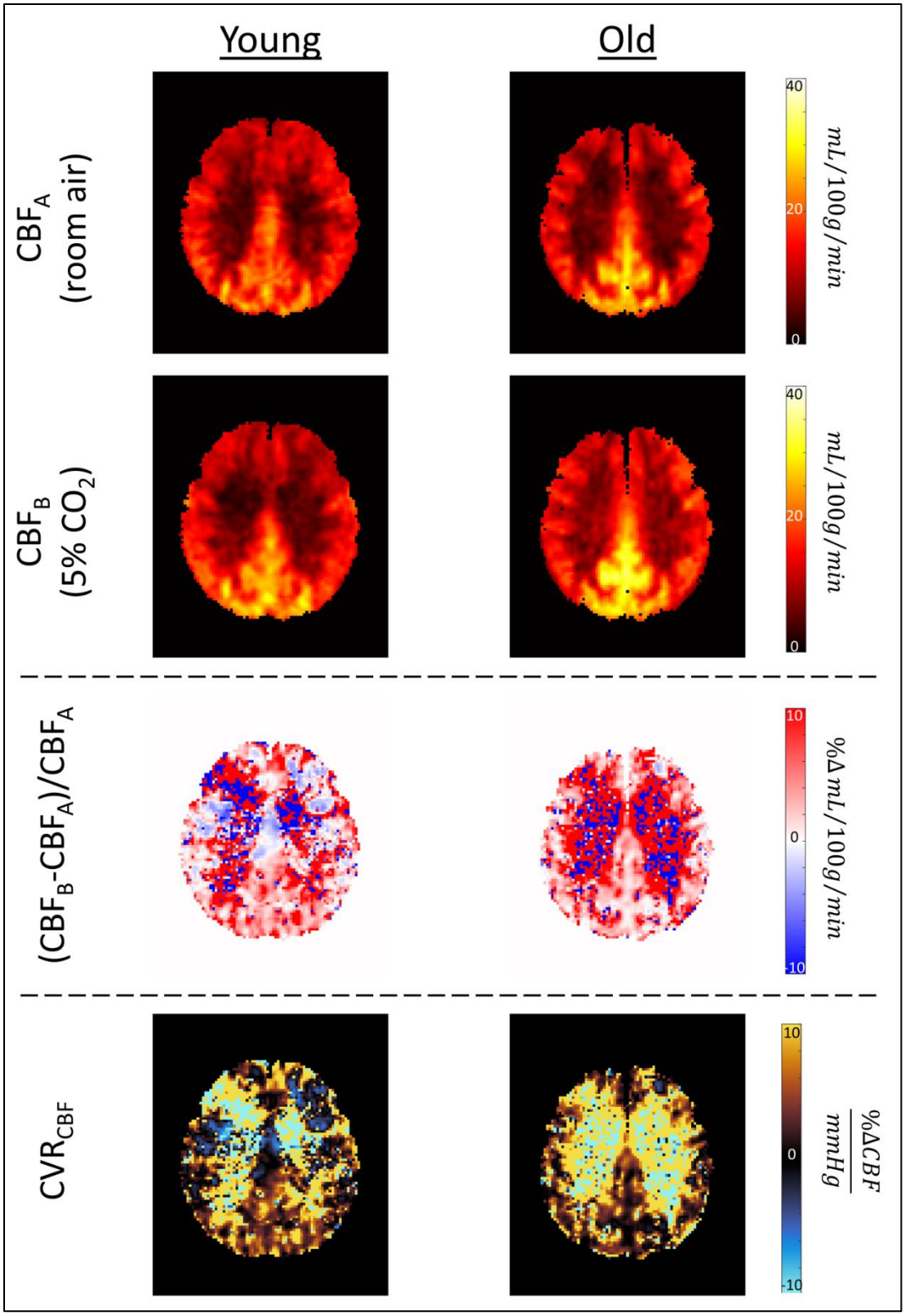


**Figure A7.5. Comparing CBF Response to Hypercapnia for Young and Old Cohorts**. Group average cerebral blood flow (CBF) maps were calculated for the ASL scan acquired during normal air breathing (1st row) and during 5% $CO_2$ gas inhalation (2nd row). The percent change in CBF was calculated for each subject and average across the group (3rd row) before being normalized to each subject's change in $EtCO_2$ during the hypercapnic scan for determination of CBF-derived cerebrovascular reactivity (CVR) and group averaging (4th row).

## C | Supplementary Tables

**Table A4.1. Modeling and Matching Method Variations**

| | Signal | Iterative | $T_2$ | Vessel Number | Virtual Voxel Size | Dictionary Size |
|---|---|---|---|---|---|---|
| **A** | Complex | No | No | Constant | Variable | 64,000 |
| **B** | Magnitude | No | No | Constant | Variable | 64,000 |
| **C** | Complex | Yes | No | Constant | Variable | 64,000 |
| **D** | Magnitude | Yes | No | Constant | Variable | 64,000 |
| **E** | Magnitude | No | Yes | Constant | Variable | 2,560,000 |
| **F** | Magnitude | Yes | Yes | Constant | Variable | 2,560,000 |
| **G** | Magnitude | No | No | Variable | Constant | 64,000 |
| **H** | Magnitude | Yes | No | Variable | Constant | 64,000 |
| **J** | Magnitude | No | Yes | Variable | Constant | 2,560,000 |
| **K** | Magnitude | Yes | Yes | Variable | Constant | 2,560,000 |

**Table A5.1. Biophysical Model Parameters Used for Generating Dictionaries with Finer Sampling in Normal Physiological Ranges**

| | Parameter Values | Number of Values |
|---|---|---|
| **Cerebral Blood Volume (CBV)** | [0.1:0.3:0.1, 1.25:0.25:5, 5.5:0.5:10, 11:1:15, 17:2:25] % | 40 |
| **Vessel Radii (R)** | [2:0.5:18, 19:1:25] μm | 40 |
| **Oxygen Saturation ($SO_2$)** | [0, 5:2.5:100] % | 40 |

**Table A6.1. Normalized Regression Coefficients of BOLD and MRvF Parameters Against $EtCO_2$ During Block Hypercapnic Stimulus in Gray Matter**

| | $\beta_0$ | $\beta_1$ | $\beta_2$ |
|---|---|---|---|
| BOLD | 0.90 ± 0.040 | 2.1e-3 ± 8.1e-4 | -3.2e-5 ± 2.0e-5 |
| CBV | 0.97 ± 0.012 | 4.0e-4 ± 2.6e-4 | 5.5e-6 ± 1.4e-5 |
| R | 1.03 ± 0.013 | -9.9e-4 ± 4.5e-4 | 8.0e-6 ± 2.1e-5 |
| $SO_2$ | 0.91 ± 0.044 | 1.7e-3 ± 6.9e-4 | 1.3e-5 ± 2.2e-5 |

Table displays the mean ± standard deviation of the regression coefficients across all four participants. Parameters were normalized to the maximum value in their time course prior to regression.

**Table A6.2. Normalized Regression Coefficients of BOLD and MRvF Parameters Against $EtCO_2$ During Block Hypercapnic Stimulus in White Matter**

| | $\beta_0$ | $\beta_1$ | $\beta_2$ |
|---|---|---|---|
| BOLD | 0.94 ± 0.024 | 1.4e-3 ± 4.8e-4 | -4.8e-5 ± 1.2e-5 |
| CBV | 0.97 ± 0.038 | 5.0e-4 ± 1.1e-4 | -2.0e-5 ± 1.7e-5 |
| R | 1.01 ± 0.068 | -1.2e-3 ± 2.7e-4 | 6.7e-5 ± 2.7e-5 |
| $SO_2$ | 0.93 ± 0.038 | 1.2e-3 ± 5.4e-4 | 1.5e-5 ± 2.6e-5 |

Table displays the mean ± standard deviation of the regression coefficients across all four participants. Parameters were normalized to the maximum value in their time course prior to regression.

**Table A7.1. Biophysical Model Parameters Used for Generating Dictionary with Evenly Spaced Sampling Throughout Physiological Range**

| | Parameter Values | Number of Values |
|---|---|---|
| **Cerebral Blood Volume (CBV)** | [0.4:0.4:24] % | 60 |
| **Vessel Radii (R)** | [2:2:50] m | 25 |
| **Oxygen Saturation ($SO_2$)** | [0:2.5:100] % | 41 |

**Table A7.2. White Matter CVR Measures from BOLD, MRvF, and CBF Parameters During Hypercapnic Stimuli**

| | Young | Old |
|---|---|---|
| $CVR_{BOLD}\left(\frac{\%\Delta BOLD}{mmHg}\right)$ | 0.10 ± 0.030 | 0.095 ± 0.014 |
| $CVR_{CBV}\left(\frac{\%\Delta CBV}{mmHg}\right)$ | 0.011 ± 0.013 | 0.024 ± 0.029 |
| $CVR_{R}\left(\frac{\%\Delta Radius}{mmHg}\right)$ | -0.16 ± 0.052 | -0.20 ± 0.12 |
| $CVR_{SO2}\left(\frac{\%\Delta SO_2}{mmHg}\right)$ | 0.067 ± 0.026 | 0.070 ± 0.017 |
| $CVR_{CBF}\left(\frac{\%\Delta CBF}{mmHg}\right)$ | 5.6 ± 20 | 8.1 ± 23 |

Table displays the mean ± standard deviation of the CVR measurements across all participants in each group

**Table A7.3. Whole-brain CVR Measures from BOLD, MRvF, and CBF Parameters During Hypercapnic Stimuli**

| | Young | Old |
|---|---|---|
| $CVR_{BOLD}\left(\frac{\%\Delta BOLD}{mmHg}\right)$ | 0.19 ± 0.048 | 0.17 ± 0.032 |
| $CVR_{CBV}\left(\frac{\%\Delta CBV}{mmHg}\right)$ | 0.0046 ± 0.0092 | 0.017 ± 0.021 |
| $CVR_{R}\left(\frac{\%\Delta Radius}{mmHg}\right)$ | -0.20 ± 0.059 | -0.22 ± 0.097 |
| $CVR_{SO2}\left(\frac{\%\Delta SO_2}{mmHg}\right)$ | 0.11 ± 0.040 | 0.11 ± 0.033 |
| $CVR_{CBF}\left(\frac{\%\Delta CBF}{mmHg}\right)$ | 3.7 ± 14 | 4.5 ± 15 |

Table displays the mean ± standard deviation of the CVR measurements across all participants in each group

## D | Copyright Acknowledgements

**Figure 2.1** reprinted from Quick et al.[15] under the terms of Creative Commons Attribution License (CC BY).

**Figure 2.2** reprinted from Vemuri et al.[28] under the terms of Creative Commons Attribution License (CC BY).

**Figure 2.3** reprinted from Bhogal et al.[41] with permission from Elsevier.

**Figure 2.4** reprinted from Sleight et al.[39] with permission from Wolters Kluwer Health, Inc.

**Figure 2.5** reprinted from Liu et al.[60] with permission from Elsevier.

**Figure 3.1** reprinted from Radiology Café[72,73] with permission from Radiology Café.

**Figure 3.2** reprinted from Radiology Café[73,75,76] with permission from Radiology Café.

**Figure 3.3** reprinted from MRIquestions.com[83] with permission courtesy of Allen D. Elster.

**Figure 3.4** reprinted from Granziera et al.[86] with permission from Oxford University Press.

**Figure 3.5** reprinted from Panda et al.[94] with permission from Elsevier.

**Figure 6.1** reprinted from Lu et al.[169] with permission from the JoVE.

**Figure 8.1** reprinted from Delphin et al.[122] under the terms of Creative Commons Attribution License (CC BY-NC-ND).

**Figure 8.2** reprinted from Velasco et al.[202] under the terms of Creative Commons Attribution License (CC BY).

**Figure 8.3** reprinted from Cao et al.[205] with permission from John Wiley & Sons, Inc.

**Figure A3.1** reprinted from Pannetier et al.[110] under the terms of Creative Commons Attribution License (CC BY).

**Figure A3.2** reprinted from Ni et al.[116] with permission from John Wiley & Sons, Inc.

**Figure A3.3** reprinted from Schmiedeskamp et al.[117] with permission from John Wiley & Sons, Inc.

**Figure A4.1** reprinted from Ni et al.[116] with permission from John Wiley & Sons, Inc.